Vacuum polarisation on asymptotically anti-de Sitter spacetimes

Thomas Morley

Submitted for the degree of Doctor of Philosophy

School of Mathematics and Statistics

November 2020

Supervisor: Prof. Elizabeth Winstanley

University of Sheffield

ABSTRACT

This thesis considers a real, massless, conformally coupled scalar field propagating on the covering space of four-dimensional anti-de Sitter space (CadS) and on four-dimensional Schwarzschild-anti de Sitter space (SadS).

Numerical results for the vacuum polarisation are obtained in CadS with Robin conditions imposed at the boundary. A proof is given to demonstrate that results approach the same finite limit at the boundary unless Dirichlet conditions are imposed.

Numerical results for the vacuum polarisation are obtained in SadS with Dirichlet conditions imposed at the boundary, using the extended coordinates method of renormalisation. These results are then extended for Robin boundary conditions, where we see qualitatively similar behaviour to that observed in CadS.

ACKNOWLEDGEMENTS

Firstly, I would like to thank my supervisor Elizabeth Winstanley for her support, guidance and incredible patience. It has been an honour to work with Elizabeth for the past four years; my research would be nowhere near the standard it is without her continued encouragement, advice and detailed feedback. Thank you for allowing me to accompany you on your journey into anti-de Sitter spacetime.

I would also like to thank Peter Taylor for introducing me to the "extended coordinates" method and for useful collaboration over the years. The original work presented in this thesis is the result of many, many fascinating and useful conversations with Peter. It's a shame that the coronavirus pandemic prevented me from visiting him in Dublin - perhaps some time in the future I will finally make it to DCU!

I acknowledge financial support from the School of Mathematics and Statistics at the University of Sheffield for allowing me to conduct research into a subject that I am extremely passionate about, and for giving me the opportunity to attend conferences across Europe - in Rome, the French Alps and Germany.

My thanks also go to members of Sheffield's CRAG group past and present, including Vis, Tom, Jake, Jake, Carl, Mohamed, Elisa, David, Axel, Richard, Elsa, Theo, Sam, Steffen and Carsten. It's been a pleasure to be involved in such a friendly and welcoming research group, thanks for all the cake.

Outside of academia, I would like to thank all members of the Elemental Theatre Company for helping keep me sane (just). Chris, Luke, Tom, Rhian, Paula, Elise, Ezra - when I'm having a difficult day, you always put a smile on my face.

Last, but by no means least, I would like to thank my parents, grandma and sister for their support and unconditional love. There's much more I could say, but you already know.

Contents

Preface

The work done in Schwarzschild spacetime in section 1.2.3 is mostly based on the calculations of [1,2], albeit simplified to the two-dimensional case. The results presented in section 1.2.4 are taken directly from [1, 3] without any prior calculation performed by the author. The calculation of the Hadamard form of the Feynman Green's function in section 1.3.2 and appendix A is taken from [4].

In chapter 2, the verification of the conformal mapping between ESU and CadS is taken from [5]. The mode solutions in adS found in section 3.2 are also given in [5]. In section 3.2.3, the generalisation of the mode solutions to encompass all possible Robin boundary conditions is first discussed in [6].

New work done by the author includes (i) the calculation of vacuum expectation values in CadS with Robin conditions imposed (published in [7], discussed in this thesis in chapter 3), (ii) the calculation of thermal expectation values in CadS with Robin conditions imposed (also published in [7] and discussed in chapter 3), (iii) the calculation of vacuum polarisation in non-spherical SadS black hole spacetimes when Dirichlet conditions are applied (published in [8], discussed in this thesis in chapter 5), and (iv) the calculation of vacuum polarisation in topological SadS black hole spacetimes when Robin conditions are applied (published in [9], discussed in this thesis in chapter 6).

The calculation of the vacuum polarisation on the spherical SadS black hole with Dirichlet conditions imposed has previously been done in [10]. In chapter 5, the calculation is repeated using the extended coordinates method. The extended coordinates method is first discussed in [11, 12] in the Schwarzschild-Tangherlini spacetime, with the SadS extension published by the author and collaborators in [8].

The work presented in section 5.7.1 is taken from [13], whilst the work presented in sections 5.7.2, 5.7.3 is original work of the author.

The author would like to acknowledge the help and support of his supervisor, Prof. Elizabeth Winstanley, as well as Dr Peter Taylor.

Part I

Introduction

Chapter 1

Quantum field theory in flat and curved spacetimes

This introductory chapter contains background material on quantum field theory (QFT) necessary for the calculations of expectation values that we present in later chapters. We begin in section 1.1 with a brief introduction to quantum field theory in flat (Minkowski) spacetime, including an overview of the canonical commutation relations and Green's functions. In section 1.2, we extend this to curved spacetimes, where we begin with a brief discussion of the Einstein field equations, before looking at the properties of the stress-energy tensor. In section 1.2.1, we introduce the concept of a Cauchy surface and explain why the existence of Cauchy surfaces is vital for a well-defined QFT. We look at the Unruh effect and the existence of multiple vacuum states in curved spacetimes in section 1.2.2, considering Schwarzschild spacetime as an example in section 1.2.3. Finally, in section 1.3, we look at various renormalisation schemes that allow us to calculate expectation values, and weigh the merits of the various methods against each other.

We will always work in 4-dimensional spacetime with Lorentzian signature $(-+++)$ unless otherwise stated (some examples in section 1.2 are set in conformally flat 2-dimensional spacetimes where calculations are much simpler). We set all constants $c = G = \hbar = k_B = 1$.

1.1 Quantum field theory in Minkowski spacetime

QFT is our best description of small scale physics. In quantum mechanics (QM) we take measurable quantities, such as position, velocity or angular momentum, and promote these to operators acting on a Hilbert space of states. In QFT, we promote classical fields to operators. As a result, an operator is assigned to every point $(t, \mathbf{x})$ in spacetime, giving us an infinite number of degrees of freedom. A set of such operators $\hat{\phi}(t, \mathbf{x})$ is then referred to as a quantum field, and particles are defined by excited states of these underlying fields. The following discussion of quantum fields in Minkowski space is taken from [14–19].

The dynamics of classical fields ϕ are governed by the Lagrangian L,

$$L(t) = \int_{\mathcal{M}} \mathcal{L}(\phi)\ d^3\mathbf{x} \tag{1.1}$$

where $\mathcal{L}$ is the Lagrangian density, defined by

$$\mathcal{L}(\phi) = -\frac{1}{2}\left(\partial^\mu\phi\partial_\mu\phi + m^2\phi^2\right) \tag{1.2}$$

for m the field mass, and $\mathcal{M}$ is the entire space. For the purposes of this thesis, we shall consider ϕ to be a real scalar field, which associates a real scalar value to every point in space and is invariant under Lorentz transformations. Scalar fields describe spin-0 particles, and real scalar fields describe particles that are uncharged.

The action S is defined by taking the integral of $\mathcal{L}$ over all spacetime, that is

$$S(\phi) = \int_{-\infty}^{\infty}\int_{\mathcal{M}} \mathcal{L}(\phi)\ d^3\mathbf{x}\ dt \tag{1.3}$$

and then we can use the principle of least action to derive the equations of motion, i.e. by insisting that

$$\delta S = 0 \tag{1.4}$$

for varying ϕ. This gives us the Klein-Gordon equation

$$\left(\partial^\mu\partial_\mu - m^2\right)\phi = 0. \tag{1.5}$$

A set of solutions to (1.5) is given by plane waves

$$\phi_{\mathbf{p}}(t,\mathbf{x}) = \phi_0 e^{-i\omega t} e^{i\mathbf{p}\cdot\mathbf{x}} \tag{1.6}$$

for frequency ω and 3-momentum $\mathbf{p}$, where $\omega^2 - |\mathbf{p}|^2 = m^2$, the field mass. We shall only consider the case where $\omega > 0$, and thus refer to $\phi_{\mathbf{p}}$ as positive frequency modes. This step is taken to ensure the modes have positive norm, and thus allow us to define an inner product. The negative frequency modes can then be obtained by taking the complex conjugate, $\phi^*_{\mathbf{p}}$. The constant ϕ_0 is defined such that the modes are normalised to 1. In order to determine this, we must define an inner product

$$\langle\phi_1,\phi_2\rangle = -i\int_{\mathcal{M}} (\phi_1^* \overleftrightarrow{\partial_t} \phi_2) d^3\mathbf{x} \tag{1.7}$$

where ϕ_1, ϕ_2 satisfy (1.5). In (1.7), we have used the notation

$$\phi_1^* \overleftrightarrow{\partial_t} \phi_2 = \phi_2\partial_t\phi_1^* - \phi_1^*\partial_t\phi_2. \tag{1.8}$$

If we define

$$\phi_1(t,\mathbf{x}) = \phi_{01}e^{-i\omega_1 t}e^{i\mathbf{p}_1\cdot\mathbf{x}},\quad \phi_2(t,\mathbf{x}) = \phi_{02}e^{-i\omega_2 t}e^{i\mathbf{p}_2\cdot\mathbf{x}} \tag{1.9}$$

then the inner product is

$$\begin{aligned}\langle \phi_1, \phi_2 \rangle &= -i \int_{\mathcal{M}} d^3\mathbf{x}\ \phi_{01}^* \phi_{02} i(\omega_1 + \omega_2) e^{-i(\omega_2 - \omega_1)t} e^{-i(\mathbf{p}_1 - \mathbf{p}_2)\cdot\mathbf{x}} \\ &= \phi_{01}^* \phi_{02} (\omega_1 + \omega_2) \delta^3(\mathbf{p}_1 - \mathbf{p}_2)(2\pi)^3 e^{-i(\omega_2 - \omega_1)t}. \end{aligned} \tag{1.10}$$

Therefore, we must set

$$\phi_0 = (2\pi)^{-3/2}(2\omega)^{-1/2} \tag{1.11}$$

for modes to be normalised.

The quantised field operator $\hat{\phi}$ must obey the equal time commutation relations

$$[\hat{\phi}(t,\mathbf{x}), \hat{\pi}(t,\mathbf{y})] = i\delta^3(\mathbf{x} - \mathbf{y}), \quad [\hat{\phi}(t,\mathbf{x}), \hat{\phi}(t,\mathbf{y})] = 0 = [\hat{\pi}(t,\mathbf{x}), \hat{\pi}(t,\mathbf{y})] \tag{1.12}$$

where

$$\hat{\pi}(t,\mathbf{x}) = \partial_t \hat{\phi}(t,\mathbf{x}) \tag{1.13}$$

is the conjugate momentum. The quantised field can be expanded in terms of the modes (1.6),

$$\hat{\phi}(t,\mathbf{x}) = \int (\hat{a}_{\mathbf{p}} \phi_{\mathbf{p}}(t,\mathbf{x}) + \hat{a}_{\mathbf{p}}^\dagger \phi_{\mathbf{p}}^*(t,\mathbf{x})) d^3\mathbf{p} \tag{1.14}$$

where $\hat{a}_{\mathbf{p}}$, $\hat{a}_{\mathbf{p}}^\dagger$ are annihilation and creation operators respectively. The integral in (1.14) is taken over all momenta. The annihilation and creation operators must obey the canonical commutation relations (CCR):

$$[\hat{a}_{\mathbf{p}}, \hat{a}_{\mathbf{p}'}^\dagger] = \delta(\mathbf{p} - \mathbf{p}'), \quad [\hat{a}_{\mathbf{p}}, \hat{a}_{\mathbf{p}'}] = 0 = [\hat{a}_{\mathbf{p}}^\dagger, \hat{a}_{\mathbf{p}'}^\dagger]. \tag{1.15}$$

These can be derived from (1.12). We use the annihilation operators to define the ground state $|0\rangle$:

$$\hat{a}_{\mathbf{p}}|0\rangle = 0. \tag{1.16}$$

We shall refer to the ground state $|0\rangle$ as the “vacuum state” throughout. It carries zero momentum, and, naïvely, one may expect it to also carry zero energy, as the state is “empty”, i.e. there are no field quanta present. However, a brief calculation of energy density in the vacuum state (see [14]) gives

$$\langle 0|H|0\rangle = \frac{1}{2}\sum_{\mathbf{p}} \omega \tag{1.17}$$

which is not only non-zero, but also appears to be divergent. This comes from the fact that, since there is no upper bound on ω, the zero-point energy can become arbitrarily large. Since this energy is not measurable in non-gravitational physics, we can renormalise this quantity by simply throwing away the $\frac{1}{2}\sum_{\mathbf{p}} \omega$. Renormalisation is not so simple in curved spacetime, where divergent parts of the energy density have a more complicated form (see section 1.3).

Vacuum expectation values of various products of field operators $\hat{\phi}$ can be identified with different Green's functions that satisfy the inhomogeneous scalar field equation

$$\left(\partial^{\mu}\partial_{\mu} - m^2\right)\mathcal{G}(x,x') = -\delta^4(x-x') \tag{1.18}$$

where $x = (t,\mathbf{x})$ are spacetime coordinates and $\mathcal{G}$ is used to represent a number of Green's functions, which we shall now introduce. The four-dimensional Dirac delta function $\delta^4(x-x')$ is defined to be infinite at $x' = x$, and zero everywhere else. It satisfies the identity

$$\int_{-\infty}^{\infty} \delta^4(x)\ d^4x = 1. \tag{1.19}$$

We define the Schwinger and Hadamard function respectively:

$$iG(x,x') = \langle 0|[\hat{\phi}(x),\hat{\phi}(x')]|0\rangle, \tag{1.20}$$

$$G^{(1)}(x,x') = \langle 0|\{\hat{\phi}(x),\hat{\phi}(x')\}|0\rangle. \tag{1.21}$$

We can split these into positive and negative frequency parts

$$iG(x,x') = G^{+}(x,x') - G^{-}(x,x'), \tag{1.22}$$

$$G^{(1)}(x,x') = G^{+}(x,x') + G^{-}(x,x'), \tag{1.23}$$

where $G^{\pm}(x,x')$ are the Wightman functions

$$G^{+}(x,x') = \langle 0|\hat{\phi}(x)\hat{\phi}(x')|0\rangle, \tag{1.24}$$

$$G^{-}(x,x') = \langle 0|\hat{\phi}(x')\hat{\phi}(x)|0\rangle. \tag{1.25}$$

The Wightman functions are not Green's functions of the scalar field equation. The Feynman propagator can be defined by introducing the time-ordering operator $\mathcal{T}$,

$$\mathcal{T}[\hat{\phi}(x)\hat{\phi}(x')] = \begin{cases} \hat{\phi}(x)\hat{\phi}(x') & \text{if } x \text{ is in the future of } x' \\ \hat{\phi}(x')\hat{\phi}(x) & \text{if } x' \text{ is in the future of } x. \end{cases} \tag{1.26}$$

Then the Feynman propagator is

$$iG_F(x,x') = \langle 0|\mathcal{T}[\hat{\phi}(x)\hat{\phi}(x')]|0\rangle = \Theta(t-t')G^{+}(x,x') + \Theta(t'-t)G^{-}(x,x') \tag{1.27}$$

for $\Theta(t-t')$ the Heaviside step function. Finally, we can define the retarded and advanced Green's functions in the following way:

$$G_{Ret}(x,x') = -\Theta(t-t')G(x,x') \tag{1.28}$$

$$G_{Adv}(x,x') = \Theta(t'-t)G(x,x'). \tag{1.29}$$

We can then write the Feynman propagator as

$$G_F(x,x') = -\bar{G}(x,x') - \frac{1}{2}iG^{(1)}(x,x') \tag{1.30}$$

where $\bar{G}(x,x')$ is the average of the retarded and advanced Green's functions

$$\bar{G}(x,x') = \frac{1}{2}[G_{Ret}(x,x') + G_{Adv}(x,x')]. \tag{1.31}$$

If we write $\mathcal{G}$ to represent any of the Green's functions in the set $\{iG_F, G_{Ret}, G_{Adv}\}$, then these can be written as

$$\mathcal{G}(x,x') = \int \frac{d^4\mathbf{k}}{(2\pi)^4} \frac{e^{i\mathbf{k}\cdot(\mathbf{x}-\mathbf{x}')+ik_0(t-t')}}{-k_0^2 + k^2 + m^2} \tag{1.32}$$

where $k^2 = k_1^2 + k_2^2 + k_3^2$. The integral has poles at $k_0^2 = k^2 + m^2$. The integral can be evaluated as a contour integral. The choice of Green's function depends on the choice of contour that we use. These contours are shown in Figure 1.1.

Equivalently, the Feynman Green's function $G_F(x,x')$ can be found by employing the $i\epsilon$-prescription, which involves writing the Green's function in the following way:

$$iG_F(x,x') = \lim_{\epsilon \to 0} \int \frac{d^4\mathbf{k}}{(2\pi)^4} \frac{e^{i\mathbf{k}\cdot(\mathbf{x}-\mathbf{x}')+ik_0(t-t')}}{-k_0^2 + k^2 + m^2 + i\epsilon}. \tag{1.33}$$

The addition of the $i\epsilon$ term shifts the integral so that we do not pass directly through the poles.

We can define thermal Green's functions with inverse temperature β by simply replacing the vacuum expectation values with thermal expectation values, i.e. for the Wightman functions

$$G_\beta^+(x,x') = \langle \beta | \hat{\phi}(x)\hat{\phi}(x') | \beta \rangle, \quad G_\beta^-(x,x') = \langle \beta | \hat{\phi}(x')\hat{\phi}(x) | \beta \rangle. \tag{1.34}$$

These satisfy the periodicity condition

$$G_\beta^\pm(t,\mathbf{x};t',\mathbf{x}') = G_\beta^\mp(t+i\beta,\mathbf{x};t',\mathbf{x}'). \tag{1.35}$$

From (1.23), we must also have

$$G_\beta^{(1)}(t,\mathbf{x};t',\mathbf{x}') = G_\beta^{(1)}(t+i\beta,\mathbf{x};t',\mathbf{x}'). \tag{1.36}$$

Now, the Schwinger function $iG(x,x')$ is an expectation value of the commutator, which is itself a c-number (a scalar multiple of the identity operator). Therefore, the vacuum and thermal expectation values of the Schwinger function are equal [14], i.e.

$$iG_\beta(x,x') = iG(x,x'). \tag{1.37}$$

We can write

$$iG(x,x') = \frac{1}{2\pi}\int_{-\infty}^{\infty} d\omega \; c(\omega;\mathbf{x},\mathbf{x}') e^{-i\omega\Delta t} \tag{1.38}$$

where $c(\omega;\mathbf{x},\mathbf{x}')$ is calculated by using the appropriate contour in (1.32), and then taking the Fourier transform of the result. We have used $\Delta t = t - t'$. Similarly, we can write the thermal Wightman functions as

$$G_\beta^\pm(x,x') = \frac{1}{2\pi}\int_{-\infty}^{\infty} d\omega \; g^\pm(\omega;\mathbf{x},\mathbf{x}') e^{-i\omega\Delta t} \tag{1.39}$$

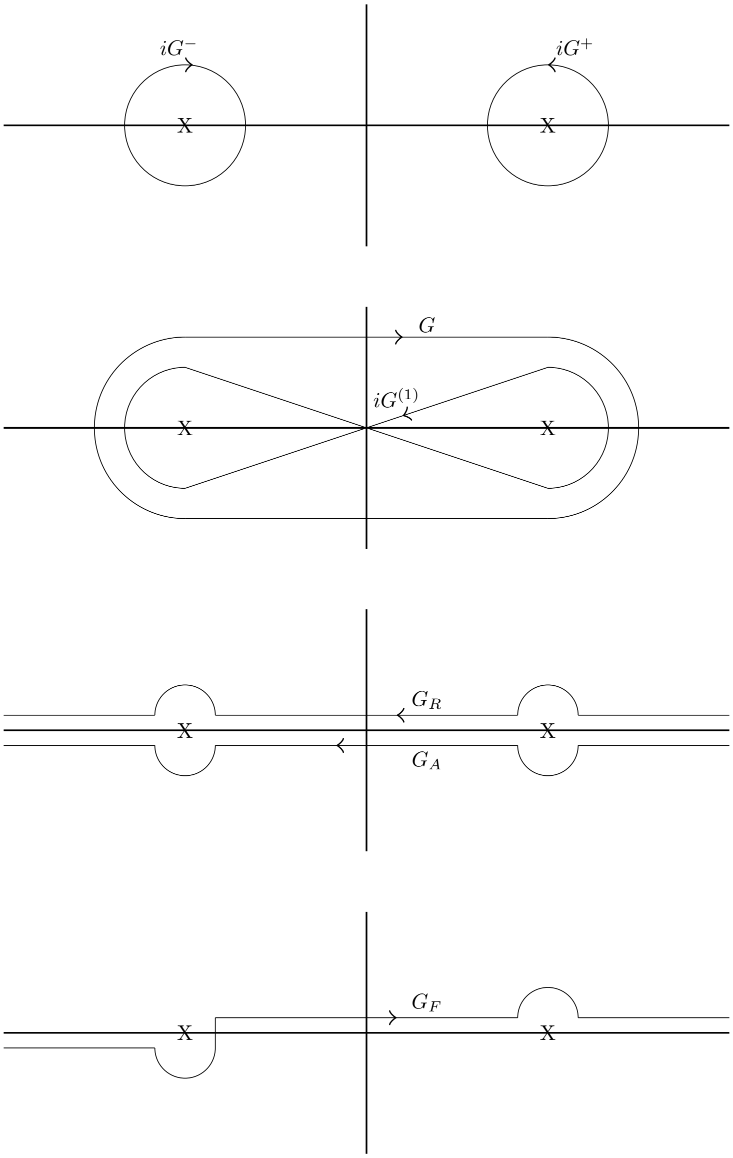

Figure 1.1: Possible contours for the k_0 integral in (1.33). A different choice of contour corresponds to a different choice of Green's function. Figure taken from [14].

where $g^{\pm}(\omega;\mathbf{x},\mathbf{x}')$ is determined by again using the appropriate contour in (1.33) and taking the Fourier transform. Using the relation (1.35), we find

$$g^{+}(\omega;\mathbf{x},\mathbf{x}') = e^{\beta\omega} g^{-}(\omega;\mathbf{x},\mathbf{x}') \tag{1.40}$$

and from (1.22), we can see that

$$c(\omega;\mathbf{x},\mathbf{x}') = g^{+}(\omega;\mathbf{x},\mathbf{x}') - g^{-}(\omega;\mathbf{x},\mathbf{x}'). \tag{1.41}$$

Combining these two relations, we can show

$$g^{\pm}(\omega;\mathbf{x},\mathbf{x}') = \pm\frac{c(\omega;\mathbf{x},\mathbf{x}')}{1-e^{\mp\beta\omega}} \tag{1.42}$$

and so

$$G^{\pm}_{\beta}(x,x') = \pm\frac{1}{2\pi}\int_{-\infty}^{\infty} d\omega\ \frac{c(\omega;\mathbf{x},\mathbf{x}')}{1-e^{\mp\beta\omega}} e^{-i\omega\Delta t}. \tag{1.43}$$

The thermal Hadamard function is then given by

$$\begin{aligned} G^{(1)}_{\beta}(x,x') &= \frac{1}{2\pi}\int_{-\infty}^{\infty} d\omega\ c(\omega;\mathbf{x},\mathbf{x}')\left\{\frac{1}{1-e^{-\beta\omega}} - \frac{1}{1-e^{\beta\omega}}\right\} e^{-i\omega\Delta t} \\ &= \frac{1}{2\pi}\int_{-\infty}^{\infty} d\omega\ c(\omega;\mathbf{x},\mathbf{x}') \coth\left(\frac{\beta\omega}{2}\right) e^{-i\omega\Delta t}. \end{aligned} \tag{1.44}$$

By studying the contour for the Feynman Green's function G_F, we notice that the contour does not pass through any poles if we perform an anti-clockwise rotation through $\pi/2$ to take it along the imaginary axis. Thus the Feynman Green's function would remain unchanged (modulo a factor of $-i$) after this rotation. This type of rotation is called a Wick rotation, and involves replacing the time coordinate t with an imaginary time coordinate τ i.e.

$$\tau = it. \tag{1.45}$$

Then the metric has signature $(+\ +\ +\ +)$ and this corresponds to considering the field $\hat{\phi}$ in the Euclidean background. The wave equation (1.18) is a hyperbolic PDE in the Lorentzian background, which leads to different possible Green's functions. In the Euclidean background, the wave equation (1.18) becomes elliptic, and so the Euclidean Green's function G_E is unique (if it exists) once appropriate boundary conditions have been specified. The Euclidean Green's function G_E is related to the Feynman Green's function by

$$G_F(t,\mathbf{x};t',\mathbf{x}') = -iG_E(i\tau,\mathbf{x};i\tau',\mathbf{x}'). \tag{1.46}$$

In the next section, we generalise the theory to a curved spacetime (CST) background.

1.2 Quantum field theory in curved spacetime

QFT in CST is a semi-classical approximation to quantum gravity. We begin with the Einstein Field Equations (EFEs),

$$G_{\mu\nu} + \Lambda g_{\mu\nu} = 8\pi T_{\mu\nu}. \tag{1.47}$$

These equations relate the curvature of spacetime, described by the Einstein tensor $G_{\mu\nu}$, to the matter within the spacetime, described by the stress-energy tensor (SET) $T_{\mu\nu}$.

The Einstein tensor is constructed from the spacetime metric $g_{\mu\nu}$ in the following way

$$G_{\mu\nu} = R_{\mu\nu} - \frac{1}{2}Rg_{\mu\nu} \tag{1.48}$$

where $R_{\mu\nu}$ is the Ricci tensor, and $R = R^{\mu}_{\mu}$ is the curvature scalar.

The SET describes the energy and momentum densities and fluxes on the spacetime. The components of the SET can be thought of in the following way:

$$T_{\mu\nu} = \begin{pmatrix} u & p_x & p_y & p_z \\ p_x & P_{xx} & \sigma_{xy} & \sigma_{xz} \\ p_y & \sigma_{yx} & P_{yy} & \sigma_{yz} \\ p_z & \sigma_{zx} & \sigma_{zy} & P_{zz} \end{pmatrix} \tag{1.49}$$

where u is the energy density, the p's are momentum densities, the P's are pressures and the σ's are shear stresses [20]. The SET is symmetric, i.e.

$$T_{\mu\nu} = T_{\nu\mu} \tag{1.50}$$

and conserved

$$\nabla^{\mu}T_{\mu\nu} = 0. \tag{1.51}$$

The SET of a Klein-Gordon field ϕ is given by [21]

$$T_{\mu\nu} = \nabla_{\mu}\phi\nabla_{\nu}\phi - \frac{1}{2}g_{\mu\nu}(\nabla_{\sigma}\nabla^{\sigma}\phi + (m^2 + \xi R)\phi^2). \tag{1.52}$$

The cosmological constant Λ is a measure of the vacuum energy density and has dimensions of length^{-2}. It was originally introduced by Einstein to achieve a static universe [22]. However, the idea was abandoned when the universe was found to be expanding [23]. In 1998, observations of supernovae found that the expansion of the universe was accelerating, and it is now widely accepted that there exists a small, nonzero, positive cosmological constant [24, 25].

The EFEs were first postulated by Einstein in 1915, and have been tested in the century since by many different experiments [26], including measurements of the perihelion of Mercury, the redshift of light from Sirius B, and more recently direct detections of gravitational waves by the LIGO collaboration [27,28] and of black holes by the Event Horizon Telescope [29].

In order to use the EFEs at a quantum scale, we would need to quantise gravity, but, to date, no full theory of quantum gravity has been developed. Instead, we can form a semi-classical approximation by quantising the RHS of (1.47), that is, promoting $T_{\mu\nu}$ to an operator and taking its expectation value,

$$G_{\mu\nu} + \Lambda g_{\mu\nu} = 8\pi\langle\hat{T}_{\mu\nu}\rangle. \tag{1.53}$$

This semi-classical approach allows us to study the backreaction effect of particle creation close to a black hole [30], for example. The equation (1.53) is only an approximation of the true dynamics of spacetime, and can only be taken seriously if the characteristic radii of curvature of the spacetime are much greater than the Planck length [31].

1.2.1 General formalism

In CST, the Lagrangian density for a scalar field ϕ, which we shall denote $\mathcal{L}_g$, is defined by

$$\mathcal{L}_g(\phi) = -\frac{1}{2}(g^{\mu\nu}\nabla_\mu\phi\nabla_\nu\phi + (m^2 + \xi R)\phi^2). \tag{1.54}$$

There are two notable differences between (1.54) and the formula for the Lagrangian density in Minkowski space (1.2). First, we have included the spacetime metric to allow us to raise indices, and we have replaced partial derivatives with covariant derivatives (although of course this reduces to a partial derivative in the case of a scalar field). Second, we have an extra "ξR" term which is included for a couple of reasons, the first of which is simply because it has the correct dimensions. The second reason is due to the fact that the special value $\xi = 1/6$ allows the action to have conformal invariance in the massless $m = 0$ case [32]. This means that the Lagrangian density remains the same under the transformation

$$g_{\mu\nu} \to \Omega^2 g_{\mu\nu}, \quad \phi \to \Omega^{-1}\phi \tag{1.55}$$

for any smooth positive function Ω.

The Klein-Gordon equation in curved spacetime takes the form

$$\left(\Box - m^2 - \xi R\right)\phi = 0 \tag{1.56}$$

where

$$\Box = g^{\mu\nu}\nabla_\mu\nabla_\nu \tag{1.57}$$

is the D'Alembertian. Similarly, the Green's functions $\mathcal{G}(x, x')$ satisfy the inhomogeneous form of the Klein-Gordon equation,

$$\left(\Box - m^2 - \xi R\right)\mathcal{G}(x, x') = -\frac{\delta^4(x - x')}{\sqrt{|g|}}. \tag{1.58}$$

We must define an inner product in order to normalise the field ϕ. In flat spacetime, the inner product is defined by (1.7). The definition of an inner product in curved spacetime is a little more involved, because we must define this over a Cauchy surface of the spacetime.

Cauchy surfaces exist in globally hyperbolic spacetimes. They allow initial data to propagate uniquely into the future without the need for any additional boundary conditions. For a more rigorous mathematical definition [21], we must first define the future and past domains of dependence for a surface Σ in a manifold $\mathcal{M}$:

$$D^+(\Sigma) = \left\{ p \in \mathcal{M} \,\middle|\, \begin{array}{l}\text{Every past inextensible causal curve} \\ \text{through } p \text{ intersects } \Sigma\end{array} \right\} \tag{1.59}$$

$$D^-(\Sigma) = \left\{ p \in \mathcal{M} \,\middle|\, \begin{array}{l}\text{Every future inextensible causal curve} \\ \text{through } p \text{ intersects } \Sigma\end{array} \right\}. \tag{1.60}$$

We can then define the full domain of dependence as being

$$D(\Sigma) = D^+(\Sigma) \cup D^-(\Sigma). \tag{1.61}$$

The surface Σ is a Cauchy surface when

$$D(\Sigma) = \mathcal{M}. \tag{1.62}$$

For now, we shall assume that the spacetime we are working in *is* globally hyperbolic, i.e. assume that there exists some hypersurface Σ for which (1.62) holds, and define a scalar product between two solutions ϕ_1, ϕ_2 of the Klein-Gordon equation (1.56) to be

$$\langle \phi_1, \phi_2 \rangle = i \int_\Sigma (\phi_1^* \overleftrightarrow{\nabla}_\mu \phi_2) \sqrt{-g}\; d\sigma^\mu \tag{1.63}$$

where $g = \det(g_{\mu\nu})$ and $d\sigma^\mu = n^\mu d^3\mathbf{x}$ for n^μ future-pointing unit normal to Σ. This scalar product must be independent of the choice of Cauchy surface, i.e. for two Cauchy surfaces Σ_1, Σ_2 we must have (see Figure 1.2):

$$i \int_{\Sigma_1} (\phi_1^* \overleftrightarrow{\nabla}_\mu \phi_2) \sqrt{-g}\; d\sigma_1^\mu = i \int_{\Sigma_2} (\phi_1^* \overleftrightarrow{\nabla}_\mu \phi_2) \sqrt{-g}\; d\sigma_2^\mu. \tag{1.64}$$

In order to prove that the above statement (1.64) holds, we use Stokes' theorem (taken from [32, eq.E14]):

$$\int_\mathcal{R} d^4x \sqrt{|g|} \nabla^\mu V_\mu = \int_{\partial\mathcal{R}} d^3\mathbf{x} \sqrt{|\gamma|} \bar{n}^\mu V_\mu. \tag{1.65}$$

The volume integral is taken over a region $\mathcal{R}$ of the manifold $\mathcal{M}$, where $\partial\mathcal{R}$ is the boundary of $\mathcal{R}$ and $\bar{n}^\mu$ is the outward-pointing unit normal to the boundary. The induced volume element on the hypersurface $\partial\mathcal{R}$ is $\sqrt{|\gamma|} d^3\mathbf{x}$.

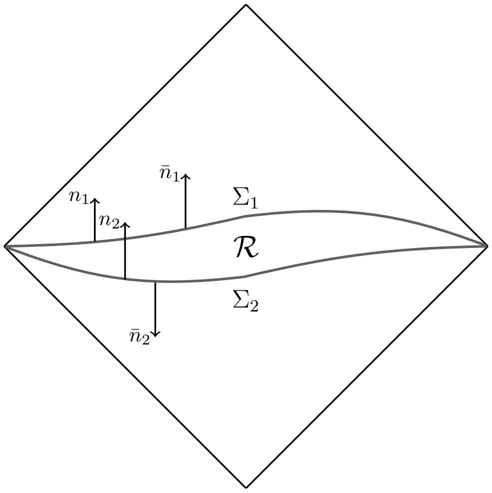

Figure 1.2: A globally hyperbolic space with two Cauchy surfaces Σ_1, Σ_2. The future-pointing unit normals n_1 and n_2 are shown, as are the outward-pointing unit normals $\bar{n}_1, \bar{n}_2$ to region $\mathcal{R}$.

We let $\mathcal{R}$ be the region between the two Cauchy surfaces, so that $\partial\mathcal{R} = \Sigma_1 \cup \Sigma_2$. We define $V_\mu = \phi_1^* \overleftrightarrow{\nabla}_\mu \phi_2$, where we assume ϕ_1 and ϕ_2 are solutions of (1.56). Then we can say

$$\begin{aligned}
\nabla^\mu V_\mu &= \nabla^\mu \left[(\nabla_\mu \phi_1^*)\phi_2 - \phi_1^*(\nabla_\mu \phi_2)\right] \\
&= (\nabla^\mu \nabla_\mu \phi_1^*)\phi_2 + (\nabla_\mu \phi_1^*)(\nabla^\mu \phi_2) - \phi_1^*(\nabla^\mu \nabla_\mu \phi_2) - (\nabla^\mu \phi_1^*)(\nabla_\mu \phi_2) \\
&= (\Box \phi_1^*)\phi_2 - \phi_1^*(\Box \phi_2) \\
&= (m^2 + \xi R)\phi_1^* \phi_2 - \phi_1^*(m^2 + \xi R)\phi_2 = 0 \qquad (1.66)
\end{aligned}$$

and thus

$$\int_{\mathcal{R}} d^4x \sqrt{|g|} \nabla^\mu V_\mu = 0. \qquad (1.67)$$

The right hand side of (1.65) can be written

$$\int_{\partial\mathcal{R}} d^3\mathbf{x}\ \bar{n}^\mu V_\mu \sqrt{|\gamma|} = \int_{\Sigma_1} d^3\mathbf{x} (\phi_1^* \overleftrightarrow{\nabla}_\mu \phi_2) \sqrt{-g} \bar{n}_1^\mu + \int_{\Sigma_2} d^3\mathbf{x} (\phi_1^* \overleftrightarrow{\nabla}_\mu \phi_2) \sqrt{-g} \bar{n}_2^\mu = 0, \quad (1.68)$$

where $\bar{n}_1^\mu$ and $\bar{n}_2^\mu$ are the outward pointing unit normals to Σ_1 and Σ_2 respectively. With these Cauchy surfaces as in Figure 1.2, we can see that $\bar{n}_1^\mu$ will point in the same direction as n_1^μ whereas $\bar{n}_2^\mu$ will point in the opposite direction to n_2^μ. Thus,

$$\int_{\partial\mathcal{R}} d^3\mathbf{x}\ \bar{n}^\mu V_\mu \sqrt{|\gamma|} = \int_{\Sigma_1} d^3\mathbf{x} (\phi_1^* \overleftrightarrow{\nabla}_\mu \phi_2) \sqrt{-g} n_1^\mu - \int_{\Sigma_2} d^3\mathbf{x} (\phi_1^* \overleftrightarrow{\nabla}_\mu \phi_2) \sqrt{-g} n_2^\mu = 0 \quad (1.69)$$

and so (1.64) holds. This proof is taken from [33, pg.9].

1.2.2 The Unruh effect

The Unruh effect [34–36] is the idea that the notion of a “particle” detected by an observer will depend on the frame in which the observer is moving. This means that an observer accelerating in the Minkowski vacuum will see a thermal bath of Rindler particles where an inertial observer will see none. We refer to Rindler particles as those associated with the positive energy modes as defined by accelerating (or Rindler) observers, and Minkowski particles as those associated with positive energy modes as defined by inertial observers.

To demonstrate this idea, we work in $1+1$-dimensional Minkowski spacetime for simplicity, as the wave equation is conformally invariant in two dimensions. Consider two observers. One observer is in an inertial frame, defined by Minkowski coordinates (t, x), and the other observer is in an accelerating frame, defined by Rindler coordinates (ξ^0, ξ^1). Firstly, it would be useful to define our Rindler coordinates in terms of Minkowski coordinates [16]. To do this, we introduce null coordinates

$$u_M = t - x,\ v_M = t + x,\ u_R = \xi^0 - \xi^1,\ v_R = \xi^0 + \xi^1. \tag{1.70}$$

A trajectory x^α of an uniformly accelerated observer in the inertial frame is described by Minkowski coordinates,

$$x^\alpha(\tau) = (u_M(\tau), v_M(\tau)) \tag{1.71}$$

where τ is the proper time. The trajectory $x^\alpha(\tau)$ satisfies the normalisation condition

$$g_{\alpha\beta}\dot{x}^\alpha(\tau)\dot{x}^\beta(\tau) = -1, \tag{1.72}$$

where $g_{\alpha\beta}$ is the spacetime metric and $\dot{x} = \frac{dx}{d\tau}$. The trajectory $x^\alpha(\tau)$ has constant acceleration a, given by

$$g_{\alpha\beta}\ddot{x}^\alpha(\tau)\ddot{x}^\beta(\tau) = a^2, \tag{1.73}$$

where $\ddot{x} = \frac{d^2x}{d\tau^2}$. In terms of Minkowski coordinates (u_M, v_M), these conditions give

$$\dot{u}_M(\tau)\dot{v}_M(\tau) = 1,\ \ \ddot{u}_M(\tau)\ddot{v}_M(\tau) = -a^2. \tag{1.74}$$

The equations (1.74) can be solved simultaneously to give

$$u_M(\tau) = -\frac{1}{a}e^{-a\tau},\ \ v_M(\tau) = \frac{1}{a}e^{a\tau} \tag{1.75}$$

where the integration constants are made to vanish by shifting the origin of the inertial frame. Now, since proper time is independent of coordinate system, this means that in Rindler coordinates, the observer’s worldline is described by

$$\xi^0(\tau) = \tau,\ \ \xi^1(\tau) = 0 \tag{1.76}$$

and so the Rindler coordinates on the worldline are

$$u_R = v_R = \tau. \tag{1.77}$$

Substituting (1.77) into (1.75) gives a relation between (u_M, v_M) and (u_R, v_R), i.e.

$$u_M = -\frac{1}{a}e^{-au_R}, \quad v_M = \frac{1}{a}e^{av_R}. \tag{1.78}$$

Using the definition of the null coordinates (1.70), we can see

$$t = \frac{1}{a}e^{a\xi^1}\sinh(a\xi^0), \quad x = \frac{1}{a}e^{a\xi^1}\cosh(a\xi^0). \tag{1.79}$$

Since the wave equation is invariant in two dimensions, we can write it in both coordinate systems in the same way:

$$\frac{\partial^2}{\partial u_M \partial v_M}\phi = 0, \quad \frac{\partial^2}{\partial u_R \partial v_R}\phi = 0. \tag{1.80}$$

Solving (1.80), we find two sets of modes

$$\phi = A_\omega e^{-i\omega u_M} + B_\omega e^{-i\omega v_M}, \quad \phi = A_\Omega e^{-i\Omega u_R} + B_\Omega e^{-i\Omega v_R} \tag{1.81}$$

for normalisation constants $A_\omega, B_\omega, A_\Omega, B_\Omega$. We fix $\omega, \Omega > 0$ and consider only positive frequency modes. Hence we can define the field operator in two different ways

$$\begin{aligned}\hat{\phi} &= \int_0^\infty d\omega \left\{ A_\omega e^{-i\omega u_M}\hat{a}_\omega + B_\omega e^{-i\omega v_M}\hat{b}_\omega + A_\omega^* e^{i\omega u_M}\hat{a}_\omega^\dagger + B_\omega^* e^{i\omega v_M}\hat{b}_\omega^\dagger \right\} \\ &= \int_0^\infty d\Omega \left\{ A_\Omega e^{-i\Omega u_R}\hat{a}_\Omega + B_\Omega e^{-i\Omega v_R}\hat{b}_\Omega + A_\Omega^* e^{i\Omega u_R}\hat{a}_\Omega^\dagger + B_\Omega^* e^{i\Omega v_R}\hat{b}_\Omega^\dagger \right\},\end{aligned} \tag{1.82}$$

where $\hat{a}_\omega, \hat{b}_\omega, \hat{a}_\Omega, \hat{b}_\Omega$ are annihilation operators, and $\hat{a}_\omega^\dagger, \hat{b}_\omega^\dagger, \hat{a}_\Omega^\dagger, \hat{b}_\Omega^\dagger$ are creation operators. The annihilation and creation operators are related by Bogoliubov transformations

$$\hat{a}_\Omega = \int_0^\infty d\omega[\alpha_{\Omega\omega}\hat{a}_\omega - \beta_{\Omega\omega}\hat{a}_\omega^\dagger] \tag{1.83}$$

where $\alpha_{\Omega\omega}, \beta_{\Omega\omega}$ are Bogoliubov coefficients satisfying the normalisation condition

$$\int_0^\infty d\omega \ (\alpha_{\Omega\omega}\alpha_{\Omega'\omega}^* - \beta_{\Omega\omega}\beta_{\Omega'\omega}^*) = \delta(\Omega - \Omega'). \tag{1.84}$$

The Bogoliubov coefficients are non-zero, and defined in [14, eq. 3.36]. The Bogoliubov transform for the creation operator $\hat{a}_\Omega^\dagger$ is found simply by taking the Hermitian conjugate of (1.83). Similar transformations to (1.83) exist for $\hat{b}_\Omega, \hat{b}_\Omega^\dagger$.

The different annihilation operators define different vacuum states. The Minkowski vacuum $|M\rangle$ is the zero eigenvector of the annihilation operators $\hat{a}_\omega, \hat{b}_\omega$, i.e.

$$\hat{a}_\omega|M\rangle = \hat{b}_\omega|M\rangle = 0. \tag{1.85}$$

The Rindler vacuum $|R\rangle$ is defined as the zero eigenvector of the annhilation operators $\hat{a}_\Omega, \hat{b}_\Omega$, i.e.

$$\hat{a}_\Omega|R\rangle = \hat{b}_\Omega|R\rangle = 0. \tag{1.86}$$

The vacua $|M\rangle$ and $|R\rangle$ are different. We can see this by computing the number of Rindler particles in the Minkowski vacuum and showing that this is nonzero. This is done by calculating the expectation value of the number operator $\hat{N}_\Omega \equiv \hat{a}^\dagger_\Omega \hat{a}_\Omega$ in the Minkowski vacuum:

$$\begin{aligned}\langle \hat{N}_\Omega \rangle =& \langle M|\hat{a}^\dagger_\Omega \hat{a}_\Omega|M\rangle \\ =& \langle M| \left(\int d\omega [\alpha^*_{\Omega\omega}\hat{a}^\dagger_\omega - \beta^*_{\Omega\omega}\hat{a}_\omega] \right) \left(\int d\omega' [\alpha_{\Omega\omega'}\hat{a}_{\omega'} - \beta_{\Omega\omega'}\hat{a}^\dagger_{\omega'}] \right) |M\rangle \\ =& \int d\omega |\beta_{\Omega\omega}|^2. \end{aligned} \tag{1.87}$$

Thus, an accelerated observer will detect particles in $|M\rangle$ and, similarly, an inertial observer will detect particles in $|R\rangle$.

This is the Unruh effect. When spacetime is curved, two observers will have different notions of “time”. This choice of time leads to two different definitions of positive frequency, and thus two different definitions of vacuum state. Therefore, different choices of time lead to different vacua.

When we have a black hole, we can find three different types of vacuum state - the Boulware vacuum $|B\rangle$ [37], the Hartle-Hawking vacuum $|H\rangle$ [38], and the Unruh vacuum $|U\rangle$ [35] (see the introduction of [39] for a brief comparison of the three states). To explain these a little more, it is easiest to consider the example of 2-dimensional Schwarzschild spacetime.

1.2.3 Vacuum states on two-dimensional Schwarzschild

Schwarzschild spacetime is one of the simplest solutions of Einstein’s equations to contain a black hole. We consider it here to demonstrate the existence of multiple vacua, and to allow us to elaborate on the properties of these vacua. In two-dimensions, the metric is conformally flat:

$$ds^2 = -\left(1 - \frac{2M}{r}\right) dt^2 + \left(1 - \frac{2M}{r}\right)^{-1} dr^2, \tag{1.88}$$

where M is the black hole mass. The spacetime is globally hyperbolic and has an event horizon at $r_h = 2M$. A conformal diagram for the spacetime is shown in Figure 1.3.

We shall refer to the coordinates (t, r) used in (1.88) as the Schwarzschild coordinates. We transform to null coordinates (u, v) by writing

$$u = t - r^*, \quad v = t + r^* \tag{1.89}$$

where r^* is the tortoise coordinate defined by

$$\frac{dr^*}{dr} = \frac{1}{1 - \frac{2M}{r}} \quad \Rightarrow \; r^* = r + 2M \ln\left(\frac{r}{2M} - 1\right). \tag{1.90}$$

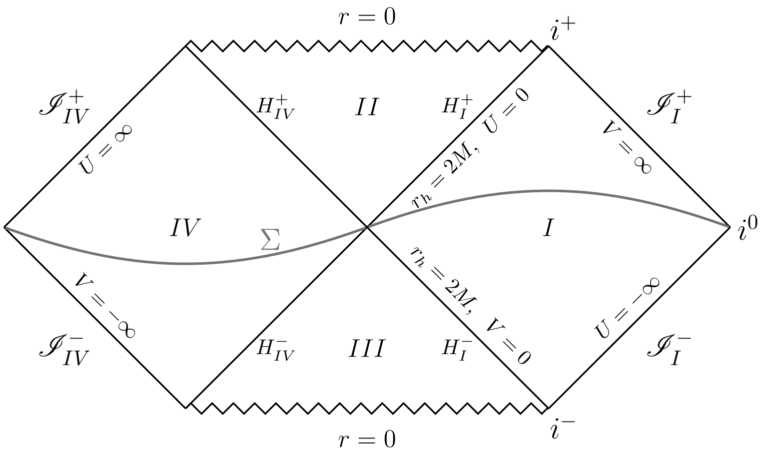

Figure 1.3: The conformal diagram for Schwarzschild spacetime. Region I corresponds to the spacetime exterior, whilst region II corresponds to the black hole interior, region III the white hole interior, and region IV a parallel universe. The horizon r_h and the singularity $r = 0$ are labelled. The values of the Kruskal coordinates (U, V) are given along the horizons and null infinities. The spacetime is globally hyperbolic - a Cauchy surface Σ is shown.

The metric is then given by

$$ds^2 = -\left(1 - \frac{2M}{r}\right) du\ dv \tag{1.91}$$

where r can now be treated as a function of u and v. These coordinates only cover the black hole exterior (region I in Figure 1.3). We can cover the whole spacetime with the Kruskal coordinates (U, V), defined by

$$U = -4Me^{-u/4M}, \quad V = 4Me^{v/4M}. \tag{1.92}$$

The metric in the Kruskal coordinate system is then given by

$$ds^2 = -\frac{2M}{r} e^{-r/2M} dU dV \tag{1.93}$$

and we can define temporal and spatial Kruskal coordinates by

$$T = \frac{U + V}{2}, \quad X = \frac{V - U}{2}. \tag{1.94}$$

The wave equation for a massless scalar field is conformally invariant in two dimensions, which means in both coordinate systems we have

$$\left(\frac{\partial^2}{\partial t^2} - \frac{\partial^2}{\partial r^{*2}}\right) \phi = 0, \tag{1.95}$$

$$\left(\frac{\partial^2}{\partial T^2} - \frac{\partial^2}{\partial X^2}\right) \phi = 0. \tag{1.96}$$

(a) "In"-Schwarzschild modes (b) "Up"-Schwarzschild modes

Figure 1.4: The "in"-Schwarzschild modes start at past null infinity $\mathscr{I}_I^-$ and travel inwards towards the future horizon H_I^+, whilst the "up"-Schwarzschild modes begin at the past horizon H_I^- and travel upwards towards the future null infinity $\mathscr{I}_I^+$. Note that this is only true in two dimensions - in higher dimensions, modes get scattered, and "in"- and "up"-modes can end on both H_I^+ and $\mathscr{I}_I^+$.

Note that this is not true in four-dimensions; the wave equation can be solved in both coordinate systems, but is not conformally invariant, so analysis of both is a little more involved. The two-dimensional case is considered here to make our analysis as simple as possible.

The Boulware state

We shall begin by solving (1.95) to find the following mode solutions (which we shall call Schwarzschild modes),

$$\phi_S^{up} = A_\omega^{up} \exp[-i\omega u], \tag{1.97}$$

$$\phi_S^{in} = A_\omega^{in} \exp[-i\omega v], \tag{1.98}$$

for $\omega \in \mathbb{R}_{>0}$ and $A_\omega^{up}, A_\omega^{in}$ normalisation constants. We use the subscript S since the modes are written in terms of Schwarzschild coordinates. We call ϕ_S^{up} the "up"-Schwarzschild modes because these travel upwards from the past horizon H_I^- and towards future null infinity $\mathscr{I}_I^+$. Similarly, the ϕ_S^{in} are referred to as "in"-Schwarzschild modes because they travel inwards towards the black hole (see Figure 1.4).

Now, to calculate normalisation constants A_ω^{up} and A_ω^{in}, we need to integrate over a Cauchy surface for region I. The actual values of these normalisation constants is not so important for the discussion here, but the calculation of them provides a useful example of evaluating scalar products. We can approximate our Cauchy surface by integrating over $\Sigma = H_I^- \cup \mathscr{I}_I^-$ - strictly speaking, the Cauchy surface will be spacelike and arbitrarily close to Σ. Each part of this surface has a different normal attached to it. The normal to H_I^- points in the V-direction and the normal to $\mathscr{I}_I^-$ points in the U-direction. The scalar product (1.63) requires unit normals, but H_I^- and $\mathscr{I}_I^-$ are both null, implying that their normals must also be null. This means that we cannot define a unit normal, because any normal n^μ to Σ will have $n^\mu n_\mu = 0$.

So how do we integrate over a null surface? We follow the working in [40] and define a hypersurface Σ by putting a restriction on the coordinates

$$f(x^\alpha) = 0. \tag{1.99}$$

The unit normal n_α is then defined by

$$n_\alpha = \frac{\epsilon f_{,\alpha}}{|g^{\mu\nu} f_{,\mu} f_{,\nu}|^{1/2}} \tag{1.100}$$

where $\epsilon = -1$ if Σ is spacelike, and $\epsilon = +1$ if Σ is timelike. The inclusion of ϵ ensures that n^α points in the direction of increasing f [40]. When Σ is null, then $g^{\mu\nu} f_{,\mu} f_{,\nu} = 0$, and the unit normal is undefined, as expected.

For a non-null surface, the line element is then defined by

$$d\Sigma^\mu = \sqrt{-g} e^\mu dy \tag{1.101}$$

where y are intrinsic coordinates on Σ and

$$e^\mu = \frac{\partial x^\mu}{\partial y} \tag{1.102}$$

is a vector tangent to curves contained in Σ.

For a null surface, we define $e_\alpha = -f_{,\alpha}$ to be the unit normal, where a negative sign is used to ensure that e^α is future pointing when f is increasing towards the future. The choice of f does not affect our work here; whilst it is possible, for example, to rescale f, it is the choice of orthonormal basis that defines the integrals in (1.108) rather than the choice of f [40].

It is useful to write our Schwarzschild modes in terms of Kruskal coordinates (U, V):

$$\phi_S^{up} = A_\omega^{up} e^{-i\omega(-4M)\ln(-U/4M)} \Theta(-U), \tag{1.103}$$

$$\phi_S^{in} = A_\omega^{in} e^{-i\omega(4M)\ln(V/4M)} \Theta(V), \tag{1.104}$$

where we have used the Heaviside function to help specify the regions on which the modes are non-trivial. To make the algebra a little easier to deal with, we let

$$\tilde{U} = U/4M, \quad \tilde{V} = V/4M, \quad \hat{\omega} = 4M\omega \tag{1.105}$$

so that

$$\phi_S^{up} = A_\omega^{up} e^{i\hat{\omega}\ln(-\tilde{U})} \Theta(-\tilde{U}) \tag{1.106}$$

$$\phi_S^{in} = A_\omega^{in} e^{-i\hat{\omega}\ln(\tilde{V})} \Theta(\tilde{V}). \tag{1.107}$$

The integral is taken over $\Sigma = H_I^- \cup \mathscr{I}_I^-$,

$$\begin{aligned}\langle \phi_S^{up}(x;\omega), \phi_S^{up}(x;\omega')\rangle =& i\int_{\mathscr{I}_I^-} (\phi_S^{up*}(x;\omega)\overleftrightarrow{\partial_\mu}\phi_S^{up}(x;\omega'))e_1^\mu\sqrt{-g}\;dy \\ &+ i\int_{H_I^-} (\phi_S^{up*}(x;\omega)\overleftrightarrow{\partial_\mu}\phi_S^{up}(x;\omega'))e_2^\mu\sqrt{-g}\;dy \end{aligned} \tag{1.108}$$

where e_1^μ and e_2^μ are unit normals to $\mathscr{I}_I^-$ and H_I^- respectively and coordinate $y = \{\tilde{U}, \tilde{V}\}$. On $\mathscr{I}_I^-$, we have $\phi_S^{up} = 0$ so we can ignore the first integral in (1.108). The unit normal $(n_2)_\mu = -f_{,\mu}$ where, on H_I^-, $f(\tilde{U}, \tilde{V}) = \tilde{V} = 0$, so

$$\left.\begin{array}{l}(n_2)_{\tilde{V}} = -1 \\ (n_2)_{\tilde{U}} = 0\end{array}\right\} \Rightarrow \begin{array}{l}(n_2)^{\tilde{V}} = 0 \\ (n_2)^{\tilde{U}} = -\frac{r}{M}e^{r/2M}.\end{array} \tag{1.109}$$

The scalar product (1.108) therefore becomes

$$\langle \phi_S^{up}(x;\omega), \phi_S^{up}(x;\omega')\rangle = -i\int_{-\infty}^{0} (\phi_S^{up*}(x;\omega)\overleftrightarrow{\partial_{\tilde{U}}}\phi_S^{up}(x;\omega'))\left(-\frac{r}{2M}e^{r/2M}\right)\sqrt{-g}\;d\tilde{U}. \tag{1.110}$$

After some rearranging, and making the replacement $X = \ln(-\tilde{U})$, we find

$$\begin{aligned}\langle \phi_S^{up}(x;\omega), \phi_S^{up}(x;\omega')\rangle &= \int_{-\infty}^{\infty} A_\omega^{up*}A_{\omega'}^{up}(\hat{\omega}+\hat{\omega}')e^{-i(\hat{\omega}-\hat{\omega}')X}dX \\ &= 2\pi A_\omega^{up*}A_{\omega'}^{up}(\omega+\omega')\delta(\omega'-\omega).\end{aligned} \tag{1.111}$$

For modes to be normalised, we therefore need to set

$$A_\omega^{up} = \frac{1}{\sqrt{4\pi\omega}}. \tag{1.112}$$

The norm of the "in"-Schwarzschild modes is calculated in a similar way. The Cauchy surface can be chosen as before, but now $\phi_S^{in} = 0$ on H_I^-, and we have to consider the unit normal $(n_1)_\mu$, where

$$(n_1)^{\tilde{V}} = -\frac{r}{M}e^{r/2M}, \quad (n_1)^{\tilde{U}} = 0. \tag{1.113}$$

The integration over $\mathscr{I}_I^-$ proceeds in a very similar way to the previous case, and we find

$$A_\omega^{in} = \frac{1}{\sqrt{4\pi\omega}}. \tag{1.114}$$

We can use the "up"- and "in"-Schwarzschild modes (1.97-1.98) to build field operators:

$$\hat{\phi}_S = \int_0^\infty d\omega\{\hat{a}_\omega^{up}\phi_S^{up} + \hat{a}_\omega^{in}\phi_S^{in} + \hat{a}_\omega^{up\dagger}\phi_S^{up*} + \hat{a}_\omega^{in\dagger}\phi_S^{in*}\}. \tag{1.115}$$

The annihilation operators $\hat{a}_\omega^{up}, \hat{a}_\omega^{in}$ define the Boulware vacuum state [37],

$$\hat{a}_\omega^{up}|B\rangle = 0, \quad \hat{a}_\omega^{in}|B\rangle = 0. \tag{1.116}$$

We can calculate Wightman function in the Boulware state by noting that

$$\hat{\phi}_S|B\rangle = \int_0^\infty d\omega \left\{ \hat{a}_\omega^{up\dagger}\phi_S^{up*} + \hat{a}_\omega^{in\dagger}\phi_S^{in*} \right\} |B\rangle, \tag{1.117}$$

$$\langle B|\hat{\phi}_S = \int_0^\infty d\omega \langle B| \left\{ \hat{a}_\omega^{up}\phi_S^{up} + \hat{a}_\omega^{in}\phi_S^{in} \right\}, \tag{1.118}$$

and so

$$\begin{aligned} G_B(x,x') &= \langle B|\hat{\phi}_S(x)\hat{\phi}_S(x')|B\rangle \\ &= \int_0^\infty d\omega \int_0^\infty d\omega' \langle B| \left\{ \hat{a}_\omega^{up}\phi_S^{up}(x;\omega) + \hat{a}_\omega^{in}\phi_S^{in}(x;\omega) \right\} \\ &\qquad \times \left\{ \hat{a}_{\omega'}^{up\dagger}\phi_S^{up*}(x';\omega') + \hat{a}_{\omega'}^{in\dagger}\phi_S^{in*}(x';\omega') \right\} |B\rangle. \end{aligned} \tag{1.119}$$

We can use the CCR (1.15) to commute the annihilation and creation operators and thus obtain

$$G_B(x,x') = \int_0^\infty d\omega \int_0^\infty d\omega' \langle B|B\rangle \delta(\omega-\omega') \left\{ \phi_S^{up}(x;\omega)\phi_S^{up*}(x';\omega') + \phi_S^{in}(x;\omega)\phi_S^{in*}(x';\omega') \right\}. \tag{1.120}$$

The Boulware state is normalised such that $\langle B|B\rangle = 1$, and we obtain a mode expression for the Boulware Wightman function $G_B(x,x')$:

$$G_B(x,x') = \int_0^\infty d\omega \left\{ \phi_S^{up}(x)\phi_S^{up*}(x') + \phi_S^{in}(x)\phi_S^{in*}(x') \right\}. \tag{1.121}$$

Substituting in (1.97-1.98) we obtain the Wightman function in the Boulware state

$$G_B(x,x') = \int_0^\infty d\omega \frac{1}{4\pi\omega} \left\{ e^{-i\omega(u-u')} + e^{-i\omega(v-v')} \right\}. \tag{1.122}$$

From the point of view of a far away observer, the Boulware vacuum contains no particles, and is as empty as possible at infinity [41]. As a result, $\langle B|T_{\mu\nu}|B\rangle \to 0$ as $r \to \infty$. This is not the case on the horizon. The expectation value of the SET in the Boulware state diverges as $r \to r_h$ [1]. The state is appropriate for the description of vacuum polarisation around a cold star with radius larger than the event horizon [42]. The Boulware vacuum is invariant under time reversal.

The Hartle-Hawking state

We now solve the wave equation in Kruskal coordinates (1.96), to find a different set of mode functions,

$$\phi_K^{up} = B_\Omega^{up} \exp[-i\Omega U] \tag{1.123}$$

$$\phi_K^{in} = B_\Omega^{in} \exp[-i\Omega V]. \tag{1.124}$$

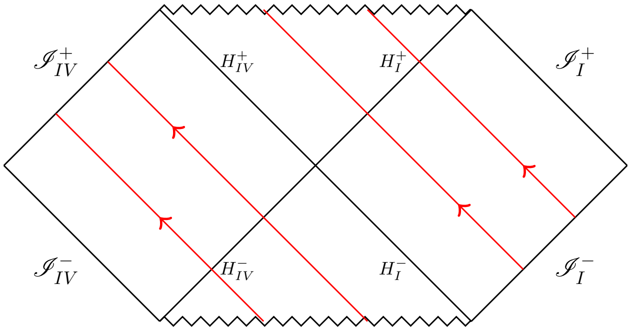

(a) "In"-Kruskal modes

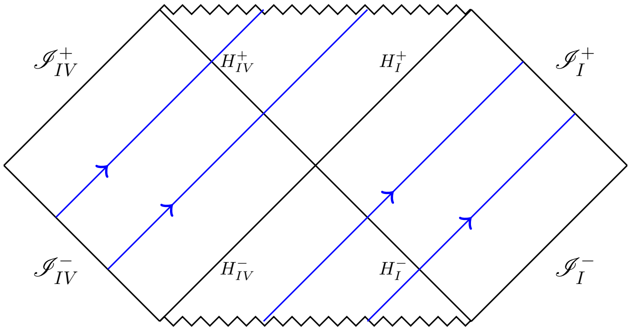

(b) "Up"-Kruskal modes

Figure 1.5: The "in"-Kruskal modes and "up"-Kruskal modes cover the entire spacetime.

We refer to these mode solutions as the "up" and "in"-Kruskal modes, labelled with a subscript K. We fix the frequency $\Omega > 0$, and consider only positive frequency modes. These modes are defined over the entire spacetime (see Figure 1.5).

The normalisation constants $B^{up}_\Omega, B^{in}_\Omega$ are determined by taking a scalar product over a Cauchy surface in a similar way to the calculation performed in the previous section. Since the modes are defined over the entire spacetime, the Cauchy surface is now approximated by a null hypersurface $\Sigma = \mathscr{I}^-_I \cup H^-_I \cup \mathscr{I}^-_{IV} \cup H^-_{IV}$. The normalisation constants are found to be

$$B^{in}_\Omega = \frac{1}{\sqrt{4\pi\Omega}}, \quad B^{up}_\Omega = \frac{1}{\sqrt{4\pi\Omega}}. \tag{1.125}$$

We can write the Kruskal modes (1.123-1.124) in terms of a linear combination of "up"- and "in"-Schwarzschild modes ϕ^{up}_S, ϕ^{in}_S, as well as unphysical "down"- and "out"-Schwarzschild modes $\phi^{down*}_S, \phi^{out*}_S$ defined on region IV. These unphysical modes are defined by taking the time reverse complex conjugates of (1.103-1.104):

$$\phi^{down}_S = (A^{up}_\Omega)^* e^{-4Mi\Omega \ln(U/4M)} \Theta(U), \tag{1.126}$$

$$\phi^{out}_S = (A^{in}_\Omega)^* e^{4Mi\Omega \ln(-V/4M)} \Theta(-V). \tag{1.127}$$

(a) “Out”-Schwarzschild modes (b) “Down”-Schwarzschild modes

Figure 1.6: The “out”-Schwarzschild modes start at future null infinity $\mathscr{I}^+_{IV}$ and travel into the white hole horizon H^-_{IV}, whilst the “down”-Schwarzschild modes begin at the black hole horizon H^+_{IV} and travel towards the past null infinity $\mathscr{I}^-_{IV}$.

The “down”-Schwarzschild modes travel from the black hole horizon H^+_{IV} to past null infinity $\mathscr{I}^-_{IV}$, whilst the “out”-Schwarzschild modes travel from future null infinity $\mathscr{I}^+_{IV}$ into the white hole, passing through H^-_{IV} (see Figure 1.6).

The Kruskal modes can then be defined via

$$\phi^{up}_K = D^{up}_\Omega(\phi^{up}_S + e^{-4M\pi\Omega}\phi^{down*}_S), \tag{1.128}$$

$$\phi^{in}_K = D^{in}_\Omega(\phi^{in}_S + e^{-4M\pi\Omega}\phi^{out*}_S) \tag{1.129}$$

for some constants $D^{up}_\Omega, D^{in}_\Omega$ where ϕ^{up}_S, ϕ^{in}_S are defined as in (1.103, 1.104) but with $\omega \to \Omega$. These modes are positive frequency for all $\Omega \in \mathbb{R}$. This fact is evident from [43, App. H], which proves the following:

$$\int_{-\infty}^{\infty} dU\ e^{-ipU}\left[e^{-iq\ln U}\Theta(U) + e^{-\pi q}e^{-iq\ln(-U)}\Theta(-U)\right] = 0, \tag{1.130}$$

for all $p > 0, q \in \mathbb{R}$, where $\Theta(U)$ is the Heaviside step function. This means that

$$e^{-iq\ln U}\Theta(U) + e^{-\pi q}e^{-iq\ln(-U)}\Theta(-U) \tag{1.131}$$

has positive frequency with respect to U for all $q \in \mathbb{R}$. Comparing (1.128, 1.129) with (1.130), we can see that this means both ϕ^{up}_K, ϕ^{in}_K are also both positive frequency with respect to Kruskal time for all $\Omega \in \mathbb{R}$.

The normalisation constants D^{up}_Ω are determined by taking the scalar product of the positive frequency "up"-Kruskal modes, that is

$$\begin{aligned}
&\langle \phi_K^{up}(x;\Omega), \phi_K^{up}(x;\Omega')\rangle \\
&\quad = D_\Omega^{up} D_{\Omega'}^{up} \langle \phi_S^{up}(x;\Omega) + e^{-4M\pi\Omega}\phi_S^{down*}(x;\Omega), \phi_S^{up}(x;\Omega') + e^{-4M\pi\Omega'}\phi_S^{down*}(x;\Omega)\rangle \\
&\quad = D_\Omega^{up} D_{\Omega'}^{up} \Big\{ \langle \phi_S^{up}(x;\Omega), \phi_S^{up}(x;\Omega')\rangle + e^{-4M\pi\Omega}\langle \phi_S^{down*}(x;\Omega), \phi_S^{up}(x;\Omega')\rangle \\
&\qquad + e^{-4M\pi\Omega'}\langle \phi_S^{up}(x;\Omega), \phi_S^{down*}(x;\Omega')\rangle + e^{-4M\pi(\Omega+\Omega')}\langle \phi_S^{down*}(x;\Omega), \phi_S^{down*}(x;\Omega')\rangle \Big\} \\
&\quad = D_\Omega^{up} D_{\Omega'}^{up} \Big\{ \delta(\Omega-\Omega') - e^{-4M\pi(\Omega+\Omega')}\delta(\Omega-\Omega') \Big\}, \qquad (1.132)
\end{aligned}$$

where we have used the fact that the scalar product is linear, and also the fact that both the "up"- and "down"-Schwarzschild modes are normalised (that is, ϕ_S^{up} are normalised to $+1$, and ϕ_S^{down*} are normalised to -1). To normalise the "up"-Kruskal modes, we set

$$D_\Omega^{up} = (e^{8M\pi\Omega} - 1)^{-1/2} = \frac{e^{-2M\pi\Omega}}{(2\sinh(4M\pi\Omega))^{1/2}}. \qquad (1.133)$$

A similar calculation for ϕ_K^{in} gives

$$D_\Omega^{in} = (1 - e^{-8M\pi\Omega})^{-1/2} = \frac{e^{2M\pi\Omega}}{(2\sinh(4M\pi\Omega))^{1/2}}. \qquad (1.134)$$

Using the Kruskal modes (1.128, 1.129) to define a field operator, we find

$$\hat{\phi}_K = \int_{-\infty}^{\infty} d\Omega \; \{\hat{b}_\Omega^{up}\phi_K^{up} + \hat{b}_\Omega^{in}\phi_K^{in} + \hat{b}_\Omega^{up\dagger}\phi_K^{up*} + \hat{b}_\Omega^{in\dagger}\phi_K^{in*}\} \qquad (1.135)$$

where the annihilation operators $\hat{b}_\Omega^{up}, \hat{b}_\Omega^{in}$ define the Hartle-Hawking vacuum state [38],

$$\hat{b}_\Omega^{up}|H\rangle = 0, \quad \hat{b}_\Omega^{in}|H\rangle = 0. \qquad (1.136)$$

The construction of the Wightman function in the Hartle-Hawking state follows that of the previous calculation (1.119 - 1.121), except this time we take the expectation of the Kruskal modes (1.128, 1.129) rather than the Schwarzschild modes:

$$G_H(x,x') \;=\; \langle H|\hat{\phi}_K(x)\hat{\phi}_K(x')|H\rangle \;=\; \int_{-\infty}^{\infty} d\Omega \left\{\phi_K^{up}(x)\phi_K^{up*}(x') + \phi_K^{in}(x)\phi_K^{in*}(x')\right\}. \qquad (1.137)$$

We now substitute the representations for the Kruskal modes in terms of Schwarzschild modes (1.128-1.129). We are only interested in the Wightman function in region I, where $\phi_S^{down}, \phi_S^{out}$ are zero. The Wightman function can therefore be written as

$$G_H(x,x') = \int_{-\infty}^{\infty} d\Omega \left\{ \frac{e^{-4M\pi\Omega}}{2\sinh(4M\pi\Omega)}\phi_S^{up*}(x)\phi_S^{up}(x') + \frac{e^{4M\pi\Omega}}{2\sinh(4M\pi\Omega)}\phi_S^{in*}(x)\phi_S^{in}(x') \right\} \qquad (1.138)$$

which matches [1, eq.5] (see also (1.149)), although note that Candelas works in four-dimensions, and so there are extra terms involving the angular coordinates.

In the coincidence limit, we can write

$$G_H(x,x) = \int_0^\infty d\Omega \ \coth(4M\pi\Omega) \left\{ |\phi_S^{up}|^2 + |\phi_S^{in}|^2 \right\}, \tag{1.139}$$

where we recover the thermal factor $\coth(4M\pi\Omega)$, which corresponds to the coth factor in the thermal Green's function (1.44). This thermal factor shows that the Hartle-Hawking state is not a vacuum state in the Lorentzian background.

The Hartle-Hawking vacuum state is defined across the entire spacetime, and has an ingoing and outgoing thermal flux at null infinity [1]. Closer examination shows that the ingoing flux is equal to the outgoing flux. This means that the Hartle-Hawking state models a black hole in unstable thermal equilibrium. It is regular on the horizon and is therefore the relevant state for black hole thermodynamics. Like the Boulware vacuum, the Hartle-Hawking vacuum is also invariant under time reversal [44].

Thermality and regularity on the horizon is vital when it comes to performing calculations on Euclidean black holes. Once we Euclideanise, the only state that we can perform calculations on is the Hartle-Hawking state. The Euclidean Schwarzschild metric is found by performing a Wick rotation (1.45),

$$ds^2 = \left(1 - \frac{2M}{r}\right) d\tau^2 + \left(1 - \frac{2M}{r}\right)^{-1} dr^2. \tag{1.140}$$

To avoid a conical singularity on the horizon, we need to impose periodicity in imaginary time τ. To see why this is, near the horizon we write $\left(1 - \frac{2M}{r}\right) = f(r) = (r - r_h)f'(r_h)$ and the Euclidean metric becomes

$$ds^2 = (r - r_h)f'(r_h)d\tau^2 + \frac{1}{(r - r_h)f'(r_h)}dr^2. \tag{1.141}$$

Setting $x = 2(r - r_h)^{1/2}(f'(r_h))^{-1/2}$, with $dx = ((r - r_h)f'(r_h))^{-1/2}dr$, the Euclidean metric is

$$ds^2 = \frac{1}{4}(f'(r_h))^2 x^2 d\tau^2 + dx^2. \tag{1.142}$$

Now we let $T = \frac{1}{2}f'(r_h)\tau = \kappa\tau$, where

$$\kappa = \frac{1}{2}f'(r_h) \tag{1.143}$$

is the surface gravity, and so

$$ds^2 = x^2 dT^2 + dx^2. \tag{1.144}$$

To avoid any conical singularities, we must have T periodic with period 2π. This means that we impose periodicity in imaginary time τ, so that $\tau \in (0, \frac{2\pi}{\kappa})$, and therefore we are in a thermal state with inverse temperature $T^{-1} = \frac{2\pi}{\kappa}$. This is the Hartle-Hawking state.

The Unruh state

In order to define the Unruh vacuum state $|U\rangle$ [35], we build a new field operator, $\hat{\phi}_U$ by taking a linear combination of the Schwarzschild and Kruskal field modes written in Kruskal coordinates, given by (1.103, 1.104) and (1.128, 1.129) respectively. Our new field operator is therefore defined by

$$\hat{\phi}_U = \int_0^\infty d\omega \; \{\hat{d}^{in}_\omega \phi^{in}_S + \hat{d}^{in\dagger}_\omega \phi^{in*}_S\} + \int_{-\infty}^\infty d\omega \; \{\hat{d}^{up}_\omega \phi^{up}_K + \hat{d}^{up\dagger}_\omega \phi^{up*}_K\} \tag{1.145}$$

which can now be written entirely in terms of Schwarzschild modes using (1.128, 1.129). The associated annihilation operators define the Unruh vacuum state,

$$\hat{d}^{in}_\omega |U\rangle = 0, \quad \hat{d}^{up}_\omega |U\rangle = 0. \tag{1.146}$$

The Wightman function in the Unruh state is

$$\begin{aligned} G_U(x,x') &= \int_{-\infty}^\infty d\omega \left\{\Theta(\omega)\phi^{in}_S(x)\phi^{in*}_S(x') + \phi^{up}_K(x)\phi^{up*}_K(x')\right\} \\ &= \int_0^\infty d\omega \left\{\phi^{in}_S(x)\phi^{in*}_S(x') + \frac{e^{-4M\pi\omega}}{2\sinh(4M\pi\omega)}\phi^{up}_S(x)\phi^{up*}_S(x')\right\}, \end{aligned} \tag{1.147}$$

where the Heaviside function $\Theta(\omega)$ is used because the "in"-Schwarzschild modes are not defined for $\omega < 0$. The Wightman function (1.147) matches [1, eq.5] (see also (1.150)), albeit in two-dimensions.

The Unruh state has no incoming flux in the past but exhibits Hawking radiation at future infinity [3]. Due to this emission of radiation, we say that the black hole is "evaporating". We assume, however, that despite the radiation escaping, the black hole remains the same size. This is a good approximation, especially for large black holes where the hole decreases in size at such a slow rate that the change is virtually insignificant. Unlike the Boulware and Hartle-Hawking vacua, the Unruh vacuum is not invariant under time reversal.

One may notice that we could construct a fourth vacuum state using the ϕ^{up}_S, ϕ^{in}_K modes. This state (sometimes referred to as the future Unruh state) assumes an influx of radiation at past infinity. This means that the radiation is effectively coming from "nowhere", and can be thought of as the white hole analogue of Hawking radiation. This is an unphysical process, and so we do not consider this state any further in this thesis. The flux of radiation in the external region of Schwarzschild spacetime for all types of vacuum state is shown in Figure 1.7.

1.2.4 Results in four-dimensions

We now extend this analysis of Green's functions to four-dimensions, quoting results for the vacuum polarisation (see section 1.3.1) taken from [1] and results for the SET taken from [3].

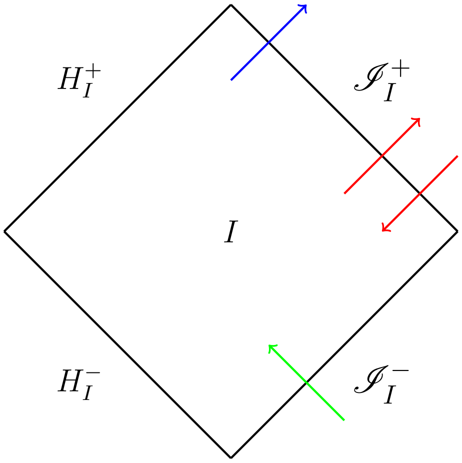

Figure 1.7: The external region of Schwarzschild. The Hartle-Hawking state has ingoing and outgoing radiation at null infinity (red arrows). The Unruh state has outgoing radiation at future infinity (blue arrow). The future Unruh state has ingoing radiation at past infinity, and is therefore unphysical (green arrow).

In four-dimensional Schwarzschild spacetime, the Wightman functions for massless, conformally coupled scalar fields are given by [1]

$$G_B(x,x') = i\sum_{\ell m}\int_0^\infty \frac{d\omega}{4\pi\omega}e^{-i\omega\Delta t}Y_{\ell m}(\theta,\varphi)Y^*_{\ell m}(\theta',\varphi')\Big[\overrightarrow{X}_{\ell\omega}(r)\overrightarrow{X}^*_{\ell\omega}(r') + \overleftarrow{X}_{\ell\omega}(r)\overleftarrow{X}^*_{\ell\omega}(r')\Big], \quad (1.148)$$

$$G_H(x,x') = i\sum_{\ell m}\int_{-\infty}^\infty \frac{d\Omega}{4\pi\Omega}\left[e^{-i\Omega\Delta t}Y_{\ell m}(\theta,\varphi)Y^*_{\ell m}(\theta',\varphi')\frac{\overrightarrow{X}_{\ell\Omega}(r)\overrightarrow{X}^*_{\ell\Omega}(r')}{1-e^{-4M\pi\Omega}} + e^{+i\Omega\Delta t}Y^*_{\ell m}(\theta,\varphi)Y_{\ell m}(\theta',\varphi')\frac{\overleftarrow{X}_{\ell\Omega}(r)\overleftarrow{X}^*_{\ell\Omega}(r')}{1-e^{-4M\pi\Omega}}\right], \quad (1.149)$$

$$G_U(x,x') = i\sum_{\ell m}\int_{-\infty}^\infty \frac{d\omega}{4\pi\omega}e^{-i\omega\Delta t}Y_{\ell m}(\theta,\varphi)Y^*_{\ell m}(\theta',\varphi')\left[\frac{\overrightarrow{X}_{\ell\omega}(r)\overrightarrow{X}^*_{\ell\omega}(r')}{1-e^{-4M\pi\omega}} + \Theta(\omega)\overleftarrow{X}_{\ell\omega}(r)\overleftarrow{X}^*_{\ell\omega}(r')\right], \quad (1.150)$$

where $Y_{\ell m}(\theta,\varphi)$ are spherical harmonics and the radial functions cannot be calculated analytically but have the asymptotic forms

$$\overrightarrow{X}_{\ell\omega}(r) \sim \begin{cases} r^{-1}e^{i\omega r^*} + \overrightarrow{A}_{\ell\omega} r^{-1} e^{-i\omega r^*}, & r \to 2M, \\ B_{\ell\omega} r^{-1} e^{i\omega r^*}, & r \to \infty, \end{cases} \tag{1.151}$$

$$\overleftarrow{X}_{\ell\omega}(r) \sim \begin{cases} B_{\ell\omega} r^{-1} e^{-i\omega r^*}, & r \to 2M, \\ r^{-1}e^{-i\omega r^*} + \overleftarrow{A}_{\ell\omega} r^{-1} e^{i\omega r^*}, & r \to \infty, \end{cases} \tag{1.152}$$

for constants $\overrightarrow{A}_{\ell\omega}, \overleftarrow{A}_{\ell\omega}, B_{\ell\omega}$. The tortoise coordinate r^* is given in (1.90). Candelas calculates the renormalised vacuum polarisation by keeping temporal coordinates split and subtracting the Hadamard parametrix (this renormalisation scheme is explained in greater detail in section 1.3.3). After renormalisation, the vacuum polarisation in each of the three cases is given by [1]:

$$\begin{aligned} \langle B|\hat{\phi}^2|B\rangle_{ren} = \frac{1}{16\pi^2}\int_0^\infty \frac{d\omega}{\omega}\Bigg[\sum_{\ell=0}^{\infty}(2\ell+1)\left[\left|\overrightarrow{X}_{\ell\omega}(r)\right|^2 + \left|\overleftarrow{X}_{\ell\omega}(r)\right|^2\right] \\ -\frac{4\omega^2}{1-2M/r}\Bigg] - \frac{M^2}{48\pi^2 r^4(1-2M/r)}, \end{aligned} \tag{1.153}$$

$$\begin{aligned} \langle H|\hat{\phi}^2|H\rangle_{ren} = \frac{1}{16\pi^2}\int_0^\infty \frac{d\omega}{\omega}\Bigg[\coth(2M\pi\omega)\sum_{\ell=0}^{\infty}(2\ell+1)\left[\left|\overrightarrow{X}_{\ell\omega}(r)\right|^2 + \left|\overleftarrow{X}_{\ell\omega}(r)\right|^2\right] \\ -\frac{4\omega^2}{1-2M/r}\Bigg] - \frac{M^2}{48\pi^2 r^4(1-2M/r)}, \end{aligned} \tag{1.154}$$

$$\begin{aligned} \langle U|\hat{\phi}^2|U\rangle_{ren} = \frac{1}{16\pi^2}\int_0^\infty \frac{d\omega}{\omega}\Bigg[\sum_{\ell=0}^{\infty}(2\ell+1)\left[\coth(2M\pi\omega)\left|\overrightarrow{X}_{\ell\omega}(r)\right|^2 + \left|\overleftarrow{X}_{\ell\omega}(r)\right|^2\right] \\ -\frac{4\omega^2}{1-2M/r}\Bigg] - \frac{M^2}{48\pi^2 r^4(1-2M/r)}. \end{aligned} \tag{1.155}$$

Candelas claims [1] that, at infinity, the leading order behaviour of (1.153) is determined by the "finite" term, that is

$$\langle B|\hat{\phi}^2|B\rangle_{ren} \to -\frac{M^2}{48\pi^2 r^4(1-2M/r)} \text{ as } r \to \infty. \tag{1.156}$$

This tells us that, far from the black hole, the Boulware vacuum behaves like the Minkowski vacuum, where

$$\langle M|\hat{\phi}^2|M\rangle = 0. \tag{1.157}$$

Similarly, for the Hartle-Hawking state [1],

$$\langle H|\hat{\phi}^2|H\rangle_{ren} \to \frac{1}{192\pi^2 M^2} \text{ as } r \to 2M \tag{1.158}$$

$$\langle H|\hat{\phi}^2|H\rangle_{ren} \to \frac{T_H^2}{12} \text{ as } r \to \infty \tag{1.159}$$

which corresponds to a black hole in thermal equilibrium at Hawking temperature $T_H = 1/8\pi M$.

Christensen and Fulling [3] calculate the renormalised SET on Schwarzschild spacetime. Rather than using Hadamard renormalisation (see section 1.3.2) and subtracting renormalisation terms, they solve the conservation equations (1.51), making assumptions about symmetry of the spacetime. From (1.53), it is clear that $\langle \hat{T}_{\mu\nu} \rangle$ must satisfy (1.51). This method allows Christensen and Fulling to find the SET without the need to do a full computation. They write the SET as [3]

$$T_\mu^\nu = T_\mu^{(1)\nu} + T_\mu^{(2)\nu} + T_\mu^{(3)\nu} + T_\mu^{(4)\nu}. \tag{1.160}$$

The tensors $T_\mu^{(i)\nu}$ can be written, in coordinates $(t, r^*, \theta, \varphi)$, where r^* is the tortoise coordinate (1.90),

$$T_\mu^{(1)\nu} = \begin{pmatrix} -\frac{1}{r^2}\left(1-\frac{2M}{r}\right)^{-1} H(r) + \frac{1}{2}T_\alpha^\alpha(r) & 0 & 0 & 0 \\ 0 & \frac{1}{r^2}\left(1-\frac{2M}{r}\right)^{-1} H(r) & 0 & 0 \\ 0 & 0 & \frac{1}{4}T_\alpha^\alpha(r) & 0 \\ 0 & 0 & 0 & \frac{1}{4}T_\alpha^\alpha(r) \end{pmatrix} \tag{1.161}$$

$$T_\mu^{(2)\nu} = \frac{K}{M^2 r^2}\left(1-\frac{2M}{r}\right)^{-1} \begin{pmatrix} 1 & -1 & 0 & 0 \\ 1 & -1 & 0 & 0 \\ 0 & 0 & 0 & 0 \\ 0 & 0 & 0 & 0 \end{pmatrix} \tag{1.162}$$

$$T_\mu^{(3)\nu} = \begin{pmatrix} -\frac{1}{r^2}\left(1-\frac{2M}{r}\right)^{-1} G(r) - 2\Theta(r) & 0 & 0 & 0 \\ 0 & \frac{1}{r^2}\left(1-\frac{2M}{r}\right)^{-1} G(r) & 0 & 0 \\ 0 & 0 & \Theta(r) & 0 \\ 0 & 0 & 0 & \Theta(r) \end{pmatrix} \tag{1.163}$$

$$T_\mu^{(4)\nu} = \frac{Q}{M^2 r^2}\left(1-\frac{2M}{r}\right)^{-1} \begin{pmatrix} -1 & 0 & 0 & 0 \\ 0 & 1 & 0 & 0 \\ 0 & 0 & 0 & 0 \\ 0 & 0 & 0 & 0 \end{pmatrix} \tag{1.164}$$

with functions

$$\Theta(r) = T_\theta^\theta(r) - \frac{1}{4}T_\alpha^\alpha(r) \tag{1.165}$$

$$H(r) = \frac{1}{2}\int_{2M}^{r} (r' - M) T_\alpha^\alpha(r') dr' \tag{1.166}$$

$$G(r) = 2\int_{2M}^{r} (r' - 3M)\Theta(r') dr'. \tag{1.167}$$

The parameters Q and K are constants of integration. The results given in equations (1.161 - 1.167) are for a general field theory. The trace $T_\alpha^\alpha(r)$ is fixed when we specialise to a particular field theory. Whilst the trace of a classical SET for a conformally invariant field theory should be zero, we obtain a trace anomaly through renormalisation since we discard direction-dependent terms [3].

In four-dimensions, trace anomalies take the general form [45]

$$T^{\alpha}_{\alpha} = k_1 C^2 + k_2 \left(R^{\alpha\beta} R_{\alpha\beta} - \frac{1}{3} R^2 \right) + k_3 \Box R + k_4 R^2 \tag{1.168}$$

where $C^2 = C^{\alpha\beta\gamma\delta} C_{\alpha\beta\gamma\delta}$ is the Weyl tensor, and constants k_i are determined once the type of field theory is fixed. For a massless, conformally coupled scalar field, we set [3]

$$k_1 = k_2 = k_3 = \frac{1}{2880\pi^2}, \quad k_4 = 0 \tag{1.169}$$

and so, for a Schwarzschild black hole,

$$T^{\alpha}_{\alpha} = \frac{1}{60\pi^2} \frac{M^2}{r^6}. \tag{1.170}$$

The Boulware vacuum $|B\rangle$ should represent essentially empty space for large radius, so we therefore expect the components of T^{ν}_{μ} to vanish as $r \to \infty$, prompting us to set $K = 0$, i.e. [3]

$$\langle B | T^{\nu}_{\mu} | B \rangle = T^{(1)\nu}_{\mu} + \tilde{T}^{(3)\nu}_{\mu} + T^{(4)\nu}_{\mu}. \tag{1.171}$$

The component $\tilde{T}^{(3)\nu}_{\mu}$ is identical to $T^{(3)\nu}_{\mu}$ except we have replaced $G(r)$ with $\tilde{G}(r)$, where

$$\tilde{G}(r) = 2 \int_{\infty}^{r} (r' - 3M) \Theta(r') dr'. \tag{1.172}$$

This change in the limits of the integral amounts merely to a redefinition of the constant Q, but is necessary to ensure that the Boulware state vanishes as $r \to \infty$.

The Hartle-Hawking vacuum $|H\rangle$ is regular on the horizon and invariant under time reversal, prompting us to set $Q = K = 0$ and thus [3]

$$\langle H | T^{\nu}_{\mu} | H \rangle = T^{(1)\nu}_{\mu} + T^{(3)\nu}_{\mu}. \tag{1.173}$$

Finally, in the Unruh vacuum $|U\rangle$, the expectation of the SET is of the form [3]

$$\langle U | T^{\nu}_{\mu} | U \rangle = T^{(1)\nu}_{\mu} + T^{(2)\nu}_{\mu} + T^{(3)\nu}_{\mu} \tag{1.174}$$

since the state is regular at the future horizon, implying $Q = 0$. We need $K \neq 0$ for outgoing Hawking flux.

1.3 Renormalisation schemes

1.3.1 Expectation values

In this section, we look at various renormalisation schemes that can be used to calculate the vacuum polarisation (VP) $\langle\hat{\phi}^2\rangle$ and the SET $\langle\hat{T}_{\mu\nu}\rangle$. The VP can be thought of as a building block for the SET (it has been referred to in the literature as the "poor man's stress-energy tensor" [1]). It can be calculated as the limit

$$\langle\hat{\phi}(x)^2\rangle = \lim_{x'\to x}\langle\hat{\phi}(x)\hat{\phi}(x')\rangle. \tag{1.175}$$

The product of two operators at the same spacetime point is divergent, whereas if we keep points separated (i.e. without taking the limit $x' \to x$) we find that the quantity is regular. In fact, we can see from (1.27) that

$$\langle\hat{\phi}(x)^2\rangle = i\lim_{x'\to x} G_F(x,x') \tag{1.176}$$

where $G_F(x,x')$ is the Feynman Green's function of the Klein-Gordon equation.

The SET can be found by acting on the Feynman Green's function by a second order differential operator $\mathcal{T}_{\mu\nu}(x,x')$ and then taking the coincidence limit [4], i.e.

$$\langle\hat{T}_{\mu\nu}\rangle = i\lim_{x'\to x}\mathcal{T}_{\mu\nu}(x,x')[G_F(x,x')]. \tag{1.177}$$

In order to obtain a finite answer from the calculation of VP (or SET), we have to renormalise. This involves performing some sort of subtraction scheme which allows us to cancel out any divergences and leave us with something from which we can glean physical information. There exist many different regularisation schemes, and it is often difficult to know which schemes are consistent and give an identical answer. In 1977, Wald [31,46] gave a list of axioms which must be satisfied by the renormalised SET (the original sources give five axioms, one of which was later dropped from the list [47]):

- **Conservation.** $\nabla^\mu\langle\hat{T}_{\mu\nu}\rangle_{ren} = 0$.
- **Casuality holds**. For a fixed "in" state, $\langle\hat{T}_{\mu\nu}\rangle_{ren}$ at a point p depends only on the causal past of p. Similarly, for a fixed "out" state, $\langle\hat{T}_{\mu\nu}\rangle_{ren}$ depends only on the future of p.
- **Consistency with the formalism**. For a pair of orthogonal states $\langle A|B\rangle = 0$, the matrix element $\langle A|\hat{T}_{\mu\nu}|B\rangle_{ren}$ agrees with the formal expression.
- **Normal ordering on Minkowski**. The renormalised SET $\langle\hat{T}_{\mu\nu}\rangle_{ren}$ should coincide the normal ordered vacuum expectation value of the SET on Minkowski, i.e. $\langle\hat{T}_{\mu\nu}\rangle_{ren} = \,:\langle\hat{T}_{\mu\nu}\rangle:$.

The first axiom is satisfied by the classical SET (1.51). If this condition were not satisfied, then (1.53) would not be consistent. The second axiom simply demands that causality follows the usual rules expected in relativity (basically, an event occurring in the past cannot depend on something that happens in the future). The third of these axioms is important since it is necessary that the renormalised SET bears some resemblance to the unrenormalised SET. The matrix element $\langle A|\hat{T}_{\mu\nu}|B\rangle$ gives a straightforward, unambiguous answer if $\langle A|B\rangle = 0$, and so it is only reasonable to assume that $\langle A|\hat{T}_{\mu\nu}|B\rangle_{ren}$ gives the same answer. The final axiom ensures that renormalisation carries over to Minkowski space, where normal ordering gives a sensible, physically reasonable prescription for $\langle\hat{T}_{\mu\nu}\rangle$.

These axioms led to a uniqueness theorem [31]:

Wald's Uniqueness Theorem *Let $\hat{T}_{\mu\nu}, \hat{T}^{(1)}_{\mu\nu}$ be defined such that their expectation values satisfy Wald's axioms. Define*

$$\hat{\Xi}_{\mu\nu} = \hat{T}_{\mu\nu} - \hat{T}^{(1)}_{\mu\nu}. \tag{1.178}$$

Then

(i) $\hat{\Xi}_{\mu\nu}$ is a multiple of the identity operator.

(ii) $\nabla^{\mu}\langle\hat{\Xi}_{\mu\nu}\rangle = 0$.

(iii) $\langle\hat{\Xi}_{\mu\nu}\rangle$ depends only on the metric and its derivatives at the spacetime point x.

The above uniqueness theorem shows that any renormalisation scheme applied to $\langle\hat{T}_{\mu\nu}\rangle$ will be unique only up to the addition of a locally conserved geometric tensor.

1.3.2 Hadamard renormalisation

Hadamard renormalisation [4,48–56] involves subtracting the singular part of the Hadamard form of the Green's function from the unrenormalised Green's function. Hadamard renormalisation can be applied to Green's functions in both the Euclidean and Lorentzian backgrounds. In this thesis, we shall apply Hadamard renormalisation to the Euclidean Green's function $G_E(x, x')$ (1.46) in four-dimensions. The Hadamard form for an arbitrary number of dimensions is explored in [4]. An object is said to satisfy the Hadamard condition if it can be written in the form of a Hadamard parametrix $G_S(x, x')$ when points x and x' are in a normal neighbourhood. Thus, $G_S(x, x')$ will capture all the divergences of the original object in the limit $x' \to x$. In order to fully appreciate the Hadamard form, we first introduce two important geometrical quantities, Synge's world function $\sigma(x, x')$ and the van Vleck-Morette determinant $\Delta(x, x')$.

Synge's world function $\sigma(x, x')$ is half the square of geodesic length between two points x and x'. Here, we must assume that x and x' belong to a normal neighbourhood. Then, there exists a unique geodesic $z(\lambda)$, where λ is an affine parameter, that connects x to x'. The geodesic $z(\lambda)$ must lie within the same normal neighbourhood as x and x'. We suppose $z(\lambda_0) = x$ and $z(\lambda_1) = x'$ and define the world function as

$$\sigma(x, x') = \frac{1}{2}(\lambda_1 - \lambda_0) \int_{\lambda_0}^{\lambda_1} g_{\mu\nu} \dot{z}^\mu \dot{z}^\nu d\lambda \tag{1.179}$$

where $\dot{z}^\mu$ refers to differentiation with respect to affine parameter λ. The world function $\sigma(x, x')$ satisfies [4, 57]

$$2\sigma = \sigma^{;\mu}\sigma_{;\mu}. \tag{1.180}$$

We also note that if x and x' are timelike separated, then $\sigma(x, x') < 0$, if x and x' are null separated then $\sigma(x, x') = 0$ and if x and x' are spacelike separated, then $\sigma(x, x') > 0$.

The van Vleck-Morette determinant $\Delta(x, x')$ was introduced by van Vleck in 1928 to aid the evaluation of the classical limit of quantum mechanics [58]. This determinant was then developed by Morette in [59] for use in the approximation of Feynman integrals. It gives us a measure of the rate at which geodesics that start at x' diverge away from, or converge toward, each other [60]. It is defined by [60]

$$\Delta(x, x') = g^{-1/2}(x) \det\{\nabla^x_\mu \nabla^{x'}_\nu \sigma(x, x')\} g^{-1/2}(x') \tag{1.181}$$

where $g(x) = \det\{g_{\mu\nu}(x)\}$ and ∇^x_μ refers to the covariant derivative taken with respect to x^μ. It satisfies the boundary condition

$$\lim_{x' \to x} \Delta(x, x') = 1 \tag{1.182}$$

and the differential equation

$$\Delta^{-1}(\Delta\sigma^{;\mu})_{;\mu} = 4. \tag{1.183}$$

From (1.183), we can derive

$$\Box\sigma = 4 - 2\Delta^{-1/2}(\Delta^{1/2})_{;\mu}\sigma^{;\mu} \tag{1.184}$$

which will prove a useful defining equation for Δ.

The Hadamard form of the Feynman Green's function is

$$G_F(x, x') = -\frac{i}{4\pi^2}\left(\frac{U(x, x')}{\sigma(x, x') + i\epsilon} + V(x, x')\ln[\sigma(x, x') + i\epsilon] + W(x, x')\right) \tag{1.185}$$

where $U(x, x'), V(x, x')$ and $W(x, x')$ are symmetric biscalars. To determine these biscalars, we must substitute (1.185) into (1.58). This is done in Appendix A. We find

$$U(x, x') = \Delta^{1/2}(x, x'), \tag{1.186}$$

$$V(x, x') = \sum_{n=0}^{\infty} V_n(x, x')\sigma^n(x, x'), \tag{1.187}$$

$$W(x, x') = \sum_{n=0}^{\infty} W_n(x, x')\sigma^n(x, x') \tag{1.188}$$

where the V_n satisfy the recurrence relation

$$\begin{aligned}0 &= 2(n+1)V_{n+1;\mu}\sigma^{;\mu} + 2(n+1)(n+2)V_{n+1} \\ &\quad - 2(n+1)V_{n+1}\Delta^{-1/2}(\Delta^{1/2})_{;\mu}\sigma^{;\mu} + (\Box - m^2 - \xi R)V_n, \end{aligned} \tag{1.189}$$

with V_0 given by

$$(\Box - m^2 - \xi R)\Delta^{1/2} + 2V_{0;\mu}\sigma^{;\mu} + 2V_0 - 2V_0\Delta^{-1/2}(\Delta^{1/2})_{;\mu}\sigma^{;\mu} = 0. \tag{1.190}$$

For the W_n we have the recurrence relation

$$\begin{aligned}(\Box - m^2 - \xi R)W_n + 2(n+1)W_{n+1;\mu}\sigma^{;\mu} + 2(n+1)(n+2)W_{n+1} \\ -2(n+1)W_{n+1}\Delta^{-1/2}(\Delta^{1/2})_{;\mu}\sigma^{;\mu} + 2V_{n+1;\mu}\sigma^{;\mu} \\ +(4n+6)V_{n+1} - 2V_{n+1}\Delta^{-1/2}(\Delta^{1/2})_{;\mu}\sigma^{;\mu} = 0\end{aligned} \tag{1.191}$$

with W_0 unrestrained by the recursion relations [4]. The freedom to choose W_0 corresponds to the freedom to add solutions of the homogeneous wave equation to G_F (by changing the boundary conditions that prescribe G_F) [61].

It can be noted, therefore, that the $V_n(x, x')$ can be determined uniquely and are purely geometric objects whilst the $W_n(x, x')$ cannot be uniquely defined and are not purely geometric. In particular, this means that the Hadamard expansion (1.185) is made up of two parts, a purely geometric part that diverges in the coincidence limit, given by

$$G_S(x, x') = \frac{1}{4\pi^2}\left(\frac{\Delta^{1/2}(x, x')}{\sigma(x, x') + i\epsilon} + V(x, x')\ln\left[\ell_0^2\sigma(x, x') + i\epsilon\right]\right) \tag{1.192}$$

where the subscript S stands for "singular" and we have added an arbitrary length scale ℓ_0 to make the term inside the logarithm dimensionless, and a regular part given by

$$G_R(x, x') = \frac{1}{4\pi^2}W(x, x'). \tag{1.193}$$

We call G_S the Hadamard parametrix; this encapsulates all of the divergences in $\langle\hat{\phi}^2\rangle$. The Hadamard parametrix can be divided into two parts, the direct part of the Hadamard parametrix, given by

$$\frac{\Delta^{1/2}(x, x')}{\sigma(x, x') + i\epsilon}, \tag{1.194}$$

and the tail of the Hadamard parametrix, given by

$$V(x, x')\ln[\ell_0^2\sigma(x, x') + i\epsilon]. \tag{1.195}$$

The renormalised VP can then be calculated by subtracting the Hadamard parametrix from the Feynman Green's function

$$\langle\hat{\phi}^2\rangle_{ren} = \lim_{x' \to x}\{iG_F - G_S\} \tag{1.196}$$

or, equivalently, in the Euclidean background

$$\langle \hat{\phi}^2 \rangle_{ren} = \lim_{x' \to x} \{ G_E - G_S \}. \tag{1.197}$$

In the case of a massless, conformally coupled scalar field ($m = 0, \xi = \frac{1}{6}$), performing a short-distance expansion reveals $V \sim \mathcal{O}(\Delta x^4)$, meaning that the log term in (1.192) does not contribute in the coincidence limit [4]. In chapter 5, when we employ Hadamard renormalisation on an anti-de Sitter black hole spacetime, we only consider massless, conformally coupled scalar fields, and so do not have to worry about calculating the tail of the Hadamard parametrix. This term must be considered when looking at a scalar field of general coupling or trying to extend the VP to the calculation of the renormalised SET.

When we use the Hadamard parametrix G_S to renormalise the SET, ambiguities are introduced thanks to the arbitrary lengthscale ℓ_0 [4]. Replacing $iG_F(x,x')$ by $iG_F(x,x') - G_S(x,x')$ in (1.177), we obtain

$$\langle \hat{T}_{\mu\nu} \rangle_{ren} = \lim_{x' \to x} \mathcal{T}_{\mu\nu}(x,x')[iG_F(x,x') - G_S(x,x')]. \tag{1.198}$$

An ambiguity arises from the tail of the Hadamard parametrix, since this contains an arbitrary lengthscale ℓ_0. To extract this ambiguity, we treat $G_S(x,x')$ as a function of ℓ_0 (and therefore write $G_S(x,x') = G_S(x,x';\ell_0)$) and write

$$G_S(x,x';\ell_0) = G_S(x,x';\ell_1) + \delta G_S(x,x';\ell_0,\ell_1) \tag{1.199}$$

where

$$\delta G_S(x,x';\ell_0,\ell_1) = \frac{1}{4\pi^2} V(x,x') \ln \left[\frac{\ell_0^2 \sigma(x,x') + i\epsilon}{\ell_1^2 \sigma(x,x') + i\epsilon} \right]. \tag{1.200}$$

Then the renormalised SET is

$$\begin{aligned} \langle \hat{T}_{\mu\nu} \rangle_{ren} &= \lim_{x' \to x} \mathcal{T}_{\mu\nu}(x,x')[iG_F(x,x') - G_S(x,x';\ell_1) - \delta G_S(x,x';\ell_0,\ell_1)] \\ &= \lim_{x' \to x} \left\{ \mathcal{T}_{\mu\nu}(x,x')[iG_F(x,x') - G_S(x,x';\ell_1)] + \Upsilon_{\mu\nu}(x,x';\ell_0,\ell_1) \right\}, \end{aligned} \tag{1.201}$$

where $\Upsilon_{\mu\nu}(x,x';\ell_0,\ell_1) = -\mathcal{T}_{\mu\nu} \delta G_S(x,x';\ell_0,\ell_1)$. In accordance with Wald's uniqueness theorem (1.178), $\Upsilon_{\mu\nu}$ is a local, conserved, geometric tensor, and hence the definition of the renormalised SET is unique only up to the addition of such a tensor. It is important to note that this ambiguity will still play a role in the four-dimensional, massless, conformally coupled case since, although $V(x,x')$ vanishes at low orders and we do not need to consider it in our calculations, it is not identically zero and so there is still a need to introduce an arbitrary lengthscale.

In (pure) anti-de Sitter (adS) spacetime, it is found that [62] $V(x,x') = 0$ identically for four-dimensional, massless, conformally coupled scalar fields. This means that there is no renormalisation ambiguity in adS spacetime, which can be explained by the fact that the spacetime is maximally symmetric. Note that this will not be the case for asymptotically adS black hole spacetimes, such as Schwarzschild-adS considered in part III.

The subtraction in (1.196) is by no means a trivial matter, and there have been various methods devised to ease this computation. We present a few of these methods here and compare their advantages and shortcomings.

1.3.3 The Candelas and Howard method

Candelas and Howard [1,2,63,64] were among the first to implement Hadamard renormalisation in their calculation of the VP for the Schwarzschild black hole. They use a special case of Hadamard renormalisation, referred to in the literature as DeWitt-Schwinger renormalisation [65,66], which writes the Hadamard parametrix and Feynman Green's function in a representation that allows for divergences to be captured by "DeWitt-Schwinger" terms G_{DS}. These terms arise from a particular (non-zero) choice of the biscalar $W(x,x')$ [67]. The Candelas-Howard method was extended to general spherically symmetric black holes by Anderson, Hiscock and Samuel [68,69].

The Candelas-Howard method works in the Euclidean background and keeps coordinates split, writing

$$G_E(\tau,r,\theta,\varphi;\tau',r',\theta',\varphi') = \frac{\kappa}{8\pi^2}\sum_{n=-\infty}^{\infty} e^{in\kappa\Delta\tau}\mathcal{G}_n(r,\theta,\varphi;r',\theta',\varphi') \tag{1.202}$$

where $\Delta\tau = \tau-\tau'$, the parameter κ is associated with the temperature T of the thermal state via $\kappa = 2\pi T$ and $\mathcal{G}_n$ is given by

$$\mathcal{G}_n(r,\theta,\varphi;r',\theta',\varphi') = \sum_{\ell=0}^{\infty} g_{n\ell}(r,r')h_\ell(\theta,\varphi;\theta'\varphi'). \tag{1.203}$$

The function $h_\ell(\theta,\varphi;\theta',\varphi')$ is an angular function that will be determined based on the background geometry of the spacetime. In a spherically symmetric spacetime, this will usually take the form of spherical harmonics. The form of $h_\ell(\theta,\varphi;\theta',\varphi')$ is unimportant for this discussion, however.

The function $\mathcal{G}_n$ is a three-dimensional Green's function of the scalar field equation with associated 3-dimensional metric of signature $(+\,+\,+)$. This means that $\mathcal{G}_n$ can be written in Hadamard form in three-dimensions (see [4] for more information on the three-dimensional Hadamard form), i.e.

$$\mathcal{G}_n(\mathbf{x},\mathbf{x}') = \frac{1}{2\pi}\left(\frac{U(\mathbf{x},\mathbf{x}')}{(2\sigma(\mathbf{x},\mathbf{x}'))^{1/2}} + W(\mathbf{x},\mathbf{x}')\right) \tag{1.204}$$

where $\mathbf{x} = (r,\theta,\varphi)$. In three-dimensions, the biscalar $U(\mathbf{x},\mathbf{x}')$ is written

$$U(\mathbf{x},\mathbf{x}') = \sum_{n=0}^{\infty} U_n(\mathbf{x},\mathbf{x}')\sigma^n(\mathbf{x},\mathbf{x}') \tag{1.205}$$

where

$$U_0(\mathbf{x},\mathbf{x}') = \Delta^{1/2}(\mathbf{x},\mathbf{x}') \tag{1.206}$$

and the $U_n(\mathbf{x},\mathbf{x}')$ satisfy the recurrence relation

$$\begin{aligned}(n+1)(2n+1)U_{n+1} + (2n+1)U_{n+1;\mu}\sigma^{;\mu} - (2n+1)U_{n+1}\Delta^{-1/2}\Delta^{1/2}_{;\mu}\sigma^{;\mu}\\ +(\Box - m^2 - \xi R)U_n = 0,\end{aligned} \tag{1.207}$$

whilst the $W_n(\mathbf{x},\mathbf{x}')$ satisfies the recurrence relation

$$\begin{aligned}(n+1)(2n+3)W_{n+1} + 2(n+1)W_{n+1;\mu}\sigma^{;\mu} - 2(n+1)W_{n+1}\Delta^{-1/2}\Delta^{1/2}_{;\mu}\sigma^{;\mu}\\ +(\Box - m^2 - \xi R)W_n = 0.\end{aligned} \tag{1.208}$$

The freedom to choose W_0 corresponds to the freedom to add solutions of the three-dimensional homogeneous wave equation to $\mathcal{G}_n$.

The Hadamard parametrix is formed the same way as in four-dimensions - the non-geometric $W(\mathbf{x},\mathbf{x}')$ can be ignored. The limits $r' \to r, \varphi' \to \varphi$ are taken, and points remain split in the angular coordinate θ. Provided the metric is spherically symmetric, we can set $\theta' = 0$ without loss of generality, and write both $\mathcal{G}_n$ and the Hadamard parametrix G_S as a series in θ:

$$\mathcal{G}_n(r,\theta,\varphi;r,0,\varphi) = \frac{X(r,\varphi)}{\theta} + \mathcal{O}(1), \tag{1.209}$$

$$G_S(r,\theta,\varphi;r,0,\varphi) = \frac{U(r,\theta,\varphi;r,0,\varphi)}{2\pi(2\sigma(r,\theta,\varphi;r,0,\varphi))^{1/2}} = \frac{X(r,\varphi)}{\theta} + \mathcal{O}(1), \tag{1.210}$$

for some function $X(r,\varphi)$. Both $\mathcal{G}_n$ and G_S have the same coefficients at order θ^{-1}, and so, performing the subtraction

$$\mathcal{G}_n(r,\theta,\varphi;r,0,\varphi) - G_S(r,\theta,\varphi;r,0,\varphi) = \mathcal{O}(1) \tag{1.211}$$

leaves us with a finite result in the coincidence limit $\theta \to 0$. This cancels the divergences in the ℓ-sum, but Candelas and Howard are not quite finished yet, because they pick up further divergences from the n-sum. To cancel these divergences out, they subtract more terms,

$$\langle\hat{\phi}^2\rangle_{ren} = \frac{\kappa}{8\pi^2}\lim_{\Delta\tau\to 0}\left(\sum_{n=-\infty}^{\infty} e^{in\kappa\Delta\tau}\left(\mathcal{G}_n - G_S\right) - G_{DS}\right). \tag{1.212}$$

These terms, G_{DS}, were found by Christensen [41] using the DeWitt-Schwinger expansion for the Green's function [65,66]. The difficulty arises in performing the subtraction $\sum_n e^{in\kappa\Delta\tau}(\mathcal{G}_n - G_S) - G_{DS}$, since $\sum_n e^{in\kappa\Delta\tau}(\mathcal{G}_n - G_S)$ and G_{DS} are both divergent in the limit $\Delta\tau \to 0$. We assume G_{DS} can be split into two parts (this decomposition is not a guarantee but can be shown to hold for spherically symmetric, black hole spacetimes [1]):

$$G_{DS} = G_{\Delta\tau} + G_r. \tag{1.213}$$

The first part $G_{\Delta\tau}$ captures all the terms in G_{DS} that have a dependence on $\Delta\tau$, and so must be kept within the limit. The terms in G_r do not depend on $\Delta\tau$ and so can be considered separately. Note that $G_{\Delta\tau}$ may also depend on r.

This means that the renormalised VP can be separated into two parts,

$$\langle\hat{\phi}^2\rangle_{ren} = \langle\hat{\phi}^2\rangle_{numeric} + \langle\hat{\phi}^2\rangle_{analytic} \tag{1.214}$$

where

$$\begin{aligned}\langle\hat{\phi}^2\rangle_{numeric} =& \frac{\kappa}{8\pi^2}\lim_{\Delta\tau\to 0}\left(\sum_{n=-\infty}^{\infty} e^{in\kappa\Delta\tau}(\mathcal{G}_n - G_S) - G_{\Delta\tau}\right), & (1.215)\\ \langle\hat{\phi}^2\rangle_{analytic} =& -\frac{\kappa}{8\pi^2}G_r. & (1.216)\end{aligned}$$

The $\langle\hat{\phi}^2\rangle_{analytic}$ has a fairly simple form and so can be computed relatively easily. The $\langle\hat{\phi}^2\rangle_{numeric}$ can only be computed numerically, as the name suggests. We do this by writing $G_{\Delta\tau}$ as a mode sum over n, i.e.

$$G_{\Delta\tau} = \sum_{n=-\infty}^{\infty} e^{in\kappa\Delta\tau} G_{\Delta\tau,n}, \tag{1.217}$$

which leaves us with

$$\langle\hat{\phi}^2\rangle_{numeric} = \frac{\kappa}{8\pi^2}\lim_{\Delta\tau\to 0}\left(\sum_{n=-\infty}^{\infty} e^{in\kappa\Delta\tau}(\mathcal{G}_n - G_S - G_{\Delta\tau,n})\right). \tag{1.218}$$

The sum in (1.218) can be approximated using a WKB expansion which gives rapid convergence in the large n limit [70]. Unfortunately, the WKB approximation suffers near the event horizon due to nonuniformity in r. In this case, more modes near the horizon would be required to achieve a good level of accuracy, and this can be computationally expensive. If we are working in a black hole spacetime, this approximation is useful when we are considering regions in the far field, but fails to capture correct behaviour close to the horizon.

Breen and Ottewill [71] tried to rectify this by using Green-Liouville (G-L) asymptotics. The G-L approximation allows us to write $\langle\hat{\phi}^2\rangle$ as a sum of terms that are manifestly finite on the horizon. This provides us with better accuracy close to the horizon, although it is very complicated. Due to this complexity, Breen and Ottewill use the G-L approximation for the $n = 0$ mode only, and the WKB expansion for all other modes. This allows for the calculation of not only the renormalised VP, but also the renormalised SET [72, 73].

The Candelas-Howard method has been applied to asymptotically flat Schwarzschild black hole spacetimes [2, 63, 74–76], to a charged, rotating black hole [77], and to asymptotically adS black holes [10, 78].

1.3.4 The extended coordinates method

More recently, Breen and Taylor [11, 12] developed a mode-by-mode renormalisation prescription for the VP on a spherically symmetric black hole spacetime. This prescription allows for much quicker convergence, and is known as the "extended coordinates" method. This method makes several significant departures from the Candelas-Howard method. The method is developed for a general spherically symmetric spacetime, described by the metric

$$ds^2 = -f(r)dt^2 + f(r)^{-1}dr^2 + r^2(d\theta^2 + \sin^2\theta\ d\varphi^2), \tag{1.219}$$

for some function $f(r)$. Breen and Taylor use the four-dimensional Hadamard form (see section 1.3.2) and renormalise by taking the Hadamard parametrix from the Euclidean Green's function whilst keeping points split in multiple directions. Even with this point-splitting, the subtraction remains difficult. Breen and Taylor overcome this by writing the world function σ (1.179) as [11, 12],

$$\sigma = \sum_{ijk} \sigma_{ijk}(r) w^i \Delta r^j s^k \tag{1.220}$$

where w and s are the "extended coordinates" defined by

$$w^2 = \frac{2}{\kappa^2}(1 - \cos\kappa\Delta\tau), \quad s^2 = f(r)w^2 + 2r^2(1 - \cos\gamma), \tag{1.221}$$

where κ is the surface gravity (1.143) and $f(r)$ appears in the metric (1.219). The parameter γ is the geodesic distance on a sphere, defined by

$$\cos\gamma = \cos\theta\cos\theta' + \sin\theta\sin\theta'\cos\Delta\varphi. \tag{1.222}$$

The extended coordinates are treated as $\mathcal{O}(\epsilon) \sim \mathcal{O}(\Delta x)$. The coefficients σ_{ijk} can then be determined by substituting (1.220) into (1.180) and equating powers of ϵ.

The van Vleck-Morette determinant (1.181) can be expanded in the extended coordinates in a similar way

$$\Delta^{1/2}(x, x') = \sum_{ijk} u_{ijk}(r) w^i \Delta r^j s^k. \tag{1.223}$$

The coefficients u_{ijk} are found by substituting (1.223) into (1.184).

Bringing radial coordinates together i.e. $\Delta r \to 0$, the direct part of the Hadamard parametrix can then be expanded in the following way:

$$\frac{\Delta^{1/2}}{\sigma} = \sum_{i=0}^{m} \sum_{j=-i}^{i} \mathcal{D}_{ij}(r) \frac{w^{2i+2j}}{s^{2j+2}} + \mathcal{O}(\epsilon^{2m}) \tag{1.224}$$

where the coefficients $\mathcal{D}_{ij}(r)$ are determined by expanding in terms of extended coordinates (w, s) and comparing coefficients. We split the sum into coefficients with non-negative j, which we call $\mathcal{D}^{(+)}_{ij}(r)$, and coefficients with negative j, which we call $\mathcal{D}^{(-)}_{ij}(r)$, and so write

$$\frac{\Delta^{1/2}}{\sigma} = \sum_{i=0}^{m}\sum_{j=0}^{i}\mathcal{D}^{(+)}_{ij}(r)\frac{w^{2i+2j}}{s^{2j+2}} + \sum_{i=0}^{m}\sum_{j=1}^{i}\mathcal{D}^{(-)}_{ij}(r)\frac{w^{2i-2j}}{s^{-2j+2}} + \mathcal{O}(\epsilon^{2m}). \tag{1.225}$$

The coefficients of $\mathcal{D}^{(-)}_{ij}(r)$ are polynomial in s^2, w^2, except for $\mathcal{D}^{(-)}_{11}(r)$. Since these terms will vanish at coincidence, when $s^2 \to 0$ and $w^2 \to 0$, we can ignore these terms and simply write

$$\frac{\Delta^{1/2}}{\sigma} = \sum_{i=0}^{m}\sum_{j=0}^{i}\mathcal{D}^{(+)}_{ij}(r)\frac{w^{2i+2j}}{s^{2j+2}} + \mathcal{D}^{(-)}_{11}(r) + \mathcal{O}(\epsilon^{2m}). \tag{1.226}$$

The reason for writing the Hadamard parametrix in this way is that we can assume the terms $\frac{w^{2i+2j}}{s^{2j+2}}$ have a mode-sum representation corresponding to G_E (1.202, 1.203), i.e.

$$\frac{w^{2i+2j}}{s^{2j+2}} = \sum_{n=-\infty}^{\infty} e^{in\kappa\Delta\tau}\sum_{\ell=0}^{\infty} h_\ell(\theta,\varphi;\theta',\varphi')\Psi_{n\ell}(i,j|r) \tag{1.227}$$

where $\Psi_{n\ell}(i,j|r)$ are regularisation parameters that can be determined by inverting (1.227) using our definitions for (w,s) in (1.221). The tail of the Hadamard parametrix, given by $V(x,x')\ln[\ell_0^2\sigma(x,x')]$, can be rearranged in a similar way. Using our extended coordinates (w,s), we can write

$$\begin{aligned} V(x,x')\log(\ell_0^2\sigma(x,x')) = {} & \log(\ell_0^2 s^2)\sum_{i=0}^{m-1}\sum_{j=0}^{i}\mathcal{T}^{(l)}_{ij}(r)s^{2i-2j}w^{2j} \\ & + \sum_{i=1}^{m-1}\sum_{j=0}^{i}\mathcal{T}^{(p)}_{ij}(r)s^{2i-2j}w^{2j} \\ & + \sum_{i=1}^{m-1}\sum_{j=0}^{m-1-i}\mathcal{T}^{(r)}_{ij}(r)s^{-2j-2}w^{2i+2j+2} + \mathcal{O}(\epsilon^{2m}\log\epsilon) \end{aligned} \tag{1.228}$$

where the coefficients $\mathcal{T}_{ij}(r)$ are divided into three types: $\mathcal{T}^{(l)}_{ij}(r)$ are terms in the expansion of the tail that contain a logarithm, $\mathcal{T}^{(p)}_{ij}$ are terms in the expansion of the tail that are polynomial in s^2 and w^2 and $\mathcal{T}^{(r)}_{ij}(r)$ are terms in the expansion of the tail that are rational in s^2 and w^2. Note that there is a factor of $\log(\ell_0^2)\mathcal{T}^{(l)}_{ij}(r)$ related to the renormalisation ambiguity that is absorbed into the $\mathcal{T}^{(p)}_{ij}(r)$ coefficients.

As before, terms polynomial in s^2 and w^2 will vanish at coincidence, and so can be ignored, leaving us with

$$\begin{aligned} V(x,x')\log(\ell_0^2\sigma(x,x')) = {} & \log(\ell_0^2 s^2)\sum_{i=0}^{m-1}\sum_{j=0}^{i}\mathcal{T}_{ij}^{(l)}(r)s^{2i-2j}w^{2j} \\ & + \mathcal{T}_{10}^{(r)}(r)s^{-2}w^4 + \mathcal{O}(\epsilon^{2m}\log\epsilon). \end{aligned} \tag{1.229}$$

We assume that logarithmic terms have a mode-sum representation corresponding to (1.202, 1.203), i.e.

$$\log(\ell_0^2 s^2)s^{2i-2j}w^{2j} = \sum_{n=-\infty}^{\infty} e^{in\kappa\Delta\tau}\sum_{\ell=0}^{\infty} h_\ell(\theta,\varphi;\theta',\varphi')\chi_{n\ell}(i,j|r) \tag{1.230}$$

where the regularisation parameters $\chi_{n\ell}(i,j|r)$ are found by inverting (1.230). Putting everything together, the Hadamard parametrix (1.192) can be written

$$\begin{aligned} G_S(x,x') = \frac{1}{4\pi^2}\Bigg(& \sum_{n=-\infty}^{\infty} e^{in\kappa\Delta\tau}\sum_{\ell=0}^{\infty} h_\ell(\theta,\varphi;\theta',\varphi')\left\{\sum_{i=0}^{m}\sum_{j=0}^{i}\mathcal{D}_{ij}^{(+)}(r)\Psi_{n\ell}(i,j|r)\right. \\ & \left. + \sum_{i=0}^{m-1}\sum_{j=0}^{i}\mathcal{T}_{ij}^{(l)}(r)\chi_{n\ell}(i,j|r)\right\} + \mathcal{D}_{11}^{(-)}(r) + \mathcal{T}_{10}^{(r)}(r)\Psi_{n\ell}(2,0|r)\Bigg). \end{aligned} \tag{1.231}$$

Then the renormalised VP can be calculated by

$$\begin{aligned} \langle\hat{\phi}^2\rangle_{ren} = {} & \frac{1}{4\pi^2}\lim_{x'\to x}\Bigg(\sum_{n=-\infty}^{\infty} e^{in\kappa\Delta\tau}\sum_{\ell=0}^{\infty} h_\ell(\theta,\varphi;\theta',\varphi') \\ & \times\left\{\frac{\kappa}{2}g_{n\ell}(r,r') - \sum_{i=0}^{m}\sum_{j=0}^{i}\mathcal{D}_{ij}^{(+)}(r)\Psi_{n\ell}(i,j|r) - \sum_{i=0}^{m-1}\sum_{j=0}^{i}\mathcal{T}_{ij}^{(l)}(r)\chi_{n\ell}(i,j|r)\right\}\Bigg) \\ & - \frac{1}{4\pi^2}\mathcal{D}_{11}^{(-)}(r) - \frac{1}{4\pi^2}\mathcal{T}_{10}^{(r)}(r)\Psi_{n\ell}(2,0|r). \end{aligned} \tag{1.232}$$

Divergences can now be subtracted mode-by-mode, where every term in the sum is manifestly finite. This allows for much quicker convergence than in the Candelas/Howard method, because there is no need to rely on high-order WKB expansions, and no difficulties in adding numerical terms to analytical terms.

The extended coordinates method can be applied to arbitrary dimensions very nicely. This method has been applied to higher-dimensional black holes, namely the Schwarzschild-Tangherlini spacetime in [11, 12]. A similar method has been developed by Freitas and Casals [79], which involves splitting in multiple directions and writing the Hadamard parametrix as a mode-sum, although this method works in the Lorentzian background. This method was applied to Bertotti-Robinson spacetime to calculate the vacuum polarisation in the Boulware vacuum state [79].

In chapter 5, we will use the extended coordinates method to renormalise VP on anti-de Sitter topological black holes for massless, conformally coupled scalar fields. Since the logarithmic terms in (1.192) do not contribute in the coincidence limit for massless, conformally coupled scalar fields, we therefore do not need to calculate the regularisation parameters $\chi_{n\ell}(i,j|r)$ in order to arrive at the results presented in section 5.6. When we try to extend this to consider scalar fields with general coupling constant, we run into problems with the calculation of the parameters $\chi_{n\ell}(i,j|r)$ - see section 5.7 for a description of these difficulties.

1.3.5 The Levi and Ori method

The Candelas-Howard and extended coordinates renormalisation schemes are only viable on the Euclidean background. Levi, Ori and collaborators [80–85] developed a renormalisation scheme on the Lorentzian background, since time-dependent backgrounds do not always admit a Euclidean sector, and the Candelas-Howard method cannot always be used. Attempts to use the Candelas-Howard method on the Lorentzian background introduce some difficulties. For large n modes, there exists a turning point at $r = r_{turn}(n)$. Below this turning point, $r < r_{turn}(n)$, the radial function grows exponentially and above this turning point, $r > r_{turn}(n)$, the radial function is essentially oscillatory. Therefore, in these two different regions, i.e. $r < r_{turn}(n)$ and $r > r_{turn}(n)$, we must use different WKB approximations. These WKB approximations break down and diverge at $r \to r_{turn}$, and so we must use another intermediate approximation to bridge between these [80]. This matching is manageable at low order, but becomes increasingly difficult as we move to higher-order WKB.

Levi and Ori's method does not encounter these problems as they do not use a WKB approximation. They renormalise by point-splitting and subtract the DeWitt-Schwinger terms. They consider two different types of point-splitting methods: t-splitting, which involves splitting in the time-direction and requires invariance under time translation, and angular splitting, splitting in the θ-direction, which requires axial symmetry. Both variants can be used to renormalise the VP, but t-splitting is insufficient in renormalisation of the SET [81].

We begin with the t-splitting method, where $r' \to r,\ \theta' \to \theta,\ \varphi' \to \varphi$ and the points are split in the temporal direction only. In the Lorentzian background, the two-point function looks like

$$\langle \hat{\phi}(t,r,\theta,\varphi), \hat{\phi}(t',r,\theta,\varphi) \rangle = \int_0^\infty F(\omega,r) e^{i\omega\Delta t} d\omega \tag{1.233}$$

where $F(\omega,r)$ is the result of computing the sum over ℓ and m modes. In the coincidence limit $\Delta\tau \to 0$, the integral of $F(\omega,r)$ over ω diverges, but it is regularised in (1.233) by the $e^{i\omega\Delta t}$ factor. To renormalise, Levi and Ori [80] subtract the DeWitt-Schwinger terms G_{DS} as in the Candelas-Howard method:

$$\langle \hat{\phi}^2 \rangle_{ren} = \lim_{\Delta t \to 0} \left[\int_0^\infty F(\omega,r) e^{i\omega\Delta t} d\omega - G_{DS}(\Delta t) \right]. \tag{1.234}$$

With this point-splitting, the DeWitt-Schwinger terms can be written in the form

$$G_{DS}(\Delta t) = a(r)\Delta t^{-2} + b(r)\ln(\Delta t) + c(r) + \mathcal{O}(\Delta t) \tag{1.235}$$

for some functions $a(r), b(r), c(r)$ that are not important for this brief description of the method. The Laplace transform is used to write

$$\Delta t^{-2} = -\int_0^\infty \omega e^{i\omega\Delta t} d\omega, \tag{1.236}$$

$$\ln(\Delta t) = -\int_0^\infty \frac{1}{1+\omega} e^{i\omega\Delta t} d\omega + const. + \mathcal{O}(\Delta t \ln \Delta t). \tag{1.237}$$

The constant terms in the above equation can simply be absorbed into $c(r)$, and we can then write

$$\langle\hat{\phi}^2\rangle_{ren} = \lim_{\Delta t\to 0}\int_0^\infty F_{reg}(\omega, r) e^{i\omega\Delta t} d\omega - c(r) \tag{1.238}$$

where

$$F_{reg}(\omega, r) = F(\omega, r) - a(r)\omega - \frac{b(r)}{1+\omega}. \tag{1.239}$$

Since the singular piece of $F(\omega, r)$ has been removed, one can assume that the integral over $F_{reg}(\omega, r)$ will converge (Levi and Ori show that this is exactly the case for Schwarzschild, but are unable to prove this in a general sense [80]), and thus

$$\langle\hat{\phi}^2\rangle_{ren} = \int_0^\infty F_{reg}(\omega, r) d\omega - c(r). \tag{1.240}$$

It is important to note that throughout this t-splitting regime, spherical symmetry has not been assumed, and if the spacetime were not spherically symmetric, everything would carry over as before, with the added possibility that $F(\omega, r)$ (and thus $a(r), b(r)$ and $c(r)$) may also depend on θ, φ.

The angular-splitting method is done in the limit $t' \to t,\ r' \to r,\ \varphi' \to \varphi$. Levi and Ori [81] keep the angular coordinate θ split by writing $\theta' \to \theta + \epsilon$ for some $\epsilon > 0$. Spherical symmetry is now assumed, and the two-point function is written as

$$\langle\hat{\phi}(t, r, \theta, \varphi), \hat{\phi}(t, r, \theta{+}\epsilon, \varphi)\rangle = \sum_{\ell=0}^\infty \int_0^\infty d\omega \sum_{m=-\ell}^{\ell} Y_{\ell m}(\theta, \varphi) Y^*_{\ell m}(\theta{+}\epsilon, \varphi) |\psi_{\omega\ell}(r)|^2, \tag{1.241}$$

where $Y_{\ell m}$ are spherical harmonics (obtained thanks to spherical symmetry) and $\psi_{\omega\ell}$ are radial functions. The order of summation over ℓ and integration over ω is not important. They evaluate the sum over m first,

$$\sum_{m=-\ell}^{\ell} Y_{\ell m}(\theta, \varphi) Y^*_{\ell m}(\theta + \epsilon, \varphi) = \frac{2l+1}{4\pi} P_\ell(\cos\epsilon) \tag{1.242}$$

and hence

$$\langle\hat{\phi}(t, r, \theta, \varphi), \hat{\phi}(t, r, \theta + \epsilon, \varphi)\rangle = \sum_{\ell=0}^\infty \frac{2l+1}{4\pi} P_\ell(\cos\epsilon) \int_0^\infty |\psi_{\omega\ell}(r)|^2 d\omega. \tag{1.243}$$

Now, some care must be taken with the integral over ω. This is not affected at all by the splitting in θ, and so actually diverges. Levi and Ori [81] regularise by introducing a further point-splitting in t, then adding and subtracting the $\ell = 0$ modes, which results in two integrals that turn out to be finite as $t' \to t$. After this rather complicated process, they are left with [81]

$$\langle\hat{\phi}^2\rangle_{ren} = \lim_{\epsilon\to 0}\left\{\sum_{\ell=0}^{\infty}\frac{2\ell+1}{4\pi}P_\ell(\cos\epsilon)F(\ell,r) - G_{DS}(\epsilon)\right\} \tag{1.244}$$

where $F(\ell, r)$ is the result from the regularised integral over ω and they have subtracted the DeWitt-Schwinger counter-terms as before. They now use a Legendre decomposition to bring these terms inside the ℓ-sum, writing

$$G_{DS}(\epsilon) = \sum_{\ell=0}^{\infty}\frac{2\ell+1}{4\pi}P_\ell(\cos\epsilon)F_{sing}(\ell,r) + W(r) \tag{1.245}$$

where $W(r)$ is some function independent of ℓ (the actual form of $W(r)$ is unimportant for this brief discussion). The VP is then

$$\langle\hat{\phi}^2\rangle_{ren} = \lim_{\epsilon\to 0}\left\{\sum_{\ell=0}^{\infty}\frac{2\ell+1}{4\pi}P_\ell(\cos\epsilon)F_{reg}(\ell,r) - W(r)\right\} \tag{1.246}$$

where

$$F_{reg}(\ell,r) = F(\ell,r) - F_{sing}(\ell,r). \tag{1.247}$$

In order to perform the sum over ℓ, they write F_{reg} as

$$F_{reg}(\ell,r) = A(\ell,r) + B(\ell,r) \tag{1.248}$$

where $B(\ell, r)$ is defined such that

$$\sum_{\ell=0}(2\ell+1)B(\ell,r)P_\ell(\cos\epsilon) = 0 \text{ for small } \epsilon, \text{ and } \sum_{\ell=0}(2\ell+1)B(\ell,r) \text{ diverges.} \tag{1.249}$$

Then the renormalised VP can be written

$$\langle\hat{\phi}^2\rangle_{ren} = \sum_{\ell=0}^{\infty}\frac{2\ell+1}{4\pi}A(\ell,r) - W(r) \tag{1.250}$$

where the summation over ℓ should now be finite. Levi and Ori show that (1.240) and (1.250) are equivalent when applied to Schwarzschild spacetime [81].

The Levi-Ori method is very important, as it allows one to calculate VP for a variety of different states (the Euclidean background automatically fixes the vacuum state to be Hartle-Hawking). However, the integrals performed over ω in (1.243) are extremely subtle - they diverge due to oscillatory behaviour at large ω. This is dealt with by multiplying by an exponentially-decaying prefactor, which damps the oscillations. We then take the prefactor to zero, leaving everything convergent. This method works well for the calculations that Levi and Ori perform in Schwarzschild spacetime, and has also been generalised for Reissner-Nordström spacetime, where the method allows for calculations to be performed inside the horizon [84]. The method has also been applied to Kerr spacetime [83], where calculations in the Euclidean background are often very complicated.

1.4 Summary

In this chapter, we have introduced various concepts that are very important in building a QFT in a non-flat spacetime. We began in section 1.1 with a discussion of QFT in Minkowski, where scalar field modes satisfy the homogeneous wave equation (1.5). We then defined various Green's functions of the inhomogeneous wave equation (1.18) on the Lorentzian background (1.20 - 1.29), associated with vacuum expectation values. Thermal expectation values are associated with thermal Green's functions (1.34), and are periodic in time (1.35, 1.36). By performing a Wick rotation (1.45), we are able to also find a Green's function in the Euclidean background (1.46). All of these concepts carry over to curved spacetime, as we saw in section 1.2.

In section 1.2, we considered field modes that satisfied the homogeneous Klein-Gordon equation (1.56), and Green's functions that satisfied the inhomogeneous Klein-Gordon equation (1.58). We defined the notion of a Cauchy surface (1.62), and why the existence of a Cauchy surface is needed to allow us to calculate scalar products (1.63). It therefore seems impossible to quantise in a spacetime that is not globally hyperbolic. We shall see in chapter 3 that we can quantise in spacetimes that do not admit Cauchy surfaces (such as anti-de Sitter space).

In section 1.2.2, we explored the Unruh effect, showing that there exist different types of vacua in curved spacetime. In Schwarzschild spacetime, there exist three different types of vacuum state, known as the Boulware vacuum, the Hartle-Hawking vacuum and the Unruh vacuum. In two-dimensional Schwarzschild, we calculated the Green's functions in all three vacuum states, and used these calculations to discuss the qualitative differences between the vacua.

To calculate the VP and SET, we need to use renormalisation schemes to remove divergent terms. In section 1.3, we discussed three of these schemes. The Candelas-Howard scheme (section 1.3.3) is applied on the Euclidean background using a WKB approximation for the radial parts of the field modes. The extended coordinates method of Breen and Taylor (section 1.3.4) uses a mode-by-mode regularisation scheme that allows for much quicker convergence, since there is no reliance on high-order WKB expansions. The Levi and Ori method (section 1.3.5) is applied on the Lorentzian background, which is beneficial when it comes to the study of multiple vacuum states. In chapter 5, we shall use the extended coordinates method to calculate vacuum expectation values on anti-de Sitter black holes. This is because the extended coordinates method is welladapted to exploit all of the symmetries of the spacetime, and overall, a more elegant method than the renormalisation scheme of Levi and Ori.

Part II

Anti-de Sitter spacetime

Chapter 2

Anti-de Sitter spacetime

Anti-de Sitter spacetime (see [86–90]) is characterised by negative cosmological constant ($\Lambda < 0$). This means that the expansion of spacetime is decelerating, and null rays can reach the boundary of the spacetime in a finite affine parameter. As a result, we must impose conditions on the timelike boundary.

In this thesis, we shall refer to "pure" anti-de Sitter spacetime as "adS", the covering space as "CadS" and the Poincaré domain of adS as "PadS". Black hole adS spacetimes are discussed in chapter 5, and shall be referred to as "SadS" (Schwarzschild-adS, containing an uncharged black hole) and "RNadS" (Reissner-Nordström-adS, containing a black hole with electric charge). In this chapter we shall look at the geometry of adS, CadS and PadS, and their conformal diagrams. We shall save any comments on quantization until the following chapters.

2.1 (Pure) adS

AdS can be visualised as a 4-dimensional hyperboloid in a 5-dimensional flat spacetime $\mathbb{E}^{(2,3)}$, a Euclidean space with two timelike coordinates. The equation for the four-dimensional hyperboloid is

$$-(\xi^0)^2 + (\xi^1)^2 + (\xi^2)^2 + (\xi^3)^2 - (\xi^4)^2 = -L^2 \tag{2.1}$$

where ξ^0, ξ^4 are timelike coordinates, ξ^1, ξ^2, ξ^3 are spacelike coordinates and L is the adS lengthscale related to the cosmological constant by $L^2 = -\frac{3}{\Lambda}$. This spacetime is shown in Figure 2.1 with two space dimensions suppressed.

The metric for the embedding space is [5, 86]:

$$ds^2 = -(d\xi^0)^2 + (d\xi^1)^2 + (d\xi^2)^2 + (d\xi^3)^2 - (d\xi^4)^2. \tag{2.2}$$

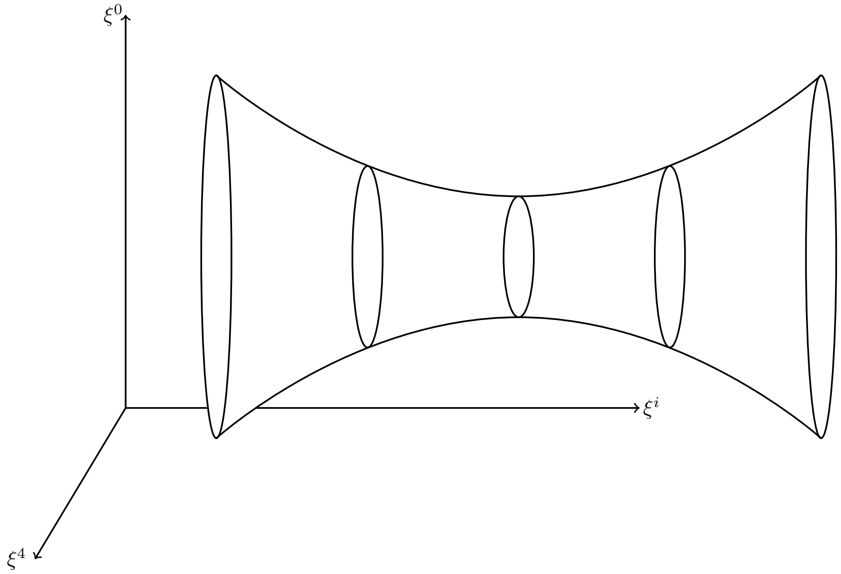

Figure 2.1: AdS space with two spatial dimensions suppressed. Worldlines around the waist of the hyperboloid form closed timelike curves.

We can perform the following coordinate transformation:

$$\begin{aligned}
\xi^0 &= L\cos t \sec\rho, \\
\xi^1 &= L\tan\rho\cos\theta, \\
\xi^2 &= L\tan\rho\sin\theta\cos\varphi, \\
\xi^3 &= L\tan\rho\sin\theta\sin\varphi, \\
\xi^4 &= L\sin t\sec\rho
\end{aligned} \tag{2.3}$$

where $0 \leq \rho \leq \frac{\pi}{2},\ 0 \leq \theta \leq \pi,\ 0 \leq \varphi \leq 2\pi$. The time coordinate $t \in (-\pi, \pi]$ is periodic with period 2π, which means that we have closed timelike curves. These are timelike worldlines that run in a loop, with the future leading into the past. Differentiating each of the above expressions, we obtain

$$\begin{aligned}
d\xi^0 &= L(\sin t\sec\rho\ dt + \cos t\sec\rho\tan\rho\ d\rho), \\
d\xi^1 &= L(\sec^2\rho\cos\theta\ d\rho - \tan\rho\sin\theta\ d\theta), \\
d\xi^2 &= L(\sec^2\rho\sin\theta\cos\varphi\ d\rho + \tan\rho\cos\theta\cos\varphi\ d\theta - \tan\rho\sin\theta\sin\varphi\ d\varphi), \\
d\xi^3 &= L(\sec^2\rho\sin\theta\sin\varphi\ d\rho + \tan\rho\cos\theta\sin\varphi\ d\theta + \tan\rho\sin\theta\cos\varphi\ d\varphi), \\
d\xi^4 &= L(\cos t\sec\rho\ dt + \sin t\sec\rho\tan\rho\ d\rho).
\end{aligned} \tag{2.4}$$

Substituting these into the metric (2.2) and using basic trigonometric identities, we obtain

$$ds^2 = L^2\sec^2\rho[-dt^2 + d\rho^2 + \sin^2\rho(d\theta^2 + \sin^2\theta\ d\varphi^2)]. \tag{2.5}$$

The Penrose diagram for adS is shown in Figure 2.2a. A spacelike hypersurface Σ is shown. The full domain of dependence $D(\Sigma)$ (1.61) is not equal to the entire manifold - in Figure 2.2a, $D(\Sigma)$ is contained within the diamond-shaped wedges. In other words, Σ is not a Cauchy surface, and adS is not globally hyperbolic [86]. Placing initial conditions on Σ is not enough to make sure everything is uniquely defined across spacetime; we must also impose boundary conditions on $\mathscr{I}, \mathscr{I}'$. We shall discuss boundary conditions in more detail when we look at quantisation in adS in chapter 3.

2.2 The covering space - CadS

The existence of closed timelike curves is very unappealing classically, but can also cause us problems when attempting to quantise fields on adS (see chapter 3) as it can be difficult to impose timelike periodicity on mode solutions. Therefore, it is often useful to remove this periodicity. This amounts to “opening up” or “unwrapping” the adS hyperboloid, which leaves us with the covering space, CadS (Figure 2.2b).

Further problems arise from the fact that CadS remains non-globally hyperbolic. We will see in the next chapter that we can bypass this problem by mapping to the Einstein Static Universe (ESU).

The ESU can be visualised as a 4-dimensional cylinder embedded in a 5-dimensional Minkowski space [86], written

$$(\eta^1)^2 + (\eta^2)^2 + (\eta^3)^2 + (\eta^4)^2 = L^2 \tag{2.6}$$

where L is the radius of the cylinder. The metric for the embedding space is the standard 5-dimensional Minkowski metric,

$$ds^2 = -(d\eta^0)^2 + (d\eta^1)^2 + (d\eta^2)^2 + (d\eta^3)^2 + (d\eta^4)^2. \tag{2.7}$$

Suppressing two spatial dimensions, ESU can be represented as the cylinder $(\eta^1)^2 + (\eta^2)^2 = L^2$. This visualisation is shown in Figure 2.3a, along with a Cauchy surface Σ. Now, initial data *can* be uniquely evolved throughout the spacetime - the ESU is globally hyperbolic. This will make our quantisation procedure in chapter 3 much simpler.

To see the connection with CadS, we perform the following coordinate transformation:

$$\begin{aligned}
\eta^0 &= Lt, \\
\eta^1 &= L\sin\rho\cos\theta, \\
\eta^2 &= L\sin\rho\sin\theta\cos\varphi, \\
\eta^3 &= L\sin\rho\sin\theta\sin\varphi, \\
\eta^4 &= L\cos\rho,
\end{aligned} \tag{2.8}$$

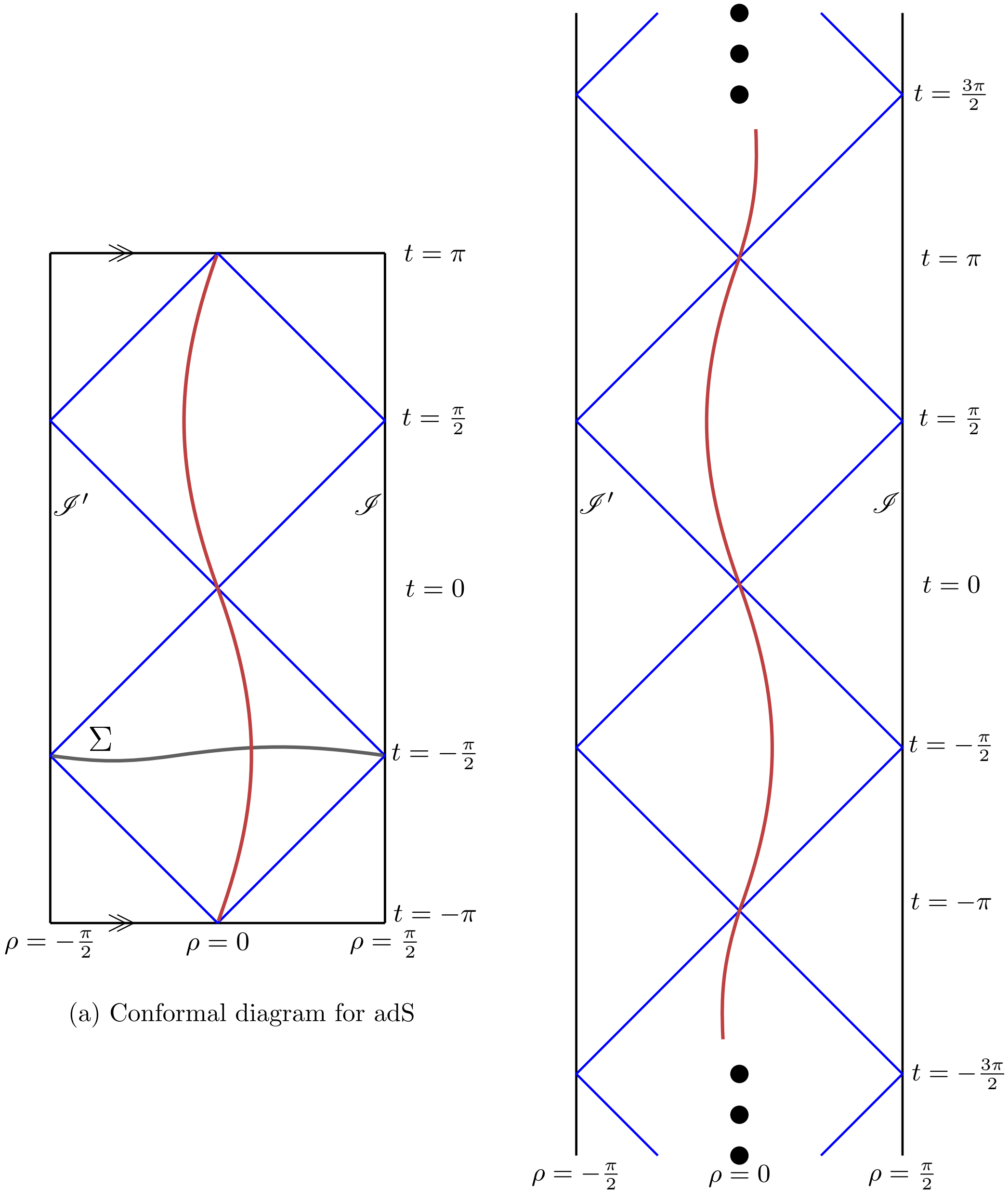

(a) Conformal diagram for adS

(b) Conformal diagram for CadS

Figure 2.2: The conformal diagrams for (pure) adS and CadS. In adS, the time coordinate t is periodic, with the lines $t = \pi$ and $t = -\pi$ being identified. The red curve shows a possible closed timelike worldine. In CadS, periodicity is removed from the time coordinate, and closed timelike curves no longer exist. Null rays are shown in blue. A spacelike surface Σ is shown in adS and the domain of dependence $D(\Sigma)$ (1.61) is given by the surrounding diamond region. Boundary data must be specified at $\mathscr{I}, \mathscr{I}'$ to allow initial data specified on Σ to propagate uniquely into the future. The same must also happen in CadS.

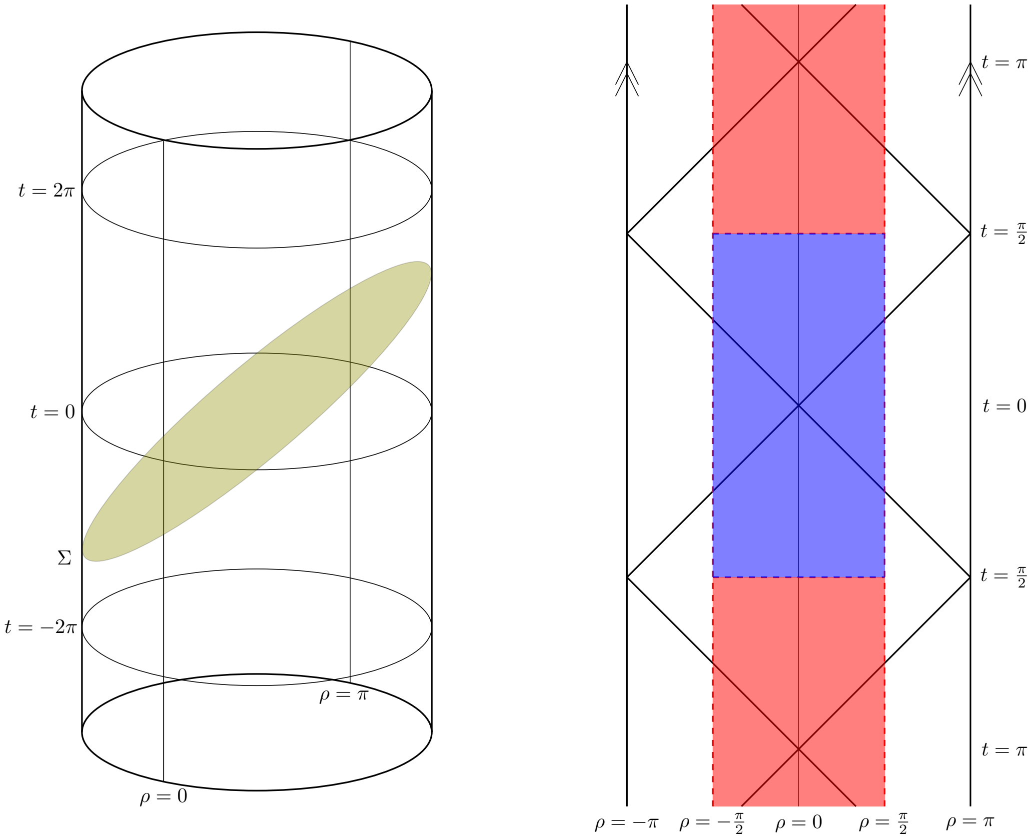

(a) ESU cylinder

(b) Conformal diagram for ESU

Figure 2.3: ESU is a globally hyperbolic spacetime [86], with Cauchy surface Σ. The coordinate ρ is periodic with period 2π. The conformal diagram demonstrates the mapping between ESU, CadS (red region) and adS (blue region). The arrows indicate that $\rho = -\pi$ is identified with $\rho = \pi$.

where $t \in (-\infty, \infty),\ \rho \in (-\pi, \pi],\ \theta \in [0, \pi],\ \varphi \in (0, 2\pi]$. The radial coordinate ρ is periodic, as can be seen in Figure 2.3. In this coordinate system, the line element (2.7) becomes

$$ds^2 = L^2[-dt^2 + d\rho^2 + \sin^2\rho\ (d\theta^2 + \sin^2\theta\ d\varphi^2)]. \tag{2.9}$$

Comparing with the line element for adS (2.5), we can see that there exists a conformal transformation between the two metrics:

$$g_{\mu\nu}^{adS} = \Omega^2 g_{\mu\nu}^{ESU}, \quad \Omega = \sec\rho. \tag{2.10}$$

This means that we can map from one spacetime to the other, provided that we also alter the prescribed domains for each coordinate, i.e. we remove periodicity on the radial coordinate ρ and alter the range of ρ such that $\rho \in (-\pi/2, \pi/2)$ to pass to CadS (note that the boundary of CadS is not part of the spacetime), and further impose periodicity on time coordinate t to pass to adS. This is illustrated in Figure 2.3b.

The fact that ESU and CadS are conformally related will become very important once we start to quantise. It is much more difficult to build a QFT in a spacetime that is not globally hyperbolic, so in chapter 3, we shall begin by defining our QFT in ESU, and then use our conformal transformation to map our classical field modes into adS.

2.3 The Poincaré patch - PadS

The Poincaré domain of adS (PadS) covers half of the full adS spacetime [91] and is used extensively in the adS/CFT correspondence (see section 2.4).

To transform the embedding space metric (2.2) to suitable coordinates for the Poincaré patch, we write [91]

$$\begin{aligned}
\xi^0 &= \frac{1}{2z}(z^2 + L^2 + \bar{x}^2 - t^2) \\
\xi^1 &= Lx^1/z \\
\xi^2 &= Lx^2/z \\
\xi^3 &= \frac{1}{2z}(z^2 - L^2 + \bar{x}^2 - t^2) \\
\xi^4 &= Lt/z
\end{aligned} \tag{2.11}$$

where $\bar{x}^2 = (x^1)^2 + (x^2)^2$. The metric for the Poincaré patch is then given by

$$ds^2 = \frac{L^2}{z^2}(-dt^2 + (dx^1)^2 + (dx^2)^2 + dz^2). \tag{2.12}$$

The Poincaré patch is conformally related to Minkowski space with conformal factor $\Omega^2 = L^2/z^2$. The coordinate z is a radial coordinate and effectively splits the adS spacetime into two regions (see Figure 2.4). We can write

$$\frac{1}{z} = \frac{\xi^0 - \xi^3}{L^2}. \tag{2.13}$$

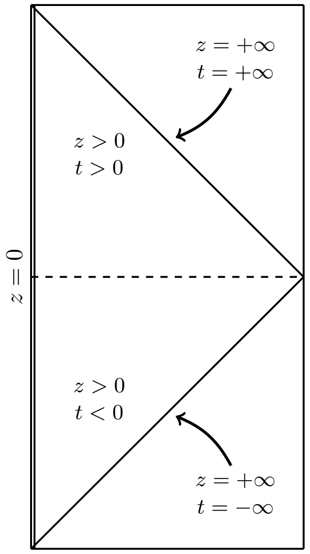

Figure 2.4: The conformal diagram for the Poincaré domain of adS, PadS. The spacetime is divided into two regions, where radial coordinate $z > 0$ (the inner wedge) and $z < 0$ (the outer triangles). The plane at $z = 0$ is a conformal timelike boundary [6].

Then the two regions are characterised by $z > 0$, i.e. $\xi^0 > \xi^3$, and $z < 0$, i.e. $\xi^0 < \xi^3$. Each of these regions corresponds to half of the adS hyperboloid. The Poincaré patch of adS refers to exactly one of these regions (usually the $z > 0$ patch is chosen).

There is a conformal, timelike boundary at $z = 0$. An obvious family of isometries are those which transform $\{t, x^1, x^2\}$ by an isometry of Minkowski space, but leave the coordinate z invariant. These isometries form the Poincaré group and exactly give the Poincaré symmetry on the boundary conformal field theory. This makes it the desirable setting for the adS/CFT correspondence.

The construction of a quantum field theory on PadS therefore also requires boundary conditions to be imposed on solutions to the Klein-Gordon equation (see, for example, [6]). Boundary conditions are discussed in more detail in section 3.1.

2.4 Why is adS important? - The adS/CFT correspondence

AdS spacetime has gained much interest in the literature in recent years, thanks to its crucial role in the adS/CFT (conformal field theory) correspondence [92–98]. The adS/CFT correspondence claims that supersymmetric Yang-Mills theory (SYM) in 4-dimensional Minkowski is equivalent to a Type IIB closed superstring theory on $adS_5 \times$

S^5 [97]. This means that there should exist some dictionary allowing us to translate objects from one theory into the other. This potentially has huge consequences for gravitational theories, since it may be easier to formulate certain quantities in one theory and then translate to the other, allowing us to perform calculations that would be too difficult or maybe even impossible otherwise.

To try to understand this correspondence a little more, we must first look at Yang-Mills theories and supersymmetric theories [99]. Yang-Mills theories are theories of interacting gauge fields. A gauge field is simply one that is invariant under gauge transformations. These theories are used in the description of the standard model of particle physics. We label Yang-Mills theories by their symmetry groups. For example, $U(N)$ Yang-Mills theory has gauge parameters which are elements of the group $U(N)$, $N \times N$ matrices. $SU(2) \times U(1)$ Yang-Mills theory is equivalent to electroweak theory which contains four gauge bosons: the photon γ and the massive gauge bosons W^+, W^- and Z^0 [98]. We can give three of these four bosons a mass by performing symmetry breaking [100].

For a more realistic theory, we must include fermions as well. Fermions are matter particles (electrons, protons, neutrons, etc.) with half-integer spin. Supersymmetry is a symmetry that relates bosons to fermions. It offers us a way of unifying matter and forces. It matches each particle with a superpartner whose spin differs by a half-integer. For instance, an electron is matched with a selectron, which is a bosonic version of the electron with the same mass. None of these superpartners have been observed in experiments, and so it is believed that supersymmetry must be spontaneously broken so that superpartners are allowed different masses.

It should be noted that these theories do not naturally include gravity. We instead must put in gravity by hand, by assuming there exists a massless particle of spin-2, called a graviton.

The fundamental objects of string theory are one-dimensional strings (see [101–104] for overviews of string theory concepts). Vibrations of these strings at different resonant frequencies lead to different fundamental particles. Strings can be "open" or "closed" [102]. An open string is a string with loose ends, whereas a closed string is one where the loose ends are connected. A consistent open string theory must necessarily include closed strings too, as it is possible for the two ends to join together to form a closed string, and then separate again. On the other hand, a closed string theory does not have to include open strings. Among excitations of closed strings, there are massless states with spin two - gravitons [104]. Thus, gravity arises naturally in string theory. A string theory with quantum states representing both bosons and fermions is called a "superstring theory" [101]. In superstring theories, it is possible to obtain unphysical states with negative norm, called ghosts. These ghosts decouple from the string spectrum when two conditions are satisfied: (i) the number of spacetime dimensions is 10, and (ii) the theory is supersymmetric [101].

In order to understand the differences between different types of superstring theories, we must first introduce the idea of orientation and handedness. A string is described

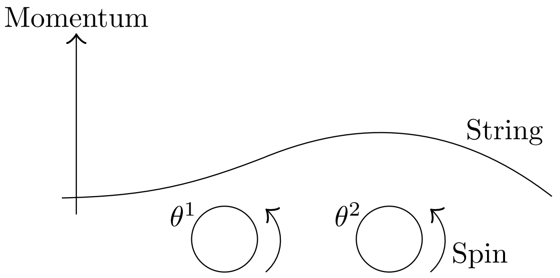

(a) Superspace coordinates (θ^1, θ^2) have the same handedness.

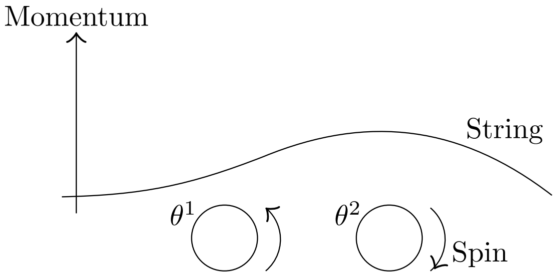

(b) Superspace coordinates (θ^1, θ^2) have opposite handedness.

Figure 2.5: Superspace coordinates have the property of handedness [102].

as oriented if it is possible to tell which way around the string you are travelling [102]. A string is unoriented if it is impossible to tell. The notion of handedness is a bit more difficult to grasp.

We can describe the path of a string using a two-dimensional surface called a worldsheet. This worldsheet is parametrised by coordinates τ, the proper time, and σ, a lengthscale related to the length of the string. Coordinates (τ, σ) on the worldsheet are mapped onto spacetime by functions $X^\mu(\tau, \sigma)$. These functions (referred to as "string coordinates") are often not enough to describe the paths that our strings take. We must also use "superspace coordinates" θ^A, where A runs from 1 to 2. The superspace coordinates behave like spin-$\frac{1}{2}$ particles and can spin one of two ways - either with the spin axis in the same direction as the string momentum, or with the spin axis in the opposite direction to the string momentum.

Coordinates θ^1 and θ^2 have the property of handedness [102]. We say that they have the same handedness if they spin in the same direction, and opposite handedness if they spin in opposite directions (see Figure 2.5). When superspace coordinates have opposite handedness, we can determine the direction of string momentum, and so the string is oriented. When superspace coordinates have the same handedness, we cannot use this to determine the direction of string momentum, and so the string can be either oriented or unoriented. Due to boundary conditions, the only consistent open string theory has unoriented strings, meaning that superspace coordinates must have the same handedness [102].

The types of string theories we find are [101, 102]:

Name	**Open/Closed?**	**Oriented?**	**Handedness**
Type I	Open (+ closed)	No	Same
Type IIA	Closed	Yes	Opposite
Type IIB	Closed	Yes	Same

We previously claimed that Type IIB superstring theory on $adS_5 \times S^5$ was equivalent to SYM on four-dimensional Minkowski spacetime. However, since all superstring theories are 10-dimensional, for this equivalence to work, those 10-dimensions must take a particular form: five dimensions form a sphere S^5, whilst the other five dimensions form a non-compact adS spacetime, adS$_5$. The 4-d Minkowski space of the CFT can be thought of as the boundary of adS$_5$ of the superstring theory [105].

The adS/CFT correspondence can be better understood from the perspective of the holographic principle. This principle, conjectured by t'Hooft [106] and subsequently developed by Susskind [105], claims that the total information content in a region of spacetime is equivalent to a theory that lives on the surrounding surface. This principle can be applied directly to adS since it is a spacetime with a boundary. Therefore a theory of gravity in the bulk of adS is equivalent to a theory on the boundary.

The adS/CFT correspondence was proposed by Maldacena [92]. The theory is still unproven but has so far stood up to all theoretical work in this area. The correspondence works both ways - the CFT in Minkowski tells us about gravity in adS, and vice versa. It is very difficult to calculate thermal states in SYM, but black holes in the bulk of adS have a temperature [107], and this is why analysis of black holes in adS (see chapter 5) is particularly important.

2.5 Summary

In this chapter, we have introduced the concept of anti-de Sitter spacetimes - that is, spacetimes with a negative cosmological constant $\Lambda < 0$. These spacetimes have a timelike boundary, on which we must impose conditions to allow information to propagate into the future.

In section 2.1, we saw that adS possesses closed timelike curves. By removing the periodicity in the time coordinate, we obtain the covering space of adS, CadS. CadS is conformally related to the Einstein Static Universe (see section 2.2), a fact which will become important when we quantise in CadS.

We also discussed the Poincaré domain, PadS, which is the desired setting for the adS/CFT correspondence. This is due to the fact that PadS is conformally related to Minkowski space and therefore possesses many symmetries.

We concluded with a brief discussion of the adS/CFT correspondence (section 2.4), which related a conformal field theory on the boundary of adS to a theory of gravity in the bulk.

In the following chapters, we will look at quantum field theory in adS. In chapter 3, we will focus on CadS, whilst in chapters 5 and 6 we will look at black hole adS spacetimes, introduced in chapter 4.

Chapter 3

Quantum field theory in adS

In this chapter, we look at quantization in adS. As discussed in section 2.1, adS is a non globally hyperbolic spacetime which makes quantization rather difficult. Instead, we quantize in ESU and map our scalar field modes to adS using a conformal transformation. Recall that boundary conditions must be imposed on field modes to ensure that data propagates uniquely into the future. As we shall see, there are different types of boundary condition we can impose. Whilst Dirichlet boundary conditions are the most popular in the literature, we choose to impose more general Robin boundary conditions. The main aim of this chapter will be to explore the effect of Robin boundary conditions on both vacuum and thermal expectation values in CadS. The work done in this chapter is based on [7].

3.1 Previous work

Quantization in adS was first explored in [5], where they introduced the concepts of reflective and transparent boundary conditions (see Section 3.2). We can choose to impose reflective conditions using Dirichlet, Neumann or Robin boundary conditions. Certain restrictions must be placed on the mass of scalar fields to ensure that mode solutions are stable. We find that, for mode solutions to be stable, we must have

$$m^2 > -d^2/4, \tag{3.1}$$

where d is the number of dimensions. Note that mode solutions can still be unstable even when this bound is satisfied, depending on the conditions imposed at the boundary i.e. this is a necessary but not sufficient condition for mode solutions to be stable. The condition 3.1 is known as the Breitenlohner-Freedman bound [108,109]. It is important to note that negative m^2 solutions are allowed in adS (provided (3.1) is satisfied) since adS includes a gravitational potential that gives negative m^2 eigenstates a positive energy. The Breitenlohner-Freedman bound (3.1) is automatically satisfied for massless, conformally coupled scalar fields.

Initial work following on from [5] focused on imposing Dirichlet conditions only (see (3.12) for a definition of Dirichlet conditions). Vacuum expectation values are calculated in [110, 111], where it is found that

$$\langle \hat{\phi}_D^2 \rangle_{ren} = -\frac{1}{48\pi^2 L^2} \tag{3.2}$$

for a massless, conformally coupled scalar field $\hat{\phi}_D$ with Dirichlet conditions imposed at the boundary. The quantity is found to be constant, which is to be expected since the scalar field respects the maximal symmetry of adS. Similarly, for Neumann conditions (again, see (3.12) for a definition), the VP is given by [110]

$$\langle \hat{\phi}_N^2 \rangle_{ren} = \frac{5}{48\pi^2 L^2}. \tag{3.3}$$

In this thesis, we would like to explore the effect of imposing Robin boundary conditions. This breaks the maximal symmetry and so the calculation of vacuum expectation values is more involved. Robin boundary conditions have been considered in the Poincaré patch of adS (PadS) in [6,112,113]. PadS is conformally related to Minkowski space with a boundary (see section 2.3), so the behaviour of expectation values in PadS is expected to be similar to the behaviour of expectation values in the Casimir effect. However, whilst the two-point functions for a scalar field are shown to be of Hadamard form for all boundary conditions in PadS, it is found that, upon imposing Robin boundary conditions, there exist bound state solutions to the Klein-Gordon equation; that is, mode solutions that exponentially decay as we approach the boundary.

Robin conditions for the Casimir effect are considered in [114, 115]. Suppose we impose a boundary in Minkowski spacetime at some constant value of r given by $r = r_\infty$. It is then found [115] that bound state solutions of the Klein-Gordon equation exist, as in PadS. The renormalised Green's functions with Dirichlet and Robin conditions imposed (denoted G^D_{Cas} and G^R_{Cas} respectively) can be written in the form [114]

$$G^D_{Cas}(\mathbf{x}, \mathbf{x}') = G^D_\infty(\mathbf{x}, \mathbf{x}') + \mathcal{O}(r - r_\infty), \tag{3.4}$$

$$G^R_{Cas}(\mathbf{x}, \mathbf{x}') = G^N_\infty(\mathbf{x}, \mathbf{x}') + \mathcal{O}(r - r_\infty), \tag{3.5}$$

where G^D_∞, G^N_∞ are the Green's functions evaluated on the boundary with Dirichlet and Neumann conditions imposed respectively. As $r \to r_\infty$, the two-point functions approach the Neumann solution for all boundary conditions that are not Dirichlet. Later, in section 3.6, we shall see that this is also the case in CadS.

Some work has already been carried out by imposing Robin boundary conditions in adS and CadS. In [116], Dappiaggi, Ferreira and Marta show that CadS does not admit bound state solutions, and so for massive scalar fields they are able to construct a 2-point function for the vacuum state satisfying all Robin boundary conditions for which the Hadamard condition is fulfilled. In adS, however, the presence of closed timelike curves hinders the quantization scheme, and no two-point function exists, except for one special value of mass, provided we use Neumann boundary conditions.

Barroso and Pitelli [117] manage to avoid these difficulties by applying Robin boundary conditions to just the $\ell = 0$ mode. According to rules set out by Ishibashi and Wald [118], this is allowed, but the physical relevance is not clear. Dirichlet conditions are applied to all other modes, and then the VP and expectation values for the stress-energy tensor are calculated. As we approach the boundary, these expectation values tend towards the results obtained when Dirichlet conditions are imposed on all of the field modes. This behaviour occurs for all Robin conditions except those equivalent to Neumann.

Finally, in [119], the effect of Wick rotations on quantization in CadS is explored. This is done for massive scalar fields only, with Dirichlet and Neumann boundary conditions imposed. The results here seem to suggest that the long range behaviours ($r \to \infty$) of Euclidean and Lorentzian theories differ drastically for sufficiently large mass. However, it is not thought that the behaviours should be different for massless scalar fields, which is all that is considered in this thesis.

3.2 Classical scalar field on CadS

In this section, we solve the wave equation (1.56) in ESU and then perform a conformal transformation to find mode solutions in CadS (section 3.2.1). We must impose boundary conditions on the mode solutions since CadS is not globally hyperbolic. These boundary conditions can take the form of transparent or reflective conditions (section 3.2.2). For reflective conditions, we can impose Dirichlet, Neumann or Robin conditions. In section 3.2.3, we consider Robin conditions, where some choices of Robin parameter α (see (3.21)) result in unstable modes (section 3.2.4).

3.2.1 Mode solutions

We consider a massless, conformally coupled scalar field $\hat{\phi}$ satisfying the Klein-Gordon equation (1.56). We must apply boundary conditions to the field modes to ensure unique evolution. It is difficult to do this in CadS, since the boundary is not physically part of the spacetime. Instead, we solve the Klein-Gordon equation in ESU, and apply boundary conditions to field modes $\phi^{ESU}_{\omega\ell m}$, before using the conformal transformation (2.10),

$$\phi_{\omega\ell m} = \cos\rho \; \phi^{ESU}_{\omega\ell m} \tag{3.6}$$

where ρ is a radial coordinate going around the circumference of the ESU cylinder (see Figure 2.3a). The field modes $\phi_{\omega\ell m}$ are solutions in CadS. Boundary conditions are imposed at $\rho = \pi/2$. The ESU metric is given in (2.9). The Klein-Gordon equation in ESU is

$$\left(\Box^{ESU} - \frac{1}{6}R^{ESU}\right)\phi^{ESU}_{\omega\ell m} = \left(\Box^{ESU} - \frac{1}{L^2}\right)\phi^{ESU}_{\omega\ell m} = 0 \tag{3.7}$$

which can be written

$$\left(-\frac{\partial^2}{\partial t^2}+\frac{1}{\sin^2\rho}\left[\frac{\partial}{\partial\rho}\left(\sin^2\rho\frac{\partial}{\partial\rho}\right)\right.\right.$$
$$\left.\left.+\frac{1}{\sin\theta}\frac{\partial}{\partial\theta}\left(\sin\theta\frac{\partial}{\partial\theta}\right)+\frac{1}{\sin^2\theta}\frac{\partial^2}{\partial\varphi^2}\right]-1\right)\phi^{ESU}_{\omega\ell m}=0. \quad (3.8)$$

Solving by separation of variables (for more details, see Appendix B), we find

$$\phi^{ESU}_{\omega\ell m}=\mathcal{C}_{\omega\ell}e^{-i\omega t}(\sin\rho)^{-1/2}\mathbf{Q}^{\ell+\frac{1}{2}}_{\omega-\frac{1}{2}}(\cos\rho)Y_{\ell m}(\theta,\varphi) \quad (3.9)$$

where $\ell\geq|m|,\omega\in\mathbb{R}$ and $\mathcal{C}_{\omega\ell}$ is a normalisation constant. The $\mathbf{Q}^{\mu}_{\nu}$ are Olver's definition of Legendre functions [120] (see equation B.17) and the $Y_{\ell m}$ are spherical harmonics.

3.2.2 Transparent and reflective boundary conditions

We now must impose boundary conditions. Avis, Isham and Storey [5] distinguish between transparent and reflective boundary conditions. A discussion of these different boundary conditions in the context of adS/CFT is given in [121].

Transparent conditions allow modes to pass through the boundary $\rho=\pi/2$ as though it were not there. In ESU, this is acceptable provided the modes are finite at this point. From an adS perspective, we must imagine the modes travelling "round the back" of the ESU cylinder, and entering at the other side (see Figure 3.1).

We first note that, up to a multiplicative constant,

$$\mathbf{Q}^{\ell+\frac{1}{2}}_{\omega-\frac{1}{2}}(\cos\rho)\sim C^{\ell+1}_{\omega-\ell-1}(\cos\rho) \quad (3.10)$$

where C^{μ}_{ν} are Gegenbauer functions (this can be derived from [120, eq. 14.9.9]). This representation makes it easier for us to compare our solutions with [5]. These modes are only finite at $\rho=\pi/2$ when they are polynomial, i.e. $\omega-\ell-1$ is a non-negative integer. Since ℓ is defined to be an integer, this means that ω must also be an integer. Hence, the mode solutions are periodic in t with period 2π, which is necessary for the solutions to "wrap around" the ESU cylinder. Therefore, we write

$$\phi^{T,ESU}_{\omega\ell m}=\mathcal{C}_{\omega\ell}e^{-i\omega t}(\sin\rho)^{\ell}C^{\ell+1}_{\omega-\ell-1}(\cos\rho)Y_{\ell m}(\theta,\varphi),\quad \omega\in\mathbb{Z},\ \omega\geq\ell+1, \quad (3.11)$$

where we write the superscript "T" to stand for "transparent".

Reflective boundary conditions require the field modes to be zero, or their derivatives to be zero, on the boundary. This amounts to field modes being "reflected" back into the spacetime (see Figure 3.1). We refer to these two types of reflective boundary conditions as Dirichlet and Neumann respectively, i.e.

$$\text{Dirichlet}:\ \lim_{\rho\to\frac{\pi}{2}}\phi^{D,ESU}_{\omega\ell m}=0,\quad \text{Neumann}:\ \lim_{\rho\to\frac{\pi}{2}}\frac{\partial}{\partial\rho}\phi^{N,ESU}_{\omega\ell m}=0. \quad (3.12)$$

To impose reflective Dirichlet conditions, we must have

$$\lim_{\rho\to\frac{\pi}{2}} C^{\ell+1}_{\omega-\ell-1}(\cos\rho) = 0. \tag{3.13}$$

This is only true if $\omega-\ell-1$ is a positive odd integer, i.e. $\omega=\ell+2n+2$ for n some non-negative integer. We can therefore write

$$\phi^{D,ESU}_{n\ell m} = \mathcal{C}_{n\ell} e^{-i(\ell+2n+2)t}(\sin\rho)^{\ell} C^{\ell+1}_{2n+1}(\cos\rho) Y_{\ell m}(\theta,\varphi), \quad n=0,1,... \tag{3.14}$$

where the superscript "D" stands for "Dirichlet". Reflective Neumann conditions can only hold if

$$\lim_{\rho\to\frac{\pi}{2}} \frac{\partial}{\partial\rho}[C^{\ell+1}_{\omega-\ell-1}(\cos\rho)] = \lim_{\rho\to\frac{\pi}{2}} [2(1+\ell)\sin\rho\; C^{\ell+2}_{\omega-\ell-2}(\cos\rho)] = 0 \tag{3.15}$$

where the derivative has been performed by using [120, eq. 18.9.19] along with the chain rule. This implies that we require

$$\lim_{\rho\to\frac{\pi}{2}} [C^{\ell+2}_{\omega-\ell-2}(\cos\rho)] = 0. \tag{3.16}$$

This can only happen if $\omega-\ell-2$ is a positive odd integer, so we now write $\omega=\ell+2n+1$ and the modes satisfying Neumann boundary conditions are

$$\phi^{N,ESU}_{n\ell m} = \mathcal{C}_{n\ell} e^{-i(\ell+2n+1)t}(\sin\rho)^{\ell} C^{\ell+1}_{2n} Y_{\ell m}(\theta,\varphi), \qquad n=0,1,.... \tag{3.17}$$

Using the conformal transformation (3.6), the positive frequency modes in CadS are

$$\phi^{T}_{\omega\ell m} = \mathcal{C}_{\omega\ell} e^{-i\omega t}\cos\rho(\sin\rho)^{\ell} C^{\ell+1}_{\omega-\ell-1}(\cos\rho) Y_{\ell m}(\theta,\varphi), \quad \omega\in\mathbb{Z},\ \omega\geq\ell+1 \tag{3.18}$$

$$\phi^{D}_{n\ell m} = \mathcal{C}_{n\ell} e^{-i(\ell+2n+2)t}\cos\rho(\sin\rho)^{\ell} C^{\ell+1}_{2n+1}(\cos\rho) Y_{\ell m}(\theta,\varphi), \quad n=0,1,... \tag{3.19}$$

$$\phi^{N}_{n\ell m} = \mathcal{C}_{n\ell} e^{-i(\ell+2n+1)t}\cos\rho(\sin\rho)^{\ell} C^{\ell+1}_{2n}(\cos\rho) Y_{\ell m}(\theta,\varphi), \quad n=0,1,.... \tag{3.20}$$

It is important to note here that $\omega\in\mathbb{Z}$, and so solutions are periodic in time with period 2π.

The positive frequency modes with Dirichlet and Neumann reflective boundary conditions appear as special cases of the positive frequency modes with transparent conditions imposed. In the following section, we generalise reflective conditions to be governed by Robin boundary conditions instead of simply Dirichlet and Neumann. In this case, modes obeying Dirichlet and Neumann conditions still arise as special cases of those obeying Robin boundary conditions, but modes obeying transparent conditions do not. This is due to the fact that the frequency does not necessarily take integer values when general Robin conditions are imposed (see, for example, (3.24) and the discussion that follows). For the remainder of this thesis, we will no longer consider imposing transparent boundary conditions, instead focusing on reflective boundary conditions - that is, Robin boundary conditions, with Dirichlet and Neumann boundary conditions as special cases.

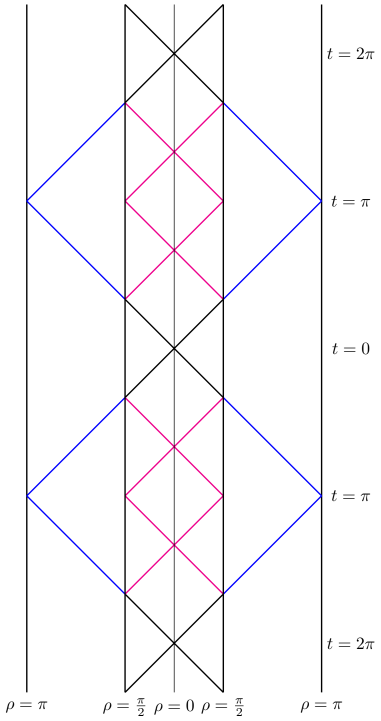

Figure 3.1: The ESU cylinder, containing CadS (see Figure 2.3b). The blue null lines obey transparent boundary conditions, whereas the magenta null lines obey reflective boundary conditions.

3.2.3 Robin boundary conditions

We define reflective modes using Robin boundary conditions by introducing a Robin parameter α and writing

$$\lim_{\rho \to \frac{\pi}{2}} \left\{ \cos\alpha \, \phi^{\alpha,ESU}_{\omega\ell m} + \sin\alpha \, \frac{\partial}{\partial\rho} \phi^{\alpha,ESU}_{\omega\ell m} \right\} = 0. \tag{3.21}$$

We have $\alpha \in [0, \pi)$ where Dirichlet conditions are recovered for $\alpha = 0$ and Neumann conditions for $\alpha = \pi/2$.

From (3.9), using [120, Eq. 14.5.3, 14.5.4], we have

$$\lim_{\rho \to \frac{\pi}{2}} \phi^{\alpha,ESU}_{\omega\ell m} = \mathcal{C}_{n\ell} e^{-i\omega t} \left(\frac{-2^{\ell - \frac{1}{2}} \pi^{\frac{1}{2}} \sin\left(\frac{1}{2}(\ell + \omega)\pi\right) \Gamma\left(\frac{\omega + \ell + 1}{2}\right)}{\Gamma\left(\frac{\omega - \ell + 1}{2}\right) \Gamma\left(\omega + \ell + 1\right)} \right) Y_{\ell m}(\theta, \varphi), \tag{3.22}$$

$$\lim_{\rho \to \frac{\pi}{2}} \frac{\partial}{\partial\rho} \phi^{\alpha,ESU}_{\omega\ell m} = \mathcal{C}_{n\ell} e^{-i\omega t} \left(\frac{-2^{\ell + \frac{1}{2}} \pi^{\frac{1}{2}} \cos\left(\frac{1}{2}(\ell + \omega)\pi\right) \Gamma\left(\frac{\omega + \ell + 2}{2}\right)}{\Gamma\left(\frac{\omega - \ell}{2}\right) \Gamma(\omega + \ell + 1)} \right) Y_{\ell m}(\theta, \varphi). \tag{3.23}$$

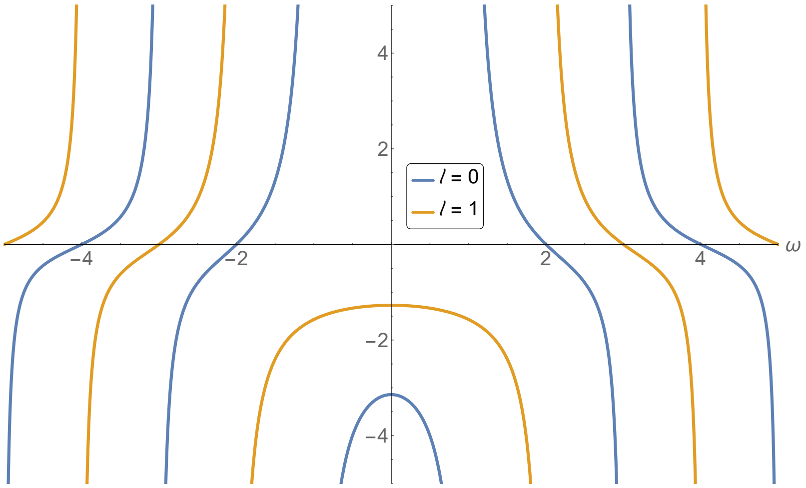

Figure 3.2: The left-hand-side of (3.24) plotted as a function of frequency ω for $\ell = 0, 1$. The function crosses the x-axis when $\omega + \ell$ is an even integer, and diverges when $\omega + \ell$ is an odd integer. For $0 < \omega < \ell + 1$, the function never crosses the x-axis. The maximum in this interval occurs at $\omega = 0$, and is greater than or equal to $-\pi$ for all ℓ.

From substituting (3.22, 3.23) in (3.21), we obtain the following quantization condition on the mode frequency ω:

$$-\tan\left(\frac{1}{2}[\ell + \omega]\pi\right)\frac{\Gamma\left(\frac{\omega-\ell}{2}\right)\Gamma\left(\frac{\omega+\ell+1}{2}\right)}{\Gamma\left(\frac{\omega+\ell+2}{2}\right)\Gamma\left(\frac{\omega-\ell+1}{2}\right)} = 2\tan\alpha. \tag{3.24}$$

This means we have a discrete set of ω for each value of ℓ. We shall label these as $\omega_{n\ell}$, where $n = 1, 2, \ldots$. It is impossible to give an explicit representation for these $\omega_{n\ell}$ for general α, but in the Dirichlet and Neumann cases, (3.24) reduces to $\omega_{n\ell} = 2n - \ell$ and $\omega_{n\ell} = 2n + 1 - \ell$ respectively. This is equivalent to the conditions that were imposed on the Gegenbauer functions in (3.14, 3.17) previously.

In the general Robin case ($\alpha \neq 0, \pi/2$), the frequencies $\omega_{n\ell}$ will not be integers. Indeed, we can see that when $\omega_{n\ell} + \ell$ is an even integer, the left-hand-side of (3.24) will be zero, and when $\omega_{n\ell} + \ell$ is an odd integer, the left-hand-side of (3.24) will diverge. Therefore, solutions of (3.24) for $\alpha \neq 0, \pi/2$ must lie in the interval $\ell + 2n - 1 \leq \omega \leq \ell + 2n + 1$ (see Figure 3.2). Note that there will be no solutions in the region $0 < \omega < \ell + 1$ unless $\tan\alpha < -\frac{\pi}{2}$. This is because the maximum of the left-hand-side of (3.24) (which occurs at $\omega = 0$) is greater than or equal to $-\pi$.

The mode solutions with general Robin conditions imposed are therefore

$$\phi^{\alpha}_{n\ell m} = \mathcal{C}_{n\ell} e^{-i\omega_{n\ell}t}\cos\rho\ (\sin\rho)^{-1/2}\mathbf{Q}^{\ell+1/2}_{\omega_{n\ell}-1/2}(\cos\rho) Y_{\ell m}(\theta, \varphi) \tag{3.25}$$

where $\omega_{n\ell}$ satisfies (3.24). It will be easier for us to consider $\phi^{\alpha}_{n\ell m}$ in general, and then reduce to the Dirichlet and Neumann cases when necessary.

3.2.4 Unstable modes

Despite the fact that a massless, conformally coupled scalar field satisfies the Breitenlohner-Freedman bound [108], we find that there will still exist unstable modes for certain values of the Robin parameter α. Mode instability is equivalent to finding solutions of the wave equation with imaginary frequency ω.

One may question whether or not ω could be set to be complex rather than purely imaginary, and whether this situation would give rise to unstable modes as well. Following the work of Ishibashi and Wald [118], we write the Klein-Gordon equation (3.8) in the form

$$\frac{\partial^2}{\partial t^2}\phi^{ESU}_{\omega\ell m} = -\hat{A}\phi^{ESU}_{\omega\ell m} \tag{3.26}$$

for some spatial operator $\hat{A}$. The operator A must have positive self-adjoint extensions. For this to happen, one requires $\omega^2 \in \mathbb{R}$ [118], and therefore only purely imaginary ω needs to be considered.

We set $\omega = i\Omega$ with $\Omega \in \mathbb{R}$, and write the quantization condition (3.24) as

$$-\frac{\left|\Gamma\left(\frac{i\Omega+\ell+1}{2}\right)\right|^2}{\left|\Gamma\left(\frac{i\Omega+\ell+2}{2}\right)\right|^2} = 2\tan\alpha \tag{3.27}$$

where $|\Gamma(x+iy)|^2 = \Gamma(x+iy)\Gamma(x-iy)$ and we have used the following relations, derived from [120, 5.5.3]

$$\Gamma\left(\frac{i\Omega-\ell}{2}\right)\Gamma\left(\frac{-i\Omega+\ell+2}{2}\right) = \frac{\pi}{\sin\left(\frac{\pi}{2}(i\Omega-\ell)\right)} \tag{3.28}$$

$$\Gamma\left(\frac{i\Omega-\ell+1}{2}\right)\Gamma\left(\frac{-i\Omega+\ell+1}{2}\right) = \frac{\pi}{\cos\left(\frac{\pi}{2}(i\Omega-\ell)\right)}. \tag{3.29}$$

Unstable modes will exist whenever (3.27) can be satisfied with $\Omega \in \mathbb{R}$. In fact, we require $\Omega \in \mathbb{R}_{>0}$. If this were not the case, then mode solutions would be exponentially decaying rather than exponentially growing, and we would obtain instabilities in the past rather than in the future. For Dirichlet ($\alpha = 0$) and Neumann conditions ($\alpha = \pi/2$) there are no solutions to (3.27) and so no unstable modes. In fact, it is clear that there are no unstable modes provided $0 < \alpha < \frac{\pi}{2}$.

Unstable modes exist for some α such that $\tan\alpha < 0$. The left-hand-side of (3.27) is an increasing function of ℓ, with minimum for fixed ℓ occurring at $\Omega = 0$. This is apparent for $\ell = 0, 1, 2$ from studying Figure 3.3, and can be seen for general ℓ by studying the derivative of the left-hand-side of (3.27)

$$\begin{aligned}\frac{\partial}{\partial\Omega}\left(-\frac{\left|\Gamma\left(\frac{i\Omega+\ell+1}{2}\right)\right|^2}{\left|\Gamma\left(\frac{i\Omega+\ell+2}{2}\right)\right|^2}\right) = -\frac{i\left|\Gamma\left(\frac{i\Omega+\ell+1}{2}\right)\right|^2}{2\left|\Gamma\left(\frac{i\Omega+\ell+2}{2}\right)\right|^2}&\left[\psi\left(\frac{1+\ell-i\Omega}{2}\right) - \psi\left(\frac{2+\ell-i\Omega}{2}\right)\right.\\ &\left.-\psi\left(\frac{1+\ell+i\Omega}{2}\right) + \psi\left(\frac{2+\ell+i\Omega}{2}\right)\right].\end{aligned} \tag{3.30}$$

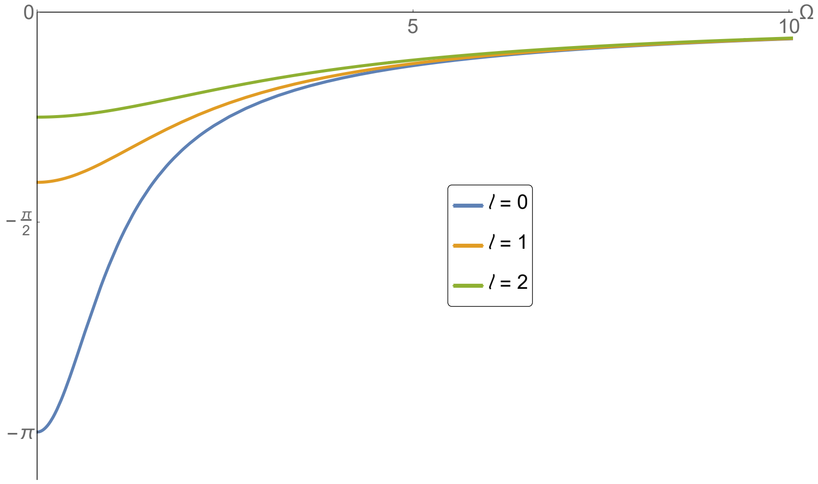

Figure 3.3: The left-hand-side of (3.27) plotted as a function of frequency Ω for $\ell = 0, 1, 2$.

The fact that there is a stationary point at $\Omega = 0$ is immediately apparent. The fact that (3.30) is positive for all nonzero Ω can be seen by using [122, eq. 44:11:1] to rearrange the digamma functions. Most importantly, the smallest possible value of the left-hand-side of (3.27) occurs at $\ell = 0, \Omega = 0$, and so

$$-\frac{\left|\Gamma\left(\frac{i\Omega+\ell+1}{2}\right)\right|^2}{\left|\Gamma\left(\frac{i\Omega+\ell+2}{2}\right)\right|^2} \geq -\pi \quad \forall\ \ell \in \mathbb{Z}_{>0}, \Omega \in \mathbb{R}_{>0}. \tag{3.31}$$

It is trivial to show that, for any fixed value of ℓ, the left-hand-side of (3.27) approaches 0 as $\Omega \to \infty$. Therefore, we must obtain unstable modes if $-\pi < 2\tan\alpha < 0$, that is

$$\alpha_{crit} < \alpha < \pi \tag{3.32}$$

where

$$\alpha_{crit} = -\tan^{-1}\left(\frac{\pi}{2}\right) \simeq 0.68\pi. \tag{3.33}$$

If $\alpha \in (\alpha_{crit}, \pi)$, then it makes no sense to attempt to calculate quantities such as the VP or SET, since there exist unstable modes and solutions are unphysical. Therefore, for the remainder of this chapter, we shall consider the Robin parameter to be in the range $\alpha \in [0, \alpha_{crit})$.

3.2.5 Normalisation constants

In this section, we calculate the constants $\mathcal{C}_{n\ell}$ by insisting that the modes are orthonormal. In section 1.2 we showed that the scalar product of two scalar field modes was independent of the choice of Cauchy surface, but this proof was only valid in a globally

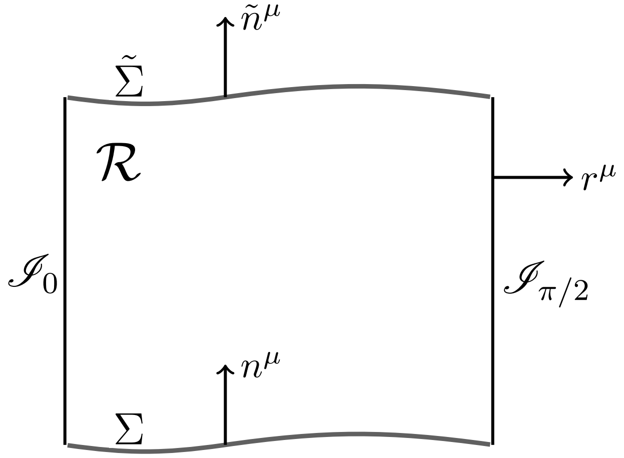

Figure 3.4: Diagram showing the volume $\mathcal{R}$ bounded by $\partial\mathcal{R} = \mathscr{I}_0 \cup \mathscr{I}_{\pi/2} \cup \Sigma \cup \tilde{\Sigma}$.

hyperbolic spacetime. We now perform a similar proof to show that scalar products are not just independent of the spacelike hypersurface on which they are defined, but also independent of the value of Robin parameter α when we impose general Robin conditions on the field modes at the boundary.

As before, we use Stokes' Theorem to prove this, where now we let $\mathcal{R}$ be the region enclosed by $\partial\mathcal{R} = \mathscr{I}_0 \cup \mathscr{I}_{\pi/2} \cup \Sigma \cup \tilde{\Sigma}$, where $\mathscr{I}_0$ is the boundary at $\rho = 0$, $\mathscr{I}_{\pi/2}$ is the boundary at $\rho = \pi/2$ and $\Sigma, \tilde{\Sigma}$ are spacelike hypersurfaces. See Figure 3.4 for a visualisation of this region.

Stokes' Theorem now gives us

$$\int_{\partial\mathcal{R}} (\phi_1^* \partial_\mu \phi_2 - \phi_2 \partial_\mu \phi_1^*) d\sigma^\mu = \int_{\mathcal{R}} \nabla^\mu (\phi_1^* \partial_\mu \phi_2 - \phi_2 \partial_\mu \phi_1^*) dV, \tag{3.34}$$

where ϕ_1, ϕ_2 are adS field modes satisfying both the Klein-Gordon equation and Robin boundary conditions and $d\sigma^\mu = n^\mu \sqrt{|\gamma|} d^3\mathbf{x}$ for n^μ the relevant unit normal (see Figure 3.4). The equation (3.34) is effectively the same as (1.65), except in this case the boundary $\partial\mathcal{R}$ is made up of four parts rather than two (this can be seen by comparing Figures 1.2 and 3.4). The right-hand-side of (3.34) vanishes due to the Klein-Gordon equation.

The radial parts of ϕ_1, ϕ_2 can be written (see Appendix B)

$$X(\rho) = \cos\rho \, (\sin\rho)^{1/2} \mathbf{Q}^{\ell+1/2}_{\omega_{n\ell}-1/2}(\cos\rho) = \frac{(-1)^{\ell+1}\pi}{2^{\ell+3/2}\Gamma(\ell+3/2)\Gamma(\omega_{n\ell}-\ell)} \rho^\ell + \mathcal{O}(\rho^{\ell+2}) \tag{3.35}$$

which vanishes on $\mathscr{I}_0$ unless $\ell = 0$. However, the derivative of the $\ell = 0$ mode will vanish at $\rho = 0$, and so the integrand in (3.34) on $\mathscr{I}_0$ will be zero. Stokes' theorem

(3.34) gives

$$\int_{\mathscr{I}_{\pi/2}} (\phi_1^* \partial_\mu \phi_2 - \phi_2 \partial_\mu \phi_1^*) r^\mu d\mathscr{I}_{\pi/2} + \int_{\tilde{\Sigma}} (\phi_1^* \partial_\mu \phi_2 - \phi_2 \partial_\mu \phi_1^*) \tilde{n}^\mu d\tilde{\Sigma} \\ - \int_{\Sigma} (\phi_1^* \partial_\mu \phi_2 - \phi_2 \partial_\mu \phi_1^*) n^\mu d\Sigma = 0. \quad (3.36)$$

Now, on $\mathscr{I}_{\pi/2}$, we impose Robin boundary conditions (3.21), and so we have

$$\phi_1^* \partial_\mu \phi_2 = \phi_2 \partial_\mu \phi_1^* = -(\cot\alpha + \tan\rho)\phi_1^* \phi_2. \quad (3.37)$$

Note that the factor of $\tan\rho$ comes from imposing Robin boundary conditions (3.21) in ESU and then applying the conformal transform (3.6). Hence the integral on the boundary $\mathscr{I}_{\pi/2}$ also vanishes. Hence, we find

$$\int_{\Sigma} (\phi_1^* \partial_\mu \phi_2 - \phi_2 \partial_\mu \phi_1^*) n^\mu d\Sigma = \int_{\tilde{\Sigma}} (\phi_1^* \partial_\mu \phi_2 - \phi_2 \partial_\mu \phi_1^*) \tilde{n}^\mu d\tilde{\Sigma} \quad (3.38)$$

and conclude that the scalar product is independent of choice of hypersurface Σ and the parameter α.

Taking the scalar product over the hypersurface Σ_0 defined where $t = 0$, we have

$$\langle \phi^\alpha_{n\ell m}(x), \phi^\alpha_{n'\ell'm'}(x) \rangle = i \int_{\Sigma_0} \left(\phi^{\alpha,*}_{n\ell m}(x) \partial_t \phi^\alpha_{n'\ell'm'}(x) - \phi^\alpha_{n'\ell'm'}(x) \partial_t \phi^{\alpha,*}_{n\ell m}(x) \right) d\Sigma_0 \quad (3.39)$$

where $d\Sigma_0 = L^2 \tan^2\rho \ \sin\theta \ d\rho \ d\theta \ d\varphi$. Applying the orthonormality of the spherical harmonics, we find

$$\begin{aligned} \langle \phi^\alpha_{n\ell m}(x), \phi^\alpha_{n'\ell'm'}(x) \rangle &= L^2 (\omega_{n\ell} + \omega_{n'\ell'}) \mathcal{C}^*_{n\ell} \mathcal{C}_{n'\ell'} \int_0^{\pi/2} \tan^2\rho \ X_{n\ell}(\rho) X_{n'\ell'}(\rho) \ d\rho \\ &\quad \times \int_0^{2\pi} \int_0^{\pi} Y^*_{\ell m}(\theta,\varphi) Y_{\ell'm'}(\theta,\varphi) \sin\theta \ d\theta \ d\varphi \\ &= L^2 \delta_{\ell\ell'} \delta_{mm'} (\omega_{n\ell} + \omega_{n'\ell}) \mathcal{C}^*_{n\ell} \mathcal{C}_{n'\ell} \int_0^{\pi/2} \tan^2\rho \ X_{n\ell}(\rho) X_{n'\ell}(\rho) \ d\rho. \end{aligned} \quad (3.40)$$

The integral here is evaluated in Appendix C, where we show that

$$\int_0^{\pi/2} \tan^2\rho \, X_{n\ell}(\rho) X_{n'\ell}(\rho) d\rho = \delta_{nn'} \frac{\pi[\pi - \sin(\pi(\omega_{n\ell} + \ell))\{\zeta(\ell + \omega_{n\ell} + 1) + \zeta(\omega_{n\ell} - \ell)\}]}{8\omega_{n\ell} \Gamma(\ell + \omega_{n\ell} + 1) \Gamma(\omega_{n\ell} - \ell)} \quad (3.41)$$

with

$$\zeta(z) = \frac{1}{2}\left[\psi\left(\frac{z+1}{2}\right) - \psi\left(\frac{z}{2}\right)\right]. \quad (3.42)$$

By insisting that the modes are orthonormal, i.e.

$$\langle \phi^\alpha_{n\ell m}(x), \phi^\alpha_{n'\ell'm'}(x) \rangle = \delta_{nn'} \delta_{\ell\ell'} \delta_{mm'} \quad (3.43)$$

we must set

$$|\mathcal{C}_{n\ell}|^2 = \frac{4\Gamma(\ell + \omega_{n\ell} + 1)\Gamma(\omega_{n\ell} - \ell)}{L^2 \pi [\pi - \sin(\pi(\omega_{n\ell} + \ell)) \{\zeta(\ell + \omega_{n\ell} + 1) + \zeta(\omega_{n\ell} - \ell)\}]}. \quad (3.44)$$

3.3 Quantum scalar field on adS

We quantize as usual by promoting the field to an operator $\phi \to \hat{\phi}$ and imposing canonical quantization conditions (1.12). The field operator can be written as a sum over the field modes in the following way:

$$\hat{\phi}^{\alpha} = \sum_{\ell=0}^{\infty}\sum_{n=1}^{\infty}\sum_{m=-\ell}^{\ell} \left\{ \hat{b}_{\omega\ell m}\phi^{\alpha}_{n\ell m} + \hat{b}^{\dagger}_{\omega\ell m}\phi^{\alpha,*}_{n\ell m} \right\}. \tag{3.45}$$

In this section, we work in the Lorentzian background, beginning with an analysis of the Wightman function G^+ with Robin boundary conditions imposed in section 3.3.1. In section 3.3.2, we focus on the cases where Dirichlet and Neumann conditions are imposed, where the mode-sums can be evaluated with relative ease due to the fact that the frequency $\omega \in \mathbb{Z}$. Results for the renormalised VP are compared with results given in [110]. In section 3.3.3, we extend our analysis to Robin conditions, where the mode-sums cannot be evaluated analytically, and discuss why numerical computation of these modes is far from straightforward.

3.3.1 Wightman function and regularisation

The Wightman function $G^+(x, x')$ (1.24) is given by

$$G^+_{\alpha}(x, x') = \sum_{\ell=0}^{\infty}\sum_{n=1}^{\infty}\sum_{m=-\ell}^{\ell} \phi^{\alpha}_{n\ell m}(x)\phi^{\alpha,*}_{n\ell m}(x') \tag{3.46}$$

where the superscript α reminds us that the field modes $\phi^{\alpha}_{n\ell m}(x), \phi^{\alpha}_{n\ell m}(x')$ satisfy Robin boundary conditions (3.21) with parameter α at $\rho = \pi/2$. The Wightman function can then be expressed as

$$\begin{aligned} G^+_{\alpha}(x, x') = {} & \frac{4}{L^2\pi}\frac{\cos\rho\cos\rho'}{\sqrt{\sin\rho\sin\rho'}} \\ & \times \sum_{\ell=0}^{\infty}\sum_{n=1}^{\infty} e^{-i\omega_{n\ell}\Delta t}\frac{\Gamma(\ell+\omega_{n\ell}+1)\Gamma(\omega_{n\ell}-\ell)\mathbf{Q}^{\ell+1/2}_{\omega_{n\ell}-1/2}(\cos\rho)\mathbf{Q}^{\ell+1/2}_{\omega_{n\ell}-1/2}(\cos\rho')}{[\pi - \sin(\pi(\omega_{n\ell}+\ell))\left\{\zeta(\ell+\omega_{n\ell}+1)+\zeta(\omega_{n\ell}-\ell)\right\}]} \\ & \times \sum_{m=-\ell}^{\ell} Y_{\ell m}(\theta,\varphi)Y^*_{\ell m}(\theta',\varphi'), \end{aligned} \tag{3.47}$$

for $\Delta t = t - t'$. The sum over frequencies (the n sum) must be performed before the ℓ sum since ω depends on ℓ. We can use a standard addition theorem for spherical harmonics to perform the sum over m, [120, eq. 14.30.9]:

$$P_{\ell}(\cos\gamma) = \frac{4\pi}{2\ell+1}\sum_{m=-\ell}^{\ell} Y_{\ell m}(\theta,\varphi)Y^*_{\ell m}(\theta',\varphi'), \tag{3.48}$$

where $P_\ell(x)$ is a Legendre polynomial and γ is the geodesic distance on a sphere, given in (1.222). The Wightman function is then

$$G_\alpha^+(x,x') = \frac{1}{L^2\pi^2}\frac{\cos\rho\cos\rho'}{\sqrt{\sin\rho\sin\rho'}}\sum_{\ell=0}^{\infty}(2\ell+1)P_\ell(\cos\gamma) \\ \times\sum_{n=1}^{\infty}e^{-i\omega_{n\ell}\Delta t}\frac{\Gamma(\ell+\omega_{n\ell}+1)\Gamma(\omega_{n\ell}-\ell)\mathbf{Q}^{\ell+1/2}_{\omega_{n\ell}-1/2}(\cos\rho)\mathbf{Q}^{\ell+1/2}_{\omega_{n\ell}-1/2}(\cos\rho')}{[\pi-\sin(\pi(\omega_{n\ell}+\ell))\left\{\zeta(\ell+\omega_{n\ell}+1)+\zeta(\omega_{n\ell}-\ell)\right\}]}. \quad (3.49)$$

The anticommutator $G_\alpha^{(1)}(x,x')$ can be calculated from the Wightman function via (1.23), and we obtain

$$G_\alpha^{(1)}(x,x') = \frac{2}{L^2\pi^2}\frac{\cos\rho\cos\rho'}{\sqrt{\sin\rho\sin\rho'}}\sum_{\ell=0}^{\infty}(2\ell+1)P_\ell(\cos\gamma) \\ \times\sum_{n=1}^{\infty}e^{-i\omega_{n\ell}\Delta t}\frac{\Gamma(\ell+\omega_{n\ell}+1)\Gamma(\omega_{n\ell}-\ell)\mathbf{Q}^{\ell+1/2}_{\omega_{n\ell}-1/2}(\cos\rho)\mathbf{Q}^{\ell+1/2}_{\omega_{n\ell}-1/2}(\cos\rho')}{[\pi-\sin(\pi(\omega_{n\ell}+\ell))\left\{\zeta(\ell+\omega_{n\ell}+1)+\zeta(\omega_{n\ell}-\ell)\right\}]}. \quad (3.50)$$

The thermal Green's function is then

$$G_{\beta,\alpha}^{(1)}(x,x') = \frac{2}{L^2\pi^2}\frac{\cos\rho\cos\rho'}{\sqrt{\sin\rho\sin\rho'}}\sum_{\ell=0}^{\infty}(2\ell+1)P_\ell(\cos\gamma) \\ \times\sum_{n=1}^{\infty}e^{-i\omega_{n\ell}\Delta t}\coth\left(\frac{\beta\omega_{n\ell}}{2}\right)\frac{\Gamma(\ell+\omega_{n\ell}+1)\Gamma(\omega_{n\ell}-\ell)\mathbf{Q}^{\ell+1/2}_{\omega_{n\ell}-1/2}(\cos\rho)\mathbf{Q}^{\ell+1/2}_{\omega_{n\ell}-1/2}(\cos\rho')}{[\pi-\sin(\pi(\omega_{n\ell}+\ell))\left\{\zeta(\ell+\omega_{n\ell}+1)+\zeta(\omega_{n\ell}-\ell)\right\}]}, \quad (3.51)$$

where β is the inverse temperature and the coth term is a result of using (1.44).

To calculate the VP, we must bring the points together $x'\to x$. As described in Section 1.3 we need to renormalise. We do this by subtracting the Hadamard parametrix $G_S(x,x')$ (1.192) from the Feynman Green's function $G_F(x,x')$ (1.30), as in (1.196). The Wightman function G^+ (3.49) can be related to the Feynman Green's function G_F using the definitions (1.23) and (1.30).

For the Hadamard parametrix (1.192), we note that, for timelike separation,

$$2\sigma = -L^2(\cos^{-1}Z)^2, \quad Z = (\cos\Delta t - \sin^2\rho)\sec^2\rho, \quad (3.52)$$

where σ is Synge's world function (1.179) (see Appendix D for further details). Evaluating at $\rho=0$, we have

$$Z = \cos\Delta t \;\Rightarrow\; 2\sigma = -L^2\Delta t^2. \quad (3.53)$$

The van Vleck-Morette determinant (1.181) is

$$\Delta^{1/2} = (\Delta t)^{3/2}\csc^{3/2}\Delta t \quad (3.54)$$

and hence

$$\frac{\Delta^{1/2}}{2\sigma} = -\frac{1}{L^2}\left(\frac{1}{\Delta t^2}+\frac{1}{4}\right)+\mathcal{O}(\Delta t^2) \text{ as } \rho \to 0. \tag{3.55}$$

Therefore, the Hadamard parametrix is

$$G_S(\rho=\rho'=0;\Delta t) = \frac{i}{4\pi^2 L^2}\left(\frac{1}{\Delta t^2}+\frac{1}{4}\right)+\mathcal{O}(\Delta t^2). \tag{3.56}$$

3.3.2 Dirichlet and Neumann boundary conditions

When Dirichlet and Neumann conditions are imposed at the boundary, we have $\sin(\pi(\omega+\ell))=0$, and so the Wightman function for vacuum states (3.49) simplifies to

$$\begin{aligned} G_D^+(x,x') = {} & \frac{1}{L^2\pi^3}\frac{\cos\rho\cos\rho'}{\sqrt{\sin\rho\sin\rho'}}\sum_{\ell=0}^{\infty}(2\ell+1)P_\ell(\cos\gamma) \\ & \times \sum_{n=1}^{\infty} e^{-i(2n-\ell)\Delta t}\Gamma(2n+1)\Gamma(2n-2\ell)\mathbf{Q}^{\ell+1/2}_{2n-\ell-1/2}(\cos\rho)\mathbf{Q}^{\ell+1/2}_{2n-\ell-1/2}(\cos\rho'), \end{aligned} \tag{3.57}$$

and

$$\begin{aligned} G_N^+(x,x') = {} & \frac{1}{L^2\pi^3}\frac{\cos\rho\cos\rho'}{\sqrt{\sin\rho\sin\rho'}}\sum_{\ell=0}^{\infty}(2\ell+1)P_\ell(\cos\gamma) \\ & \times \sum_{n=0}^{\infty} e^{-i(2n+1-\ell)\Delta t}\Gamma(2n+2)\Gamma(2n+1-2\ell)\mathbf{Q}^{\ell+1/2}_{2n-\ell+1/2}(\cos\rho)\mathbf{Q}^{\ell+1/2}_{2n-\ell+1/2}(\cos\rho') \end{aligned} \tag{3.58}$$

respectively. The main point to note here is that the frequencies are now integers, each individual mode is periodic in t with period 2π, and so the Wightman functions (3.57, 3.58) are periodic in t, despite the fact that we removed periodicity in t in the transition from adS to CadS. This implies that, when Dirichlet or Neumann conditions are imposed, the vacuum states in CadS are the same as those in adS. This is not true for general Robin conditions - whilst each individual mode is periodic in time for general α, this periodicity is dependent on ω_n, and after taking the sum over n, the result is not periodic in time at all. This can be seen from looking at the anticommutators (3.50, 3.51), which are not periodic in time unless $\alpha = 0, \pi/2$. Hence, the equivalence between adS and CadS vacuum states only holds for Dirichlet and Neumann conditions.

The renormalised VP in CadS for vacuum states when Dirichlet and Neumann conditions are imposed is well-known and given in (3.2-3.3), but it is useful to calculate these results using (3.57, 3.58) in order to verify our representation of the Wightman function. In the following calculation, we make use of the fact that the vacuum states are maximally symmetric when Dirichlet or Neumann conditions are imposed [5], and hence the choice of origin is irrelevant. Therefore, computing the VP at $\rho = 0$ will give the correct answer throughout the spacetime.

Considering the Dirichlet case first, when $\rho \to 0$, using [120, eq. 14.8.5] we have

$$\frac{\mathbf{Q}^{\ell+1/2}_{2n-\ell-1/2}(\cos\rho)}{\sqrt{\sin\rho}} \sim \frac{(-1)^{\ell+1}\pi\sin^{\ell}\rho}{2^{\ell+3/2}\Gamma(\ell+3/2)\Gamma(2n-2\ell)} \quad \text{as } \rho \to 0. \tag{3.59}$$

Therefore, near the origin, only the $\ell = 0$ mode contributes, as observed in [123]. We then have

$$\frac{\mathbf{Q}^{1/2}_{2n-1/2}(\cos\rho)}{\sqrt{\sin\rho}} \sim -\sqrt{\frac{\pi}{2}}\frac{1}{\Gamma(2n)} \quad \text{as } \rho \to 0. \tag{3.60}$$

At the origin, the Wightman function (3.57) becomes

$$G_D^{+}(\rho=\rho'=0;\Delta t) = \frac{1}{\pi^2L^2}\sum_{n=1}^{\infty} n\; e^{-2ni\Delta t} \tag{3.61}$$

where we note that $P_0(\cos\gamma) = 1$ and, as expected, there is no dependence on the angles θ and φ. The Gamma functions cancel using standard definitions [120, eq. 5.4.1].

The sum in (3.61) is not convergent, so we use an $i\epsilon$-prescription, replacing Δt with $\Delta t - i\epsilon$, where the sum

$$\sum_{n=1}^{\infty} ne^{-2ni(\Delta t - i\epsilon)} \tag{3.62}$$

converges very rapidly provided $\epsilon > 0$. To evaluate the sum in (3.62), we first note the following relation using geometric series:

$$\sum_{n=1}^{\infty} e^{-2in(\Delta t - i\epsilon)} = \frac{e^{-2i(\Delta t - i\epsilon)}}{1 - e^{-2i(\Delta t - i\epsilon)}}. \tag{3.63}$$

We can differentiate both sides of (3.63) with respect to Δt to obtain

$$\sum_{n=1}^{\infty} (-2in)e^{-2in(\Delta t - i\epsilon)} = \frac{-2ie^{-2i(\Delta t - i\epsilon)}}{(1 - e^{-2i(\Delta t - i\epsilon)})^2}. \tag{3.64}$$

The Wightman function (3.61) is then

$$G_D^{+}(\rho=\rho'=0;\Delta t) = \frac{1}{\pi^2L^2}\lim_{\epsilon\to 0}\frac{e^{-2i(\Delta t - i\epsilon)}}{(1 - e^{-2i(\Delta t - i\epsilon)})^2} = -\frac{1}{4\pi^2L^2}\lim_{\epsilon\to 0}\frac{1}{\sin^2(\Delta t - i\epsilon)}. \tag{3.65}$$

The anticommutator $G^{(1)}$ can be calculated from the Wightman function via (1.23), and so we obtain

$$G_D^{(1)}(\rho=\rho'=0;\Delta t) = -\frac{1}{2\pi^2L^2\sin^2\Delta t}. \tag{3.66}$$

To calculate the renormalised VP (1.196) we need to start with the Feynman Green's function $G_F(x,x')$, which can be obtained from the Wightman function via (1.30). The average of the advanced and retarded Green's functions $\bar{G}(x,x')$ can be ignored if we assume that x and x' are not connected by a null geodesic (which is the case since we are considering temporal point-splitting). Then we have

$$G_F(x,x') = -\frac{1}{2}iG^{(1)}(x,x'). \tag{3.67}$$

Writing this as a series in Δt, we find

$$G_{F,D}(\rho=\rho'=0;\Delta t) = \frac{i}{4\pi^2L^2}\left(\frac{1}{\Delta t^2}+\frac{1}{3}\right)+\mathcal{O}(\Delta t^2). \tag{3.68}$$

The VP for a scalar field with Dirichlet conditions is then (1.196)

$$\langle 0|\hat{\phi}_D^2|0\rangle_{ren} = i\lim_{x'\to x}[G_{F,D}(x,x')-G_S(x,x')] = -\frac{1}{48\pi^2L^2}. \tag{3.69}$$

This is to be expected from (3.2).

For Neumann boundary conditions we find

$$\frac{\mathbf{Q}^{\ell+1/2}_{2n-\ell+1/2}(\cos\rho)}{\sqrt{\sin\rho}} \sim \frac{(-1)^{\ell+1}\pi\sin^\ell\rho}{2^{\ell+3/2}\Gamma(\ell+3/2)\Gamma(2n-2\ell+1)} \quad \text{as } \rho\to 0 \tag{3.70}$$

and, as before, only the $\ell=0$ mode contributes near the origin, so we only need to concern ourselves with the term

$$\frac{\mathbf{Q}^{1/2}_{2n+1/2}(\cos\rho)}{\sqrt{\sin\rho}} \sim -\sqrt{\frac{\pi}{2}}\frac{1}{\Gamma(2n+1)} \quad \text{as } \rho\to 0. \tag{3.71}$$

The Wightman function (3.58) with Neumann boundary conditions imposed is therefore

$$G_N^+(\rho=\rho'=0;\Delta t) = \frac{1}{2L^2\pi^2}\sum_{n=0}^{\infty}(2n+1)e^{-i(2n+1)\Delta t}, \tag{3.72}$$

and, using the fact that,

$$\sum_{n=0}^{\infty}(2n+1)e^{-(2n+1)i\Delta t} = \frac{e^{-i\Delta t}+e^{-3i\Delta t}}{(1-e^{-2i\Delta t})^2}, \tag{3.73}$$

we obtain

$$G_N^+(\rho=\rho'=0;\Delta t) = -\frac{e^{i\Delta t}+e^{-i\Delta t}}{8L^2\pi^2\sin^2\Delta t} = -\frac{\cos\Delta t}{4L^2\pi^2\sin^2\Delta t}. \tag{3.74}$$

The anti-commutator is then

$$G_N^{(1)}(\rho=\rho'=0;\Delta t) = -\frac{\cos\Delta t}{2L^2\pi^2\sin^2\Delta t}. \tag{3.75}$$

We write the Feynman propagator as a series in Δt,

$$G_{F,N}(\rho=\rho'=0;\Delta t) = \frac{i}{4\pi^2L^2}\left(\frac{1}{\Delta t^2}-\frac{1}{6}\right)+\mathcal{O}(\Delta t^2), \tag{3.76}$$

and, subtracting the Hadamard parametrix (3.56) and taking the limit $\Delta t \to 0$, the renormalised VP is

$$\langle 0|\hat{\phi}_N^2|0\rangle_{ren} = \frac{5}{48\pi^2 L^2}. \tag{3.77}$$

This matches (3.3).

Anti-commutators for thermal states with Dirichlet and Neumann boundary conditions applied are given in [110, eq 2.10],

$$G^{(1)}_{\beta,\pm}(x,x') = -\frac{1}{4L^2\pi^2}\left[\frac{1}{1-Z} \pm \frac{1}{1+Z} - 4\cos\rho\cos\rho' \right.$$
$$\left. \times \sum_{k=1}^{\infty}\left(\frac{\sin k\eta_+}{\sin\eta_+} \pm (-1)^k \frac{\sin k\eta_-}{\sin\eta_-}\right)\frac{\cos k\Delta t}{e^{k\beta}-1}\right] \tag{3.78}$$

where $G^{(1)}_{\beta,+} \equiv G^{(1)}_{\beta,D}$ is the Green's function with Dirichlet conditions imposed, $G^{(1)}_{\beta,-} \equiv G^{(1)}_{\beta,N}$ is the Green's function with Neumann conditions imposed, and

$$\eta_\pm = \cos^{-1}(\cos\rho\cos\rho' \pm \sin\rho\sin\rho'\cos\gamma), \tag{3.79}$$

$$Z = \frac{\cos\Delta t - \sin\rho\sin\rho'\cos\gamma}{\cos\rho\cos\rho'}. \tag{3.80}$$

The results (3.78) are obtained by making use of the fact that both $G^{(1)}_{\beta,D}$ and $G^{(1)}_{\beta,N}$ are doubly periodic functions of imaginary time τ. That is, the functions are periodic with period 2π (as can be seen from (3.80)) and also periodic with period β, which is imposed when we perform a Wick rotation and demand that thermal states are held at temperature $1/\beta$. Hence, both $G^{(1)}_{\beta,D}$ and $G^{(1)}_{\beta,N}$ are meromorphic functions, which allows one to use properties of elliptic functions to derive the appropriate closed form expression [110]. This double-periodicity is broken when we impose Robin conditions (as opposed to Dirichlet or Neumann conditions) and so the same method cannot be used to derive Green's functions or expectation values with Robin conditions imposed on fields.

After taking the coincidence limit $x' \to x$ and using Hadamard renormalisation, Allen, Folacci and Gibbons [110] obtain the following closed form expressions for the renormalised VP with Dirichlet (+) and Neumann (−) conditions imposed on fields at the boundary:

$$\langle\beta|\hat{\phi}^2|\beta\rangle_{\pm,ren} = \frac{1}{8L^2\pi^2}\left\{\left[\frac{1}{3} + 4\cos^2\rho\ f_1(\beta)\right] \pm \left[-\frac{1}{2} + 2\cot\rho\ S_0(\beta,\rho)\right]\right\}, \tag{3.81}$$

where

$$f_1(\beta) = \sum_{n=1}^{\infty}\frac{n}{e^{n\beta/L}-1}, \quad S_0(\beta,\rho) = \sum_{n=1}^{\infty}(-1)^n\frac{\sin 2n\rho}{e^{n\beta/L}-1}. \tag{3.82}$$

It can be verified that at the boundary of the spacetime $\rho \to \pi/2$, the results (3.81) approach the vacuum expectation values (3.69, 3.77).

The formula (3.78) should be equivalent to (3.51) with $\alpha = 0$ for $G^{(1)}_{\beta,D}$ and $\alpha = \pi/2$ for $G^{(1)}_{\beta,N}$. It has proven very difficult to show this equivalence algebraically, but it has been verified numerically. In Figure 3.5 we compare the results (3.78) and (3.51) in the Neumann case. We find good agreement between both sets of results, which gives us confidence that our results for $\alpha = 0, \pi/2$ are correct.

3.3.3 Robin boundary conditions

It now remains to consider scalar field modes with Robin boundary conditions imposed. Maximal symmetry is broken when we impose Robin boundary conditions [6, 113], so we cannot simply calculate the VP at $\rho = 0$ as we did in the previous case. Instead, we expect expectation values to be dependent on ρ. The calculation is further complicated since it is impossible to express the anticommutator (3.50) in closed form for general α. Instead we must compute the VP by regularising mode-by-mode. Although several methods have been developed to achieve this type of regularisation on the Lorentzian background (see [80, 81] and section 1.3.5), these cannot be employed in this case. This is because the Hadamard parametrix $G_S(x, x')$ remains insensitive to boundary conditions, and so the decomposition of frequencies will not be the same as that for the Hadamard function $G^{(1)}(x, x')$.

Barroso and Pitelli [117] avoid this problem by applying Robin conditions to the $\ell = 0$ modes only, with all other modes satisfying Dirichlet boundary conditions. Their results suggest that expectation values with Robin conditions applied to the $\ell = 0$ modes approach the same limit at the boundary for all $\alpha \in (0, \alpha_{crit})$. This limit is equivalent to the expectation value when Dirichlet conditions are applied to all modes, given by (3.2).

In this section, we seek to calculate the difference between the vacuum and thermal expectation values when Robin boundary conditions are imposed, that is the difference between (3.50) and (3.51) in the coincidence limit. Both (3.50) and (3.51) involve sums over the same frequencies, meaning that we do not encounter the same problems faced by Barroso and Pitelli [117]. Therefore, the mode-sums can be combined to give

$$\begin{aligned}\langle\beta|\hat{\phi}^2|\beta\rangle_\alpha - \langle 0|\hat{\phi}^2|0\rangle_\alpha &= \lim_{x'\to x}\{G^{(1)}_\alpha(x,x') - G^{(1)}_{\beta,\alpha}(x,x')\}\\ &= \frac{4}{L^2\pi^2}\frac{\cos^2\rho}{\sin\rho}\sum_{\ell=0}^{\infty}(2\ell+1)\sum_{n=1}^{\infty}\frac{1}{e^{\beta\omega_{n\ell}}-1}\\ &\times\frac{\Gamma(\ell+\omega_{n\ell}+1)\Gamma(\omega_{n\ell}-\ell)\left[\mathbf{Q}^{\ell+1/2}_{\omega_{n\ell}-1/2}(\cos\rho)\right]^2}{[\pi-\sin(\pi(\omega_{n\ell}+\ell))\{\zeta(\ell+\omega_{n\ell}+1)+\zeta(\omega_{n\ell}-\ell)\}]}.\end{aligned} \tag{3.83}$$

This is by no means a straightforward calculation, but it lacks the numerical complexity of renormalising with the Hadamard parametrix where mode-sums cannot be combined.

We perform this calculation in the case $L = 1$ and $\kappa = 1$, where temperature $T = \kappa/2\pi$. First, since we know that ℓ can only take integer values, we must solve the quantization

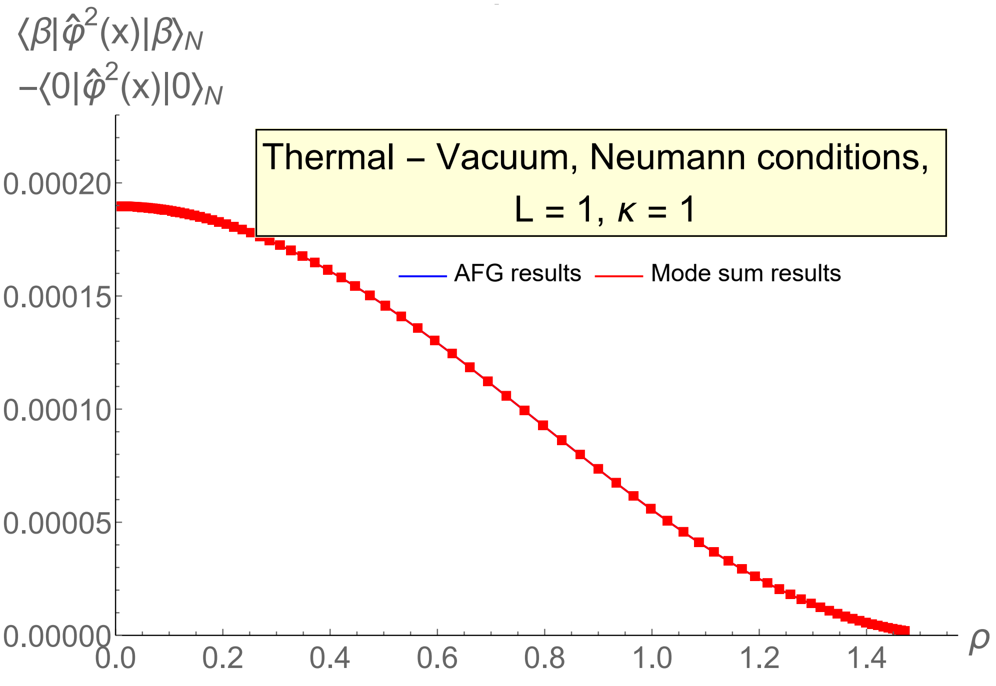

(a) $\kappa = 1$

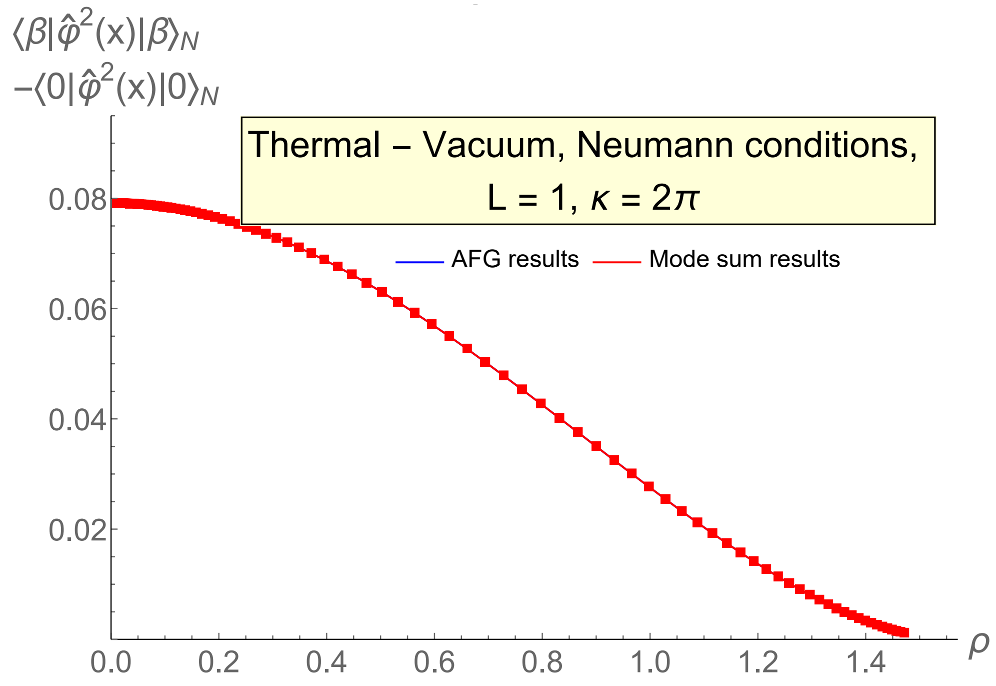

(b) $\kappa = 2\pi$

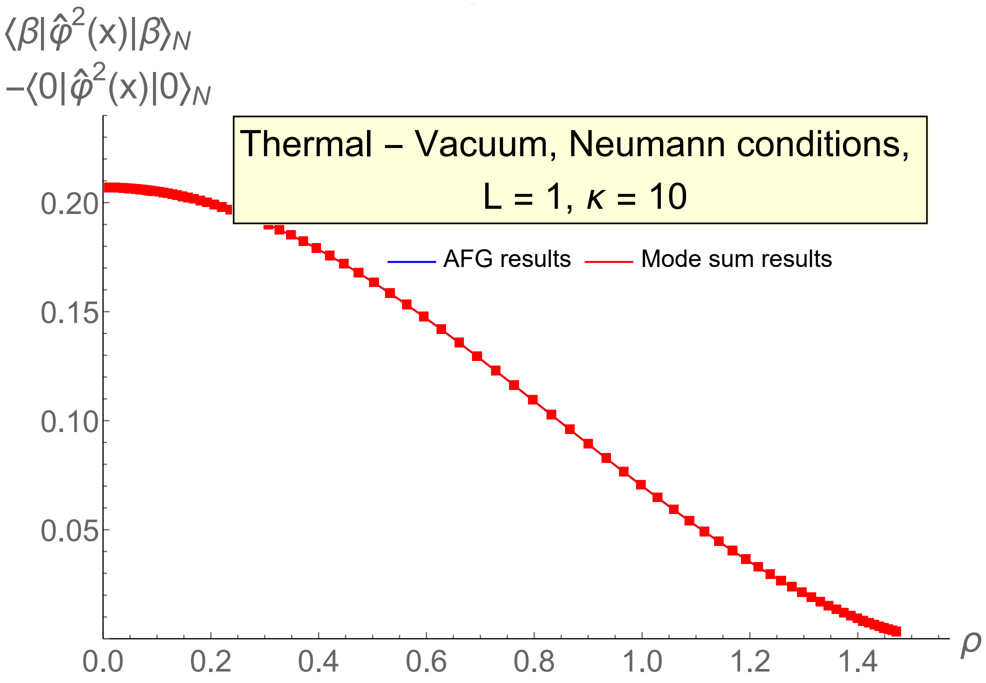

(c) $\kappa = 10$

Figure 3.5: Results for the difference in vacuum and thermal expectation values with Neumann conditions applied, $\langle\beta|\hat{\phi}(x)|\beta\rangle_N - \langle 0|\hat{\phi}(x)|0\rangle_N$. This is a direct comparison of differences calculated using the results from [110] (3.78), and the mode sum (3.83). The temperature $T = \kappa/2\pi$ is varied in each case, with the value of κ given. In all cases, the difference between the results is 10^{-22} and therefore cannot be seen on the scale of these plots. This verifies that the mode-sum (3.83) matches results in [110].

condition (3.24) to find the values of $\omega_{n\ell}$ that we are then to sum over. For $\kappa = 1$, we find all the values of $\omega_{n\ell} < 100$ for $\ell \in [0, 50]$. We then calculate all summands in (3.83) to 20 digits. This is a rather time-consuming numerical calculation, since each mode has to be calculated over a grid of values of ρ and each individual calculation requires the evaluation of Legendre functions. We create a grid over the radial coordinate ρ by writing

$$\rho = \tan^{-1}\left(\frac{10^{-2+3i/100}}{L}\right) \tag{3.84}$$

and consider values of i ranging from 1 up to 100. Note that as $\rho \to \pi/2$, the sum converges more slowly and we require more ℓ or n modes to obtain convergence.

These results are shown in Figure 3.6(a) as a three-dimensional plot over radius ρ and Robin parameter α. The difference between thermal and vacuum expectation values appears to be smooth in α and diverges as $\alpha \to \alpha_{crit}$. This divergence indicates the breakdown of the semiclassical approximation as $\alpha \to \alpha_{crit}$, which is to be expected due to the presence of unstable modes when $\alpha_{crit} < \alpha < \pi$.

As we increase the value of κ, thus increasing the temperature of the thermal state, we begin to see different behaviour in our results. Note that we do not vary the value of the adS lengthscale L as this just amounts to a rescaling of the solutions. In Figures 3.6(b), 3.6(c), we present results for $\kappa = 2\pi$ and $\kappa = 10$ respectively, both calculated with the same number of modes and to the same number of digits of precision as in the $\kappa = 1$ calculation. We see an apparent discontinuity as we pass through the Neumann value $\alpha = \pi/2$, despite the fact that we expect there to be a smooth transition across all $\alpha \in [0, \alpha_{crit})$. Since we know from Figure 3.5 that numerical results when $\alpha = \pi/2$ are correct, this leads us to suspect that there is some error in the calculation of the difference with Robin parameter $\alpha \neq \pi/2$ (and that results in Figure 3.6(a) are likely to be incorrect too).

The errors can therefore be attributed to a fundamental issue with the representation of the Green's function. One of these issues is that Robin conditions can only be imposed on CadS and not on adS. In CadS, null geodesics are reflected at the boundary. As explained in [82] (see also [124, 125]), the Hadamard parametrix will diverge for any pair of points connected by a null geodesic, even if they are far from each other. This long-distance divergence leads to undamped oscillations in the mode contributions at large frequency. Levi and Ori [82] use a generalised integral to ensure these oscillations are properly damped. This divergence suggests that the '$i\epsilon$' prescription employed in this section is not correct.

These issues do not arise in the Euclidean background, which we consider in the next section. The Euclidean Green's function $G_E(\mathbf{x}, \mathbf{x}')$ is unique and gives us a well-defined distribution without the need for an '$i\epsilon$' prescription. Since our spacetime is static, there exists a unique correspondence between the Euclidean Green's function and the Feynman Green's function defined on the Lorentzian section.

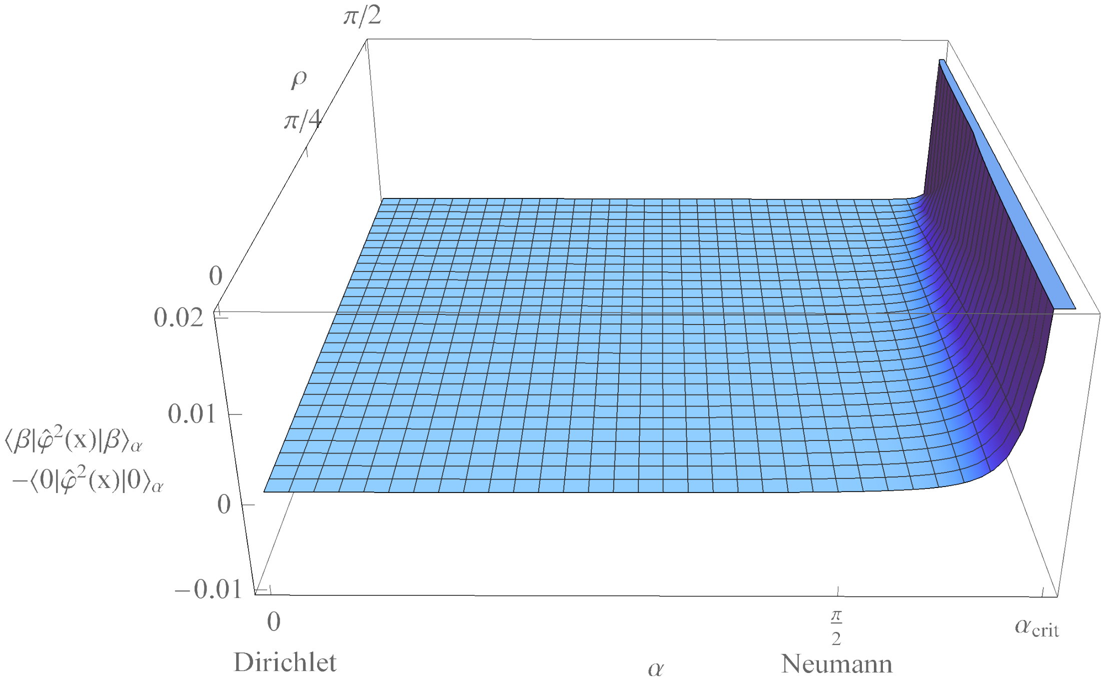

(a) $\kappa = 1$

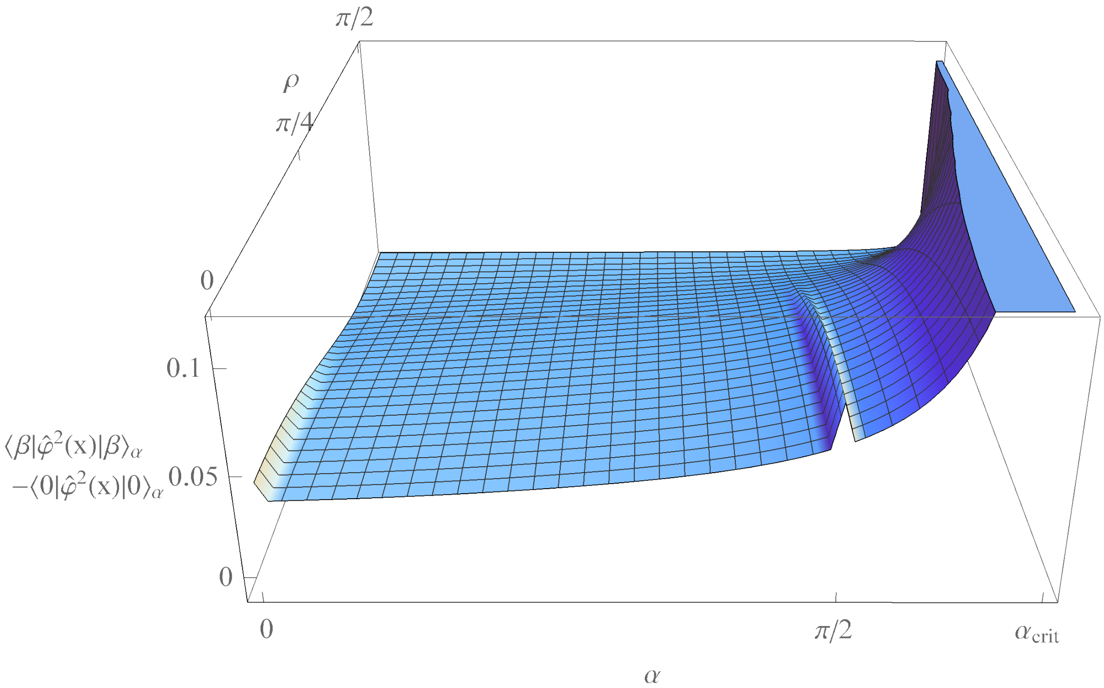

(b) $\kappa = 2\pi$

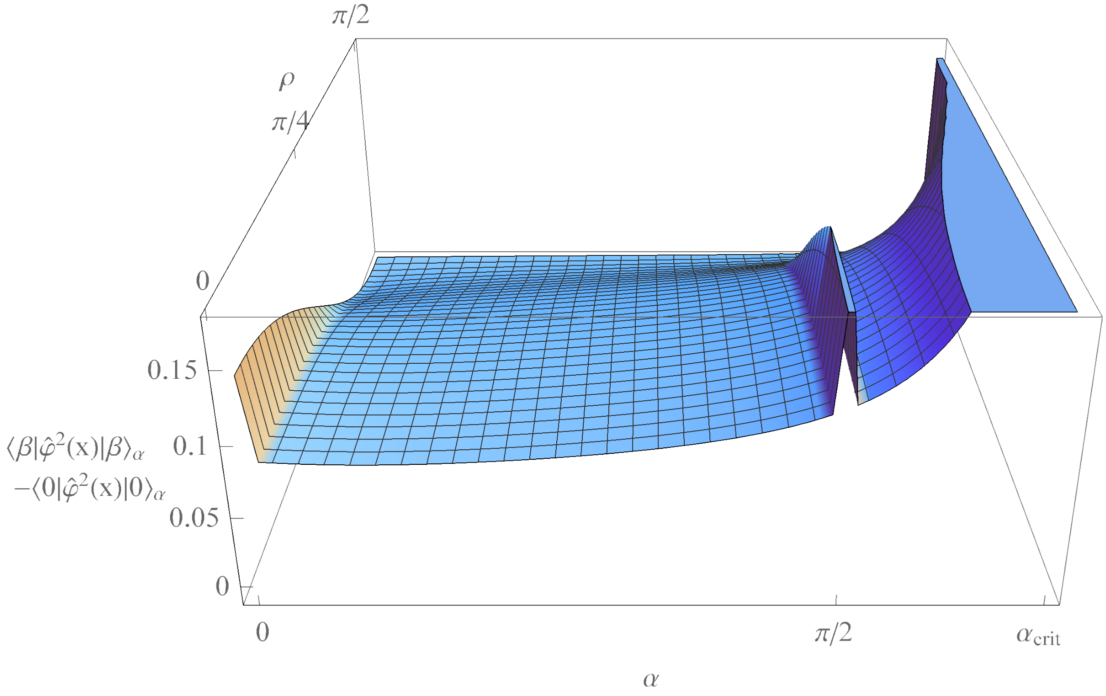

(c) $\kappa = 10$

Figure 3.6: Plots of the difference in thermal and vacuum expectation values with Robin boundary conditions imposed, $\langle\beta|\hat{\phi}(x)|\beta\rangle_\alpha - \langle 0|\hat{\phi}(x)|0\rangle_\alpha$. The temperature $T = \kappa/2\pi$ is fixed in each case, with the value of κ given. The results are functions of the radius ρ and Robin parameter α. In all cases, the difference diverges as $\alpha \to \alpha_{crit}$. For small κ, the results are smooth in α, but for larger κ, there appears to be a discontinuity at the Neumann value $\alpha = \pi/2$. This discontinuity is due to the representation of the Green's function as discussed in the text.

3.4 Quantization on Euclidean section

In this section, we perform a Wick rotation (1.45) and consider scalar fields on the Euclidean background, where the Green's function is unique. In section 3.4.1, we solve the Klein-Gordon equation (1.58) in Euclidean ESU and then perform the conformal transformation (3.6) to find the Euclidean Green's function in CadS. We apply Robin boundary conditions to the Euclidean Green's function. In section 3.4.2 we focus on Dirichlet and Neumann boundary conditions in order to demonstrate that results for the thermal Green's function in the Euclidean background correspond to similar results in the Lorentzian background. Finally, in section 3.4.3, we find thermal and vacuum expectation values with Robin boundary conditions imposed on the fields, and renormalise using the Hadamard prescription.

3.4.1 The Euclidean Green's function

Computing vacuum and thermal expectation values on the Euclidean background significantly simplifies our calculations. We perform a Wick rotation (1.45) on the Lorentzian CadS metric (2.5) and obtain the Euclidean CadS metric

$$ds^2 = L^2 \sec^2\rho \left(d\tau^2 + d\rho^2 + \sin^2\rho \, \left(d\theta^2 + \sin^2\theta \, d\varphi^2\right)\right). \tag{3.85}$$

We can evaluate the VP by computing

$$\langle 0|\hat{\phi}^2_\alpha|0\rangle_{ren} = \lim_{x'\to x}[G^E_\alpha(x,x') - G_S(x,x')] \tag{3.86}$$

where the Euclidean Green's function can be found by solving the inhomogeneous wave equation (1.58) in ESU, applying appropriate boundary conditions and then performing a conformal transformation (3.6). In ESU, the Euclidean Green's function $G^E_{ESU}(x,x')$ satisfies

$$\left(\widetilde{\Box} - \frac{1}{L^2}\right) G^E_{\alpha,ESU}(\tau,\rho,\theta,\varphi;\tau',\rho',\theta',\varphi') = -\frac{1}{L^4\sin^2\rho}\delta(\tau-\tau')\delta(\rho-\rho')\delta(\Omega,\Omega') \tag{3.87}$$

where $\widetilde{\Box}$ is the d'Alembertian on Euclidean ESU and $\delta(\Omega,\Omega')$ is the angular delta function defined by

$$\delta(\Omega,\Omega') = \frac{1}{\sin\theta}\delta(\theta-\theta')\delta(\varphi-\varphi'). \tag{3.88}$$

Using the d'Alembertian in Euclidean ESU, (3.87) can be written

$$\left(\frac{\partial^2}{\partial\tau^2} + \frac{1}{\sin^2\rho}\left[\frac{\partial}{\partial\rho}\left(\sin^2\rho\frac{\partial}{\partial\rho}\right) + \frac{1}{\sin\theta}\frac{\partial}{\partial\theta}\left(\sin\theta\frac{\partial}{\partial\theta}\right) + \frac{1}{\sin^2\theta}\frac{\partial^2}{\partial\varphi^2}\right] - 1\right) G^E_{\alpha,ESU} = -\frac{1}{L^2\sin^2\rho}\delta(\tau-\tau')\delta(\rho-\rho')\delta(\Omega,\Omega'). \tag{3.89}$$

The delta function $\delta(\tau-\tau')$ can be written as an integral representation

$$\delta(\tau-\tau') = \frac{1}{2\pi}\int_{-\infty}^{\infty} e^{i\omega\Delta\tau} d\omega \tag{3.90}$$

so it makes sense to search for a Green's function of the form

$$G^E_{\alpha,ESU}(x,x') = \frac{1}{2\pi}\int_{-\infty}^{\infty} e^{i\omega\Delta\tau}\mathcal{G}_\omega(\rho,\theta,\varphi;\rho',\theta',\varphi')d\omega \tag{3.91}$$

where $\mathcal{G}_\omega(\rho,\theta,\varphi;\rho',\theta',\varphi')$ is the three-dimensional Green's function satisfying

$$\begin{aligned}\left(-\omega^2 + \frac{1}{\sin^2\rho}\left[\frac{\partial}{\partial\rho}\left(\sin^2\rho\frac{\partial}{\partial\rho}\right) + \frac{1}{\sin\theta}\frac{\partial}{\partial\theta}\left(\sin\theta\frac{\partial}{\partial\theta}\right) + \frac{1}{\sin^2\theta}\frac{\partial^2}{\partial\varphi^2}\right] - 1\right)\mathcal{G}_\omega \\ = -\frac{1}{L^2\sin^2\rho}\delta(\rho-\rho')\delta(\Omega,\Omega').\end{aligned} \tag{3.92}$$

The equation for $\mathcal{G}_\omega$ (3.92) can be found by substituting (3.91) into the wave equation (3.89). The angular delta function can be written as a series representation [1],

$$\delta(\Omega,\Omega') = \frac{1}{4\pi}\sum_{\ell=0}^{\infty}(2\ell+1)P_\ell(\cos\gamma) \tag{3.93}$$

where γ is the geodesic distance on the sphere (1.222). We write

$$\mathcal{G}_\omega(\rho,\theta,\varphi;\rho',\theta',\varphi') = \frac{1}{4\pi}\sum_{\ell=0}^{\infty}(2\ell+1)P_\ell(\cos\gamma)g^{ESU}_{\omega\ell}(\rho;\rho') \tag{3.94}$$

where $g^{ESU}_{\omega\ell}(\rho;\rho')$ is the radial Green's function in Euclidean ESU. Substituting (3.94) in (3.92) gives the defining equation for the radial function

$$\left(-\omega^2 + \frac{1}{\sin^2\rho}\frac{\partial}{\partial\rho}\left(\sin^2\rho\frac{\partial}{\partial\rho}\right) - \frac{1}{\sin^2\rho}\ell(\ell+1) - 1\right)g^{ESU}_{\omega\ell} = -\frac{1}{L^2\sin^2\rho}\delta(\rho-\rho'). \tag{3.95}$$

The radial Green's function $g^{ESU}_{\omega\ell}(\rho;\rho')$ can be constructed as follows:

$$g^{ESU}_{\omega\ell}(\rho;\rho') = \mathcal{N}_{\omega\ell}p^{ESU}_{\omega\ell}(\rho_<)q^{ESU}_{\omega\ell}(\rho_>) \tag{3.96}$$

where $p^{ESU}_{\omega\ell}, q^{ESU}_{\omega\ell}$ are solutions of the homogeneous version of (3.95), $\rho_< = \min\{\rho,\rho'\}$, $\rho_> = \max\{\rho,\rho'\}$ and $\mathcal{N}_{\omega\ell}$ is a normalisation constant obtained from taking the Wronskian of the two homogeneous solutions - see equation (3.114). The function $p^{ESU}_{\omega\ell}$ has regularity imposed at the origin, whilst $q^{ESU}_{\omega\ell}$ has Robin conditions imposed at the boundary $\rho = \pi/2$.

The general solution of the homogeneous version of (3.95) can be expressed in terms of Mehler (conical) functions

$$p^{ESU}_{\omega\ell}(\rho;\rho') = (\sin\rho)^{-1/2}\left[C_1 P^{-\ell-\frac{1}{2}}_{i\omega-\frac{1}{2}}(\cos\rho) + C_2 P^{-\ell-\frac{1}{2}}_{i\omega-\frac{1}{2}}(-\cos\rho)\right], \tag{3.97}$$

$$q^{ESU}_{\omega\ell}(\rho;\rho') = (\sin\rho)^{-1/2}\left[C_3 P^{-\ell-\frac{1}{2}}_{i\omega-\frac{1}{2}}(\cos\rho) + C_4 P^{-\ell-\frac{1}{2}}_{i\omega-\frac{1}{2}}(-\cos\rho)\right], \tag{3.98}$$

where C_1, C_2, C_3, C_4 are constants of integration. To impose regularity at the origin in (3.97), we must set $C_2 = 0$. The constant C_1 can then be absorbed into the normalisation constant $\mathcal{N}_{\omega\ell}$, and therefore we have

$$p_{\omega\ell}^{ESU} = (\sin\rho)^{-1/2} P_{i\omega-\frac{1}{2}}^{-\ell-\frac{1}{2}}(\cos\rho). \tag{3.99}$$

We impose Robin boundary conditions on $q_{\omega\ell}^{ESU}$ by using the Robin parameter α as before, that is

$$\cos\alpha \; q_{\omega\ell}^{ESU}\left(\frac{\pi}{2}\right) + \sin\alpha \; \frac{\partial}{\partial\rho} q_{\omega\ell}^{ESU}\left(\frac{\pi}{2}\right) = 0. \tag{3.100}$$

Using [120, 14.5.1, 14.5.2], we find that we must have

$$\frac{C_3 + C_4}{C_4 - C_3} = \frac{2\tan\alpha \; |\Gamma\left(\frac{1}{2}(i\omega + \ell + 2)\right)|^2}{|\Gamma(\frac{1}{2}(i\omega + \ell + 1))|^2}. \tag{3.101}$$

We can set $C_4 = 1$ without loss of generality, and then we find

$$C_3 = \frac{2\tan\alpha \; |\Gamma\left(\frac{1}{2}(i\omega + \ell + 2)\right)|^2 - |\Gamma\left(\frac{1}{2}(i\omega + \ell + 1)\right)|^2}{2\tan\alpha \; |\Gamma\left(\frac{1}{2}(i\omega + \ell + 2)\right)|^2 + |\Gamma\left(\frac{1}{2}(i\omega + \ell + 1)\right)|^2}. \tag{3.102}$$

The constant C_3 is therefore undefined when

$$2\tan\alpha = -\frac{|\Gamma\left(\frac{1}{2}(i\omega + \ell + 1)\right)|^2}{|\Gamma\left(\frac{1}{2}(i\omega + \ell + 2)\right)|^2}. \tag{3.103}$$

This is exactly the same as the quantization condition for unstable modes (3.27). Note that when we impose Dirichlet boundary conditions ($\alpha = 0$) then $C_3 = -1$ and when we impose Neumann boundary conditions ($\alpha = \frac{\pi}{2}$) then $C_3 = 1$.

Since we have imposed boundary conditions, we can now perform the conformal transformation (3.6) to arrive at the radial Green's function in CadS, that is

$$g_{\omega\ell}^{CadS}(\rho;\rho') = \mathcal{N}_{\omega\ell}(\cos\rho\cos\rho') p_{\omega\ell}^{ESU}(\rho_<) q_{\omega\ell}^{ESU}(\rho_>) = \mathcal{N}_{\omega\ell} p_{\omega\ell}^{CadS}(\rho_<) q_{\omega\ell}^{CadS}(\rho_>) \tag{3.104}$$

where

$$p_{\omega\ell}^{CadS}(\rho;\rho') = \frac{\cos\rho}{(\sin\rho)^{1/2}} P_{i\omega-\frac{1}{2}}^{-\ell-\frac{1}{2}}(\cos\rho), \tag{3.105}$$

$$q_{\omega\ell}^{CadS}(\rho;\rho') = \frac{\cos\rho}{(\sin\rho)^{1/2}} \left[C_3 P_{i\omega-\frac{1}{2}}^{-\ell-\frac{1}{2}}(\cos\rho) + P_{i\omega-\frac{1}{2}}^{-\ell-\frac{1}{2}}(-\cos\rho) \right]. \tag{3.106}$$

It now just remains to calculate the normalisation constant $\mathcal{N}_{\omega\ell}$. To determine this, we multiply both sides of (3.95) by $\sin^2\rho$ and then integrate with respect to ρ between $\rho' - \delta$ and $\rho' + \delta$ for some small, positive δ [69]. We then take the limit $\delta \to 0$. Integrating the right-hand-side of (3.95) is straightforward:

$$-\lim_{\delta\to 0} \frac{1}{L^2} \int_{\rho'-\delta}^{\rho'+\delta} \delta(\rho - \rho') d\rho = -\frac{1}{L^2}. \tag{3.107}$$

Integrating and taking $\delta \to 0$ on the left-hand-side of (3.95) gives us

$$\lim_{\delta\to 0}\int_{\rho'-\delta}^{\rho'+\delta}\left\{\left[-\omega^2\sin^2\rho-\ell(\ell+1)-\sin^2\rho\right]g_{\omega\ell}^{ESU}+\frac{\partial}{\partial\rho}\left[\sin^2\rho\frac{\partial g_{\omega\ell}^{ESU}}{\partial\rho}\right]\right\}d\rho$$
$$=\lim_{\delta\to 0}\left[\sin^2\rho\frac{\partial g_{\omega\ell}^{ESU}}{\partial\rho}\right]_{\rho'-\delta}^{\rho'+\delta}. \quad (3.108)$$

The radial Green's function $g_{\omega\ell}^{ESU}$ is continuous, and hence bounded. Therefore, we have

$$\left|\int_{\rho'-\delta}^{\rho'+\delta}\left[-\omega^2\sin^2\rho-\ell(\ell+1)-\sin^2\rho\right]g_{\omega\ell}^{ESU}d\rho\right|$$
$$\leq\int_{\rho'-\delta}^{\rho'+\delta}\left|\left[-\omega^2\sin^2\rho-\ell(\ell+1)-\sin^2\rho\right]g_{\omega\ell}^{ESU}\right|d\rho$$
$$\leq\int_{\rho'-\delta}^{\rho'+\delta}\max\left\{\left[-\omega^2\sin^2\rho-\ell(\ell+1)-\sin^2\rho\right]g_{\omega\ell}^{ESU}\right\}d\rho$$
$$\leq\int_{\rho'-\delta}^{\rho'+\delta}\mathcal{M}\;d\rho=2\delta\mathcal{M} \quad (3.109)$$

where $\mathcal{M}$ is some positive constant. The first integral in (3.108) therefore vanishes in the limit $\delta \to 0$. Thus, from (3.107, 3.108), we obtain

$$-\frac{1}{L^2}=\sin^2\rho\lim_{\delta\to 0}\left[\left.\frac{\partial g_{\omega\ell}^{ESU}}{\partial\rho}\right|_{\rho'+\delta}-\left.\frac{\partial g_{\omega\ell}^{ESU}}{\partial\rho}\right|_{\rho'-\delta}\right]. \quad (3.110)$$

Defining the radial Green's function using (3.96), this becomes

$$-\frac{1}{L^2}=\sin^2\rho\;\mathcal{N}_{\omega\ell}W\{p_{\omega\ell}^{ESU},q_{\omega\ell}^{ESU}\} \quad (3.111)$$

where $W\{p_{\omega\ell}^{ESU},q_{\omega\ell}^{ESU}\}$ is the Wronskian, defined by

$$W\{p_{\omega\ell}^{ESU},q_{\omega\ell}^{ESU}\}=p_{\omega\ell}^{ESU}\frac{\partial q_{\omega\ell}^{ESU}}{\partial\rho}-\frac{\partial p_{\omega\ell}^{ESU}}{\partial\rho}q_{\omega\ell}^{ESU}. \quad (3.112)$$

The normalisation constant $\mathcal{N}_{\omega\ell}$ in ESU is therefore given by

$$\mathcal{N}_{\omega\ell}=-\frac{1}{L^2\sin^2\rho\;W\{p_{\omega\ell}^{ESU},q_{\omega\ell}^{ESU}\}}. \quad (3.113)$$

The normalisation constant in CadS is found by applying the conformal transformation (3.6) to (3.113) to obtain

$$\mathcal{N}_{\omega\ell}=-\frac{\cot^2\rho}{L^2W\{p_{\omega\ell}^{CadS},q_{\omega\ell}^{CadS}\}}. \quad (3.114)$$

The normalisation constant is found to be the same in both cases, as we would expect from (3.104). The Wronskian is

$$W\{p^{CadS}_{\omega\ell}, q^{CadS}_{\omega\ell}\} = p^{CadS}_{\omega\ell}\frac{\partial q^{CadS}_{\omega\ell}}{\partial\rho} - \frac{\partial p^{CadS}_{\omega\ell}}{\partial\rho}q^{CadS}_{\omega\ell} = -\frac{2\cot^2\rho}{|\Gamma(i\omega+\ell+1)|^2}. \tag{3.115}$$

The normalisation constant is therefore

$$\mathcal{N}_{\omega\ell} = \frac{1}{2L^2}|\Gamma(i\omega+\ell+1)|^2. \tag{3.116}$$

Putting everything together, the Euclidean Green's function in CadS is

$$\begin{aligned} G^E_{\alpha,CadS}(x,x') &= \frac{1}{16\pi^2L^2}\frac{\cos\rho\cos\rho'}{\sqrt{\sin\rho\sin\rho'}}\int_{-\infty}^{\infty}d\omega\ e^{i\omega\Delta\tau}\sum_{\ell=0}^{\infty}(2\ell+1)P_\ell(\cos\gamma) \\ &\times|\Gamma(i\omega+\ell+1)|^2P^{-\ell-\frac{1}{2}}_{i\omega-\frac{1}{2}}(\cos\rho_<)\left[C_3P^{-\ell-\frac{1}{2}}_{i\omega-\frac{1}{2}}(\cos\rho_>)+P^{-\ell-\frac{1}{2}}_{i\omega-\frac{1}{2}}(-\cos\rho_>)\right]. \end{aligned} \tag{3.117}$$

The integral over ω in (3.117) does not depend on α, unlike the sum over ω in the Lorentzian background where values of ω depended on α implicitly via the quantization condition (3.24). This makes the representation in the Euclidean background highly preferable to the Lorentzian background, and implies that calculations of the VP for a range of α can be computed more easily.

From now on, we shall work entirely in CadS, and so drop the subscript "CadS" on the Euclidean Green's function. In the Euclidean background, we can also compute the Euclidean Green's function for thermal states by assuming that the imaginary time coordinate τ is periodic with periodicity $2\pi/T$, where T is some arbitrary temperature - see (1.35). There exist thermal states on CadS satisfying the Hadamard condition at any temperature (in black hole spacetimes, explored in chapters 4-6, we shall see that there is a natural temperature associated to states, defined by surface gravity $\kappa = 2\pi T$ (1.143)). We impose this periodicity in τ by using a different representation of the delta function in (3.89), that is

$$\delta(\tau-\tau') = \frac{\kappa}{2\pi}\sum_{n=-\infty}^{\infty}e^{in\kappa\Delta\tau}, \tag{3.118}$$

which is valid for any $\kappa > 0$. Then, the derivation of the thermal Green's function is very similar to that for the vacuum Green's function, and we find

$$\begin{aligned} G^E_{\beta,\alpha}(x,x') &= \frac{\kappa}{16\pi^2L^2}\frac{\cos\rho\cos\rho'}{\sqrt{\sin\rho\sin\rho'}}\sum_{n=-\infty}^{\infty}e^{in\kappa\Delta\tau}\sum_{\ell=0}^{\infty}(2\ell+1)P_\ell(\cos\gamma) \\ &\times|\Gamma(in\kappa+\ell+1)|^2P^{-\ell-\frac{1}{2}}_{in\kappa-\frac{1}{2}}(\cos\rho_<)\left[C_3P^{-\ell-\frac{1}{2}}_{in\kappa-\frac{1}{2}}(\cos\rho_>)+P^{-\ell-\frac{1}{2}}_{in\kappa-\frac{1}{2}}(-\cos\rho_>)\right] \end{aligned} \tag{3.119}$$

where C_3 is given by (3.102) and the frequency is given by $\omega = n\kappa$.

The Dirichlet Green's functions for vacuum and thermal states are then given by

$$G_D^E(x,x') = \frac{1}{16\pi^2 L^2}\frac{\cos\rho\cos\rho'}{\sqrt{\sin\rho\sin\rho'}}\int_{-\infty}^{\infty} d\omega\ e^{i\omega\Delta\tau}\sum_{\ell=0}^{\infty}(2\ell+1)P_\ell(\cos\gamma)$$
$$\times|\Gamma(i\omega+\ell+1)|^2 P_{i\omega-\frac{1}{2}}^{-\ell-\frac{1}{2}}(\cos\rho_<)\left[-P_{i\omega-\frac{1}{2}}^{-\ell-\frac{1}{2}}(\cos\rho_>)+P_{i\omega-\frac{1}{2}}^{-\ell-\frac{1}{2}}(-\cos\rho_>)\right], \quad (3.120)$$

$$G_{\beta,D}^E(x,x') = \frac{\kappa}{16\pi^2 L^2}\frac{\cos\rho\cos\rho'}{\sqrt{\sin\rho\sin\rho'}}\sum_{n=-\infty}^{\infty} e^{in\kappa\Delta\tau}\sum_{\ell=0}^{\infty}(2\ell+1)P_\ell(\cos\gamma)$$
$$\times|\Gamma(in\kappa+\ell+1)|^2 P_{in\kappa-\frac{1}{2}}^{-\ell-\frac{1}{2}}(\cos\rho_<)\left[-P_{in\kappa-\frac{1}{2}}^{-\ell-\frac{1}{2}}(\cos\rho_>)+P_{in\kappa-\frac{1}{2}}^{-\ell-\frac{1}{2}}(-\cos\rho_>)\right]. \quad (3.121)$$

The Neumann Green's functions are given by

$$G_N^E(x,x') = \frac{1}{16\pi^2 L^2}\frac{\cos\rho\cos\rho'}{\sqrt{\sin\rho\sin\rho'}}\int_{-\infty}^{\infty} d\omega\ e^{i\omega\Delta\tau}\sum_{\ell=0}^{\infty}(2\ell+1)P_\ell(\cos\gamma)$$
$$\times|\Gamma(i\omega+\ell+1)|^2 P_{i\omega-\frac{1}{2}}^{-\ell-\frac{1}{2}}(\cos\rho_<)\left[P_{i\omega-\frac{1}{2}}^{-\ell-\frac{1}{2}}(\cos\rho_>)+P_{i\omega-\frac{1}{2}}^{-\ell-\frac{1}{2}}(-\cos\rho_>)\right], \quad (3.122)$$

$$G_{\beta,N}^E(x,x') = \frac{\kappa}{16\pi^2 L^2}\frac{\cos\rho\cos\rho'}{\sqrt{\sin\rho\sin\rho'}}\sum_{n=-\infty}^{\infty} e^{in\kappa\Delta\tau}\sum_{\ell=0}^{\infty}(2\ell+1)P_\ell(\cos\gamma)$$
$$\times|\Gamma(in\kappa+\ell+1)|^2 P_{in\kappa-\frac{1}{2}}^{-\ell-\frac{1}{2}}(\cos\rho_<)\left[P_{in\kappa-\frac{1}{2}}^{-\ell-\frac{1}{2}}(\cos\rho_>)+P_{in\kappa-\frac{1}{2}}^{-\ell-\frac{1}{2}}(-\cos\rho_>)\right]. \quad (3.123)$$

We can write the Robin Green's functions as a linear combination of Dirichlet and Neumann Green's functions along with an additional regular part,

$$G_\alpha^E(x,x') = \cos^2\alpha\ G_D^E(x,x') + \sin^2\alpha\ G_N^E(x,x') + \sin 2\alpha\ G_R^E(x,x'), \quad (3.124)$$
$$G_{\beta,\alpha}^E(x,x') = \cos^2\alpha\ G_{\beta,D}^E(x,x') + \sin^2\alpha\ G_{\beta,N}^E(x,x') + \sin 2\alpha\ G_{\beta,R}^E(x,x'), \quad (3.125)$$

where

$$G_R^E(x,x') = \frac{1}{16\pi^2 L^2}\frac{\cos\rho\cos\rho'}{\sqrt{\sin\rho\sin\rho'}}\int_{-\infty}^{\infty} d\omega\ e^{i\omega\Delta\tau}\sum_{\ell=0}^{\infty}(2\ell+1)P_\ell(\cos\gamma)|\Gamma(i\omega+\ell+1)|^2$$
$$\times\left[\frac{2\cos\alpha|\Gamma(\frac{1}{2}(i\omega+\ell+2))|^2-\sin\alpha|\Gamma(\frac{1}{2}(i\omega+\ell+1))|^2}{2\sin\alpha|\Gamma(\frac{1}{2}(i\omega+\ell+2))|^2+\cos\alpha|\Gamma(\frac{1}{2}(i\omega+\ell+1))|^2}\right]$$
$$\times P_{i\omega-\frac{1}{2}}^{-\ell-\frac{1}{2}}(\cos\rho)P_{i\omega-\frac{1}{2}}^{-\ell-\frac{1}{2}}(\cos\rho'), \quad (3.126)$$

$$
\begin{aligned}
G^E_{\beta,R}(x,x') = \frac{\kappa}{16\pi^2 L^2}\frac{\cos\rho\cos\rho'}{\sqrt{\sin\rho\sin\rho'}}\sum_{n=-\infty}^{\infty} e^{in\kappa\Delta\tau}\sum_{\ell=0}^{\infty}(2\ell+1)P_\ell(\cos\gamma)|\Gamma(in\kappa+\ell+1)|^2 \\
\times\left[\frac{2\cos\alpha|\Gamma(\frac{1}{2}(in\kappa+\ell+2))|^2-\sin\alpha|\Gamma(\frac{1}{2}(in\kappa+\ell+1))|^2}{2\sin\alpha|\Gamma(\frac{1}{2}(in\kappa+\ell+2))|^2+\cos\alpha|\Gamma(\frac{1}{2}(in\kappa+\ell+1))|^2}\right] \\
\times P^{-\ell-\frac{1}{2}}_{in\kappa-\frac{1}{2}}(\cos\rho)P^{-\ell-\frac{1}{2}}_{in\kappa-\frac{1}{2}}(\cos\rho'). \quad (3.127)
\end{aligned}
$$

It should be noted that G^E_R and $G^E_{\beta,R}$ are not Green's functions, but rather arise as regular contributions to the Green's function with general Robin conditions imposed. These do not contribute when Dirichlet or Neumann conditions are imposed due to the factor of $\sin 2\alpha$ in (3.124, 3.125). The fact that the contributions are regular is apparent when we consider that the Dirichlet and Neumann's Green's functions both satisfy the Hadamard condition, and so all singularities must be contained in the first two terms in (3.124, 3.125).

In order to evaluate (3.124, 3.125), we must first consider the Dirichlet and Neumann Green's functions. In the next section, we show that (3.120, 3.122) give the same results for the renormalised VP in the Euclidean background as they do in the Lorentzian background (3.2, 3.3), and use these to calculate the thermal Green's function in Euclidean space.

3.4.2 Euclidean Green's functions for Dirichlet and Neumann boundary conditions

The representations (3.124, 3.125) allow us to employ known results for the Dirichlet and Neumann Green's functions in order to calculate the effect on the VP of imposing Robin boundary conditions on both vacuum and thermal states. The thermal Green's functions for Dirichlet and Neumann conditions can be obtained as infinite image sums over the vacuum Green's function on the Lorentzian background [110]. In this section we derive the results from [110] using our representations (3.121, 3.123).

We can evaluate the sums in (3.121, 3.123) to give us

$$
\begin{aligned}
G^E_{\beta,D}(x,x') = \frac{\cos\rho\cos\rho'}{8\pi^2L^2}\Bigg\{\frac{1}{\cosh\Delta\tau+\cos\psi}-\frac{1}{\cosh\Delta\tau+\cos\psi^*} \\
-4\sum_{k=1}^{\infty}\frac{(-1)^k\cosh(k\Delta\tau)}{e^{2k\pi/\kappa}-1}\left(\frac{\sin k\psi}{\sin\psi}-\frac{\sin k\psi^*}{\sin\psi^*}\right)\Bigg\}, \quad (3.128)
\end{aligned}
$$

and

$$
\begin{aligned}
G^E_{\beta,N}(x,x') = \frac{\cos\rho\cos\rho'}{8\pi^2L^2}\Bigg\{\frac{1}{\cosh\Delta\tau+\cos\psi}+\frac{1}{\cosh\Delta\tau+\cos\psi^*} \\
-4\sum_{k=1}^{\infty}\frac{(-1)^k\cosh(k\Delta\tau)}{e^{2k\pi/\kappa}-1}\left(\frac{\sin k\psi}{\sin\psi}+\frac{\sin k\psi^*}{\sin\psi^*}\right)\Bigg\} \quad (3.129)
\end{aligned}
$$

where

$$\psi = \cos^{-1}(-\cos\rho\cos\rho' - \cos\gamma\sin\rho\sin\rho') \tag{3.130}$$

$$\psi^* = \pi + \cos^{-1}(-\cos\rho\cos\rho' + \cos\gamma\sin\rho\sin\rho'). \tag{3.131}$$

For more details of this calculation, see Appendix E. It is useful to compare this with results on the Lorentzian background in [110, eq 2.10], given in (3.78). We define $\beta = 2\pi/\kappa$ to be the inverse temperature. We can note that $\eta_\pm$ is related to ψ, ψ^* as follows:

$$\eta_+ = \psi + \pi, \quad \eta_- = \psi^*. \tag{3.132}$$

With some rearranging, (3.78) becomes

$$\begin{aligned} G^{(1)}_{\beta,\pm}(x,x') = \frac{\cos\rho\cos\rho'}{4\pi^2L^2}\Bigg\{ &\frac{1}{\cos\Delta t + \cos\psi} \mp \frac{1}{\cos\Delta t + \cos\psi^*} \\ &-4\sum_{k=1}^{\infty}\frac{(-1)^k\cos(k\Delta t)}{e^{2k\pi/\kappa}-1}\left(\frac{\sin k\psi}{\sin\psi} \mp \frac{\sin k\psi^*}{\sin\psi^*}\right)\Bigg\}. \end{aligned} \tag{3.133}$$

Making the replacement $t \to i\tau$, we recover our representation on the Euclidean section given by (3.128, 3.129). Thus, the results that we have found in the Euclidean background match those found in the Lorentzian background in [110].

By taking the zero temperature limit $\kappa \to 0$ in (3.128, 3.129) we can derive closed-form expressions for the vacuum Euclidean Green's functions for Dirichlet and Neumann boundary conditions imposed on the fields. The limit and summation can be interchanged, since the sums over k are uniformly convergent for $2\pi/\kappa > \Delta\tau$, and our results are

$$G^E_D(x,x') = \frac{\cos\rho\cos\rho'}{8\pi^2L^2}\left\{\frac{1}{\cosh\Delta\tau + \cos\psi} - \frac{1}{\cosh\Delta\tau + \cos\psi^*}\right\}, \tag{3.134}$$

$$G^E_N(x,x') = \frac{\cos\rho\cos\rho'}{8\pi^2L^2}\left\{\frac{1}{\cosh\Delta\tau + \cos\psi} + \frac{1}{\cosh\Delta\tau + \cos\psi^*}\right\}. \tag{3.135}$$

All divergences as $x' \to x$ are contained within the first term.

3.4.3 Renormalised vacuum polarisation with Robin conditions

Using the expression (3.124) together with (3.134, 3.135) we obtain the following result for the vacuum Green's function with Robin boundary conditions imposed

$$G^E_\alpha(x,x') = \frac{\cos\rho\cos\rho'}{8\pi^2L^2}\left\{\frac{1}{\cosh\Delta\tau + \cos\psi} - \frac{\cos 2\alpha}{\cosh\Delta\tau + \cos\psi^*}\right\} + \sin 2\alpha \; G^E_R(x,x') \tag{3.136}$$

where G^E_R is given by (3.126).

Using (3.125) together with (3.128, 3.129), we obtain the following result for the thermal Green's function with Robin conditions imposed

$$G^E_{\beta,\alpha}(x,x') = \frac{\cos\rho\cos\rho'}{8\pi^2L^2}\left\{\frac{1}{\cosh\Delta\tau+\cos\psi} - \frac{\cos 2\alpha}{\cosh\Delta\tau+\cos\psi^*}\right.$$
$$\left. -4\sum_{k=1}^{\infty}\frac{(-1)^k\cosh(k\Delta\tau)}{e^{2k\pi/\kappa}-1}\left(\frac{\sin k\psi}{\sin\psi} - \cos 2\alpha\frac{\sin k\psi^*}{\sin\psi^*}\right)\right\} + \sin 2\alpha\; G^E_{\beta,R}(x,x') \quad (3.137)$$

where $G^E_{\beta,R}$ is given by (3.127).

To renormalise the expectation values, we must look at the Hadamard parametrix. In Euclideanised CadS space, the van Vleck-Morette determinant and Synge world function are given by [126]

$$\Delta^{1/2}(x,x') = \left(\frac{2\sigma(x,x')}{L^2}\right)^{3/4}\operatorname{cosech}^{3/2}\left(\sqrt{\frac{2\sigma(x,x')}{L^2}}\right) \quad (3.138)$$

$$2\sigma(x,x') = L^2\left[\cos^{-1}\left(\frac{\cosh\Delta\tau - \cos\gamma\sin\rho\sin\rho'}{\cos\rho\cos\rho'}\right)\right]^2. \quad (3.139)$$

Here, we have used the results of Appendix D with $t\to i\tau$. We bring spatial coordinates together and keep temporal coordinates split, to give us

$$\Delta^{1/2} = \left(\frac{\cos^{-1}\zeta(\Delta\tau,\rho)}{\sinh\left(\cos^{-1}\zeta(\Delta\tau,\rho)\right)}\right)^{3/2}, \quad (3.140)$$

$$2\sigma/L^2 = \left[\cos^{-1}\zeta(\Delta\tau,\rho)\right]^2, \quad (3.141)$$

where

$$\zeta(\Delta\tau,\rho) = \frac{\cosh\Delta\tau - \sin^2\rho}{\cos^2\rho}. \quad (3.142)$$

The Hadamard parametrix (1.192) is then

$$\begin{aligned} G_S(\Delta\tau;\rho) =& \frac{1}{4\pi^2L^2}\left[\cos^{-1}\zeta(\Delta\tau,\rho)\right]^{-1/2}\left[\sinh\zeta(\Delta\tau,\rho)\right]^{-3/2} \\ =& \frac{\cos^2\rho}{4\pi^2L^2\Delta\tau^2} - \frac{1}{48\pi^2L^2}(2+\cos^2\rho) + \mathcal{O}(\Delta\tau^2). \end{aligned} \quad (3.143)$$

To bring spatial coordinates together in the Euclidean Green's function (3.136, 3.137), we first note that, in the limit $\rho'\to\rho, \cos\gamma\to 1$, we obtain

$$\cos\psi = -1, \quad \cos\psi^* = \cos 2\rho, \quad (3.144)$$

where ψ, ψ^* are given by (3.130, 3.131). Then we set $\psi = \pi, \psi^* = 2\rho$ in the coincidence limit and write

$$G^E_{\beta,\alpha}(\Delta\tau;\rho) = \frac{\cos^2\rho}{8\pi^2L^2}\left\{\frac{1}{\cosh\Delta\tau-1} - \frac{\cos 2\alpha}{\cosh\Delta\tau+\cos 2\rho}\right.$$
$$\left. -4\sum_{k=1}^{\infty}\frac{(-1)^k\cosh k\Delta\tau}{e^{2k\pi/\kappa}-1}\left((-1)^{k+1}k - \cos 2\alpha\;\frac{\sin 2k\rho}{\sin 2\rho}\right)\right\} + \sin 2\alpha\; G^E_{\beta,R}(\Delta\tau;\rho) \quad (3.145)$$

where we note that

$$\lim_{\psi\to\pi}\frac{\sin k\psi}{\sin\psi}=\lim_{\psi\to\pi}\frac{k\cos k\psi}{\cos\psi}=(-1)^{k+1}k \tag{3.146}$$

using L'Hopital's rule. We now consider each part of (3.145) separately, writing the first part as

$$\frac{1}{\cosh\Delta\tau-1}-\frac{\cos 2\alpha}{\cosh\Delta\tau+\cos 2\rho}=\frac{2}{\Delta\tau^2}-\frac{1}{6}\left(1+\frac{3\cos 2\alpha}{\cos^2\rho}\right)+\mathcal{O}(\Delta\tau). \tag{3.147}$$

The second part of (3.145) can be written as

$$\begin{aligned}&-4\sum_{k=1}^{\infty}\frac{(-1)^k\cosh k\Delta\tau}{e^{2k\pi/\kappa}-1}\left((-1)^{k+1}k-\cos 2\alpha\frac{\sin 2k\rho}{\sin 2\rho}\right)\\&\qquad=-4\sum_{k=1}^{\infty}\frac{(-1)^k}{e^{2k\pi/\kappa}-1}\left((-1)^{k+1}k-\cos 2\alpha\frac{\sin 2k\rho}{\sin 2\rho}\right)+\mathcal{O}(\Delta\tau^2)\end{aligned} \tag{3.148}$$

and the regular Robin function has the form

$$G^E_{\beta,R}(\Delta\tau;\rho)=\frac{\kappa}{16\pi^2L^2}\frac{\cos^2\rho}{\sin\rho}\sum_{n=-\infty}^{\infty}e^{in\kappa\Delta\tau}\sum_{\ell=0}^{\infty}(2\ell{+}1)|\Gamma(\ell{+}1{+}in\kappa)|^2C^{\alpha}_{n\ell}\left[P^{-\ell-\frac{1}{2}}_{in\kappa-\frac{1}{2}}(\cos\rho)\right]^2 \tag{3.149}$$

where

$$C^{\alpha}_{n\ell}=\frac{2\cos\alpha|\Gamma(\frac{1}{2}(in\kappa+\ell+2))|^2-\sin\alpha|\Gamma(\frac{1}{2}(in\kappa+\ell+1))|^2}{2\sin\alpha|\Gamma(\frac{1}{2}(in\kappa+\ell+2))|^2+\cos\alpha|\Gamma(\frac{1}{2}(in\kappa+\ell+1))|^2}. \tag{3.150}$$

Expanding $G^E_{\beta,R}(\Delta\tau;\rho)$ as a series in $\Delta\tau$, we find

$$\begin{aligned}G^E_{\beta,R}(\Delta\tau;\rho)&=\frac{\kappa}{16\pi^2L^2}\frac{\cos^2\rho}{\sin\rho}\sum_{n=-\infty}^{\infty}(1+i\kappa n\Delta\tau)\sum_{\ell=0}^{\infty}(2\ell+1)|\Gamma(\ell+1+in\kappa)|^2\\&\qquad\times C^{\alpha}_{n\ell}\left[P^{-\ell-\frac{1}{2}}_{in\kappa-\frac{1}{2}}(\cos\rho)\right]^2+\mathcal{O}(\Delta\tau^2)\\&=\frac{\kappa}{16\pi^2L^2}\frac{\cos^2\rho}{\sin\rho}\sum_{n=-\infty}^{\infty}\sum_{\ell=0}^{\infty}(2\ell+1)|\Gamma(\ell+1+in\kappa)|^2\\&\qquad\times C^{\alpha}_{n\ell}\left[P^{-\ell-\frac{1}{2}}_{in\kappa-\frac{1}{2}}(\cos\rho)\right]^2+\mathcal{O}(\Delta\tau^2)\end{aligned} \tag{3.151}$$

where in the second line we have used the fact that terms linear in $\Delta\tau$ sum to zero.

The Euclidean Green's function for thermal states (3.145) can then be written as

$$\begin{aligned} G^E_{\beta,\alpha}(\Delta\tau;\rho) = &\frac{\cos^2\rho}{4\pi^2L^2\Delta\tau^2} - \frac{1}{48\pi^2L^2}\left(\cos^2\rho + 3\cos 2\alpha\right) && (3.152)\\ &-\frac{\cos^2\rho}{2\pi^2L^2}\sum_{k=1}^{\infty}\frac{(-1)^k}{e^{2k\pi/\kappa}-1}\left((-1)^{k+1}k - \cos 2\alpha\frac{\sin 2k\rho}{\sin 2\rho}\right) && (3.153)\\ &+\frac{\kappa\sin 2\alpha}{16\pi^2L^2}\frac{\cos^2\rho}{\sin\rho}\sum_{n=-\infty}^{\infty}\sum_{\ell=0}^{\infty}(2\ell+1)|\Gamma(\ell+1+in\kappa)|^2\\ &\times C^{\alpha}_{n\ell}\left[P^{-\ell-\frac{1}{2}}_{in\kappa-\frac{1}{2}}(\cos\rho)\right]^2 + \mathcal{O}(\Delta\tau^2). && (3.154)\end{aligned}$$

Subtracting the Hadamard parametrix (3.143) and taking the limit $\Delta\tau \to 0$ gives us the thermal expectation values with Robin conditions imposed,

$$\begin{aligned}\langle\beta|\hat{\phi}^2_\alpha|\beta\rangle = &-\frac{1}{48\pi^2L^2}(3\cos 2\alpha - 2)\\ &-\frac{\cos^2\rho}{2\pi^2L^2}\sum_{k=1}^{\infty}\frac{(-1)^k}{e^{2k\pi/\kappa}-1}\left((-1)^{k+1}k - \cos 2\alpha\frac{\sin 2k\rho}{\sin 2\rho}\right)\\ &+\frac{\kappa\sin 2\alpha}{16\pi^2L^2}\frac{\cos^2\rho}{\sin\rho}\sum_{n=-\infty}^{\infty}\sum_{\ell=0}^{\infty}(2\ell+1)|\Gamma(\ell+1+in\kappa)|^2\\ &\times C^{\alpha}_{n\ell}\left[P^{-\ell-\frac{1}{2}}_{in\kappa-\frac{1}{2}}(\cos\rho)\right]^2. && (3.155)\end{aligned}$$

When Dirichlet and Neumann conditions are imposed, the final term in (3.155) vanishes due to the $\sin 2\alpha$ term and, with some rearranging and making the replacement $2\pi/\kappa = \beta/L$, we can recover the results from [110], given in (3.81).

The vacuum expectation values are found in a similar way,

$$\begin{aligned}\langle 0|\hat{\phi}^2_\alpha|0\rangle = &-\frac{1}{48\pi^2L^2}(3\cos 2\alpha - 2)\\ &+\frac{\sin 2\alpha}{16\pi^2L^2}\frac{\cos^2\rho}{\sin\rho}\int_{\omega=-\infty}^{\infty}d\omega\sum_{\ell=0}^{\infty}(2\ell+1)|\Gamma(\ell+1+i\omega)|^2\\ &\times C^{\alpha}_{\omega\ell}\left[P^{-\ell-\frac{1}{2}}_{i\omega-\frac{1}{2}}(\cos\rho)\right]^2, && (3.156)\end{aligned}$$

where constants $C^{\alpha}_{\omega\ell}$ are given by replacing $n\kappa \to \omega$ in (3.150). For Dirichlet and Neumann conditions, the second term in (3.156) vanishes due to the $\sin 2\alpha$ term, and we recover the results that we found in Lorentzian CadS (3.69, 3.77). Equations (3.155, 3.156) are new results.

3.5 Numerical results

In this section we present the numerical results for vacuum expectation values (3.156) and thermal expectation values (3.155) in CadS with Robin conditions imposed on the boundary.

To calculate (3.156) numerically, we first swap the order of sum and integral. The integral over ω can be calculated relatively quickly by fixing α and ℓ and using the `NIntegrate` function in `Mathematica` between $\omega = -\infty$ and $\omega = \infty$. The working precision is set at 10, and we calculate the integral for $\ell = 0, ..., 20$. The sum over ℓ is then truncated at $\ell = 20$, as contributions from larger ℓ values are found to be negligible.

In Figure 3.7(a), we show the vacuum expectation value as a function of Robin parameter α and radial coordinate ρ, whilst in Figure 3.7(b) we consider a set of values of α and show the vacuum expectation values as functions of ρ only.

For Dirichlet ($\alpha = 0$) and Neumann ($\alpha = \pi/2$), the vacuum expectation values are constant, as shown in (3.69, 3.77). For $\alpha \in [\alpha_{crit}, \pi)$, there exist unstable modes (see section 3.2.4). For this reason, we restrict our plot in Figure 3.7(a) to values of α for which there are no unstable modes. For $\alpha \in (0, \pi/2)$, the vacuum expectation value is monotonically increasing from the origin ($\rho = 0$) to the boundary ($\rho = \pi/2$), and is monotonically decreasing for $\alpha \in (\pi/2, \alpha_{crit})$. We can see from Figure 3.7(a) that values at the origin increase monotonically as α increases. Expectation values diverge as $\alpha \to \alpha_{crit}$, which is indicative of the breakdown of the semiclassical approximation that we use (due to the presence of classical instabilities for $\alpha > \alpha_{crit}$).

We also notice that, at the boundary, all results approach the Neumann constant value $5/48\pi^2 L^2$, apart from when Dirichlet conditions are used. This is most evident in Figure 3.7(b). This point is discussed further in section 3.6.

We now look at thermal expectation values, calculated for $\kappa = 1/2, 2$ and 2π from (3.155). The temperature T is related to κ via $T = \kappa/2\pi$. Thermal expectation values (3.155) are a little more straightforward to calculate, since we have a summation over values of n rather than an integral. We truncate the sum over ℓ at $\ell = 100$ and the sum over n at $n = 100$, with each value calculated to 100 digits of precision.

To check that this number of terms is satisfactory, we can compare with the results given in Allen, Folacci and Gibbons (AFG) [110], which are easier to calculate but do not allow for the extension to Robin boundary conditions. The AFG thermal expectation values with Dirichlet and Neumann boundary conditions imposed are given in (3.81), where we note that the sums over n in $f_1(\beta), S_0(\beta, \rho)$ can be performed to a high value of n very quickly. We take one away from the other, and then take the coincidence limit, that is

$$\langle \beta | \hat{\phi}_N^2 | \beta \rangle - \langle \beta | \hat{\phi}_D^2 | \beta \rangle. \tag{3.157}$$

To compare, we plot the difference in Dirichlet and Neumann results using both our mode-sum representation (3.155) and AFG's representation (3.81). Although both are

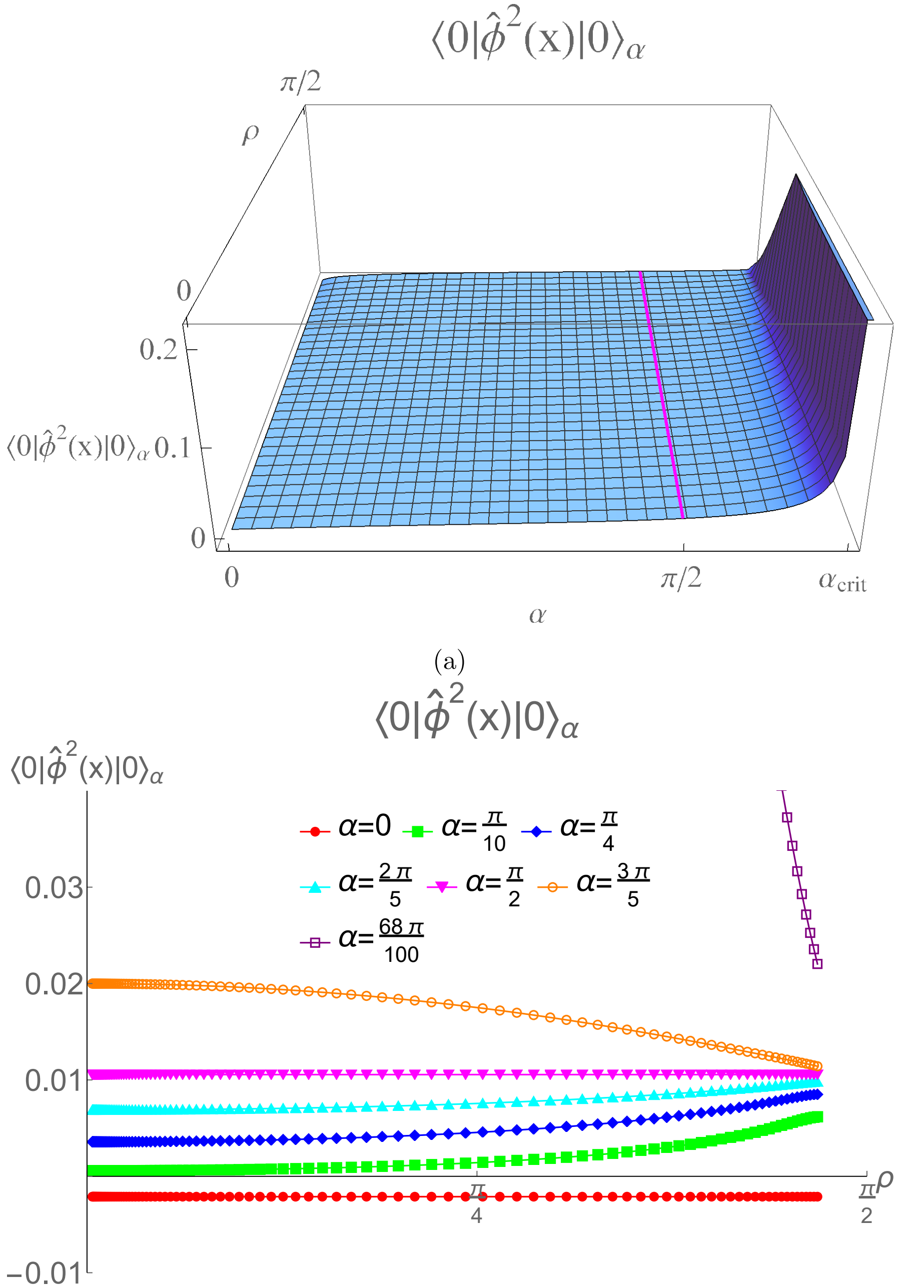

(a)

(b)

Figure 3.7: Plots of vacuum expectation values $\langle 0|\hat{\phi}_\alpha|0\rangle$ calculated from (3.156). The upper plot shows these values as a function of the radial coordinate ρ and the Robin parameter α. The magenta line marks the VP for Neumann conditions ($\alpha = \pi/2$), for which vacuum expectation values are constant. The lower plot considers a set of values of α and presents the vacuum expectation values as functions of ρ only. We use units in which the adS radius $L = 1$.

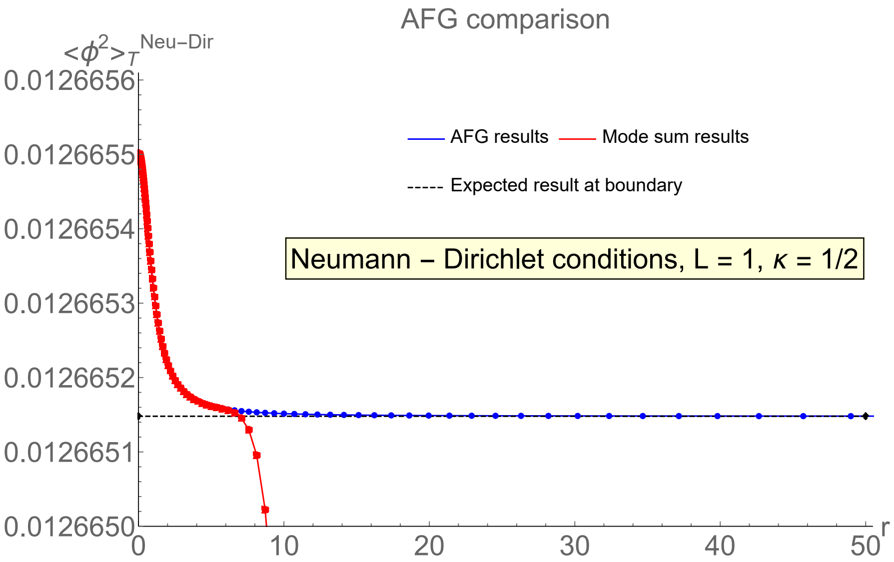
AFG comparison
$<\phi^2>_T^{\text{Neu-Dir}}$
0.0126656
0.0126655
0.0126654
0.0126653
0.0126652
0.0126651
0.0126650
AFG results
Mode sum results
Expected result at boundary
Neumann – Dirichlet conditions, L = 1, κ = 1/2
0
10
20
30
40
50
r

(a)

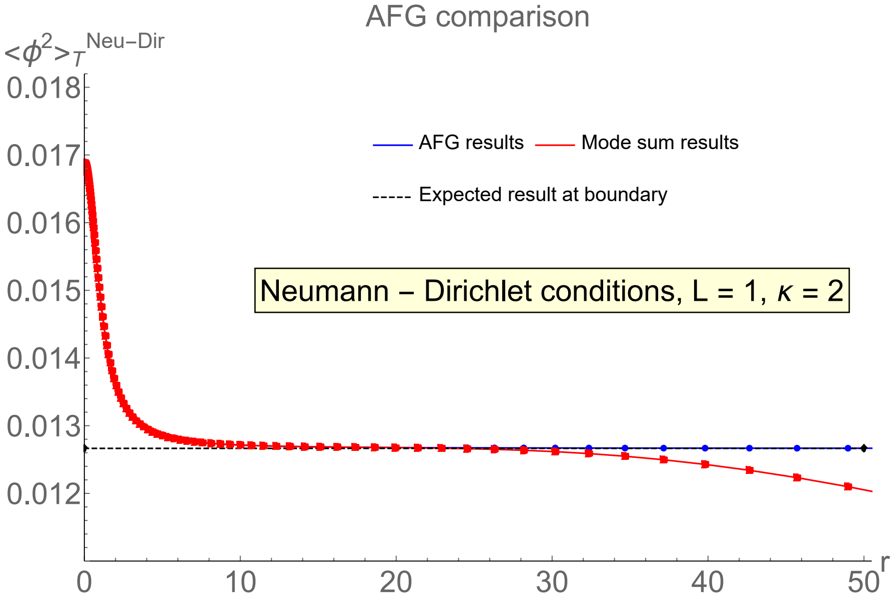
AFG comparison
$<\phi^2>_T^{\text{Neu-Dir}}$
0.018
0.017
0.016
0.015
0.014
0.013
0.012
AFG results
Mode sum results
Expected result at boundary
Neumann – Dirichlet conditions, L = 1, κ = 2
0
10
20
30
40
50
r

(b)

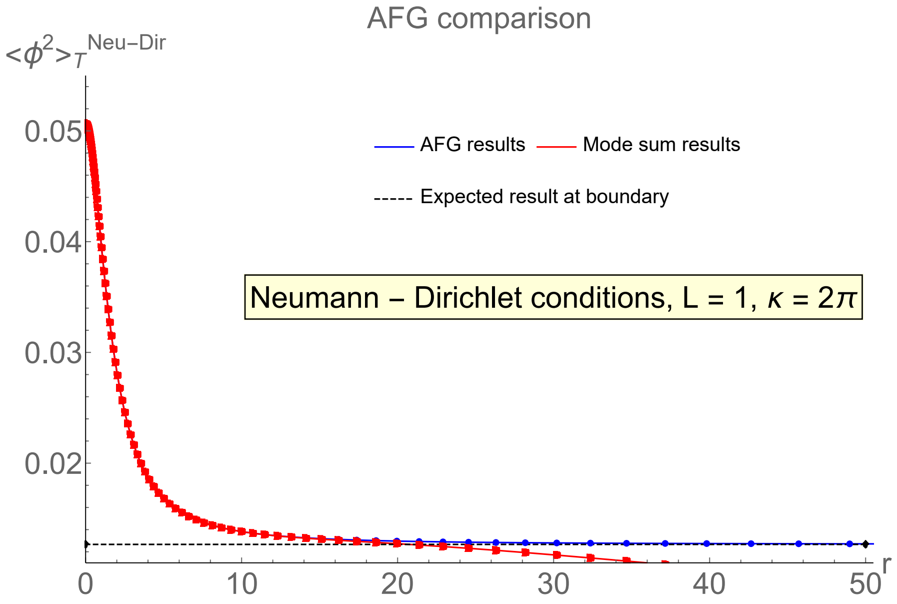

(c)

Figure 3.8: We plot the difference between Dirichlet and Neumann results for thermal expectation values using both our representation (3.155) and AFG's representation (3.81). Our representation is a mode-sum which requires a lot more computation time to calculate compared to AFG's representation. We use 100 terms in both the n- and ℓ-sums. To increase the accuracy of our results for larger values of r, we would need to increase the number of terms in each sum.

equivalent when we consider $\alpha = 0, \pi/2$, the AFG results provide better accuracy, since the sums can be computed with better numerical precision. Plotting the difference allows us to test the accuracy of our numerical computations.

Comparison plots between (3.155) and (3.81) are shown in Figure 3.8. To plot, we use the radial coordinate r, defined by

$$\rho = \tan^{-1}\left(\frac{r}{L}\right), \tag{3.158}$$

so that the boundary $\rho = \pi/2$ is at $r = \infty$, whilst the origin is still placed at $r = 0$. This allows us to see more clearly where our numerical computations break down as we approach the boundary ($r \to \infty$). In Figure 3.8(a), we see that our computation breaks down for relatively small r when we have small temperature ($\kappa = 1/2$). As the temperature increases ($\kappa = 2$ in Figure 3.8(b) and $\kappa = 2\pi$ in Figure 3.8(c)) then we find that our results do not break down until we reach larger values of r. In all cases, we still capture the fact that results converge to the expected difference $6/48\pi^2L^2$ as we increase r. This is regardless of the value of r for which our numerical computations break down. This implies that our results have been calculated to a satisfactory value of r in order to obtain the correct behaviour close to the boundary.

In Figures 3.9(a), (c), (e) we show the thermal expectation values for three different temperatures as functions of the radial coordinate ρ and Robin parameter α. As we did for the vacuum expectation values, in Figures 3.9(b), (d), (f) we show the results for specific values of α. To generate the surface plots, we calculate the expectation values for $\alpha = i\pi/100$, where $i = 0, 1, ..., n$ such that $n > 50$ and $n\pi/100 \sim \alpha_{crit}$.

When we have small temperature, $\kappa = 1/2$, the plot in Figure 3.9(b) looks very similar to that in Figure 3.7(b) - the differences between the two are indistinguishable at this scale. However, it is important to note that in the thermal case, the expectation values with Neumann and Dirichlet boundary conditions are no longer constant. At the boundary, both results approach the constant vacuum expectation values - that is, $-1/48\pi^2L^2$ for Dirichlet conditions and $5/48\pi^2L^2$ for Neumann conditions.

The surface plot in Figure 3.9(a) uses a different scale to that in Figure 3.7(a). The monotonically increasing behaviour at the origin can be clearly seen. When Dirichlet boundary conditions are applied, the thermal expectation values have their maximum at the origin, and monotonically decrease as we approach the boundary. For $\alpha \in (0, \pi/2)$, thermal expectation values are monotonically increasing as ρ increases, and are monotonically decreasing for $\alpha \in [\pi/2, \alpha_{crit})$.

As we increase the temperature from $\kappa = 1/2$ to $\kappa = 2$ and again to $\kappa = 2\pi$, we see that the thermal expectation value at the origin increases regardless of the boundary condition imposed. In addition, the thermal expectation value at the origin is monotonically increasing as α increases, and appears to be diverging as $\alpha \to \alpha_{crit}$. Away from the origin, the behaviour is not so straightforward to describe, as it depends on the value of α and κ. For Dirichlet and Neumann conditions, the thermal expectation value is always monotonically decreasing as we move towards the boundary, regardless

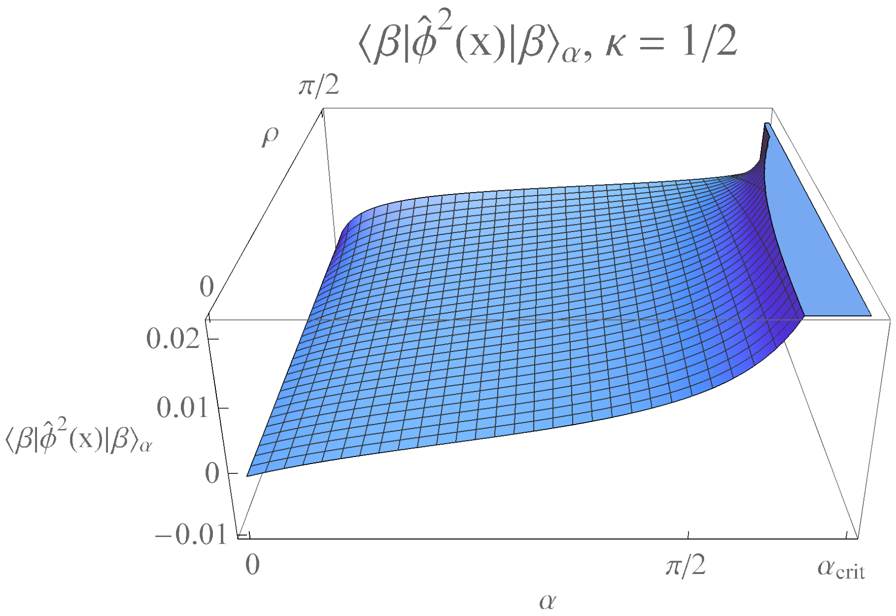
$\langle\beta|\hat{\phi}^2(\mathrm{x})|\beta\rangle_\alpha$, $\kappa = 1/2$
$\pi/2$
ρ
0
0.02
0.01
$\langle\beta|\hat{\phi}^2(\mathrm{x})|\beta\rangle_\alpha$
0
−0.01
0
$\pi/2$
α_{crit}
α

(a)

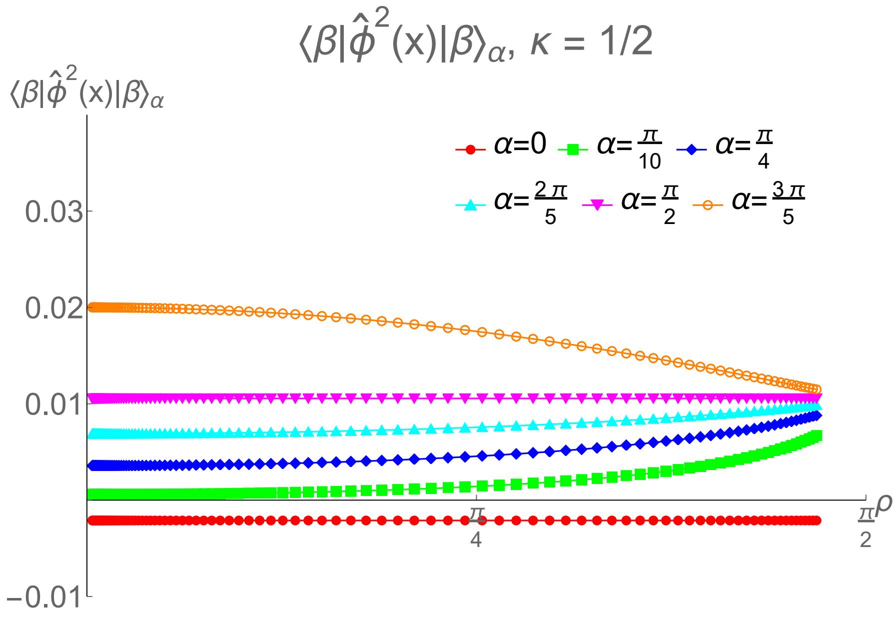
$\langle\beta|\hat{\phi}^2(\mathrm{x})|\beta\rangle_\alpha$, $\kappa = 1/2$
$\langle\beta|\hat{\phi}^2(\mathrm{x})|\beta\rangle_\alpha$
$\alpha=0$
$\alpha=\frac{\pi}{10}$
$\alpha=\frac{\pi}{4}$
$\alpha=\frac{2\pi}{5}$
$\alpha=\frac{\pi}{2}$
$\alpha=\frac{3\pi}{5}$
0.03
0.02
0.01
−0.01
$\frac{\pi}{4}$
$\frac{\pi}{2}$
ρ

(b)

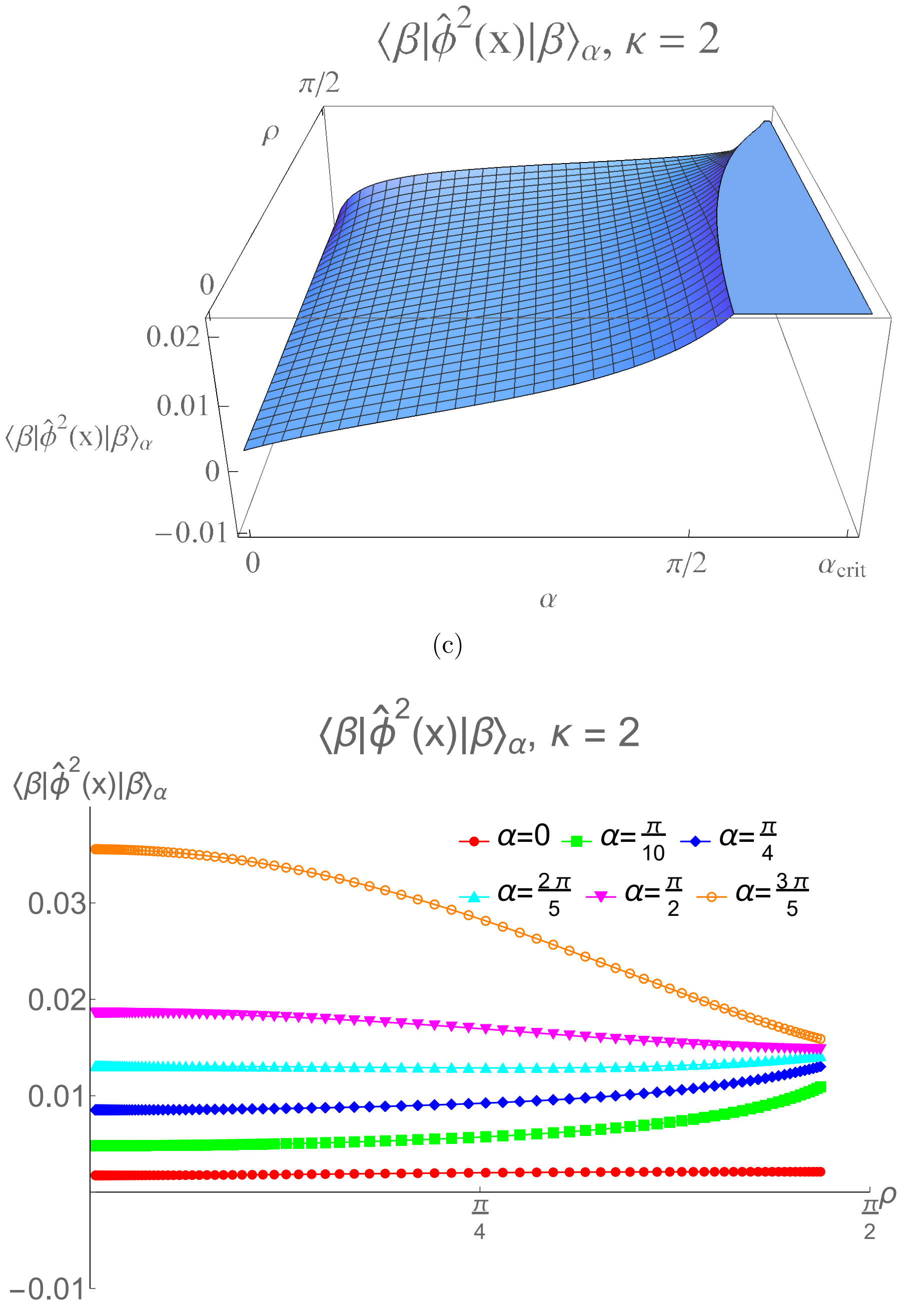
$\langle\beta|\hat{\phi}^2(x)|\beta\rangle_\alpha$, $\kappa = 2$
$\pi/2$
ρ
0
0.02
0.01
$\langle\beta|\hat{\phi}^2(x)|\beta\rangle_\alpha$
0
−0.01
0
$\pi/2$
α_{crit}
α
$\langle\beta|\hat{\phi}^2(x)|\beta\rangle_\alpha$, $\kappa = 2$
$\langle\beta|\hat{\phi}^2(x)|\beta\rangle_\alpha$
$\alpha=0$
$\alpha=\frac{\pi}{10}$
$\alpha=\frac{\pi}{4}$
$\alpha=\frac{2\pi}{5}$
$\alpha=\frac{\pi}{2}$
$\alpha=\frac{3\pi}{5}$
0.03
0.02
0.01
−0.01
$\frac{\pi}{4}$
$\frac{\pi}{2}$
ρ

(c)

(d)

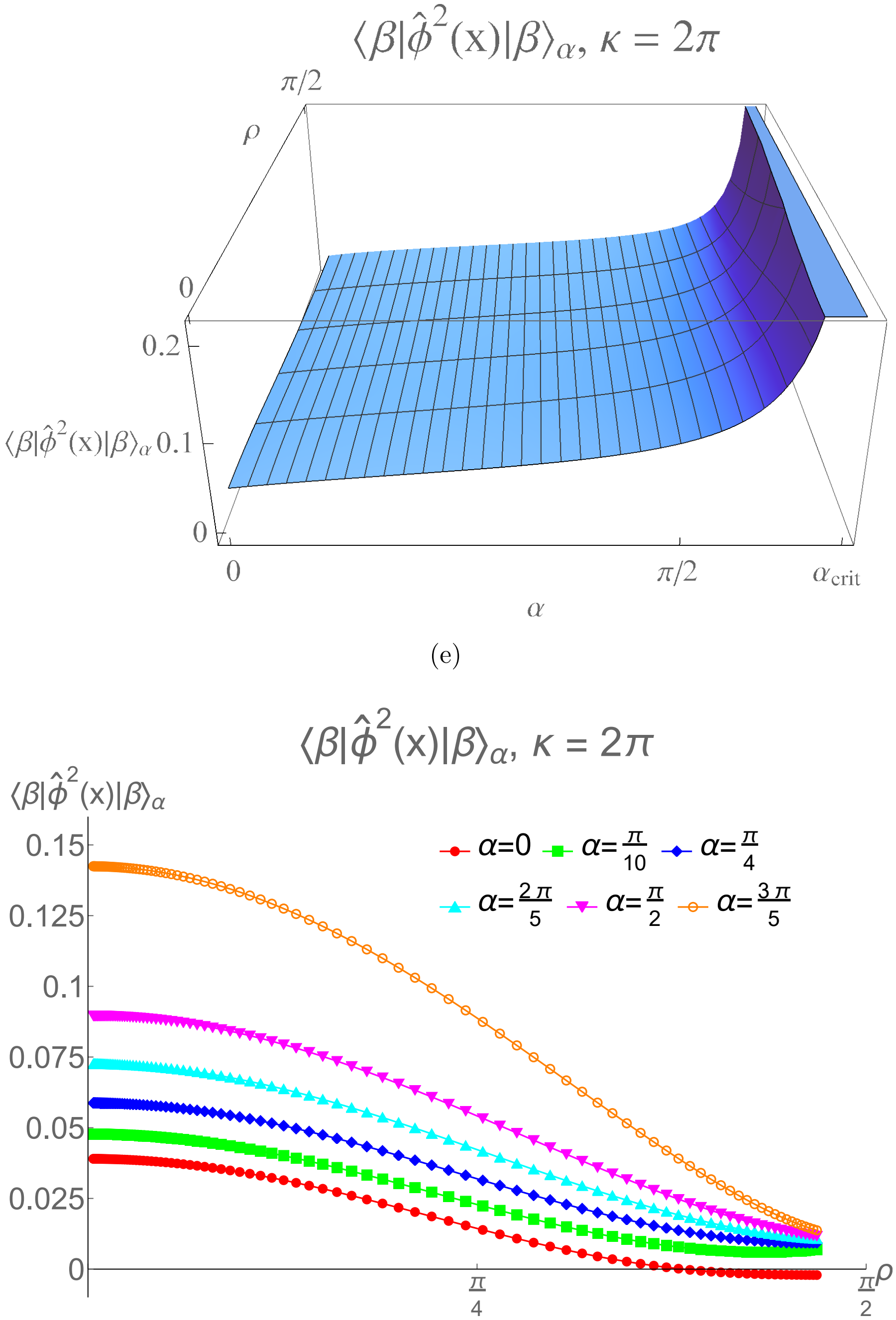

(e)

(f)

Figure 3.9: Plots of thermal expectation values $\langle\beta|\hat{\phi}_\alpha|\beta\rangle$ calculated from (3.155). Plots (a), (c), (e) show these values as functions of the radial coordinate ρ and the Robin parameter α. Plots (b), (d), (f) show a selection of values of α and present the thermal expectation values as functions of ρ only. We use units in which the adS radius $L = 1$.

of the value of κ. When κ is small, we find that the expectation values monotonically increase for sufficiently small α, and monotonically decrease for sufficiently large α. When $\kappa = 2\pi$, it appears that the results monotonically decrease for all α, although it is possible that there exist some small values of α for which this is not true.

As we saw in the case of vacuum expectation values, thermal expectation values approach the limit $5/48\pi^2 L^2$ for all values of α except $\alpha = 0$. This is discussed in further detail in section 3.6. For all values of temperature T and parameter α, we can see that thermal expectation values are larger than vacuum expectation values for all ρ. This difference tends to zero as we approach the spacetime boundary. This property can be interpreted as the thermal radiation "clumping" close to the origin due to the infinite gravitational potential at the boundary [62].

3.6 Vacuum polarisation at the boundary

In the previous section, our numerical results showed that the expectation values at the boundary approached $5/48\pi^2 L^2$ for all values of $\alpha \in (0, \alpha_{crit})$. This behaviour is noticeably different from the behaviour observed in [117] where Robin conditions were only applied to the $\ell = 0$ terms. In the latter case, all vacuum expectation values tended to the Dirichlet limit $-1/48\pi^2 L^2$ as ρ approached the boundary.

In this section, we look at the values of (3.155, 3.156) on the boundary to try to derive the fact that these expectation values approach $5/48\pi^2 L^2$ for all $\alpha \in (0, \alpha_{crit})$. The sum over k in (3.155) converges uniformly for all ρ, and thanks to the factor of $\cos^2 \rho$, this will vanish on the boundary. Therefore, it is the final double sum (or sum and integral combination in (3.156)) that we need to evaluate on the boundary. This is a difficult task, however, since the sums are not uniformly convergent in ρ. We test this convergence in Figure 3.10, where we swap the order of the sums, perform the n-sum and plot the ℓ-summand. For each fixed value of ρ, the ℓ-sum is convergent, but the rate of this convergence gets worse as ρ increases towards the spacetime boundary, meaning that we cannot naively interchange sum and limit.

When deriving equations (3.155, 3.156), we used the representations (3.124, 3.125). From studying our numerical results, we choose instead to write the Green's functions in the following way:

$$G^E_\alpha(x, x') = G^E_N(x, x') + [G^E_D(x, x') - G^E_N(x, x')] \cos^2 \alpha + \sin 2\alpha \; G^E_R(x, x'), \qquad (3.159)$$

$$G^E_{\beta,\alpha}(x, x') = G^E_{\beta,N}(x, x') + [G^{\beta,E}_D(x, x') - G^E_{\beta,N}(x, x')] \cos^2 \alpha + \sin 2\alpha \; G^E_{\beta,R}(x, x'). \qquad (3.160)$$

Using equations (3.120 - 3.123, 3.126, 3.127), we can write the vacuum and thermal

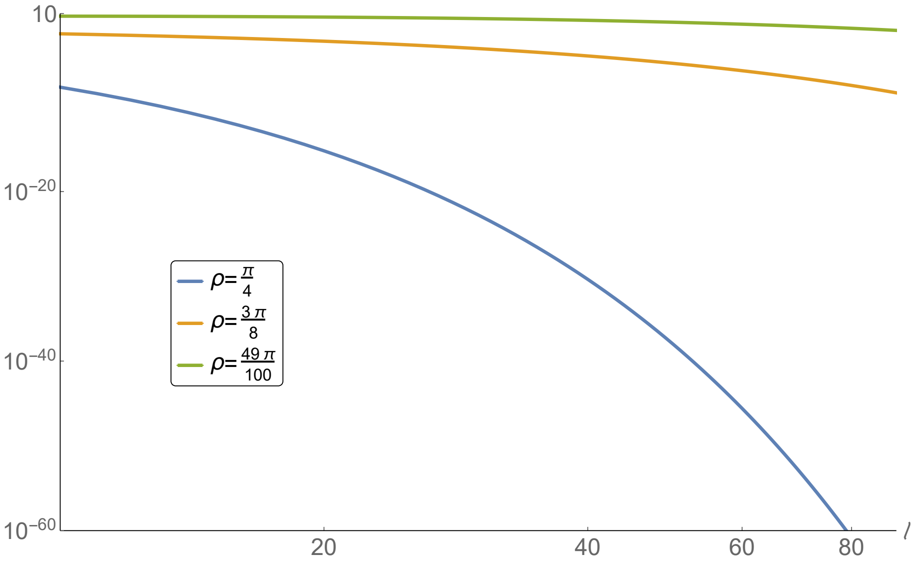

Figure 3.10: Log-log plot of the ℓ-summand in the final term in (3.155). We have swapped the sums in this equation, fixed $\alpha = \pi/4$ and performed the n-sum, for various values of ρ.

expectation values in the following alternative form

$$\begin{aligned}&\langle 0|\hat{\phi}_\alpha^2|0\rangle = \langle 0|\hat{\phi}_N^2|0\rangle \\ &- \frac{\sin 2\alpha}{16\pi^2 L^2}\frac{\cos^2\rho}{\sin\rho}\int_{\omega=-\infty}^{\infty} d\omega \sum_{\ell=0}^{\infty}(2\ell+1)|\Gamma(\ell+1+i\omega)|^2 D_{\omega\ell}^{\alpha}\left[P_{i\omega-\frac{1}{2}}^{-\ell-\frac{1}{2}}(\cos\rho)\right]^2, \quad (3.161)\end{aligned}$$

and

$$\begin{aligned}&\langle \beta|\hat{\phi}_\alpha^2|\beta\rangle = \langle \beta|\hat{\phi}_N^2|\beta\rangle \\ &\quad - \frac{\kappa\sin 2\alpha}{16\pi^2 L^2}\frac{\cos^2\rho}{\sin\rho}\sum_{n=-\infty}^{\infty}\sum_{\ell=0}^{\infty}(2\ell+1)|\Gamma(\ell+1+in\kappa)|^2 D_{n\ell}^{\alpha}\left[P_{in\kappa-\frac{1}{2}}^{-\ell-\frac{1}{2}}(\cos\rho)\right]^2. \quad (3.162)\end{aligned}$$

Our new constants $D_{\omega\ell}^{\alpha}$ are defined by

$$D_{\omega\ell}^{\alpha} = \cot\alpha - C_{\omega\ell}^{\alpha} = \frac{|\Gamma(\frac{i\omega+\ell+2}{2})|^2\csc\alpha}{2|\Gamma(\frac{i\omega+\ell+2}{2})|^2\sin\alpha + |\Gamma(\frac{i\omega+\ell+1}{2})|^2\cos\alpha} \quad (3.163)$$

where the constants $C_{\omega\ell}^{\alpha}$ are defined in (3.150). As before, the constants $D_{n\ell}^{\alpha}$ are obtained by taking $\omega \to n\kappa$ in (3.163). Using our expression for $\langle\beta|\hat{\phi}_N^2|\beta\rangle$ from (3.155), we can write

$$\langle\beta|\hat{\phi}^2_\alpha|\beta\rangle = \langle 0|\hat{\phi}^2_N|0\rangle - \frac{\cos^2\rho}{2\pi^2L^2}\sum_{k=1}^{\infty}\frac{(-1)^k}{e^{2k\pi/\kappa}-1}\left((-1)^{k+1}k - \frac{\sin 2k\rho}{\sin 2\rho}\right)$$
$$-\frac{\kappa\sin 2\alpha}{16\pi^2L^2}\frac{\cos^2\rho}{\sin\rho}\sum_{n=-\infty}^{\infty}\sum_{\ell=0}^{\infty}(2\ell+1)|\Gamma(\ell+1+in\kappa)|^2 D^{\alpha}_{n\ell}\left[P^{-\ell-\frac{1}{2}}_{in\kappa-\frac{1}{2}}(\cos\rho)\right]^2. \quad (3.164)$$

As $\ell \to \infty$, we can use asymptotic properties of Γ functions [120, 5.11.12] to show

$$C^{\alpha}_{n\ell} = \frac{2\cos\alpha\frac{|\Gamma(\frac{1}{2}(in\kappa+\ell+2))|^2}{|\Gamma(\frac{1}{2}(in\kappa+\ell+1))|^2} - \sin\alpha}{2\sin\alpha\frac{|\Gamma(\frac{1}{2}(in\kappa+\ell+2))|^2}{|\Gamma(\frac{1}{2}(in\kappa+\ell+1))|^2} + \cos\alpha} \sim \frac{\ell\cos\alpha - \sin\alpha}{\ell\sin\alpha + \cos\alpha} \sim \cot\alpha \text{ as } \ell \to \infty \quad (3.165)$$

and so

$$D^{\alpha}_{n\ell} \to 0 \text{ as } \ell \to \infty. \quad (3.166)$$

On the boundary, numerical investigations suggest that these sums in (3.161, 3.162) diverge. This is complicated, however, by the presence of a factor of $\cos^2\rho$ which vanishes on the boundary. The question remains whether the additional contributions in (3.161, 3.162) vanish on the boundary.

Attempting to address this question on CadS is complicated since $\rho = \pi/2$ is not part of the spacetime. Instead, we can consider the Euclidean background of ESU, discussed in the early part of section 3.4. Divergences close to a boundary are studied in [114], and we follow their method here by applying Stokes' Theorem to the vacuum Euclidean Green's functions $G^E_{ESU,N}(x,x')$ and $G^E_{ESU,\alpha}(x,x')$ on the region $V \subset$ ESU defined by $\rho \in [0,\pi/2]$. If $S = \partial V$, the boundary of the region V, then we find

$$\int_S \left[G^E_{N,ESU}(x,y)\widetilde{\nabla}_\mu G^E_{\alpha,ESU}(y,x') - G^E_{\alpha,ESU}(x,y)\widetilde{\nabla}_\mu G^E_{N,ESU}(y,x')\right] dS^\mu$$
$$= \int_V \widetilde{\nabla}^\mu\left[G^E_{N,ESU}(x,y)\widetilde{\nabla}_\mu G^E_{\alpha,ESU}(y,x') - G^E_{\alpha,ESU}(x,y)\widetilde{\nabla}_\mu G^E_{N,ESU}(y,x')\right] dV$$
$$= \int_V \left[G^E_{N,ESU}(x,y)\widetilde{\Box} G^E_{\alpha,ESU}(y,x') - G^E_{\alpha,ESU}(x,y)\widetilde{\Box} G^E_{N,ESU}(y,x')\right] dV \quad (3.167)$$

where covariant derivatives $\widetilde{\nabla}$ and the D'Alembertian $\widetilde{\Box} = \widetilde{\nabla}^\mu\widetilde{\nabla}_\mu$ are defined with respect to the Euclidean ESU metric, and all integrals are taken over spacetime points y. Using the wave equation on Euclidean ESU (3.87), we can write the right-hand side of (3.167) as

$$\int_V \left[G^E_{N,ESU}(x,y)\widetilde{\Box} G^E_{\alpha,ESU}(y,x') - G^E_{\alpha,ESU}(x,y)\widetilde{\Box} G^E_{N,ESU}(y,x')\right] dV$$
$$= \int_V \left\{G^E_{N,ESU}(x,y)\left[-\frac{1}{\sqrt{g}}\delta^{(4)}(y,x') + \frac{1}{L^2}G^E_{\alpha,ESU}(y,x')\right]\right.$$
$$\left. - G^E_{\alpha,ESU}(x,y)\left[-\frac{1}{\sqrt{g}}\delta^{(4)}(y,x') + \frac{1}{L^2}G^E_{N,ESU}(y,x')\right]\right\} dV$$
$$= -G^E_{N,ESU}(x,x') + G^E_{\alpha,ESU}(x,x'), \quad (3.168)$$

where $\delta^4(x,x')$ is defined in (1.19). To evaluate the surface integral on the left-hand side of (3.167), we note that the boundary S consists of two surfaces $\mathscr{I}_0 \cup \mathscr{I}_{\pi/2}$, where $\mathscr{I}_0$ is the timelike hypersurface in ESU at $\rho = 0$ and $\mathscr{I}_{\pi/2}$ is the timelike hypersurface in ESU at $\rho = \pi/2$. The contribution from the integral over $\mathscr{I}_0$ is zero. This is explained in CadS in section 3.2.5 - we can write the Green's functions as sums over modes (3.35) which were shown to vanish on $\mathscr{I}_0$. The analysis from section 3.2.5 carries over to ESU since the conformal factor $\cos\rho = 1$ on $\mathscr{I}_0$. Imposing Robin conditions on $\mathscr{I}_{\pi/2}$, we find

$$\int_S \left[G^E_{N,ESU}(x,y)\widetilde{\nabla}_\mu G^E_{\alpha,ESU}(y,x') - G^E_{\alpha,ESU}(x,y)\widetilde{\nabla}_\mu G^E_{N,ESU}(y,x')\right] dS^\mu \\ = -L^{-1}\cot\alpha \int_{\mathscr{I}_{\pi/2}} G^E_{N,ESU}(x,y) G^E_{\alpha,ESU}(y,x')\ dS. \quad (3.169)$$

Combining (3.168) and (3.169) and rearranging, we have

$$G^E_{\alpha,ESU}(x,x') = G^E_{N,ESU}(x,x') - L^{-1}\cot\alpha \int_{\mathscr{I}_{\pi/2}} G^E_{N,ESU}(x,y) G^E_{\alpha,ESU}(y,x')\ dS. \quad (3.170)$$

Since $G^E_{N,ESU}(x,x')$ satisfies the Hadamard condition, in general all singularities in $G^E_{\alpha,ESU}(x,x')$ are contained within the first term of (3.170), and the integral will be finite in the limit $x' \to x$ (except, possibly, if x lies on the boundary). Note that the factor of $\cot\alpha$ indicates that this expansion is valid for all $0 < \alpha < \pi$, but not for Dirichlet conditions when $\alpha = 0$.

Following [114], we can substitute the expression for $G^E_{\alpha,ESU}(x,x')$ given in (3.170) into the integral on the right-hand-side of (3.170). This procedure forms the basis of an iterative expression for the Euclidean Green's function with Robin boundary conditions, that is

$$G^E_{\alpha,ESU}(x,x') = G^E_{N,ESU}(x,x') - L^{-1}\cot\alpha\, G^{E,(1)}_{\alpha,ESU}(x,x') + L^{-2}\cot^2\alpha\, G^{E,(2)}_{\alpha,ESU}(x,x') + ... \quad (3.171)$$

where

$$G^{E,(1)}_{\alpha,ESU}(x,x') = \int_{\mathscr{I}_{\pi/2}} G^E_{N,ESU}(x,y) G^E_{N,ESU}(y,x')\ dS, \quad (3.172)$$

$$G^{E,(2)}_{\alpha,ESU}(x,x') = \int_{\mathscr{I}_{\pi/2}} G^E_{N,ESU}(x,y) \left[\int_{\mathscr{I}_{\pi/2}} G^E_{N,ESU}(y,z) G^E_{N,ESU}(z,x')\ dS\right] dS. \quad (3.173)$$

In (3.172), we take the integral over spacetime point y, whilst in (3.173), we take the scalar integral over z and the outer integral over y. Further terms in (3.171) will contain additional integrals over $\mathscr{I}_{\pi/2}$.

We now note that $G^E_{N,ESU}(x,x')$ can be written in closed form by applying the conformal transformation (3.6) to (3.135):

$$G^E_{N,ESU}(x,x') = \frac{1}{8\pi^2 L^2}\left\{\frac{1}{\cosh\Delta\tau + \cos\psi} + \frac{1}{\cosh\Delta\tau + \cos\psi^*}\right\}. \tag{3.174}$$

If we take the partial coincidence limit and keep points split in the τ-direction, then we have $\cos\psi = -1$ and $\cos\psi^* = \cos 2\rho$ and thus

$$\begin{aligned} G^E_{N,ESU}(\Delta\tau,\rho,\theta,\varphi) &= \frac{1}{8\pi^2 L^2}\left\{\frac{1}{\cosh\Delta\tau - 1} + \frac{1}{\cosh\Delta\tau + \cos 2\rho}\right\} \\ &= \frac{1}{8\pi^2 L^2}\left\{\frac{2}{\Delta\tau^2} + \left(\frac{1}{1+\cos 2\rho} - \frac{1}{6}\right)\right\} + \mathcal{O}(\Delta\tau^2). \end{aligned} \tag{3.175}$$

We need to renormalise this by subtracting the Hadamard parametrix $G_{S,ESU}(x,x')$. With points split in the temporal direction, the world function is given by $2\sigma = L^2\Delta\tau^2$ and the van Vleck-Morette determinant is $\Delta^{1/2} = 1 + \mathcal{O}(\Delta\tau^3)$ (see Appendix F), and therefore

$$G_{S,ESU}(\Delta\tau,\rho,\theta,\varphi) = \frac{\Delta^{1/2}}{8\pi^2\sigma} = \frac{1}{4\pi^2 L^2 \Delta\tau^2} + \mathcal{O}(\Delta\tau). \tag{3.176}$$

The renormalised VP on ESU with Neumann boundary conditions is therefore

$$\begin{aligned} \langle 0|\hat{\phi}^2_N|0\rangle_{ESU} &= \lim_{\Delta\tau\to 0}\left\{G^E_{N,ESU}(\Delta\tau,\rho,\theta,\varphi) - G_{S,ESU}(\Delta\tau,\rho,\theta,\varphi)\right\} \\ &= \frac{5-\cos 2\rho}{48\pi^2 L^2(1+\cos 2\rho)}. \end{aligned} \tag{3.177}$$

It should be noted that, whilst the vacuum expectation value with Neumann boundary conditions on CadS is a constant, this is not the case on ESU. This is because, although the Green's functions on CadS and ESU are conformally related, the Hadamard parametrices $G_{S,ESU}(x,x')$ and $G_S(x,x')$ are not. This can be seen by comparing (3.176) with (3.143).

The vacuum expectation value (3.177) is finite for all $0 \le \rho < \pi/2$, but diverges as ρ approaches $\pi/2$. If we write $\rho = \pi/2 - \epsilon$, then we can see that in the limit $\epsilon \to 0$,

$$\langle 0|\hat{\phi}^2_N|0\rangle_{ESU} = \frac{1}{16\pi^2 L^2 \epsilon^2} + \mathcal{O}(\epsilon^2). \tag{3.178}$$

This divergence as $\mathcal{O}(\epsilon^2)$ agrees with analysis performed in [114]. In [114], it is shown that $G^{E,(1)}_{\alpha,ESU}(x,x')$ (3.172) is expected to diverge as $\mathcal{O}(\epsilon^{-1})$ on the boundary, whilst all other terms are expected to be finite on the boundary. We can test this with an explicit evaluation of the integral (3.172) using the closed-form representation (3.174).

To perform this integral, we fix $\rho' = \pi/2$ so that $\cos\psi = \cos\psi^* = -\cos\gamma\sin\rho$. Then (3.174) becomes

$$G^E_{N,ESU}(\tau,\rho,\theta,\varphi;\tau',\pi/2,\theta',\varphi') = \frac{1}{4\pi^2 L^2}\frac{1}{\cosh\Delta\tau - \cos\gamma\sin\rho}. \tag{3.179}$$

Since $G^{E,(1)}_{\alpha,ESU}(x,x')$ is finite in the limit $x' \to x$, we set $x' = x$ and then

$$G^{E,(1)}_{\alpha,ESU}(x,x) = \frac{1}{16\pi^4 L^4} \int_{\mathscr{I}_{\pi/2}} \frac{1}{(\cosh \Delta\tau - \cos\gamma \sin\rho)^2} dS \tag{3.180}$$

where x is a general point in ESU with coordinates $(\tau, \rho, \theta, \varphi)$ and we take the integral over $y = (\tau_y, \pi/2, \theta_y, \varphi_y)$, where $\Delta\tau = \tau_y - \tau$ and γ is the geodesic distance (1.222) with $\theta' = \theta_y$ and $\Delta\varphi = \varphi_y - \varphi$. Without loss of generality, we can set $\theta = 0$, $\varphi = 0$ and then $\cos\gamma = \cos\theta_y$. Noting that $dS = L^3 \sin\theta_y \, d\Delta\tau \, d\theta_y \, d\varphi_y$, the integral becomes

$$\begin{aligned} G^{E,(1)}_{\alpha,ESU}(x,x') &= \frac{1}{16\pi^4 L} \int_{-\infty}^{\infty} d\Delta\tau \int_0^{\pi} d\theta_y \int_0^{2\pi} d\varphi_y \frac{\sin\theta_y}{(\cosh\Delta\tau - \cos\theta_y \sin\rho)^2} \\ &= \frac{1}{8\pi^3 L} \int_{-\infty}^{\infty} d\Delta\tau \int_0^{\pi} d\theta_y \frac{\sin\theta_y}{(\cosh\Delta\tau - \cos\theta_y \sin\rho)^2} \\ &= \frac{1}{4\pi^3 L} \int_{-\infty}^{\infty} d\Delta\tau \frac{1}{\cosh^2\Delta\tau - \sin^2\rho}. \end{aligned} \tag{3.181}$$

The integral (3.181) is regular for all $\Delta\tau$ when $0 \leq \rho < \pi/2$, but if $\rho = \pi/2$ then the integral is singular at $\Delta\tau = 0$. We can perform the integral for $0 < \rho < \pi/2$ by making the substitution $z \to \coth\Delta\tau$. Then

$$dz = -\operatorname{cosech}^2 \Delta\tau = (1 - \coth^2\Delta\tau) \, d\Delta\tau = (1 - z^2) \, d\Delta\tau. \tag{3.182}$$

The integral becomes

$$\int_{-\infty}^{\infty} \frac{d\Delta\tau}{\cosh^2\Delta\tau - \sin^2\rho} = 2 \int_1^{\infty} \frac{dz}{(z^2-1)(\cosh^2\Delta\tau - \sin^2\rho)} \tag{3.183}$$

where we have used the fact that the integrand is an even function to allow us to only consider half the integration region. From standard hyperbolic identities, we can write

$$\cosh^2\Delta\tau = \frac{z^2}{z^2-1} \tag{3.184}$$

and therefore, after some rearranging,

$$2 \int_1^{\infty} \frac{dz}{(z^2-1)\left(\frac{z^2}{z^2-1} - \sin^2\rho\right)} = \frac{2}{\cos^2\rho} \int_1^{\infty} \frac{dz}{z^2 + \tan^2\rho}. \tag{3.185}$$

Performing the integral,

$$\begin{aligned} \frac{2}{\cos^2\rho} \int_1^{\infty} \frac{dz}{z^2+\tan^2\rho} &= \frac{2}{\cos\rho\sin\rho} \left[\tan^{-1}\left(\frac{z}{\tan\rho}\right)\right]_1^{\infty} \\ &= \frac{2}{\cos\rho\sin\rho} \left[\frac{\pi}{2} - \tan^{-1}\left(\frac{1}{\tan\rho}\right)\right]. \end{aligned} \tag{3.186}$$

Using the fact that $\tan^{-1}(x) = \frac{\pi}{2} - \cot^{-1}(x)$, we find

$$G^{E,(1)}_{\alpha,ESU}(x,x) = \frac{1}{2\pi^3 L} \frac{\rho}{\sin\rho\cos\rho}. \tag{3.187}$$

As we approach the boundary, we write $\rho = \pi/2 - \epsilon$, and then

$$G^{E,(1)}_{\alpha,ESU}(x,x) = \frac{1}{4\pi^2 L\epsilon} + \mathcal{O}(1) \tag{3.188}$$

as $\epsilon \to 0$. The divergence as $\mathcal{O}(\epsilon^{-1})$ is as expected. Higher-order terms in (3.171) will be finite so we do not need to consider these terms in great detail. Using the conformal transformation (3.6) along with (3.171), we find in CadS

$$G^E_\alpha(x,x') = G^E_N(x,x') - L^{-1}\cos\rho\cos\rho'\cot\alpha \int_{\mathscr{I}_{\pi/2}} G^E_{N,ESU}(x,y) G^E_{N,ESU}(y,x')\ dS + ... \tag{3.189}$$

Renormalising and taking the limit $x' \to x$, we have

$$\langle 0|\hat{\phi}^2_\alpha|0\rangle = \langle 0|\hat{\phi}^2_N|0\rangle - L^{-1}\cos^2\rho\cot\alpha \int_{\mathscr{I}_{\pi/2}} G^E_{N,ESU}(x,y) G^E_{N,ESU}(y,x)\ dS + ... \tag{3.190}$$

Subsequent terms in the expansion are finite on the boundary and are multiplied by the conformal factor $\cos^2\rho$, which means that we do not need to consider these terms when looking in the limit $\rho \to \pi/2$. The integral in (3.190) will diverge as $\mathcal{O}(\epsilon^{-1})$ from (3.188). In (3.190), we multiply this integral by the conformal factor $\cos^2\rho$. Writing $\rho = \pi/2 - \epsilon$, we obtain $\cos^2\rho = \epsilon^2 + \mathcal{O}(\epsilon^3)$, and so, on the boundary,

$$\lim_{\rho\to\frac{\pi}{2}} \langle 0|\hat{\phi}^2_\alpha|0\rangle = \lim_{\rho\to\frac{\pi}{2}} \langle 0|\hat{\phi}^2_N|0\rangle = \frac{5}{48\pi^2 L^2}. \tag{3.191}$$

This completes the justification that, for all values of Robin parameter $\alpha \in (0, \alpha_{crit})$, the vacuum expectation values approach those for Neumann boundary conditions as $\rho \to \pi/2$. This is in agreement with our numerical results (see Figure 3.7).

It remains to show that we obtain similar behaviour at the boundary for thermal expectation values. We can use the method of [114] for thermal Euclidean Green's functions in ESU to write

$$G^E_{\beta,\alpha,ESU}(x,x') = G^E_{N,ESU}(x,x') - L^{-1}\cot\alpha \int_{\mathscr{I}_{\pi/2}} G^E_{N,ESU}(x,y) G^E_{\beta,\alpha,ESU}(y,x')\ dS. \tag{3.192}$$

This is obtained by using the same method as in equations (3.167-3.169), this time applied to $G^E_{\beta,\alpha,ESU}(x,x')$ instead of $G^E_{\alpha,ESU}(x,x')$. The similarities between (3.192) and (3.170) can be noted. The main point to notice is that the first term on the left-hand-side of (3.192) is the vacuum Green's function with Neumann boundary conditions imposed, rather than the thermal Green's function. Substituting $G^E_{\beta,\alpha,ESU}(y,x')$ in the integral, we obtain

$$G^E_{\beta,\alpha,ESU}(x,x') = G^E_{N,ESU}(x,x') - L^{-1}\cot\alpha \int_{\mathscr{I}_{\pi/2}} G^E_{N,ESU}(x,y) G^E_{N,ESU}(y,x')\ dS$$
$$+ L^{-2}\cot\alpha \int_{\mathscr{I}_{\pi/2}} G^E_{N,ESU}(x,y) \left[\int_{\mathscr{I}_{\pi/2}} G^E_{N,ESU}(y,z) G^E_{\beta,\alpha,ESU}(z,x')\ dS\right] dS \quad (3.193)$$

and repeating this, we again form an iterative expression similar to that given for the vacuum Green's function (3.170). We obtain the thermal Green's function in CadS by again performing the conformal transform (3.6), which gives us

$$G^E_{\beta,\alpha}(x,x') = G^E_N(x,x') - L^{-1}\cos\rho\cos\rho'\cot\alpha \int_{\mathscr{I}_{\pi/2}} G^E_{N,ESU}(x,y) G^E_{N,ESU}(y,x')\ dS + ... \quad (3.194)$$

Comparing the expression (3.194) with (3.189), we see that both have equivalent leading order terms. Other terms in the sum will vanish as $\rho \to \pi/2$ according to a similar argument as presented for the vacuum case, meaning that, as the boundary is approached, thermal expectation values will approach the same limit as vacuum expectation values. The first integral in (3.194) will not contribute at the boundary due to the conformal factor which vanishes when $\rho \to \pi/2$. This means that for thermal expectation values in CadS

$$\lim_{\rho\to\frac{\pi}{2}} \langle\beta|\hat{\phi}^2_\alpha|\beta\rangle = \lim_{\rho\to\frac{\pi}{2}} \langle 0|\hat{\phi}^2_N|0\rangle = \frac{5}{48\pi^2 L^2}. \quad (3.195)$$

This result again matches the behaviour we have observed in our numerical results (see Figures 3.9(b), (d) and (f)).

3.7 Summary

In this chapter, we have explored the effect of imposing Robin boundary conditions on the VP in the covering space of adS. The work covered in this chapter was based on [7]. We began by considering the classical field, with a brief look at transparent boundary conditions (3.18), before focusing our efforts on reflective boundary conditions (3.19-3.20).

When imposing Robin boundary conditions on these reflective modes (3.25), we found that some modes were unstable, depending on the value of the Robin parameter α. This can be seen by considering values of α in the quantization condition (3.24) that allow for imaginary frequency ω. This prompted us to only consider values of α which did not admit unstable modes, that is $\alpha \in [0, \alpha_{crit})$, where $\alpha_{crit} = -\tan^{-1}(\pi/2)$.

In section 3.3, we quantized our scalar field by promoting it to an operator (3.45), and then calculated the Wightman function G^+ with Robin boundary conditions imposed (3.49). We attempted to regularise by taking differences (see section 3.3.3), but problems arose due to the fact that the correct $i\epsilon$ prescription had not been employed.

The Wightman function simplified greatly for the cases of Dirichlet and Neumann conditions (see section 3.3.2), where results for the vacuum expectation values were found to be $\langle 0|\hat{\phi}^2_D|0\rangle_{ren} = -1/48\pi^2L^2$ and $\langle 0|\hat{\phi}^2_N|0\rangle_{ren} = 5/48\pi^2L^2$.

To evaluate the VP for Robin conditions, we moved to the Euclidean sector (see section 3.4), which involved transforming to the imaginary time coordinate $t \to i\tau$ (1.45). We began by looking at the Euclidean Green's functions with Dirichlet and Neumann boundary conditions imposed (3.120-3.123) to verify that results in the Lorentzian and Euclidean backgrounds are equivalent (see section 3.4.2).

We imposed Robin boundary conditions on the Euclidean Green's function via (3.117). To regularise our results, we subtracted the Euclidean Green's function with Dirichlet conditions imposed. Performing this subtraction in the Lorentzian background was difficult since both mode-sums have different frequency decomposition, but in the Euclidean section, the mode sums are the same (3.156).

The thermal Euclidean Green's function is found by imposing periodicity on τ (3.127). The thermal expectation values are renormalised by subtracting the Hadamard parametrix from the thermal Green's function and taking the coincidence limit, which leaves us with a finite value (3.155).

In section 3.5, we presented numerical results for the vacuum (Figure 3.7) and thermal (Figure 3.9) expectation values with Robin conditions imposed. From our numerical results, it appeared that all results approached the so-called "Neumann limit" $5/48\pi^2L^2$ at the boundary, apart from in the case when Dirichlet conditions were imposed.

In section 3.6, we showed analytically that all expectation values with $\alpha \neq 0$ did indeed approach the Neumann limit at the boundary. This was done by evaluating the vacuum expectation values on the boundary of CadS. To do this, we had to consider expectation values on ESU (3.170), since the boundary is not part of CadS. We used an iterative procedure to write the Euclidean vacuum Green's function with Robin boundary conditions imposed as a series of terms involving integrals over Euclidean vacuum Green's functions with Neumann boundary conditions imposed (3.171-3.173). After a conformal transformation to find the equivalent representation for the Euclidean Green's function at the boundary in CadS, we performed Hadamard renormalisation and took the coincidence limit to find vacuum expectation values (3.190). We were then able to show that, as the boundary was approached, all terms in the expansion vanished except the expectation values with Neumann conditions imposed. This allowed us to draw the conclusion that vacuum expectation values with Robin conditions imposed must approach the "Neumann limit" at the boundary (3.191). This conclusion agrees with numerical results given in Figure 3.7.

A similar calculation for thermal states resulted in us being able to write the thermal Euclidean Green's function with Robin boundary conditions imposed as a series of integrals over the vacuum Euclidean Green's function with Neumann boundary conditions imposed (3.192). Performing Hadamard renormalisation, taking the coincidence limit and looking close to the boundary, we were able to draw the same conclusions - that thermal expectation values with Robin conditions imposed must also approach the "Neumann limit" at the boundary (3.195). This matches numerical results given in Figure 3.9.

Part III

Black holes

Chapter 4

Topological black holes

In the second half of this thesis, we turn our attention to adS spacetimes with black holes. In this chapter, we introduce the concept of topological black holes along with conformal diagrams for the various black hole spacetimes.

4.1 Topological black hole spacetimes

The Schwarzschild-adS (SadS) and Reissner-Nordström-adS (RNadS) spacetimes are asymptotically adS spacetimes with black holes [107, 127–136]. In this section, we shall mainly discuss RNadS, but everything can be reduced to SadS by setting the charge parameter $Q = 0$. The metric in four dimensions is given by [127]

$$ds^2 = -f(r)dt^2 + f(r)^{-1}dr^2 + r^2 d\Omega_k^2 \tag{4.1}$$

where

$$f(r) = k - \frac{2M}{r} + \frac{Q^2}{r^2} + \frac{r^2}{L^2}. \tag{4.2}$$

The parameter k is discrete and can take the values $+1, -1$ or 0, M is the black hole mass, Q is the charge parameter and L is the adS lengthscale. The metric $d\Omega_k^2$ is the two-dimensional metric given by

$$d\Omega_k^2 = d\theta^2 + \mathcal{F}_k^2(\theta)d\varphi^2, \quad \mathcal{F}_k(\theta) = \begin{cases} \sin\theta, & k = 1 \\ \theta, & k = 0 \\ \sinh\theta, & k = -1. \end{cases} \tag{4.3}$$

For all k, the azimuthal coordinate $\varphi \in [0, 2\pi)$, whilst $\theta \in [0, \pi]$ when $k = 1$ and $\theta \in [0, \infty)$ when $k = 0, -1$.

Throughout the literature [107, 127–136], SadS (or RNadS) only refers to the $k = 1$ solution, with the $k = 0$ and $k = -1$ solutions seen as extensions to this solution. Throughout this thesis, however, we shall use the terminology "SadS" and "RNadS" to mean the entire set of $k = 1, 0, -1$ solutions rather than just the latter.

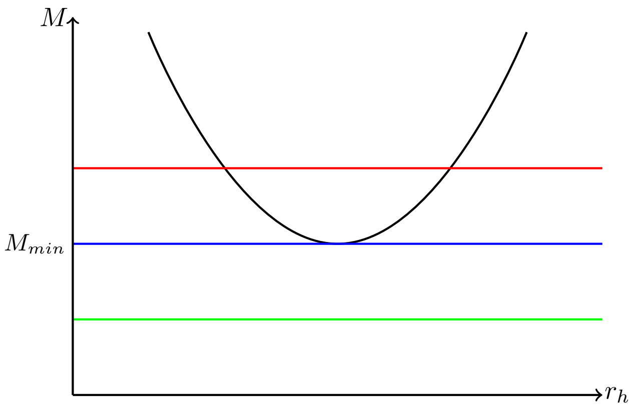

Figure 4.1: The quartic M (4.4) plotted against r_h. When we fix M at a value $M > M_{min}$ (red line), we have two distinct real roots of $f(r)$ (4.2). When we fix $M = M_{min}$ (blue line), we have one repeated real root, and when $M < M_{min}$ (green line) we have no real roots.

For all positive Q, L and all real M, we have a coordinate singularity at $r = 0$.

The black hole horizon is defined as the two-surface on which $r = r_h$, where $f(r_h) = 0$ for $r_h \in \mathbb{R}$. Since the polynomial $f(r)$ (4.2) is a quartic, we must have four roots. These roots cannot all be real as there is no r^3 term, but we can have two distinct real roots, two repeated real roots, or no real roots.

Rearranging (4.2) allows us to write M as a function of r_h, i.e.

$$M = \frac{r_h k}{2} + \frac{Q^2}{2r_h} + \frac{r_h^3}{2L^2}. \tag{4.4}$$

By looking at the first and second derivatives, that is

$$\frac{dM}{dr_h} = \frac{k}{2} - \frac{Q^2}{2r_h^2} + \frac{3r_h^2}{2L^2} \tag{4.5}$$

$$\frac{d^2M}{dr_h^2} = \frac{3r_h}{L^2} + \frac{Q^2}{r_h^3} \tag{4.6}$$

we can see that M must have a minimum value at

$$r_{h\ min}^2 = \frac{L^2}{6}\left(\sqrt{k^2 + 12\left(\frac{Q}{L}\right)^2} - k\right) \tag{4.7}$$

where we choose the positive root since $r_h^2 > 0$. Then the minimum mass is

$$M_{min} = \frac{L}{3\sqrt{6}}\left(\sqrt{k^2 + 12\left(\frac{Q}{L}\right)^2} + 2k\right)\left(\sqrt{k^2 + 12\left(\frac{Q}{L}\right)^2} - k\right)^{1/2} \tag{4.8}$$

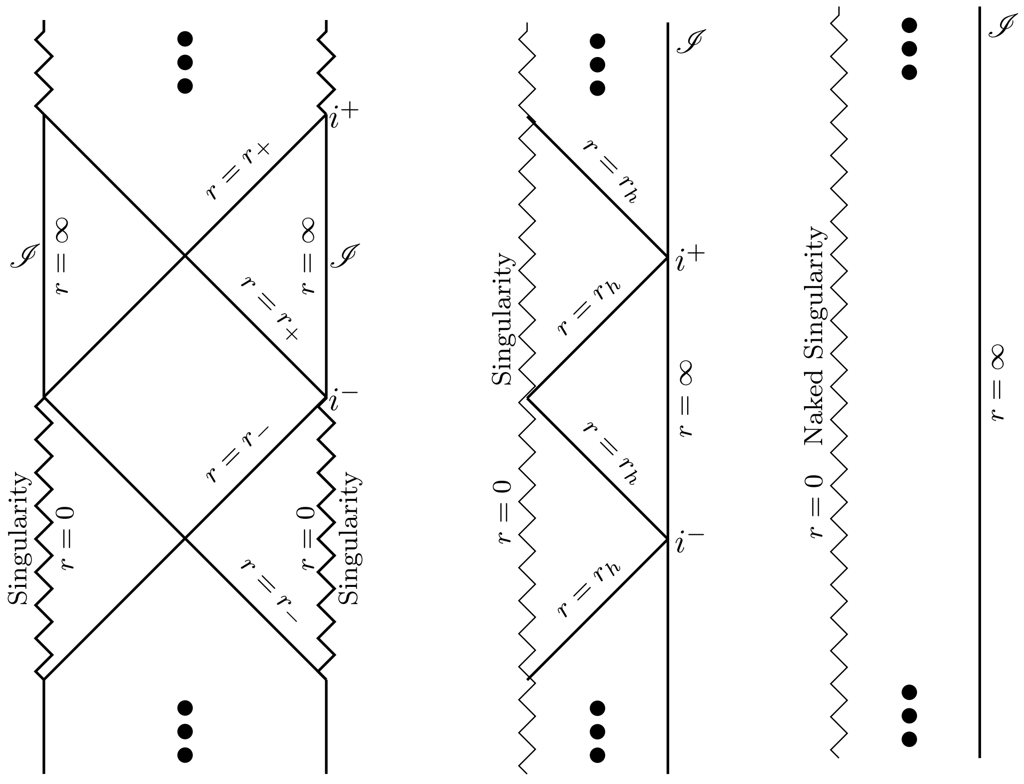

(a) Non-extremal (b) Extremal (c) Naked singularity

Figure 4.2: Conformal diagrams for RNadS black holes. All three cases have a curvature singularity at $r = 0$. The non-extremal black hole has inner horizon $r = r_-$ and outer horizon r_+, allowing for observers to pass through to another universe. The extremal black hole only has one horizon, and all observers that pass through it are lost to the singularity. In the final case, there is no horizon, and the singularity is naked. In (a) and (b), past and future timelike infinity are shown, denoted by i^- and i^+ respectively. The spacelike and null infinity coincide and is denoted by $\mathscr{I}$. In (c), spacelike, timelike and null infinity coincide on $\mathscr{I}$.

which is positive for $k = 1, 0$ but can be negative for $k = -1$. Therefore, in the case where $k = -1$, it is possible to have black holes of negative mass [135], whilst in $k = 1, 0$ we must have positive mass for all horizon radius values.

We now consider the following three cases: $M > M_{min}$ (see the red line in Figure 4.1), $M = M_{min}$ (blue line) and $M < M_{min}$ (green line). When $M > M_{min}$, we can find two real distinct roots to equation (4.2), and hence two horizons, the inner horizon r_- and outer horizon r_+. The conformal diagram in this case is shown in Figure 4.2a. As in adS and CadS, the spacetime is not globally hyperbolic.

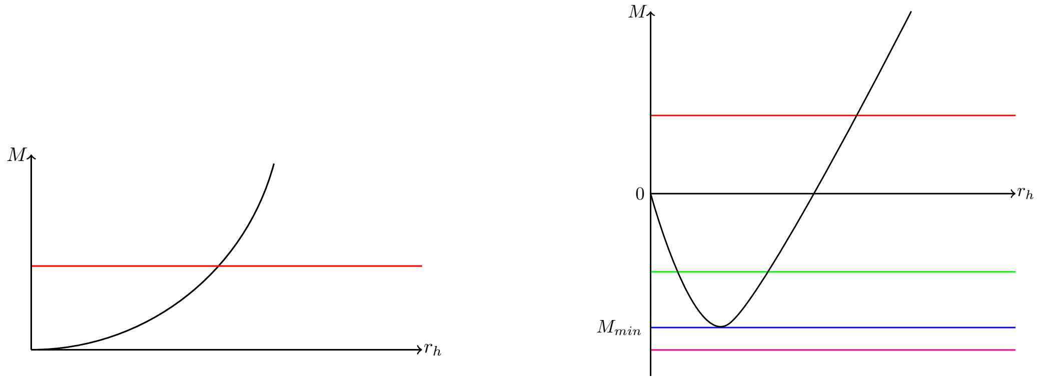

(a) Sketch of M against r_h in the cases $k = 1, 0$. In these cases we must have $M > 0$. The point $r_h = 0$ is a stationary point when $k = 0$ but not when $k = 1$. For all $M > 0$, we always find exactly one horizon (red line, for example).

(b) Sketch of M against r_h in the case $k = -1$. In this case, we can have negative mass. For $M > 0$, we find exactly one root of $f(r) = 0$ (e.g. red line). When $M_{min} < M < 0$, where M_{min} is given in (4.12), we find two distinct roots (e.g. green line). For $M = M_{min}$ (blue line), we have one repeated root, and when $M < M_{min}$ (magenta line), then we have no roots.

Figure 4.3: Plots of M against r_h.

For $M = M_{min}$, there is only one real repeated root to (4.2). In this case, the inner and outer horizons coincide i.e. $r_- = r_+ = r_h$. This case describes an extremal black hole - it is the smallest possible black hole that can exist for a given charge. A horizon does not exist in the case where $M < M_{min}$ and we have a naked singularity. The conformal diagrams for these two cases are given in Figure 4.2b and 4.2c respectively.

We now consider the event horizons in SadS, that is, when $Q = 0$. Now $f(r)$ is a cubic, and, in similar fashion to before, we write M as a function of r_h, i.e.

$$M(r_h) = \frac{r_h^3}{2L^2} + \frac{kr_h}{2}. \tag{4.9}$$

Differentiating and setting equal to zero we find that stationary points are given by

$$r_h^2 = -\frac{kL^2}{3}. \tag{4.10}$$

Then, when $k = 1$, we do not have any stationary points, and when $k = 0$, we have a point of inflection at $r_h = 0$. This means that, in these two cases, we have exactly one solution to $f(r_h) = 0$ for all $M > 0$, i.e. we have exactly one horizon (see Figure 4.3a). The conformal diagram is then given by Figure 4.4.

Things are a little different for the case $k = -1$. Now we have a stationary point (minimum) at

$$r_{h\ min} = \frac{L}{\sqrt{3}}, \tag{4.11}$$

where we assume $r_h > 0$. This corresponds to

$$M_{min} = -\frac{L}{3\sqrt{3}}. \tag{4.12}$$

This gives us four different cases (see Figure 4.3b). These are as follows:

- $M < M_{min}$. Here, $f(r) = 0$ has no roots, so we have a naked singularity. The conformal diagram is given in Figure 4.2c.
- $M = M_{min}$. Now $f(r) = 0$ has one repeated root, so we have an extremal black hole, with conformal diagram given by Figure 4.2b.
- $M_{min} < M < 0$. We have two distinct real roots to $f(r) = 0$, and hence the conformal diagram is given by Figure 4.2a.
- $M > 0$. The equation $f(r) = 0$ has only one non-degenerate root, so we have the same conformal diagram as for the $k = 0, 1$ SadS black holes, shown in Figure 4.4.

In [135], it is shown that hyperbolic black holes of negative mass can still admit an event horizon and have positive temperature, which means that regions of negative energy can still undergo gravitational collapse to a black hole. From here on, we shall only consider SadS black holes of positive mass, with conformal diagram shown in Figure 4.4.

One of the earliest discussions of asymptotically adS black holes was in [137], where Hawking and Page considered thermodynamical properties of black holes with a negative cosmological constant. They showed that asymptotically adS black holes have a natural temperature T associated with the surface gravity κ, where

$$T = \frac{\kappa}{2\pi}, \quad \kappa = \frac{1}{2}f'(r_h) = \frac{M}{r_h^2} + \frac{r_h}{L^2} = \frac{kL^2 + 3r_h^2}{2r_hL^2}, \tag{4.13}$$

where we have used (4.9). The analysis of [137] is concerned only with the $k = 1$ case, where they show that there exists a minimum temperature

$$T_{min}^{k=1} = \frac{\sqrt{3}}{2\pi L} \tag{4.14}$$

when the event horizon $r_h = r_0 = 3^{-1/2}L$. For $r_h > r_0$, the temperature increases with mass.

We now turn our attention to the geometry of the event horizon in order to understand exactly what happens to the black holes when we vary the parameter k. These black

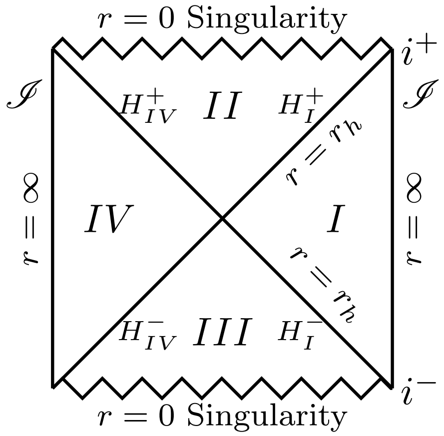

Figure 4.4: The conformal diagram for the SadS black hole with positive mass. There exists an event horizon at $r = r_h$, and a curvature singularity at $r = 0$. The regions are labelled I-IV. Region I is the exterior spacetime, II the black hole interior, III the white hole interior, and IV the parallel universe. Future and past timelike infinities are denoted by i^+ and i^- respectively. Null and spacelike infinities coincide and are denoted by $\mathscr{I}$.

holes are often referred to in the literature as “topological” black holes [107], and from the following discussion, it is easy to understand why. The horizon geometry can be determined by looking at the induced metric on the $r = const., t = const.$ hypersurface (which we shall denote by Σ_k.) In RNadS/SadS, this induced metric is given by $d\Omega_k$ (4.1). For each value of k, the metric $d\Omega_k$ leads to a different topology for Σ_k.

For the $k = 1$ case, Σ_1 has the local isometry group $SO(3)$, i.e. spherical rotational symmetry. The event horizon is the two-sphere S^2 with the round metric [127] and bears close resemblance to the standard Schwarzschild black hole. For the $k = 0$ case, Σ_0 has local isometry group E^2, i.e. flat translation and rotational symmetry. The horizon in this case is $\mathbb{R}^2$ with the flat metric. This is a flat plane. For the $k = -1$ case, Σ_{-1} has local isometry group $SO_c(2,1)$. This is the connected space of hyperbolic Lorentz transforms. The horizon topology is that of the hyperbolic plane, $\mathbb{H}^2$.

The correspondence between spherical adS black holes and CFT is discussed in [94], where Witten uses adS/CFT to give a holographic explanation for the Bekenstein-Hawking entropy of these black holes. This is extended to topological black holes in [107], where the entropy scales holographically in the correct manner, again providing holographic interpretations of the entropy formula.

We can compactify event horizons in the $k = 0, -1$ cases [138]. Let us begin with the $k = 0$ case, the flat black hole. We can form compact surfaces by tessellating the

Euclidean plane, taking a region of the plane (which we call the fundamental domain) and imposing periodic boundary conditions. This effectively “glues” the edges of the fundamental domain together to create different surfaces. In the Euclidean plane, geodesics are straight lines, and so the plane becomes a grid of quadrilaterals (see Figure 4.5). We select two non-parallel shifts that generate the geodesics, and identify all points connected by these discrete translations (this is our fundamental domain). We can glue the opposite edges of this domain together to form our compact surface. In this way, we can form a cylinder, torus, Klein bottle or Möbius strip [128,130,131,139,140]. However, in order for our integrals in the scalar product to be defined, we must have an orientable spacetime, so we cannot quantize over the Klein bottle or Möbius strip using our usual conventions.

There are infinitely many different types of fundamental domain for the hyperbolic plane. The periodic structure can be thought of as a crystal lattice, and the fundamental domains that we form will be polygons. In order for us to “glue” the sides together suitably, our polygons must be $2n$-gons. The simplest case is the octagon (see Figure 4.6). By setting periodic boundary conditions so that opposite sides are “glued” together, we can form a two-hole torus, which is a compact, hyperbolic surface (see [136] for a visual representation of this compactification). We can form higher genus surfaces by looking at $2n$-gons for higher n.

In chapter 5, we shall quantise on these topological black holes, to see how horizon topology affects quantum modes throughout the spacetime, but we shall not consider compactifications for $k = 0, -1$.

4.2 Classical scalar field on topological black holes

A scalar field ϕ satisfies the homogeneous Klein-Gordon equation (1.56). We consider scalar fields of mass $m = 0$ and coupling $\xi = 1/6$.

Mode solutions of this equation take the form

$$\phi_{\omega\ell m}(t, r, \theta, \varphi) = e^{i\omega t}\mathcal{N}_{\omega\ell}X_{\omega\ell}(r)Z_{\ell m}(\theta, \varphi) \tag{4.15}$$

where ω is the frequency, ℓ is a separation constant and m is an integer. The angular function $Z_{\ell m}(\theta, \varphi)$ is

$$Z_{\ell m}(\theta, \varphi) = \begin{cases} Y_{\ell m}(\theta, \varphi), & k = 1, \\ J_m(\ell\theta)e^{im\varphi}, & k = 0, \\ P^{|m|}_{-\frac{1}{2}+i\ell}(\cosh\theta)e^{im\varphi}, & k = -1. \end{cases} \tag{4.16}$$

The separation constant ℓ is a discrete variable when $k = 1$, taking any non-negative integer value. When $k = 1$, the angular function $Z_{\ell m}(\theta, \varphi)$ is the spherical harmonics $Y_{\ell m}(\theta, \varphi)$. For $k = 0, -1$, the separation constant ℓ is a continuous variable and takes

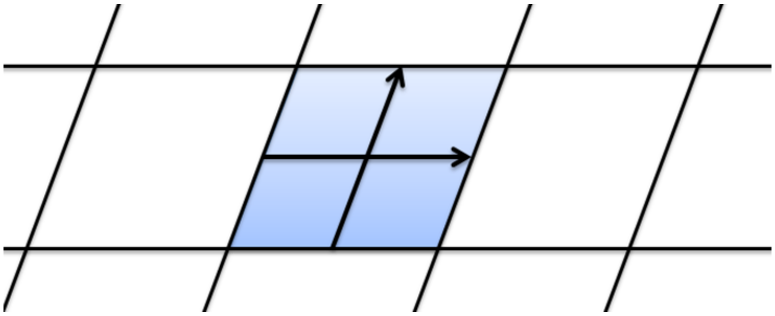

Figure 4.5: Geodesics in the Euclidean plane are straight lines. Two discrete non-parallel shifts are shown by the arrows, and these determine a fundamental domain, shown in blue.

any value in the interval $[0, \infty)$. We obtain Bessel functions $J_m(\ell\theta)$ when $k = 0$ and conical functions $P^{|m|}_{-\frac{1}{2}+i\ell}(\cosh\theta)$ when $k = -1$.

The radial function $X_{\omega\ell}(r)$ satisfies the equation

$$\left\{\frac{d}{dr}\left(r^2 f(r)\frac{d}{dr}\right) - \frac{\omega^2 r^2}{f(r)} - \nu_\ell^{(k)} - \frac{r^2}{6}R\right\} X_{\omega\ell}(r, r') = 0 \tag{4.17}$$

for

$$\nu_\ell^{(k)} = \left[\ell + \frac{1}{4}k(k+1)\right]^2 - \frac{1}{4}k. \tag{4.18}$$

The radial function $X_{\omega\ell}(r)$ must have boundary conditions imposed at $r \to \infty$ in order for the quantum field theory to be well-defined. In chapter 5, we impose Dirichlet boundary conditions on $X_{\omega\ell}(r)$ (5.29). In chapter 6, we extend this to general Robin boundary conditions (6.1).

The constant $\mathcal{N}_{\omega\ell}$ is determined by normalising the modes.

To quantise, we promote the scalar field ϕ to an operator $\hat{\phi}$. Quantization on SadS black holes was first explored in [10]. Flachi and Tanaka focus on the calculation of the VP $\langle\hat{\phi}^2\rangle$ in the spherical black hole case, performing renormalisation via the point-splitting procedure of Christensen [3, 41]. In their analysis, they impose Dirichlet boundary conditions at the spacetime boundary. Their numerical results show that, for spherical black holes, the VP is monotonically decreasing as radius r increases, and approaches the CadS vacuum expectation value $-1/48\pi^2 L^2$ (3.2) at the boundary.

In chapter 5, we shall use the extended coordinates method [11, 12] to renormalise the VP with Dirichlet boundary conditions applied. This is then extended to include Robin boundary conditions in chapter 6.

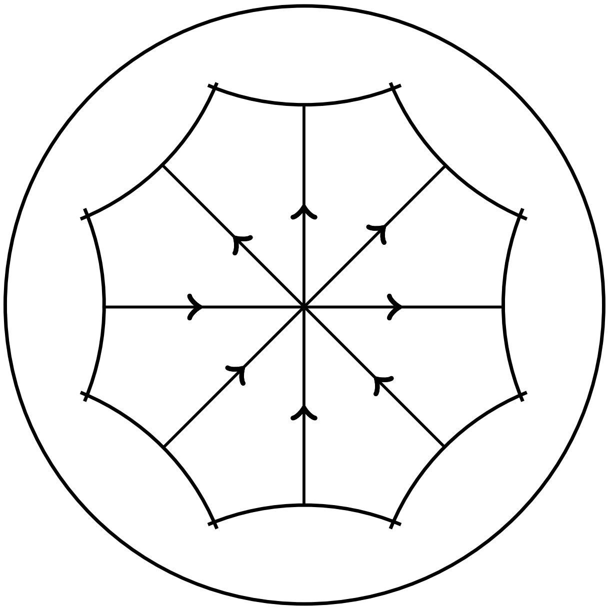

Figure 4.6: A regular octagon formed in the Poincaré disc. When opposite sides are identified as demonstrated, a two-hole torus is formed.

Chapter 5

Quantum field theory on topological black holes

In this chapter we discuss quantum field theory on topological black holes , or Schwarzschild-adS (SadS). These were discussed in chapter 4, where we described three different types of solutions, spherical, flat and hyperbolic. These solutions were distinguished via the parameter k, which can take the values $k = 1, 0$ and -1, corresponding to the spherical, flat and hyperbolic black holes respectively.

In this chapter, we calculate the renormalised VP for conformally coupled, massless scalar fields on all three backgrounds. We begin in section 5.1 by reparametrising the metric. The reparametrisation will prove useful when we plot the results of the renormalised VP. We also discuss (section 5.2) the scaling symmetries present in the $k = 0$ metric, which will make calculations on the flat black hole background much simpler.

In section 5.3, we solve the wave equation to find the Euclidean Green's function in SadS. This has a different form depending on the event horizon topology. We impose Dirichlet boundary conditions on the scalar field modes. This is extended to general Robin boundary conditions in chapter 6.

We calculate the renormalised VP (section 5.4) on each of these backgrounds using the extended coordinates method, first discussed in section 1.3.4. This involves writing the Hadamard parametrix in a mode-sum representation that is similar to the Euclidean Green's function, to allow us to perform the subtraction mode-by-mode. This means that we must find three different representations for the Hadamard parametrix, each corresponding to a different value of k.

Details of the numerical procedures carried out in `Mathematica` are given in section 5.5. In section 5.6, we present numerical results for all three cases, with varying black hole temperature and event horizon radius. The work in this chapter is based on [8].

This work was recently extended [13] to include scalar fields of varying mass and coupling on adS black holes with spherical horizon. This work is discussed in section 5.7, where we also discuss how one may extend this to include adS black holes with flat and hyperbolic horizons.

5.1 Reparametrisation of the metric

Our analysis in this chapter will take place on the Euclideanised background of SadS. The vacuum state is therefore the Hartle-Hawking state. On the Euclidean background, the wave equation (1.58) is elliptic, and so its solutions are unique once appropriate boundary conditions have been imposed. The Euclideanised metric for SadS is

$$ds^2 = f(r)d\tau^2 + f(r)^{-1}dr^2 + r^2 d\Omega_k^2 \tag{5.1}$$

where

$$f(r) = k - \frac{2M}{r} + \frac{r^2}{L^2} \tag{5.2}$$

and $d\Omega_k^2$ is given by (4.3). The parameter k can take the value $+1, 0, -1$, corresponding to positive, zero or negative event horizon curvature, as discussed in chapter 4.

It is helpful to reparametrise the metric using the dimensionless coordinate η, where

$$\eta = \frac{4\chi^2 + k}{M} r - 1 \tag{5.3}$$

for χ defined implicitly via

$$\chi L(4\chi^2 + k) = M. \tag{5.4}$$

Note that, in the $k = -1$ case, since $L, M > 0$, we must have $\chi > 1/2$. The metric (5.1) now takes the form

$$ds^2 = \bar{f}(\eta)d\tau^2 + \frac{\chi^2 L^2 d\eta^2}{\bar{f}(\eta)} + \chi^2 L^2 (\eta + 1)^2 d\Omega_k^2, \tag{5.5}$$

where

$$\bar{f}(\eta) = f(r) = \frac{\eta - 1}{\eta + 1} h(\eta), \quad h(\eta) = k + \chi^2(\eta^2 + 4\eta + 7). \tag{5.6}$$

The event horizon radius $r = r_h$ is then fixed at $\eta = 1$ regardless of the values of k, M and L. The curvature singularity at $r = 0$ is located at $\eta = -1$. For $k = 1, 0$ the function $h(\eta)$ has no real roots. For $k = -1$, the function $h(\eta)$ has no real roots provided $\chi^2 > 1/4$, so we restrict to $\chi^2 \in (1/4, \infty)$ in this case.

We can now parametrise our black holes by (k, χ, M) rather than (k, L, M). In terms of χ, the surface gravity and Ricci scalar can be written

$$\kappa = \frac{1}{2} f'(r_h) = \frac{1}{4M}(12\chi^2 + k)(4\chi^2 + k), \tag{5.7}$$

$$R = -\frac{12}{L^2} = -\frac{12\chi^2(4\chi^2 + k)^2}{M^2}. \tag{5.8}$$

This reparametrisation will be useful when we calculate numerical results for the renormalised VP in section 5.6.

5.2 Scaling symmetries of the $k = 0$ metric

When $k = 1$ or $k = -1$, the metric has two natural length scales. These are the radius of curvature of adS and the curvature of the horizon. We can fix one and vary the other to give different solutions.

This is not the case when $k = 0$ due to vanishing event horizon curvature. Here, we only have one length scale - the cosmological constant. We cannot keep the horizon radius fixed and vary the cosmological constant since changing one automatically affects the other (this can be seen from (5.4), by fixing χ and varying L).

We look at the following scaling symmetries of the $k = 0$ metric. In the first case, we fix χ (5.4) and vary M using an arbitrary scaling constant $\tilde{\rho}_1$, which is equivalent to

$$\eta \to \eta, \quad L \to \tilde{\rho}_1 L, \quad M \to \tilde{\rho}_1 M, \quad \chi \to \chi, \quad \tau \to \tilde{\rho}_1 \tau. \tag{5.9}$$

From this, we find

$$f(\eta) \to f(\eta) \tag{5.10}$$

and then the line element

$$ds^2 \to \tilde{\rho}_1^2 ds^2 \tag{5.11}$$

supposing $\theta \to \theta, \varphi \to \varphi$. We find that

$$\kappa \to \tilde{\rho}_1^{-1} \kappa, \quad R \to \tilde{\rho}_1^{-2} R. \tag{5.12}$$

The second scaling we look at involves fixing M and varying χ, again using an arbitrary scaling constant $\tilde{\rho}_2$, i.e.

$$\eta \to \eta, \quad L \to \tilde{\rho}_2^{-3} L, \quad M \to M, \quad \chi \to \tilde{\rho}_2 \chi. \tag{5.13}$$

In this case, we have

$$f(\eta) \to f(\eta) \tag{5.14}$$

and the metric is invariant if we have

$$\tau \to \tilde{\rho}_2^{-4} \tau, \ \theta \to \tilde{\rho}_2^{-1} \theta, \ \varphi \to \varphi. \tag{5.15}$$

With this rescaling, we find

$$\kappa \to \tilde{\rho}_2^4 \kappa, \quad R \to \tilde{\rho}_2^6 R. \tag{5.16}$$

5.3 Quantum scalar fields on SadS

In this section we find the Euclidean Green's function G^E in SadS. The Euclidean Green's function for a massless, conformally coupled scalar field satisfies the inhomogeneous Klein-Gordon equation

$$\left(\Box - \frac{1}{6} R\right) G^E(\tau, r, \theta, \varphi; \tau', r', \theta', \varphi') = -\frac{1}{r^2} \delta(\tau - \tau') \delta(r - r') \delta(\Omega_k, \Omega_k') \tag{5.17}$$

where

$$\delta(\Omega_k,\Omega_k') = \frac{1}{\mathcal{F}_k(\theta)}\delta(\theta-\theta')\delta(\varphi-\varphi') \tag{5.18}$$

and $\mathcal{F}_k(\theta)$ is given by (4.3). We incorporate periodicity in τ by setting, for any $\kappa > 0$,

$$\delta(\tau-\tau') = \frac{\kappa}{2\pi}\sum_{n=-\infty}^{\infty} e^{in\kappa\Delta\tau}, \tag{5.19}$$

where $\Delta\tau = \tau-\tau'$. It then makes sense to search for solutions of (5.17) of the form

$$G^E(\tau,r,\theta,\varphi;\tau',r',\theta',\varphi') = \frac{\kappa}{2\pi}\sum_{n=-\infty}^{\infty} e^{in\kappa\Delta\tau}\mathcal{G}_n^{(k)}(r,\theta,\varphi;r',\theta',\varphi'). \tag{5.20}$$

From the analysis performed in Appendix G, we find $\mathcal{G}_n^{(k)}$ to have the following form in each case:

$$\mathcal{G}_n^{(1)} = \frac{1}{4\pi}\sum_{\ell=0}^{\infty}(2\ell+1)P_\ell(\cos\gamma_S)X_{n\ell}^{(k)}(r,r'), \tag{5.21}$$

$$\mathcal{G}_n^{(0)} = \frac{1}{2\pi}\int_{\ell=0}^{\infty}\ell J_0(\ell\gamma_R)X_{n\ell}^{(k)}(r,r')\,d\ell, \tag{5.22}$$

$$\mathcal{G}_n^{(-1)} = \frac{1}{2\pi}\int_{\ell=0}^{\infty}\ell\tanh(\ell\pi)P_{-\frac{1}{2}+i\ell}(\cosh\gamma_H)X_{n\ell}^{(k)}(r,r')\,d\ell, \tag{5.23}$$

where $X_{n\ell}^{(k)}(r,r')$ is the radial Green's function satisfying

$$\left\{\frac{d}{dr}\left(r^2 f(r)\frac{d}{dr}\right) - \frac{n^2\kappa^2 r^2}{f(r)} - \nu_\ell^{(k)} - \frac{r^2}{6}R\right\}X_{n\ell}^{(k)}(r,r') = -\delta(r-r') \tag{5.24}$$

where $\nu_\ell^{(k)}$ is defined in (4.18). The quantity $\{\gamma_S,\gamma_R,\gamma_H\}$ is the geodesic distance on the sphere, flat plane and hyperbolic plane, defined by

$$\cos\gamma_S = \cos\theta\cos\theta' + \sin\theta\sin\theta'\cos(\varphi-\varphi'), \tag{5.25}$$

$$\gamma_R^2 = \frac{1}{2}\left(\theta^2+\theta'^2-2\theta\theta'\cos(\varphi-\varphi')\right), \tag{5.26}$$

$$\cosh\gamma_H = \cosh\theta\cosh\theta' - \sinh\theta\sinh\theta'\cos(\varphi-\varphi'). \tag{5.27}$$

Note that we have already met γ_S before, defined in (1.222). In order to numerically solve this ODE (5.24), we can write the radial function in the same way as we did in ESU (3.96), that is

$$X_{n\ell}^{(k)}(r,r') = \mathcal{N}_{n\ell}p_{n\ell}(r_<)q_{n\ell}(r_>) \tag{5.28}$$

for $r_< = \min\{r,r'\}$, $r_> = \max\{r,r'\}$. The functions $p_{n\ell}$ and $q_{n\ell}$ are both solutions of the homogeneous version of (5.24), although $p_{n\ell}$ has regularity conditions imposed on the horizon, and $q_{n\ell}$ has appropriate conditions imposed on the boundary. In this chapter, we shall only consider Dirichlet conditions imposed on $q_{n\ell}$ as $r\to\infty$, but in the next chapter, we shall extend this to Neumann and Robin conditions. As $r \to \infty$, we insist

$$\Omega \; q_{n\ell}(r, r') = 0, \tag{5.29}$$

where Ω is the conformal factor relating SadS to ESU. Note that this is not equivalent to (2.10), which is the conformal factor relating CadS to ESU. The conformal factor relating SadS to ESU is not known in closed form but is known in certain limits - see equation (6.2). The inclusion of the conformal factor in (5.29) is due to imposing the boundary conditions in ESU and then performing a conformal transform to obtain mode solutions in SadS, as we did in CadS in section 3.2.

The normalisation constant $\mathcal{N}_{n\ell}$ is determined by the Wronskian relation,

$$\mathcal{N}_{n\ell} = -\frac{1}{r^2 f(r) W\{p_{n\ell}(r), q_{n\ell}(r)\}}. \tag{5.30}$$

This can be seen by integrating the radial equation (5.24) over r for $r \in [r' - \delta, r' + \delta]$ for some $\delta > 0$. We then take the limit $\delta \to 0$. This is very similar to the method used in section 3.4.1. Performing this procedure on the right-hand-side of (5.24) we obtain

$$-\lim_{\delta \to 0} \int_{r'-\delta}^{r'+\delta} \delta(r - r') dr = -1. \tag{5.31}$$

Performing this procedure on the left-hand-side of (5.24), we obtain

$$\lim_{\delta' \to 0} \int_{r'-\delta}^{r'+\delta} \left\{ \left[-\frac{n^2 \kappa^2 r^2}{f(r)} - \nu_\ell^{(k)} - \frac{r^2}{6} R \right] X_{n\ell}^{(k)} + \frac{d}{dr} \left(r^2 f(r) \frac{dX_{n\ell}^{(k)}}{dr} \right) \right\} dr$$
$$= \lim_{\delta \to 0} \left[r^2 f(r) \frac{dX_{n\ell}^{(k)}}{dr} \right]_{r'-\delta}^{r'+\delta}, \tag{5.32}$$

where the first terms in the integral vanish in the limit following a similar procedure to (3.109). Putting (5.31, 5.32) together, we find

$$-1 = r^2 f(r) \mathcal{N}_{n\ell} W\{p_{n\ell}(r) q_{n\ell}(r)\} \tag{5.33}$$

which gives us the desired definition of the normalisation constant (5.30).

Under the first scaling symmetry (5.9), the radial equation (5.24), and thus the radial functions $p_{n\ell}, q_{n\ell}$ remain unchanged. The normalisation constant (5.30) scales as

$$\mathcal{N}_{n\ell} \to \tilde{\rho}_1^{-2} \mathcal{N}_{n\ell}. \tag{5.34}$$

Under the second scaling symmetry (5.13), the radial equation (5.24) again remains unchanged, as does the normalisation constant (5.30), that is

$$\mathcal{N}_{n\ell} \to \mathcal{N}_{n\ell}. \tag{5.35}$$

5.4 Renormalisation of vacuum polarisation

We perform Hadamard renormalisation on the Euclidean Green's function by subtracting the Hadamard parametrix (1.192) and then taking the coincidence limit. This method of renormalisation is described in section 1.3.2. In order to perform this renormalisation quickly and efficiently, we use the extended coordinates method (see section 1.3.4 as well as [11, 12]). Since we are working in the massless, conformally coupled case, we can ignore the tail terms of the Hadamard parametrix (given by $V(x,x')$ in equation (1.192)). In section 5.7, we shall comment on the complexities involved with finding the correct representation for $V(x,x')$ on topological black hole backgrounds.

The extended coordinates method (section 1.3.4) requires us to write the direct part of the Hadamard parametrix as a series in "extended coordinates" (w,s). In order to do this, we must write both the world function $\sigma(x,x')$ and the van Vleck-Morette determinant $\Delta(x,x')$ as a series in (w,s), as in equations (1.220) and (1.223) respectively. The definitions of (w,s), given in (1.221), will be slightly different depending on the curvature of the background.

Writing the direct part of the Hadamard parametrix in this way allows us to find a mode-sum representation for the Hadamard parametrix that matches the mode-sum representation for the Green's function (5.20-5.23). Then the subtraction (1.232) can be carried out mode-by-mode, where each individual mode is manifestly finite, making for much faster convergence of numerical results.

In this section, we first focus on writing the world function $\sigma(x,x')$ and the van-Vleck Morette determinant $\Delta(x,x')$ as a series in (w,s), before finding closed-form expressions for the regularisation parameters $\Psi_{n\ell}(i,j|r)$ that allow us to write G_S as a mode-sum of the same form as G^E.

We write the world function $\sigma(x,x')$ (1.179) as a series in our "extended coordinates" (w,s), i.e.

$$\sigma(x,x') = \sum_{i,j,k=0}^{\infty} \sigma_{ijk}(r) w^i \Delta r^j s^k \tag{5.36}$$

where

$$w^2 = \frac{2}{\kappa^2}(1-\cos\kappa\Delta\tau), \quad s^2 = \begin{cases} f(r)w^2 + 2r^2(1-\cos\gamma_S), & k=1 \\ f(r)w^2 + 2r^2\gamma_R^2, & k=0 \\ f(r)w^2 + 2r^2(\cosh\gamma_H - 1), & k=-1. \end{cases} \tag{5.37}$$

The extended coordinates are formally treated as $\mathcal{O}(\epsilon) \sim \mathcal{O}(\Delta x)$ quantities. To leading order,

$$\sigma(x,x') = \frac{1}{2}\epsilon^2(s^2 + (\Delta r)^2/f) + \mathcal{O}(\epsilon^3). \tag{5.38}$$

This means we can set $\sigma_{000} = \sigma_{100} = \sigma_{010} = \sigma_{001} = 0$. We can then substitute the expansion (5.36) into the defining equation (1.180) and equate coefficients of powers of

ϵ in order to find the $\sigma_{ijk}(r)$. We expand the van Vleck-Morette determinant $\Delta(x,x')$ in a similar way,

$$\Delta^{1/2}(x,x') = \sum_{ijk} u_{ijk}(r) w^i \Delta r^j s^k \tag{5.39}$$

and substitute into (1.184) to find the coefficients u_{ijk}. To do this, we must calculate $\Box\sigma$ - see Appendix H. From calculations in `Mathematica`, we find that, for all cases of k, to leading order,

$$\begin{aligned} G_S(x,x') = \frac{1}{8\pi^2}\Bigg(& \frac{2}{s^2+f(r)^{-1}(\Delta r)^2} + \frac{w^2\Delta r(2f(r)-rf'(r))}{r(s^2+f(r)^{-1}(\Delta r)^2)^2} \\ & + \frac{(\Delta r)^3(2f(r)+rf'(r))}{rf(r)^2(s^2+f(r)^{-1}(\Delta r)^2)^2} - \frac{2\Delta r}{r(s^2+f(r)^{-1}(\Delta r)^2)}\Bigg) + \mathcal{O}(1). \end{aligned} \tag{5.40}$$

We now point-split in temporal and angular directions, taking $\Delta r \to 0$. The direct part of the Hadamard parametrix can now be expanded in the following way:

$$\frac{\Delta^{1/2}}{\sigma} = \sum_{i=0}^{m}\sum_{j=-i}^{i} \mathcal{D}_{ij}(r)\frac{w^{2i+2j}}{s^{2j+2}} + \mathcal{O}(\epsilon^{2m}) \tag{5.41}$$

where the coefficients $\mathcal{D}_{ij}(r)$ are listed in Table 5.1 for $i = 0, 1, 2$. We require our Hadamard parametrix to have a mode-sum representation corresponding to the appropriate representation for the Euclidean Green's function. This will allow us to perform our subtraction mode-by-mode when calculating $\langle\hat{\phi}^2\rangle_{ren}$.

In the direct part of the parametrix, when $j < 0$, all terms are polynomial in w and s and so vanish when the coincidence limit is taken. It is not necessary to look for mode-sum expansions for these terms. For $j \geq 0$, there exist some terms that are distributionally subtle at coincidence. For example, w^6/s^4 is $\mathcal{O}(\epsilon^2)$ which tends to 0 when $\Delta x \to 0$. However, we must include these terms to speed up the convergence of the mode-sum. This is because these terms capture more of the high frequency behaviour of the Green's function. We now find a mode-sum representation for the direct part of the Hadamard parametrix, considering each type of horizon one at a time.

5.4.1 Spherical horizons

To find a mode-sum representation of the Hadamard parametrix in the spherical $k = 1$ case, we assume the terms $\frac{w^{2i+2j}}{s^{2j+2}}$ have a mode-sum representation corresponding to (5.20, 5.21), i.e.

$$\frac{w^{2i+2j}}{s^{2j+2}} = \sum_{n=-\infty}^{\infty} e^{in\kappa\Delta\tau}\sum_{\ell=0}^{\infty}(2\ell+1)P_\ell(\cos\gamma_S)\Psi_{n\ell}(i,j|r) \tag{5.42}$$

for some regularisation parameters $\Psi_{n\ell}(i,j|r)$. We need to invert (5.42) to obtain an expression for these regularisation parameters. We multiply both sides by $e^{-in'\kappa\Delta\tau}P_{\ell'}(\cos\gamma_S)$

i	j	$\mathcal{D}_{ij}$
0	0	2
1	-1	$-\frac{f'}{6r}$
	0	$\frac{kf}{6r^2} - \frac{f^2}{6r^2} + \frac{ff'}{6r} - \frac{1}{12}ff''$
	1	$-\frac{f(r)^2f'(r)}{6r} + \frac{1}{24}f(r)f'(r)^2 - \frac{kf(r)^2}{6r^2} + \frac{f(r)^3}{6r^2} - \frac{1}{6}\kappa^2 f(r)$
2	-2	$\frac{k^2}{240r^4} - \frac{f^2}{240r^4} - \frac{kf'}{72r^3} + \frac{ff'}{180r^3} + \frac{7f'^2}{720r^2} + \frac{ff''}{80r^2}$
	-1	$\frac{kff'}{72r^3} + \frac{f^2f'}{360r^3} - \frac{f^2f''}{60r^2} + \frac{7ff'f''}{360r} + \frac{f^2f^{(3)}}{120r}$
	0	$\frac{k\kappa^2 f}{72r^2} + \frac{k^2f^2}{720r^4} - \frac{\kappa^2f^2}{72r^2} - \frac{kf^3}{36r^4} + \frac{19f^4}{720r^4} + \frac{\kappa^2ff'}{72r} + \frac{kf^2f'}{36r^3} - \frac{19f^3f'}{360r^3} - \frac{kff'^2}{288r^2} + \frac{43f^2f'^2}{1440r^2} - \frac{ff'^3}{288r}$ $-\frac{1}{144}\kappa^2ff'' - \frac{kf^2f''}{144r^2} + \frac{7f^3f''}{360r^2} - \frac{7f^2f'f''}{360r} + \frac{1}{576}ff'^2f'' + \frac{1}{320}f^2f''^2 - \frac{f^3f^{(3)}}{120r} + \frac{1}{240}f^2f'f^{(3)}$
	1	$-\frac{1}{45}\kappa^4 f - \frac{k\kappa^2f^2}{24r^2} - \frac{7k^2f^3}{360r^4} + \frac{\kappa^2f^3}{24r^2} + \frac{kf^4}{18r^4} - \frac{13f^5}{360r^4} - \frac{\kappa^2f^2f'}{24r} - \frac{kf^3f'}{18r^3} + \frac{13f^4f'}{180r^3} + \frac{1}{144}\kappa^2ff'^2 + \frac{kf^2f'^2}{96r^2}$ $-\frac{67f^3f'^2}{1440r^2} + \frac{f^2f'^3}{96r} - \frac{ff'^4}{2880} + \frac{1}{144}\kappa^2f^2f'' + \frac{kf^3f''}{144r^2} - \frac{11f^4f''}{720r^2} + \frac{11f^3f'f''}{720r} - \frac{11f^2f'^2f''}{2880}$
	2	$\frac{1}{72}\kappa^4f^2 + \frac{k\kappa^2f^3}{36r^2} + \frac{k^2f^4}{72r^4} - \frac{\kappa^2f^4}{36r^2} - \frac{kf^5}{36r^4} + \frac{f^6}{72r^4} + \frac{\kappa^2f^3f'}{36r} + \frac{kf^4f'}{36r^3} - \frac{f^5f'}{36r^3} - \frac{1}{144}\kappa^2f^2f'^2 - \frac{kf^3f'^2}{144r^2} + \frac{f^4f'^2}{48r^2} - \frac{f^3f'^3}{144r} + \frac{f^2f'^4}{1152}$

Table 5.1: The coefficients $\mathcal{D}_{ij}$ for $i = 0, 1, 2$. All derivatives of the function f are with respect to r.

and integrate over $\cos\gamma_S$ and $\Delta\tau$. Using the orthogonality relation for the Legendre functions [120, eq. 14.17.6] and standard completeness relations for exponentials, we obtain

$$\Psi_{n\ell}(i,j|r) = \frac{\kappa}{4\pi}\int_{\Delta\tau=0}^{2\pi/\kappa}\int_{\cos\gamma_S=-1}^{1} e^{-in\kappa\Delta\tau}P_\ell(\cos\gamma_S)\frac{w^{2i+2j}}{s^{2+2j}}d(\cos\gamma_S)\ d\Delta\tau \tag{5.43}$$

where it should be noted that

$$s^2 = 2r^2(z-\cos\gamma_S), \quad z = 1+\frac{f(r)}{r^2\kappa^2}(1-\cos\kappa\Delta\tau). \tag{5.44}$$

We calculate the integral over $\cos\gamma_S$ first. Using Neumann's integral [120, eq. 14.12.13] we can write

$$Q_\ell(z) = \frac{1}{2}\int_{\cos\gamma_S=-1}^{1}\frac{P_\ell(\cos\gamma_S)}{z-\cos\gamma_S}d(\cos\gamma_S). \tag{5.45}$$

Differentiating with respect to z,

$$\frac{d}{dz}Q_\ell(z) = -\frac{1}{2}\int_{\cos\gamma_S=-1}^{1}\frac{P_\ell(\cos\gamma_S)}{(z-\cos\gamma_S)^2}d(\cos\gamma_S). \tag{5.46}$$

We can repeat this step j times to obtain

$$\frac{d^j}{dz^j}Q_\ell(z) = \frac{(-1)^j j!}{2}\int_{\cos\gamma_S-1}^{1}\frac{P_\ell(\cos\gamma_S)}{(z-\cos\gamma_S)^{1+j}}d(\cos\gamma_S). \tag{5.47}$$

Using (5.47) in (5.43), and substituting in our expression for w (5.37), we find

$$\Psi_{n\ell}(i,j|r) = \frac{\kappa}{4\pi}\frac{2^i(-1)^j}{\kappa^{2i+2j}r^{2+2j}j!}\int_{\Delta\tau=0}^{2\pi/\kappa} e^{in\kappa\Delta\tau}(1-\cos\kappa\Delta\tau)^{i+j}\left(\frac{d}{dz}\right)^j Q_\ell(z)\ d\Delta\tau. \tag{5.48}$$

We set

$$\mu_1 = \sqrt{1+\frac{f(r)}{\kappa^2 r^2}}, \tag{5.49}$$

so that

$$z = \mu_1^2(1-\cos\kappa\Delta\tau)-\cos\kappa\Delta\tau \tag{5.50}$$

and therefore

$$\frac{d}{dz} = \frac{1}{2(1-\cos\kappa\Delta\tau)}\left(\frac{1}{\mu_1}\frac{\partial}{\partial\mu_1}\right). \tag{5.51}$$

The ordinary derivatives become partial derivatives since z depends on both μ_1 and $\Delta\tau$. Using (5.51), the regularisation parameters (5.48) become

$$\Psi_{n\ell}(i,j|r) = \frac{\kappa}{4\pi}\frac{2^{i-j}(-1)^j}{\kappa^{2i+2j}r^{2+2j}j!}\left(\frac{1}{\mu_1}\frac{\partial}{\partial\mu_1}\right)^j\int_0^{2\pi/\kappa} e^{-in\kappa\Delta\tau}(1-\cos\kappa\Delta\tau)^i Q_\ell(z)\ d\Delta\tau \tag{5.52}$$

where we can differentiate with respect to μ_1 after performing the integral, since μ_1 and $\Delta\tau$ are independent. The problem that we now have is that z depends on both μ_1

and $\Delta\tau$, so in order to integrate over $\Delta\tau$, we need to separate out the dependence in $Q_\ell(z)$. We do this by using [120, eq. 14.18.5],

$$\begin{aligned}&Q_\nu(\cosh\xi_1\ \cosh\xi_2 - \sinh\xi_1\ \sinh\xi_2\ \cos\phi)\\ &\quad= P_\nu(\cosh\xi_1)Q_\nu(\cosh\xi_2) + 2\sum_{m=1}^{\infty}(-1)^m P_\nu^{-m}(\cosh\xi_1)Q_\nu^m(\cosh\xi_2)\cos(m\phi)\end{aligned} \tag{5.53}$$

where $\xi_1, \xi_2 \in \mathbb{R}_{>0}$ and $\phi, \nu \in \mathbb{R}$. By replacing $\cosh\xi_1, \cosh\xi_2 \to \mu_1$, $\phi \to \kappa\Delta\tau$, $\nu \to \ell$, this allows us to write (5.52) as

$$\begin{aligned}\Psi_{n\ell}(i,j|r) &= \frac{\kappa}{4\pi}\frac{2^{i-j}(-1)^j}{\kappa^{2i+2j}r^{2+2j}j!}\left(\frac{1}{\mu_1}\frac{\partial}{\partial\mu_1}\right)^j\int_0^{2\pi/\kappa} e^{-in\kappa\Delta\tau}(1-\cos\kappa\Delta\tau)^i\\ &\quad\times\left[P_\ell(\mu_1)Q_\ell(\mu_1) + 2\sum_{m=1}^{\infty}(-1)^m P_\ell^{-m}(\mu_1)Q_\ell^m(\mu_1)\cos(m\kappa\Delta\tau)\right]d\Delta\tau.\end{aligned} \tag{5.54}$$

We now evaluate the integral over $\Delta\tau$,

$$\begin{aligned}I &= \int_0^{2\pi/\kappa} e^{-in\kappa\Delta\tau}(1-\cos\kappa\Delta\tau)^i\cos(m\kappa\Delta\tau)\ d\Delta\tau\\ &= \frac{1}{\kappa}\int_0^{2\pi} e^{-inx}(1-\cos x)^i\cos(mx)\ dx\\ &= \frac{1}{\kappa}\int_0^{2\pi} e^{-inx}\left(2\sin^2\frac{x}{2}\right)^i\cos(mx)\ dx\\ &= \frac{2^i}{\kappa}\int_0^{2\pi} e^{-inx}\left(\frac{e^{ix/2}-e^{-ix/2}}{2i}\right)^{2i}\frac{e^{imx}+e^{-imx}}{2}\ dx\\ &= \frac{(-1)^i}{2^{i+1}\kappa}\int_0^{2\pi} e^{-inx}\sum_{p=0}^{2i}(e^{ix/2})^p(-e^{-ix/2})^{2i-p}\binom{2i}{p}[e^{imx}+e^{-imx}]\ dx\\ &= \frac{1}{2^{i+1}\kappa}\sum_{p=0}^{2i}\binom{2i}{p}(-1)^{i-p}\left[\int_0^{2\pi} e^{i[-i+p-n+m]x}\ dx + \int_0^{2\pi} e^{i[-i+p-n-m]x}\ dx\right]\\ &= \frac{\pi}{2^i\kappa}\sum_{p=0}^{2i}\binom{2i}{p}(-1)^{i-p}[\delta_{p,i+n-m}\Theta(i+n-m)\Theta(i-n+m)\\ &\qquad\qquad + \delta_{p,i+n+m}\Theta(i+n+m)\Theta(i-n-m)]\end{aligned} \tag{5.55}$$

where we have used the Binomial Theorem in the third line, and in the final line we have introduced the Heaviside function Θ to ensure that we remain within the limits of the summation. Performing the summation, we obtain

$$\begin{aligned}I = \frac{\pi}{2^i\kappa}&\left[(-1)^{-n+m}\binom{2i}{i+n-m}\Theta(i+n-m)\Theta(i-n+m)\right.\\ &\left.+(-1)^{-n-m}\binom{2i}{i+n+m}\Theta(i+n+m)\Theta(i-n-m)\right].\end{aligned} \tag{5.56}$$

Using the definition of the binomial coefficients, and some standard relations for Gamma functions [120, eq. 5.5.5], we arrive at

$$I = \frac{\sqrt{\pi}}{\kappa}\ i!\ 2^i\ \Gamma\left(i+\frac{1}{2}\right)\left[(-1)^{n-m}\frac{\Theta(i+n-m)\Theta(i-n+m)}{(i-n+m)!(i+n-m)!}\right. \\ \left. +(-1)^{n+m}\frac{\Theta(i+n+m)\Theta(i-n-m)}{(i-n-m)!(i+n+m)!}\right]. \tag{5.57}$$

Note that the first integral in (5.54) is simply given by (5.57) with $m \to 0$. Substituting (5.57) into (5.54), we have

$$\Psi_{n\ell}(i,j|r) = \frac{2^{2i-j-1} i!\Gamma\left(i+\frac{1}{2}\right)(-1)^{n+j}}{\sqrt{\pi}\kappa^{2i+2j}r^{2+2j}j!}\left(\frac{1}{\mu_1}\frac{\partial}{\partial\mu_1}\right)^j\left[\frac{P_\ell(\mu_1)Q_\ell(\mu_1)}{(i-n)!(i+n)!}\right. \\ \left. +\sum_{m=\max\{1,n-i\}}^{i+n}\frac{P_\ell^{-m}(\mu_1)Q_\ell^m(\mu_1)}{(i-n+m)!(i+n-m)!}+\sum_{m=\max\{1,-i-n\}}^{i-n}\frac{P_\ell^{-m}(\mu_1)Q_\ell^m(\mu_1)}{(i-n-m)!(i+n+m)!}\right]. \tag{5.58}$$

Rearranging the summations and using formulae for Gamma functions, we obtain

$$\Psi_{n\ell}(i,j|r) = \frac{2^{i-j}i!(2i-1)!!(-1)^{n+j}}{\kappa^{2i+2j}r^{2j+2}j!}\sum_{m=n-i}^{n+i}\left(\frac{1}{\mu_1}\frac{\partial}{\partial\mu_1}\right)^j\frac{P_\ell^{-|m|}(\mu_1)Q_\ell^{|m|}(\mu_1)}{(i-n+m)!(i+n-m)!} \tag{5.59}$$

where the double factorial is defined by [120, eq. 5.4.2]

$$x!! = \begin{cases} 2^{n/2}\Gamma(\frac{1}{2}n+1), & n \text{ even}, \\ \pi^{-1/2}2^{(n+1)/2}\Gamma(\frac{1}{2}n+1), & n \text{ odd}. \end{cases} \tag{5.60}$$

We arrive at this result by taking $m \to -m$ in the second summation in (5.58).

5.4.2 Flat horizons

In the flat $k = 0$ case, we assume the following mode-sum representation, corresponding to (5.20, 5.22):

$$\frac{w^{2i+2j}}{s^{2+2j}} = \sum_{n=-\infty}^{\infty} e^{in\kappa\Delta\tau}\int_{\ell=0}^{\infty}\ell J_0(\ell\gamma_R)\Psi_{n\ell}(i,j|r)\ d\ell \tag{5.61}$$

where $\Psi_{n\ell}(i,j|r)$ are again regularisation parameters for which we seek an analytic representation. We invert (5.61) to write $\Psi_{n\ell}(i,j|r)$ in closed form. We multiply both sides by $e^{-in'\kappa\Delta\tau}\gamma_R J_0(\ell'\gamma_R)$ and integrate over γ_R and $\Delta\tau$ using the completeness relation [120, eq. 1.17.13]. We obtain

$$\Psi_{n\ell}(i,j|r) = \frac{\kappa}{2\pi}\int_{\Delta\tau=0}^{2\pi/\kappa}\int_{\gamma_R=0}^{\infty}\gamma_R e^{-in\kappa\Delta\tau}J_0(\ell\gamma_R)\frac{w^{2i+2j}}{s^{2+2j}}\ d\gamma_R\ d\Delta\tau \tag{5.62}$$

where we note

$$s^2 = 2r^2(z^2 + \gamma_R^2), \quad z^2 = \frac{f(r)}{\kappa^2 r^2}(1 - \cos\kappa\Delta\tau). \tag{5.63}$$

The integral over γ_R can be performed using [141, eq. 6.532(4)],

$$\int_0^\infty \frac{\gamma_R J_0(\ell\gamma_R)}{(z^2 + \gamma_R^2)} d\gamma_R = K_0(\ell z) \tag{5.64}$$

where K_0 is the modified Bessel function. Differentiating this statement j times with respect to z, we have

$$\int_0^\infty \frac{(-1)^j j! \gamma_R J_0(\ell\gamma_R)}{(z^2 + \gamma_R^2)^{j+1}} d\gamma_R = \frac{d^j}{dz^j} K_0(\ell z). \tag{5.65}$$

With

$$\mu_0 = \sqrt{\frac{f(r)}{\kappa^2 r^2}}, \tag{5.66}$$

we can write

$$z^2 = 2\mu_0^2(1 - \cos\kappa\Delta\tau). \tag{5.67}$$

It is helpful to write z as $z = \lim_{\mu_0' \to \mu_0} \left[\mu_0^2 + \mu_0'^2 - 2\mu_0\mu_0' \cos\kappa\Delta\tau\right]$, which then allows us to use [142, eq. 11.3.8] to write

$$K_0(\ell\sqrt{\mu_0^2 + \mu_0'^2 - 2\mu_0\mu_0'\cos\kappa\Delta\tau}) = \sum_{m=-\infty}^{\infty} I_m(\ell\mu_0)K_m(\ell\mu_0')\cos(m\kappa\Delta\tau). \tag{5.68}$$

Taking the limit $\mu_0' \to \mu_0$, we obtain

$$K_0(\ell z) = \sum_{m=-\infty}^{\infty} I_m(\ell\mu_0)K_m(\ell\mu_0)\cos(m\kappa\Delta\tau). \tag{5.69}$$

Finally, we can note

$$\frac{d}{dz} = \frac{1}{2(1 - \cos\kappa\Delta\tau)}\left(\frac{1}{\mu_0}\frac{\partial}{\partial\mu_0}\right). \tag{5.70}$$

Using (5.65, 5.69, 5.70) in (5.62), we obtain

$$\Psi_{n\ell}(i,j|r) = \frac{\kappa}{4\pi}\frac{2^{i-j}(-1)^j}{\kappa^{2i+2j}r^{2+2j}j!}\left(\frac{1}{\mu_0}\frac{\partial}{\partial\mu_0}\right)^j \int_0^{2\pi/\kappa} e^{-in\kappa\Delta\tau}(1-\cos\kappa\Delta\tau)^i \times \sum_{m=-\infty}^{\infty} I_m(\ell\mu_0)K_m(\ell\mu_0)\cos(m\kappa\Delta\tau)d\Delta\tau. \tag{5.71}$$

The integral over $\Delta\tau$ is then exactly the same as in (5.55). Evaluating this integral and then using standard relations for Gamma functions as before, we obtain

$$\Psi_{n\ell}(i,j|r) = \frac{2^{i-j-1}i!(2i-1)!!(-1)^{n+j}}{\kappa^{2i+2j}r^{2j+2}j!}\sum_{m=n-i}^{n+i}\left(\frac{1}{\mu_0}\frac{\partial}{\partial\mu_0}\right)^j \frac{(-1)^m I_m(\ell\mu_0)K_m(\ell\mu_0)}{(i-n+m)!(i+n-m)!}. \tag{5.72}$$

Under the first scaling symmetry (5.9), it is important to note that the regularisation parameters (5.72) scale as

$$\mathcal{D}_{ij}(r) \to \tilde{\rho}_1^{-2i}\mathcal{D}_{ij}(r), \quad \Psi_{n\ell}(i,j|r) \to \tilde{\rho}_1^{2i-2}\Psi_{n\ell}(i,j|r), \tag{5.73}$$

whilst under the second scaling symmetry (5.13), the regularisation parameters (5.72) scale as

$$\mathcal{D}_{ij}(r) \to \tilde{\rho}_2^{8i+2j}\mathcal{D}_{ij}(r), \quad \Psi_{n\ell}(i,j|r) \to \tilde{\rho}_2^{4-2j-8i}\Psi_{n\ell}(i,j|r). \tag{5.74}$$

5.4.3 Hyperbolic horizons

We now consider the hyperbolic $k=-1$ case, where we assume the extended coordinates have the mode-sum representation

$$\frac{w^{2i+2j}}{s^{2+2j}} = \sum_{n=-\infty}^{\infty} e^{in\kappa\Delta\tau}\int_{\ell=0}^{\infty} \ell\tanh(\ell\pi)P_{-\frac{1}{2}+i\ell}(\cosh\gamma_H)\Psi_{n\ell}(i,j|r)\;d\ell \tag{5.75}$$

corresponding to (5.20, 5.23). To invert the above equation, we multiply both sides by $e^{-in'\kappa\Delta\tau}P_{-\frac{1}{2}+i\ell'}(\cosh\gamma_H)$, and integrate over $\cosh\gamma_H$ and $\Delta\tau$ using the completeness relation that we derived in (G.41). We obtain

$$\Psi_{n\ell}(i,j|r) = \frac{\kappa}{2\pi}\int_{\Delta\tau=0}^{2\pi/\kappa}\int_{\cosh\gamma_H=1}^{\infty} e^{-in\kappa\Delta\tau}P_{-\frac{1}{2}+i\ell}(\cosh\gamma_H)\frac{w^{2i+2j}}{s^{2+2j}}\;d(\cosh\gamma_H)\;d\Delta\tau \tag{5.76}$$

where

$$s^2 = 2r^2(z+\cosh\gamma_H), \quad z = -1+\frac{f(r)}{\kappa^2r^2}(1-\cos\kappa\Delta\tau). \tag{5.77}$$

The range of z is $z\in[-1,\frac{2f(r)}{r^2\kappa^2}-1]$. We integrate over $\cosh\gamma_H$ first. From [120, eq. 14.20.13], we can write

$$P_{-\frac{1}{2}+i\ell}(z) = \frac{\cosh(\ell\pi)}{\pi}\int_1^{\infty}\frac{P_{-\frac{1}{2}+i\ell}(\cosh\gamma_H)}{z+\cosh\gamma_H}\;d(\cosh\gamma_H) \tag{5.78}$$

which is valid for $z\geq -1$. Differentiating (5.78) j times with respect to z, we find

$$\frac{d^j}{dz^j}P_{-\frac{1}{2}+i\ell}(z) = \frac{\cosh(\ell\pi)}{\pi}j!(-1)^j\int_1^{\infty}\frac{P_{-\frac{1}{2}+i\ell}(\cosh\gamma_H)}{(z+\cosh\gamma_H)^{j+1}}\;d(\cosh\gamma_H). \tag{5.79}$$

We define

$$\mu_{-1} = \sqrt{1-\frac{f(r)}{\kappa^2r^2}}, \tag{5.80}$$

so that

$$\frac{d}{dz} = -\frac{1}{2(1-\cos\kappa\Delta\tau)}\left(\frac{1}{\mu_{-1}}\frac{\partial}{\partial\mu_{-1}}\right). \tag{5.81}$$

The regularisation parameters (5.76) can then be written as

$$\Psi_{n\ell}(i,j|r) = \frac{\kappa}{4}\frac{2^{i-j}}{\kappa^{2i+2j}r^{2+2j}j!\cosh(\pi\ell)}\left(\frac{1}{\mu_{-1}}\frac{\partial}{\partial\mu_{-1}}\right)^j \times \int_0^{2\pi/\kappa} e^{-in\kappa\Delta\tau}(1-\cos\kappa\Delta\tau)^i P_{-\frac{1}{2}+i\ell}(z)\, d\Delta\tau. \quad (5.82)$$

The parameter z depends on both $\Delta\tau$ and μ_{-1}, so we need to factor out the time-dependence in order to perform the integral. We can use the addition theorem [120, eq. 14.18.1] to write

$$P_\nu(-\cos\psi\cos\psi' - \sin\psi\sin\psi'\cos\kappa\Delta\tau) = \sum_{m=-\infty}^{\infty} P_\nu^{-m}(-\cos\psi)P_\nu^m(\cos\psi')\cos(m\kappa\Delta\tau). \quad (5.83)$$

To use this relation in (5.82), we need to set $\cos\psi = \cos\psi' = \mu$. The addition theorem above assumes $0 < \psi' < \psi < \pi$ and does not converge in the limit $\psi' \to \psi$. This is different from the $k = 1, 0$ cases where the addition theorems involved convergent sums. The convergence properties turn out to be irrelevant, however, since the time integral makes all terms in the infinite sum vanish except for the finite range where $m \in \{n-i, ..., n+i\}$. If we were to approach this calculation rigorously, we would have to keep ψ' distinct from ψ and not take the limit until after the time integral has been performed. However, the result is the same if we set $\psi' = \psi$ immediately after applying the addition theorem. Following this method gives

$$\Psi_{n\ell}(i,j|r) = \frac{\kappa}{4}\frac{2^{i-j}}{\kappa^{2i+2j}r^{2+2j}j!\cosh(\pi\ell)}\left(\frac{1}{\mu_{-1}}\frac{\partial}{\partial\mu_{-1}}\right)^j \sum_{m=-\infty}^{\infty} P^{-m}_{-\frac{1}{2}+i\ell}(-\mu_{-1})P^{m}_{-\frac{1}{2}+i\ell}(\mu_{-1}) \times \int_0^{2\pi/\kappa} e^{-in\kappa\Delta\tau}(1-\cos\kappa\Delta\tau)^i \cos(m\kappa\Delta\tau)\, d\Delta\tau. \quad (5.84)$$

The time integral is then identical to (5.55), and so

$$\Psi_{n\ell}(i,j|r) = \frac{\pi 2^{i-j-1} i!(2i-1)!!(-1)^n}{\kappa^{2i+2j}r^{2+2j}j!\cosh(\pi\ell)} \sum_{m=n-i}^{n+i}\left(\frac{1}{\mu_{-1}}\frac{\partial}{\partial\mu_{-1}}\right)^j \times \frac{(-1)^m P^{-m}_{-\frac{1}{2}+i\ell}(-\mu_{-1})P^{m}_{-\frac{1}{2}+i\ell}(\mu_{-1})}{(i-n+m)!(i+n-m)!}. \quad (5.85)$$

5.4.4 General result

Here we summarise the results obtained in the previous subsections 5.4.1 - 5.4.3. For each type of event horizon topology that we consider, the Hadamard parametrix can be written as a mode-sum representation of the form

$$G_S(\Delta\tau,\gamma,r) = \frac{1}{8\pi^2}\sum_{n=-\infty}^{\infty} e^{in\kappa\Delta\tau}\int_0^\infty d\ell\, \mathcal{P}_\ell(\gamma)\sum_{i=0}^{2}\sum_{j=0}^{i}\mathcal{D}_{ij}(r)\Psi_{n\ell}(i,j|r) - \frac{f'(r)}{48\pi^2 r} \quad (5.86)$$

where the coefficients $\mathcal{D}_{ij}(r)$ are given in Table 5.1, γ is taken to be either $\{\gamma_S, \gamma_R, \gamma_H\}$ depending on the case under consideration, and we have

$$\mathcal{P}_\ell(\gamma) = \begin{cases} (\ell + \frac{1}{2}) P_\ell(\cos \gamma_S), & k = 1, \\ \ell J_0(\ell \gamma_R), & k = 0, \\ \ell \tanh(\pi \ell) P_{-\frac{1}{2}+i\ell}(\cosh \gamma_H), & k = -1. \end{cases} \tag{5.87}$$

In the $k = 1$ case, the integral over the ℓ modes is understood to be a summation over non-negative integer ℓ. The regularisation parameters are given by

$$\Psi_{n\ell}(i, j|r) = \frac{2^{i-j} i! (2i-1)!! (-1)^n}{\kappa^{2i+2j} r^{2j+2} j!} \sum_{m=n-i}^{n+i} \left(\frac{1}{\mu_k} \frac{\partial}{\partial \mu_k} \right)^j \frac{\mathcal{R}_{m\ell}(\mu_k)}{(i-n+m)!(i+n-m)!} \tag{5.88}$$

with

$$\mathcal{R}_{m\ell}(\mu_k) = \begin{cases} (-1)^j P_\ell^{-|m|}(\mu_1) Q_\ell^{|m|}(\mu_1), & k = 1, \\ \\ \frac{1}{2}(-1)^{j+m} I_m(\ell\mu_0) K_m(\ell\mu_0), & k = 0, \\ \\ \frac{\pi}{2\cosh(\pi\ell)} (-1)^{n+m} P^{-m}_{-\frac{1}{2}+i\ell}(-\mu_{-1}) P^{m}_{-\frac{1}{2}+i\ell}(\mu_{-1}), & k = -1, \end{cases} \tag{5.89}$$

and, from (5.49, 5.66, 5.80), μ_k is defined by

$$\mu_k = \sqrt{\left| k + \frac{f(r)}{\kappa^2 r^2} \right|}. \tag{5.90}$$

5.5 Numerical calculation

In this section, we discuss the process of numerically calculating both the radial functions $p_{n\ell}, q_{n\ell}$ (5.28) and the regularisation parameters $\Psi_{n\ell}(i, j|r)$ (5.88) in the Hadamard parametrix.

The radial functions $p_{n\ell}, q_{n\ell}$ (5.28) are found by solving the homogeneous version of (5.24). These solutions cannot be found analytically, so we use `Mathematica`'s `NDSolve` function to find them numerically. We approximate both $p_{n\ell}$ and $q_{n\ell}$ using Frobenius series solutions to give us appropriate initial conditions for this numerical integration.

Beginning near the regular singular point $r = r_h$, we can rewrite (5.24) as

$$\frac{d^2}{dr^2} p_{n\ell}(r) + u_h(r) \frac{d}{dr} p_{n\ell}(r) - v_h(r) p_{n\ell}(r) = 0 \tag{5.91}$$

where

$$u_h(r) = \frac{2}{r} + \frac{f'(r)}{f(r)}, \quad v_h(r) = \frac{R}{6f(r)} + \frac{n^2\kappa^2}{f(r)^2} - \frac{\nu_\ell}{r^2 f(r)}. \tag{5.92}$$

We search for a Frobenius series solution of the form

$$p_{n\ell}(r \sim r_h) \simeq \sum_{j=0}^{\infty} a_j (r - r_h)^{\alpha_1 + j}, \tag{5.93}$$

where α_1, a_j are constants. From Appendix I, we find

$$\alpha_1 = \pm \frac{n}{2}. \tag{5.94}$$

Since $p_{n\ell}$ must be regular on the horizon, we must have $\alpha_1 > 0$, so we set

$$\alpha_1 = \left| \frac{n}{2} \right|. \tag{5.95}$$

Near the boundary, it is useful to write $r = s^{-1}$, so that $s \in (0, r_h^{-1})$ and $s \to 0$ as $r \to \infty$. The radial equation (5.24) can now be written in the form

$$\frac{d^2}{ds^2} q_{n\ell}(s) + u_\infty(s) \frac{d}{ds} q_{n\ell}(s) - v_\infty(s) q_{n\ell}(s) = 0 \tag{5.96}$$

where

$$u_\infty(s) = \frac{1}{f(s)} \frac{df}{ds}, \quad v_\infty(s) = \frac{R}{6 f(s) s^4} + \frac{n^2 \kappa^2}{f(s)^2 s^4} - \frac{\nu_\ell}{f(s) s^2}. \tag{5.97}$$

We now search for a Frobenius series solution in s, that is

$$q_{n\ell}(s \sim 0) \simeq \sum_{j=0}^{\infty} b_j s^{\alpha_2 + j} \tag{5.98}$$

where α_2, b_j are constants. From Appendix I, we find

$$\alpha_2 = \frac{3}{2} \pm \frac{1}{2} \sqrt{9 + \frac{2L^2}{3} R}. \tag{5.99}$$

In SadS, the Ricci curvature scalar is given by

$$R = -\frac{12}{L^2} \tag{5.100}$$

and so

$$\alpha_2 = \frac{3}{2} \pm \frac{1}{2}. \tag{5.101}$$

Therefore, both values of α_2 are positive, and hence both solutions will be regular at the boundary. The + sign corresponds to imposing Dirichlet boundary conditions, whilst the − sign corresponds to Neumann boundary conditions.

With the Frobenius solutions (5.93, 5.98) for $p_{n\ell}$ and $q_{n\ell}$ as initial conditions, we use the `NDSolve` function from `Mathematica` with the "Stiffness Switching" method to find numerical solutions for both radial functions. It is useful to write $p_{n\ell} = (r - r_h)^{n/2} \bar{p}_{n\ell}$ and then solve the ODE for $\bar{p}_{n\ell}$. This results in a faster calculation.

The normalisation constant $\mathcal{N}_{n\ell}$ can be found from the Wronskian relation (5.30). We calculate this using different values of $p_{n\ell}$ and $q_{n\ell}$ for a range of r values. Regardless of the value of r, the value of $\mathcal{N}_{n\ell}$ should remain constant. We can use this fact to check the accuracy of our solutions. This check is performed by calculating the relative error

$$\frac{\max\{\mathcal{N}_{n\ell}(r)\} - \min\{\mathcal{N}_{n\ell}(r)\}}{\min\{\mathcal{N}_{n\ell}(r)\}} \tag{5.102}$$

which, for each calculation performed in both this chapter and the next, for varying Λ and event horizon topology, ranges from $\sim 10^{-47}$ to $\sim 10^{-50}$. This gives us a great deal of confidence in the numerical integration performed.

To calculate the radial modes numerically, we reintroduce the dimensionless parameter η (5.3). This dimensionless parameter fixes the event horizon radius at $\eta = 1$ in all cases of event horizon topology, making comparison between the cases easier. The Frobenius series (5.93, 5.98) can then be written

$$p_{n\ell}(\eta \sim 1) \simeq \sum_{j=0}^{\infty} a_j (\eta - 1)^{\frac{n}{2}+j} \tag{5.103}$$

$$q_{n\ell}(\frac{1}{\eta} \sim 0) \simeq \sum_{j=0}^{\infty} b_j \left(\frac{1}{\eta}\right)^{\frac{3}{2}\pm\frac{1}{2}+j} . \tag{5.104}$$

We then evaluate the modes over a grid in η, by setting $\eta = 1 + 10^{-2+3i/100}$ for $i \in [1, 100]$, so that $\eta - 1 \in (0, 10]$. However, calculating the modes in this way results in some numerical errors near the horizon. This is because η depends on L, which in turn depends on the cosmological constant Λ, and therefore in some cases it is difficult to define which values of η are appropriately “close to” or “far from” the horizon. It is actually more useful to calculate the modes using the coordinate r, and then to export these results using the grid in η, which we choose to be

$$\eta = 1 + 10^{-2+3i/100} \;\Rightarrow\; r = \frac{M}{4\chi^2 + k}(2 + 10^{-2+3i/100}) \text{ for } i \in [1, 100]. \tag{5.105}$$

For the regularisation parameters $\Psi_{n\ell}(i, j|r)$, we can straightforwardly substitute for r in (5.88) and export over the same grid in η. To perform these numerical calculations in `Mathematica`, it is useful to perform the derivatives explicitly by hand. `Mathematica` is able to perform these derivatives itself, but this increases computation time and can introduce some numerical errors. `Mathematica` also does not recognise various relations for Legendre, Bessel and conical functions that help to simplify these expressions. Since we only calculate regularisation parameters up to $j = 2$ (for $j > 2$, regularisation parameters vanish in the coincidence limit), we only need to simplify expressions for the first and second derivatives in μ_k. These simplified expressions are found by using [120, eq. 14.7.8, 14.7.9] in the $k = \pm 1$ cases, and using [120, eq. 10.29.4] in the $k = 0$ cases. We note that

k = 1

$$\begin{aligned}\left(\frac{1}{\mu}\frac{\partial}{\partial\mu}\right)\mathcal{R}_{m\ell}(\mu) = \frac{(-1)^j}{\mu(1-\mu^2)}\Big[&(\ell-|m|)P_{\ell-1}^{-|m|}(\mu)Q_\ell^{|m|}(\mu) \\ &+(\ell+|m|)P_\ell^{-|m|}(\mu)Q_{\ell-1}^{|m|}(\mu) - 2\ell\mu P_\ell^{-|m|}(\mu)Q_\ell^{|m|}(\mu)\Big],\end{aligned} \tag{5.106}$$

$$\begin{aligned}\left(\frac{1}{\mu}\frac{\partial}{\partial\mu}\right)^2\mathcal{R}_{m\ell}(\mu) = \frac{(-1)^j}{\mu^2(1-\mu^2)^2}\Bigg[\Bigg(4(1-\ell)\mu-\frac{1}{\mu}\Bigg)\Big[&(\ell-|m|)P_{\ell-1}^{-|m|}(\mu)Q_\ell^{|m|}(\mu) \\ +(\ell+|m|)P_\ell^{-|m|}(\mu)Q_{\ell-1}^{|m|}(\mu)\Big] &+ 2(\ell-|m|)(\ell+|m|)P_{\ell-1}^{-|m|}(\mu)Q_{\ell-1}^{|m|}(\mu) \\ +4(\ell-1)\ell\mu^2P_\ell^{-|m|}(\mu)Q_\ell^{|m|}(\mu) &+ (\ell-|m|)(\ell-|m|-1)P_{\ell-2}^{-|m|}(\mu)Q_\ell^{|m|}(\mu) \\ &+(\ell+|m|)(\ell+|m|-1)P_\ell^{-|m|}(\mu)Q_{\ell-2}^{|m|}(\mu)\Bigg]\end{aligned} \tag{5.107}$$

k = 0

$$\begin{aligned}\left(\frac{1}{\mu}\frac{\partial}{\partial\mu}\right)\mathcal{R}_{m\ell}(\mu) = \frac{(-1)^{j+m}}{2\mu}\Big[&\ell I_{m-1}(\ell\mu)K_m(\ell\mu) + \ell e^{-\pi i}I_m(\ell\mu)K_{m-1}(\ell\mu) \\ &-\frac{2m}{\mu}I_m(\ell\mu)K_m(\ell\mu)\Big]\end{aligned} \tag{5.108}$$

$$\begin{aligned}\left(\frac{1}{\mu}\frac{\partial}{\partial\mu}\right)^2\mathcal{R}_{m\ell}(\mu) = \frac{(-1)^{j+m}}{2\mu^3}\Big[&\,\ell^2\mu\left(I_{m-2}(\ell\mu)K_m(\ell\mu) + I_m(\ell\mu)K_{m-2}(\ell\mu)\right. \\ +2e^{-\pi i}I_{m-1}(\ell\mu)K_{m-1}(\ell\mu)\big) &- 4m\ell\left\{I_{m-1}(\ell\mu)K_m(\ell\mu) + e^{-\pi i}I_m(\ell\mu)K_{m-1}(\ell\mu)\right\} \\ &+\frac{4m(1+m)}{\mu}I_m(\ell\mu)K_m(\ell\mu)\Big]\end{aligned} \tag{5.109}$$

k = −1

$$\begin{aligned}\left(\frac{1}{\mu}\frac{\partial}{\partial\mu}\right)\mathcal{R}_{m\ell}(\mu) = \frac{\pi(-1)^{n+m}}{2\mu(1-\mu^2)\cosh(\pi\ell)}\Bigg[&-\left(-\frac{1}{2}+i\ell-m\right)P^{-m}_{-\frac{3}{2}+i\ell}(-\mu)P^{m}_{-\frac{1}{2}+i\ell}(\mu) \\ +\left(-\frac{1}{2}+i\ell+m\right)P^{-m}_{-\frac{1}{2}+i\ell}(-\mu)P^{m}_{-\frac{3}{2}+i\ell}(\mu) &- 2\left(-\frac{1}{2}+i\ell\right)\mu P^{-m}_{-\frac{1}{2}+i\ell}(-\mu)P^{m}_{-\frac{1}{2}+i\ell}(\mu)\Bigg]\end{aligned} \tag{5.110}$$

$$\begin{aligned}\left(\frac{1}{\mu}\frac{\partial}{\partial\mu}\right)^2 \mathcal{R}_{m\ell}(\mu) = {} & \frac{\pi(-1)^{n+m}}{2\mu^2(1-\mu^2)^2\cosh(\pi\ell)}\left[\left(\frac{1}{\mu}+4\left(-\frac{3}{2}+i\ell\right)\mu\right)\right. \\ \times \left[\left(-\frac{1}{2}+i\ell-m\right)\right. & P^{-m}_{-\frac{3}{2}+i\ell}(-\mu)P^{m}_{-\frac{1}{2}+i\ell}(\mu)-\left.\left(-\frac{1}{2}+i\ell+m\right)P^{-m}_{-\frac{1}{2}+i\ell}(-\mu)P^{m}_{-\frac{3}{2}+i\ell}(\mu)\right] \\ & +\left(-\frac{1}{2}+i\ell-m\right)\left(-\frac{3}{2}+i\ell-m\right)P^{-m}_{-\frac{5}{2}+i\ell}(-\mu)P^{m}_{-\frac{1}{2}+i\ell}(\mu) \\ & +\left(-\frac{1}{2}+i\ell+m\right)\left(-\frac{3}{2}+i\ell+m\right)P^{-m}_{-\frac{1}{2}+i\ell}(-\mu)P^{m}_{-\frac{5}{2}+i\ell}(\mu) \\ & -2\left(-\frac{1}{2}+i\ell+m\right)\left(-\frac{1}{2}+i\ell-m\right)P^{-m}_{-\frac{3}{2}+i\ell}(-\mu)P^{m}_{-\frac{3}{2}+i\ell}(\mu) \\ & \left.+4\left(-\frac{1}{2}+i\ell\right)\left(-\frac{3}{2}+i\ell\right)\mu^2P^{-m}_{-\frac{1}{2}+i\ell}(-\mu)P^{m}_{-\frac{1}{2}+i\ell}(\mu)\right].\end{aligned}\tag{5.111}$$

It is also useful to redefine the Legendre functions in terms of hypergeometric functions to ensure more precise results, that is, [120, eq. 14.3.1, 14.3.2]

$$P^{\mu}_{\nu}(x)=\left(\frac{1+x}{1-x}\right)^{\mu/2}\frac{1}{\Gamma(1-\mu)}F(\nu+1,-\nu;1-\mu,\frac{1}{2}-\frac{1}{2}x),\tag{5.112}$$

$$\begin{aligned}Q^{\mu}_{\nu}(x)= & \frac{\pi}{2\sin(\mu\pi)}\left(\cos(\mu\pi)\left(\frac{1+x}{1-x}\right)^{\mu/2}\frac{1}{\Gamma(1-\mu)}F(\nu+1,-\nu;1-\mu;\frac{1}{2}-\frac{1}{2}x)\right. \\ & \left.-\frac{\Gamma(\nu+\mu+1)}{\Gamma(\nu-\mu+1)}\left(\frac{1-x}{1+x}\right)^{\mu/2}\frac{1}{\Gamma(1+\mu)}F(\nu+1,-\nu;1+\mu;\frac{1}{2}-\frac{1}{2}x)\right).\end{aligned}\tag{5.113}$$

To increase computation speed, we also ask `Mathematica` to focus on the real part only in the Mehler functions (Mehler functions are, of course, real functions, but numerical computation gives us an incredibly small, non-zero imaginary part).

5.6 Numerical results

In this section we present the numerical results for the VP in all three cases of topological black hole. The VP is calculated by subtracting the Hadamard parametrix (5.86) from the Euclidean Green's function (5.20) and then bringing points together. Thanks to our mode-sum representation for the Hadamard parametrix, this can be done mode-by-mode, leaving us with

$$\begin{aligned}\langle\hat{\phi}^2\rangle_{ren}=\lim_{x'\to x}\left\{\frac{1}{4\pi^2}\sum_{n=-\infty}^{\infty}e^{in\kappa\Delta\tau}\int_{\ell=0}^{\infty}d\ell\;\mathcal{P}_{\ell}(\gamma)\left[\kappa X^{(k)}_{n\ell}(r,r')\right.\right. \\ \left.\left.-\frac{1}{2}\sum_{i=0}^{2}\sum_{j=0}^{i}\mathcal{D}_{ij}(r)\Psi_{n\ell}(i,j|r)\right]-\frac{f'(r)}{48\pi^2 r}\right\}\end{aligned}\tag{5.114}$$

where $\mathcal{P}_\ell(\gamma)$ is given in (5.87), $X^{(k)}_{n\ell}$ is the radial Green's function satisfying (5.24), the coefficients $\mathcal{D}_{ij}$ are given in Table 5.1 and the regularisation parameters $\Psi_{n\ell}(i,j|r)$ are given in (5.88). The integral over ℓ is understood to be a sum over non-negative integers in the $k=1$ case. In the coincidence limit, the expansion variables s and w (5.37) both tend to 0. It makes sense to take $w \to 0$ before $s \to 0$, since s depends on w. This means taking temporal coordinates to coincidence prior to angular coordinates, which corresponds to performing the n-sum first, and then the ℓ-integral [11]. In the coincidence limit, we find

$$\langle \hat{\phi}^2 \rangle_{ren} = \frac{1}{4\pi^2} \int_{\ell=0}^{\infty} d\ell \sum_{n=-\infty}^{\infty} \mathcal{P}_\ell(0) \left[\kappa X^{(k)}_{n\ell}(r) - \frac{1}{2} \sum_{i=0}^{2} \sum_{j=0}^{i} \mathcal{D}_{ij}(r) \Psi_{n\ell}(i,j|r) \right] - \frac{f'(r)}{48\pi^2 r}. \tag{5.115}$$

In the $k=0$ case, we can use our scaling symmetries to simplify numerical calculations. Under the first scaling, using (5.9-5.12) as well as (5.34) and (5.73), the VP scales as

$$\langle \hat{\phi}^2 \rangle_{ren} \to \tilde{\rho}_1^{-2} \langle \hat{\phi}^2 \rangle_{ren}. \tag{5.116}$$

Under the second scaling, using (5.13-5.16) as well as (5.35) and (5.74), the VP scales as

$$\langle \hat{\phi}^2 \rangle_{ren} \to \tilde{\rho}_2^{6} \langle \hat{\phi}^2 \rangle_{ren}. \tag{5.117}$$

Applying both scalings at the same time, the VP therefore scales as

$$\langle \hat{\phi}^2 \rangle_{ren} \to \tilde{\rho}_1^{-2} \tilde{\rho}_2^{6} \langle \hat{\phi}^2 \rangle_{ren}. \tag{5.118}$$

The convergence of the sum over n in (5.115) can be shown numerically to be [11, 12],

$$\kappa X^{(k)}_{n\ell}(r) - \mathcal{D}_{00}(r) \Psi_{n\ell}(0,0|r) \sim \mathcal{O}(n^{-3}), \tag{5.119}$$

$$\kappa X^{(k)}_{n\ell}(r) - \sum_{i=0}^{1} \sum_{j=0}^{i} \mathcal{D}_{ij}(r) \Psi_{n\ell}(i,j|r) \sim \mathcal{O}(n^{-5}). \tag{5.120}$$

$$\kappa X^{(k)}_{n\ell}(r) - \sum_{i=0}^{2} \sum_{j=0}^{i} \mathcal{D}_{ij}(r) \Psi_{n\ell}(i,j|r) \sim \mathcal{O}(n^{-7}). \tag{5.121}$$

These facts provide us with a good check for the convergence of the summations, as we shall see later on.

We now present the results, alongside an analysis of convergence and accuracy, for each case of topological event horizon, starting with $k=1$.

5.6.1 Numerical results for spherical horizons

We calculate the renormalised VP on SadS black holes with spherical event horizon for black hole mass $M = 1$, cosmological constant $\Lambda = -3$ and horizon radius $r_h = 2$. This choice was made so that results matched [10], allowing us to compare results before repeating the calculation for different values of Λ. We calculate the modes as described in section 5.5, with all calculations performed to 100 digits of precision.

In Figure 5.1, we examine the convergence of sums over n by constructing the following log plots:

$$\text{Blue line}: \quad \log\left(n^3|\kappa\, \mathcal{N}_{n\ell}p_{n\ell}(r)q_{n\ell}(r) - D_{00}(r)\Psi_{n\ell}(0,0|r)|\right) \tag{5.122}$$

$$\text{Orange line}: \quad \log\left(n^5|\kappa\, \mathcal{N}_{n\ell}p_{n\ell}(r)q_{n\ell}(r) - \sum_{i=0}^{1}\sum_{j=0}^{i}\mathcal{D}_{ij}^{(+)}(r)\Psi_{n\ell}(i,j|r)|\right) \tag{5.123}$$

$$\text{Green line}: \quad \log\left(n^7|\kappa\, \mathcal{N}_{n\ell}p_{n\ell}(r)q_{n\ell}(r) - \sum_{i=0}^{2}\sum_{j=0}^{i}\mathcal{D}_{ij}^{(+)}(r)\Psi_{n\ell}(i,j|r)|\right). \tag{5.124}$$

Each plot is constructed for a specific value of r and ℓ. In all cases, we find that the plot converges to a constant value, meaning that the summand has the appropriate order in n predicted by (5.119-5.121).

The results take more time to converge to the expected order when ℓ is large. This is simply because the individual modes get smaller, and in fact become negligible, as we increase ℓ. To improve convergence in these modes with larger ℓ, we would need more digits of precision, but this is not actually necessary, because the large ℓ terms are so small that disregarding them will not affect our final answer (as can be seen in Figure 5.2).

In Figure 5.2, we construct a three-dimensional plot to examine the convergence of the sum over ℓ. We plot the summand

$$\mathcal{P}_\ell(0)\sum_{n=-70}^{70}\left(\kappa\mathcal{N}_{n\ell}p_{n\ell}q_{n\ell} - \sum_{i=0}^{2}\sum_{j=0}^{2}\mathcal{D}_{ij}\Psi_{n\ell}(i,j|r)\right). \tag{5.125}$$

The summand converges sufficiently quickly to zero for each fixed η as we increase ℓ, but this convergence is not uniform in η. Furthermore, the convergence depends on the value of χ. As we shall see in section 5.6.1, increasing χ requires us to include more terms in the ℓ-sum and truncate at a higher value in order to see convergence to zero in (5.125). This convergence to zero implies a rapid convergence in the calculation of the renormalised VP (5.115).

Convergence of the ℓ-summand also drops off as we get further from the event horizon. This is to be expected, since individual terms in the n and ℓ sums are larger for larger r, and so we require more terms in n and ℓ to obtain convergence further from the

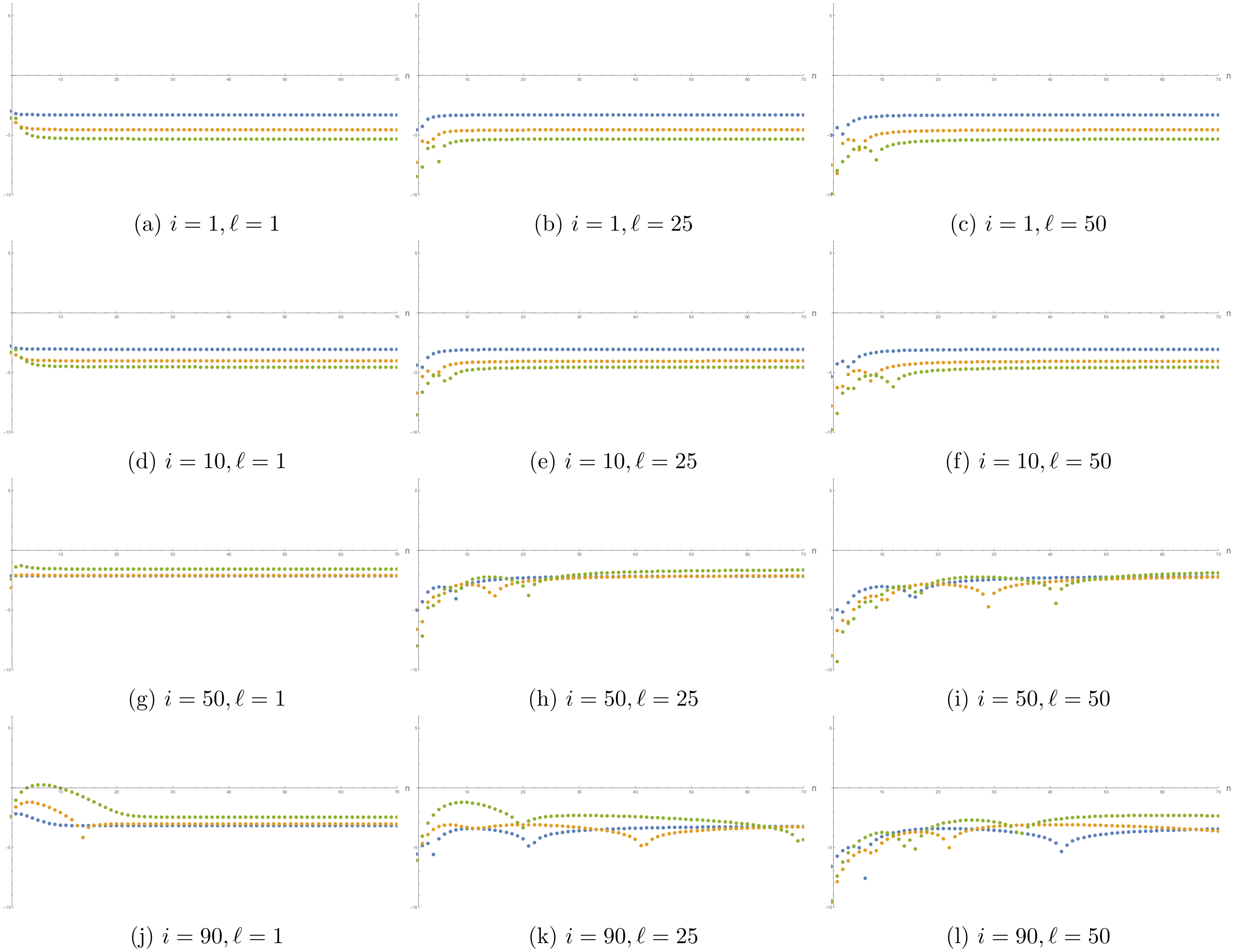

(a) $i = 1, \ell = 1$ (b) $i = 1, \ell = 25$ (c) $i = 1, \ell = 50$

(d) $i = 10, \ell = 1$ (e) $i = 10, \ell = 25$ (f) $i = 10, \ell = 50$

(g) $i = 50, \ell = 1$ (h) $i = 50, \ell = 25$ (i) $i = 50, \ell = 50$

(j) $i = 90, \ell = 1$ (k) $i = 90, \ell = 25$ (l) $i = 90, \ell = 50$

Figure 5.1: Log plots showing convergence of the inner sum over n for the case of an adS black hole with spherical horizon, $M = 5$, $\Lambda = -3$. The blue line represents (5.122), the orange line represents (5.123) and the green line represents (5.124). The value of n runs along the x-axis. The calculation was performed at each integer value of n for $n \in [0, 70]$. Each individual point in the plot represents a different value of n. The radius is given by $r = r_h + 10^{-2+3i/100}$, where i is given below each plot. The value of ℓ is also given. Each line approaches a constant as n increases, indicating good convergence for all values of ℓ and r. Qualitatively similar behaviour is obtained for other values of ℓ and r.

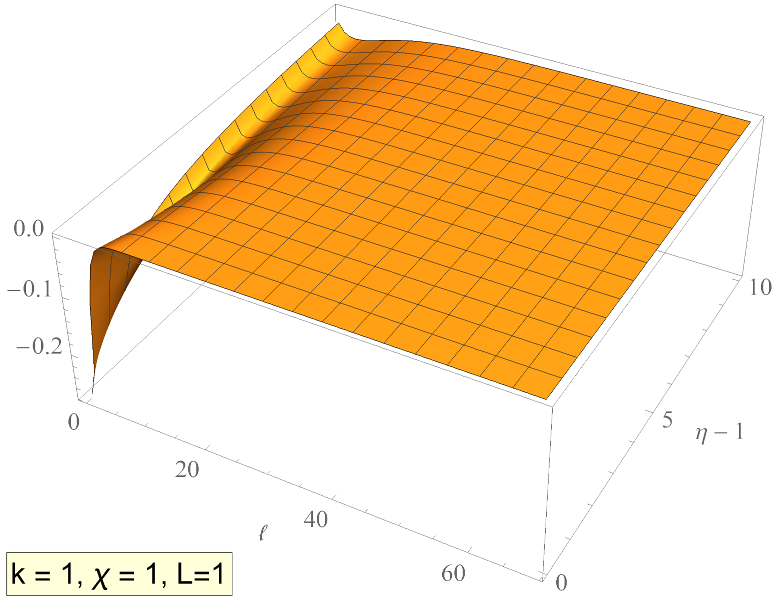

Figure 5.2: The ℓ-summand (5.125) in the case of a SadS black hole with spherical horizon, $M = 5$, $\Lambda = -3$. This converges quickly to zero as ℓ increases, but this convergence is not uniform in η. The convergence is more rapid for small values of η.

event horizon. We would find that, were we to attempt to increase the value of r (or, equivalently, η), we would lose convergence. For our purposes, we find that using 70 n-modes and 50 ℓ-modes is enough to obtain good convergence up to $\eta = 11$.

Our results for the renormalised VP in SadS with a spherical event horizon and Dirichlet conditions imposed on the fields at the boundary are shown in Figure 5.3. The VP approaches the value $-1/48\pi^2$, the value found in CadS with Dirichlet conditions imposed (3.2). This plot matches exactly the plot given in [10], although it is important to note that here we have used a renormalisation method that allows for much quicker computation and much faster convergence. The "extended coordinates" method also allows for the extension to other black hole topologies. It is not clear how straightforward the extension to other topologies would be when using the method of [10].

Accuracy tests for $k = 1$

In the case of a spherical black hole horizon, errors arise in the calculation of $\langle\hat{\phi}^2\rangle_{ren}$ from truncating both the n-sum and the ℓ-sum. We can quantify the errors introduced by these truncations by increasing/decreasing the number of terms in each sum and then comparing with previous results. This gives us an idea of how many digits of accuracy have been obtained.

We perform the same calculation but truncate the n-sum at $n = \pm 60$. The relative error between these two values of $\langle\hat{\phi}^2\rangle_{ren}$ is given in Table 5.4. We can see that truncating

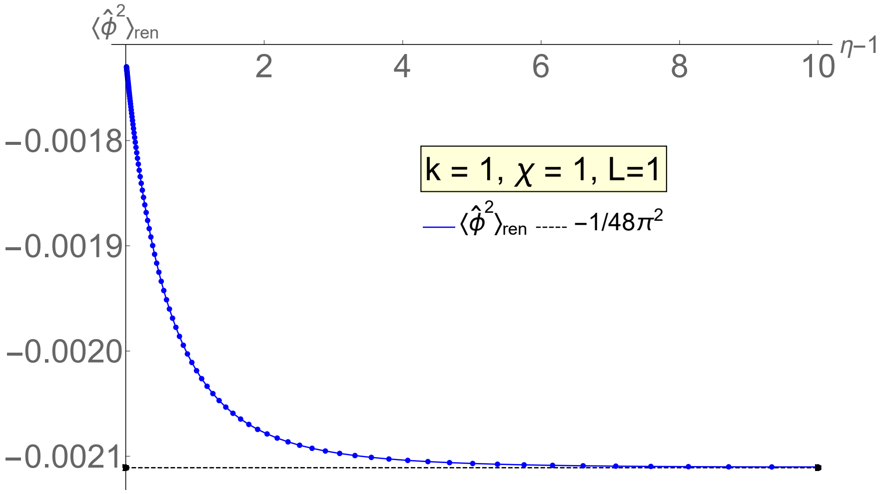

Figure 5.3: The behaviour of $\langle\hat{\phi}^2\rangle_{ren}$ with Dirichlet boundary conditions imposed for an adS black hole with spherical horizon, $M=5,\ \Lambda=-3$, calcuated using 50 terms in the ℓ-sum and 70 terms in the n-sum. The VP was calculated over a grid of values in η and then these points were interpolated over - each individual point is displayed on the plot. The VP is a monotonically decreasing function of η, approaching the CadS value $-1/48\pi^2$. This value is shown with a dashed black line.

i	Relative error
10	2.2071×10^{-12}
20	1.5212×10^{-11}
30	9.1696×10^{-11}
40	4.3125×10^{-10}
50	1.3169×10^{-9}
60	2.0321×10^{-9}
70	1.1755×10^{-9}
80	8.1475×10^{-11}
90	-1.3759×10^{-10}
100	-7.1015×10^{-11}

Table 5.4

i	Relative error
10	2.4354×10^{-7}
20	2.2430×10^{-7}
30	1.9008×10^{-7}
40	1.3546×10^{-7}
50	6.4015×10^{-8}
60	-1.1402×10^{-9}
70	-3.0364×10^{-8}
80	-2.2630×10^{-8}
90	6.6137×10^{-6}
100	0.001859

Table 5.5

Relative errors for $k=1,\ M=5,\Lambda=-3$. The radial coordinate is given by $r=r_h+10^{-2+3i/100}$, where the value of i is given in the left-hand column.

Table 5.4: The relative error $\frac{\langle\hat{\phi}^2\rangle_{70}-\langle\phi^2\rangle_{60}}{\langle\hat{\phi}^2\rangle_{60}}$, where $\langle\hat{\phi}^2\rangle_y$ is the VP calculated with the n-sum truncated at $\pm y$.

Table 5.5: The relative error $\frac{\langle\hat{\phi}^2\rangle_{60}-\langle\hat{\phi}^2\rangle_{50}}{\langle\hat{\phi}^2\rangle_{50}}$, where $\langle\hat{\phi}^2\rangle_y$ is the VP calculated with the ℓ-sum truncated at y.

the n-sum at ±60 instead of at ±70 leaves us with a small relative error, suggesting that this truncation does not contribute a huge error in the overall calculation. Similarly, we truncate the ℓ-sum at $\ell = 60$ instead of 50 and again calculate the relative error. The error here is greater, especially far from the horizon (see Table 5.5).

Far from the horizon, we can compare our results with analytical results found in CadS, given in (3.2). By comparing our numerical results with this analytical result, we see that, far from the horizon, our results at $\eta = 11$ agrees with (3.2) to 6 significant figures when we truncate the ℓ-sum at $\ell = 50$, and to 7 significant figures when we truncate the ℓ-sum at $\ell = 70$.

Varying Λ

In order to compare the results in Figure 5.3 with different values of the cosmological constant, we introduce the coordinate η (5.3) and the parameter χ (5.4). By looking at (5.4), we see that we can consider a variety of values of Λ by fixing $M = \frac{1}{2}$ and varying χ.

We look at three different values of χ. The first of these is $\chi = 0.5$, which corresponds to $\Lambda = -12$. The renormalised VP in this case is shown in Figure 5.6. This is calculated with 50 terms in the ℓ-sum and 70 terms in the n-sum. The behaviour is very similar to the previous case (note that Λ is of the same order of magnitude in both cases, so we do not expect to see a huge difference). We can then test accuracy in a similar way to before, by increasing and decreasing the number of modes. The relative errors are given in Tables 5.7 (where we compare different truncations of the n-sum) and 5.8 (where we vary the number of terms in the ℓ-sum). This suggests that truncating the n-sum at $n = 70$ and truncating the ℓ-sum at $\ell = 50$ secures a satisfactory convergence in the VP in the region $\eta \in [1, 11]$. We expect that, according to the results in CadS (3.2), far from the horizon,

$$\langle \hat{\phi}^2 \rangle_{\chi=0.5} \to -\frac{1}{12\pi^2} \sim -0.00844 \text{ as } r \to \infty. \tag{5.126}$$

At $\eta = 11$, our results, calculated with 50 terms in the ℓ-sum and 70 terms in the n-sum, differ from this by 10^{-6}, which is the same as the previous case. The relative difference will decrease if we increase the number of terms in either of the sums.

The second case we look at is $\chi = 0.05$, which corresponds to $\Lambda = -\frac{30603}{1002001} \approx -0.03054$. The VP in this case is shown in Figure 5.9. Now, Λ is much smaller, and we see that we have to travel a little further from the horizon to see the VP converge to the expected value,

$$\langle \hat{\phi}^2 \rangle_{\chi=0.05} \to -\frac{10201}{48096048\pi^2} \approx -2 \times 10^{-5} \text{ as } r \to \infty. \tag{5.127}$$

We also notice that at the horizon, the VP has a positive value, before becoming negative as we move towards the boundary. This is in contrast to other cases, where the VP remains negative throughout the spacetime. This could be explained by the

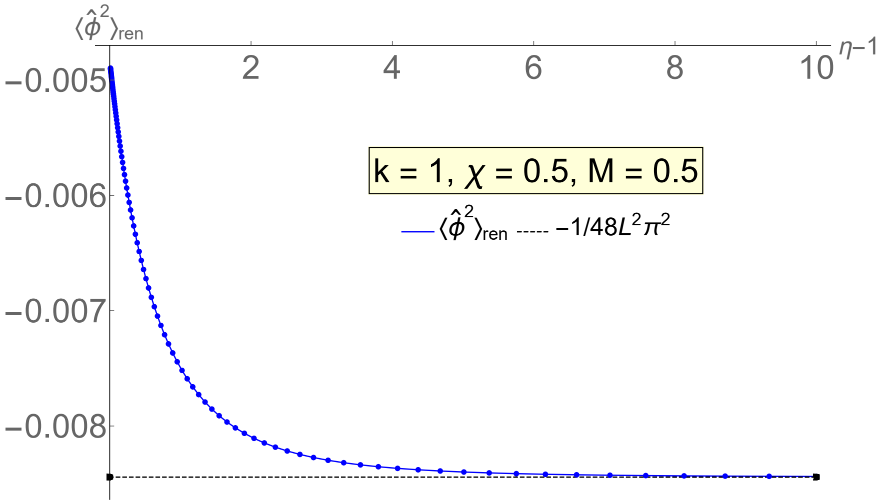

Figure 5.6: The behaviour of $\langle\hat{\phi}^2\rangle_{ren}$ with Dirichlet boundary conditions imposed on an adS black hole with spherical horizon, $M = 0.5$, $\chi = 0.5$, calculated with 50 ℓ-modes and 70 n-modes. The VP is a monotonically decreasing function, approaching the CadS limit $-1/48\pi^2L^2$. This limit is shown by a black dashed line. The VP is always negative throughout the spacetime.

i	Relative error
10	1.9196×10^{-11}
20	1.2087×10^{-10}
30	6.1249×10^{-10}
40	2.0794×10^{-9}
50	3.4255×10^{-9}
60	8.9518×10^{-10}
70	-2.4493×10^{-9}
80	-2.1851×10^{-9}
90	-9.4595×10^{-10}
100	-3.0556×10^{-10}

Table 5.7

i	Relative error
10	-1.4710×10^{-7}
20	-1.3168×10^{-7}
30	-1.0532×10^{-7}
40	-6.6146×10^{-8}
50	-2.1129×10^{-8}
60	1.1427×10^{-8}
70	1.9785×10^{-8}
80	1.2985×10^{-8}
90	3.9253×10^{-9}
100	-0.00001659

Table 5.8

Relative errors for $\chi = 0.5$. The radial coordinate is given by $\eta = 1 + 10^{-2+3i/100}$, where the value of i is given in the left-hand column.

Table 5.7: The relative error $\frac{\langle\hat{\phi}^2\rangle_{70}-\langle\hat{\phi}^2\rangle_{60}}{\langle\hat{\phi}^2\rangle_{60}}$, where $\langle\hat{\phi}^2\rangle_y$ is the VP calculated with the n-sum truncated at $\pm y$.

Table 5.8: The relative error $\frac{\langle\hat{\phi}^2\rangle_{60}-\langle\hat{\phi}^2\rangle_{50}}{\langle\hat{\phi}^2\rangle_{50}}$, where $\langle\hat{\phi}^2\rangle_y$ is the VP calculated with the ℓ-sum truncated at y.

fact that this black hole is thermodynamically unstable, whilst other spherical black holes are thermodynamically stable [137]. The black holes that we consider with flat or hyperbolic horizon curvature are also thermodynamically stable [127]. It could be the case that the sign of the VP on the horizon is governed by whether or not the black hole is thermodynamically stable. If this is the case, it must only be true for Dirichlet boundary conditions - we shall see in the next chapter that the same does not hold for Neumann or Robin conditions.

At $\eta = 11$, our results agree with (5.127) to three significant figures, whereas at $\eta = 21$, we find agreement to four significant figures. In this case, however, truncating the n-sum at $n = 70$ and the ℓ-sum at $\ell = 50$ results in a much higher accuracy, as can be seen in Tables 5.10 and 5.11 respectively. This suggests that when Λ is small (i.e. $\Lambda \ll 1$), we do not require as many terms in in the n- or ℓ-sums to achieve good convergence, but we do need a greater range of η.

The final case we consider is $\chi = 5$, which corresponds to $\Lambda = -3060300$. The results for the renormalised VP in this case are shown in Figure 5.12. Now we find that the convergence to the expected value occurs much closer to the horizon, but that accuracy breaks down much sooner as well. We can see that increasing the number of terms in the n-sum makes no difference (see Table 5.13 for relative errors), suggesting that, in order to improve accuracy far from the horizon, we need to increase the number of terms in the ℓ-sum (the relative errors gained from the ℓ-sum truncation are given in Table 5.14 - note that errors are large far from the horizon and in order to obtain any sensible results past $\eta \sim 5$, we would require more terms in the ℓ-sum). The expected value far from the horizon is

$$\langle \hat{\phi}^2 \rangle_{\chi=5} \to -\frac{255025}{12\pi^2} \approx -2153 \text{ as } r \to \infty. \tag{5.128}$$

We get closest to this value around $\eta = 4$, and then lose accuracy as we increase η. More ℓ-sum terms would have to be calculated to get closer to the expected value.

To conclude, in order to obtain accurate answers for $\langle \hat{\phi}^2 \rangle_{ren}$, we do not require as many ℓ-sum terms for small Λ, but we must travel a little further away from the horizon. Conversely, for large Λ, we need more ℓ-sum terms, and then find that $\langle \hat{\phi}^2 \rangle_{ren}$ converges pretty close to the horizon.

5.6.2 Numerical results for flat horizons

The calculation for the flat horizon was originally performed for black hole mass $M = 4$, cosmological constant $\Lambda = -3$ and horizon radius $r_h = 2$. These values were chosen to allow us to compare easily with the spherical case where $r_h = 2, \Lambda = -3$, as both results are expected to approach the value $-1/48\pi^2 L^2$, with radius of curvature L the same in both cases.

We examine convergence over the n-sum by constructing log plots given by (5.122-5.124). These convergence plots are given in Figure 5.15. The log plots approach a

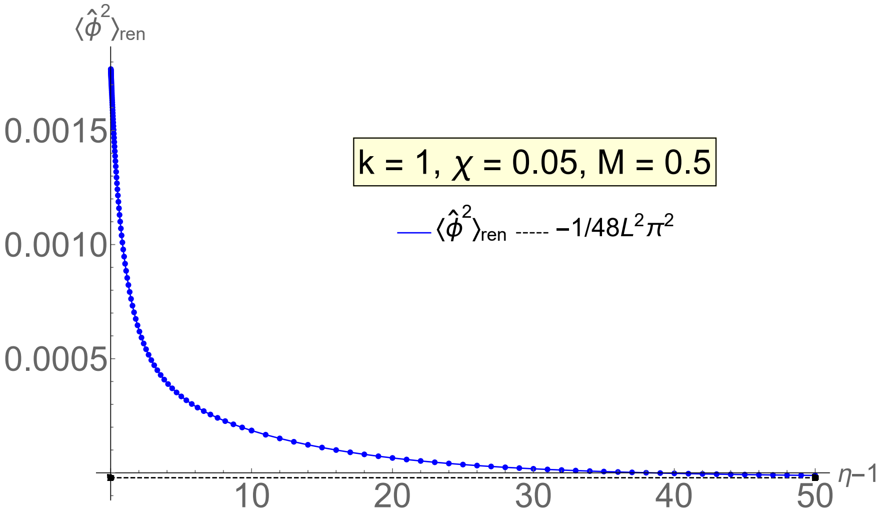

Figure 5.9: The behaviour of $\langle\hat{\phi}^2\rangle_{ren}$ with Dirichlet boundary conditions imposed on an adS black hole with spherical horizon, $M = 0.5,\ \chi = 0.05$, calculated with 50 ℓ-modes and 70 n-modes. Unlike in the previous cases, the VP is positive rather than negative at the event horizon, and then monotonically decreases to the CadS limit $-1/48\pi^2L^2$. This limit is shown by a black dashed line.

i	Relative error
10	-4.0217×10^{-11}
20	-1.7359×10^{-10}
30	-3.2805×10^{-10}
40	8.3909×10^{-10}
50	4.0553×10^{-9}
60	4.0424×10^{-9}
70	2.1122×10^{-9}
80	3.3803×10^{-9}
90	4.6563×10^{-9}
100	3.1707×10^{-9}

Table 5.10

i	Relative error
10	2.0674×10^{-10}
20	6.8776×10^{-10}
30	1.4848×10^{-9}
40	2.1253×10^{-9}
50	2.1750×10^{-9}
60	4.0823×10^{-9}
70	5.5413×10^{-9}
80	2.6347×10^{-9}
90	-1.1794×10^{-10}
100	-5.2882×10^{-10}

Table 5.11

Relative errors for $\chi = 0.05$. The radial coordinate is given by $\eta = 1 + 10^{-2+3i/100}$, where the value of i is given in the left-hand column.

Table 5.10: The relative error $\frac{\langle\hat{\phi}^2\rangle_{70}-\langle\hat{\phi}^2\rangle_{60}}{\langle\hat{\phi}^2\rangle_{60}}$ where $\langle\hat{\phi}^2\rangle_y$ is the VP calculated with the n-sum truncated at $\pm y$.

Table 5.11: The relative error $\frac{\langle\hat{\phi}^2\rangle_{60}-\langle\hat{\phi}^2\rangle_{50}}{\langle\hat{\phi}^2\rangle_{50}}$, where $\langle\hat{\phi}^2\rangle_y$ is the VP calculated with the ℓ-sum truncated at y.

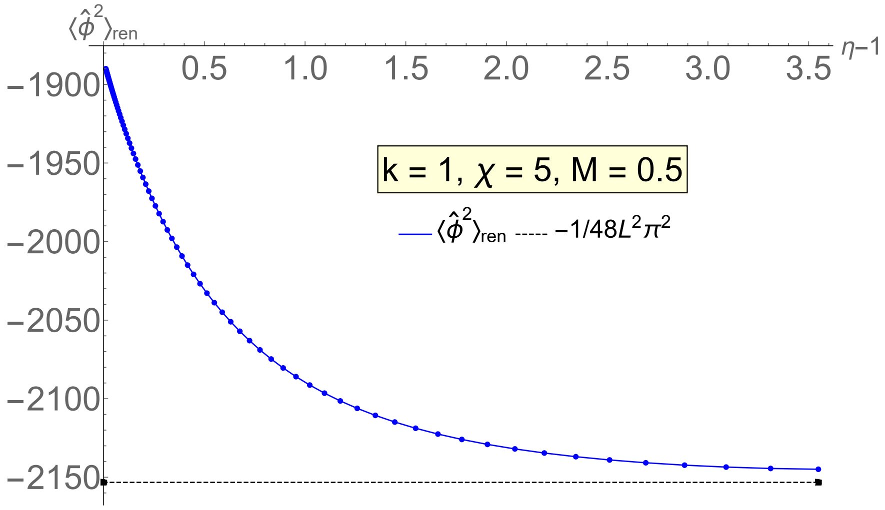

Figure 5.12: The behaviour of $\langle\hat{\phi}^2\rangle_{ren}$ with Dirichlet boundary conditions imposed on an adS black hole with spherical horizon, $M = 0.5,\ \chi = 5$, calculated with 130 ℓ-modes and 70 n-modes. The VP is always negative and monotonically decreasing. The CadS limit $-1/48\pi^2L^2$ is shown as a black dashed line to demonstrate convergence near $\eta = 4$. Accuracy is lost for $\eta > 4$ - in order to increase this accuracy, we would need to calculate more terms in the ℓ-sum.

i	Relative error
10	4.3154×10^{-13}
20	3.0520×10^{-12}
30	1.9325×10^{-11}
40	9.9498×10^{-11}
50	3.5532×10^{-10}
60	7.0550×10^{-10}
70	6.2295×10^{-10}
80	2.1759×10^{-10}
90	2.6822×10^{-11}
100	-3.6506×10^{-12}

Table 5.13

i	Relative error
10	1.5668×10^{-6}
20	1.4525×10^{-6}
30	1.2476×10^{-6}
40	9.1572×10^{-7}
50	4.7103×10^{-7}
60	8.6794×10^{-8}
70	2.3266×10^{-6}
80	0.0001464
90	0.004320
100	0.04398

Table 5.14

Relative errors for $\chi = 5$. The radial coordinate is given by $\eta = 1 + 10^{-2+3i/100}$, where the value of i is given in the left-hand column.

Table 5.13: The relative error $\frac{\langle\hat{\phi}^2\rangle_{70} - \langle\hat{\phi}^2\rangle_{60}}{\langle\hat{\phi}^2\rangle_{60}}$, where $\langle\hat{\phi}^2\rangle_y$ is the VP calculated with the n-sum truncated at $\pm y$.

Table 5.14: The relative error $\frac{\langle\hat{\phi}^2\rangle_{60} - \langle\hat{\phi}^2\rangle_{50}}{\langle\hat{\phi}^2\rangle_{50}}$, where $\langle\hat{\phi}^2\rangle_y$ is the VP calculated with the ℓ-sum truncated at y.

constant value as n increases, suggesting good convergence in the n-sum for all values of ℓ and r.

In order for us to obtain rapid convergence in $\langle\hat{\phi}^2\rangle_{ren}$, we expect the ℓ-integrand to converge quickly to zero. In this case, we find that convergence becomes faster as we move away from the event horizon (see Figure 5.16). This is in contrast to the $k = 1$ case, where we saw faster convergence for small η.

The convergence plots (Figure 5.15) suggest that truncating the n-sum at $n = 70$, with each individual term calculated to 100 digits of precision, is enough to obtain good convergence. For the ℓ-integral, we must calculate a grid over the ℓs and then interpolate between these values to create an interpolation function in ℓ that we can integrate over. We calculate the integrand for every half-integer $\ell \in [4, 50]$, and every 1/10-integer $\ell \in (0, 4]$. This is due to the fact that behaviour in ℓ is more interesting close to $\ell = 0$, and we must use a finer grid to correctly capture all information.

The integral over ℓ is performed by interpolating between the ℓ-modes using built-in interpolation methods in `Mathematica`. We then execute a numerical integration, and cut off the integral at $\ell_1 = 50$. The resulting plot of VP with Dirichlet conditions imposed at the boundary is shown in Figure 5.17, in terms of the coordinate η. The VP is a monotonically decreasing function of η, approaching the value $-1/48\pi^2$, the value of the VP found on CadS when Dirichlet conditions are imposed. Comparing this result to the $k = 1$ case, we can see that the value of the VP is smaller, but still negative, at the horizon. The approach to the CadS limit is slower in the $k = 0$ case, with convergence not occurring until around $\eta = 10$. For a comparison plot, see Figure 5.30.

Accuracy tests for $k = 0$

In the calculation of $\langle\hat{\phi}^2\rangle_{ren}$ in the $k = 0$ case, we have made three different approximations which could lead to errors. These errors could arise from truncating the n-sum at $n = 50$, from cutting off the ℓ-integral at $\ell = \ell_1$, and from the density of the grid used to perform the ℓ-integration.

We can test accuracy in the n-sum by decreasing the number of terms in the n-sum and calculating the relative error, similar to the way in which we tested accuracy in the $k = 1$ case. The relative error between $\langle\hat{\phi}^2\rangle_{ren}$ calculated with 70 terms in the n-sum and 60 terms in the n-sum is given in Table 5.18.

As the integration over ℓ cannot be performed analytically, we calculate the integrand over a discrete number of ℓs and then form an interpolating function over which we then integrate. The size of the steps between these ℓs can be varied to check our accuracy. We can calculate the relative error between the VP when the step size close to $\ell = 0$ is 1/20 and when the step size is 1/10. In both cases, we only use half-integer steps in ℓ for $\ell > 4$. The relative errors for varying radius are given in Table 5.19.

The interval of integration over ℓ is infinite, but we cut it off at $\ell_1 = 50$. To check that

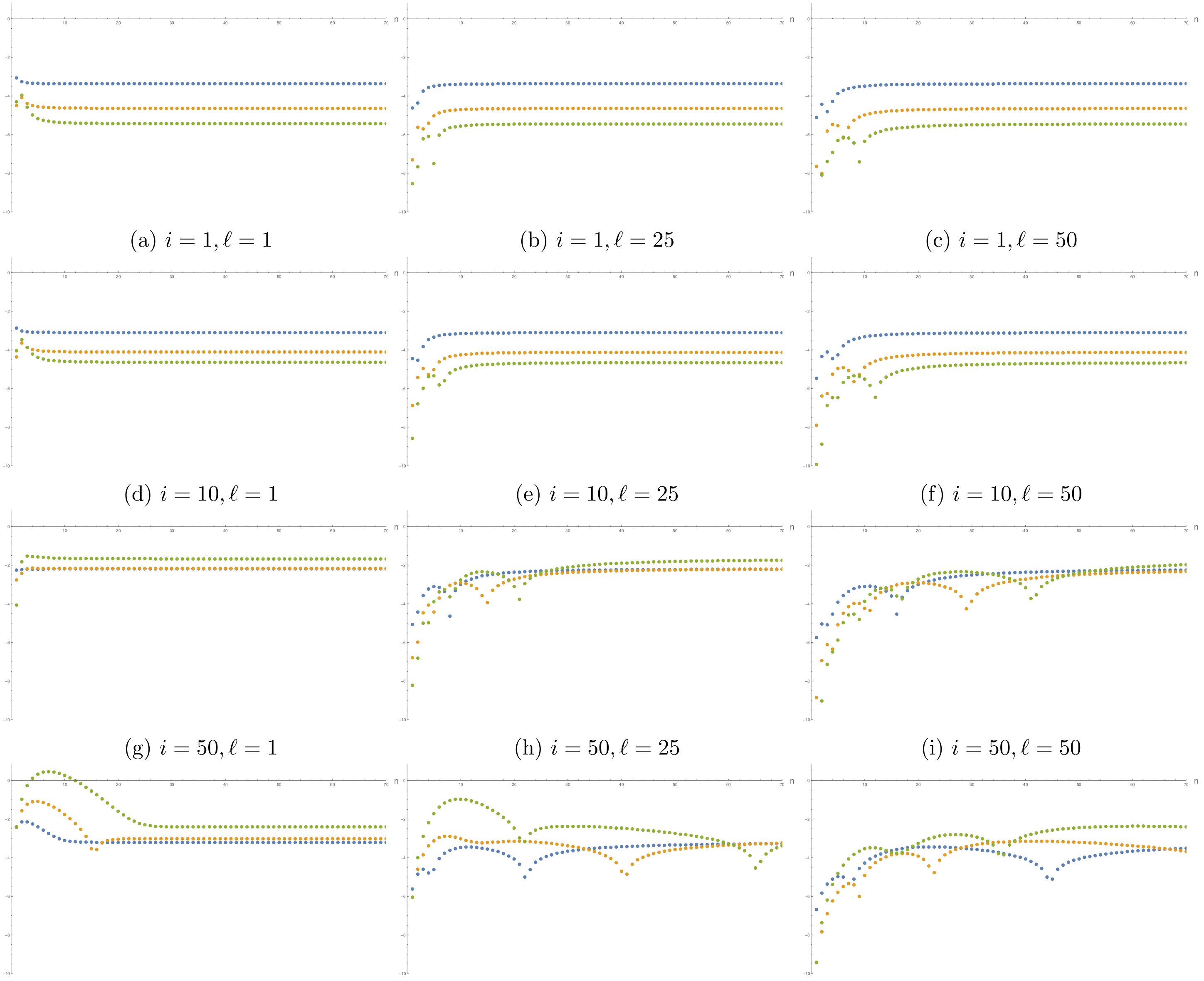

(a) $i = 1, \ell = 1$

(b) $i = 1, \ell = 25$

(c) $i = 1, \ell = 50$

(d) $i = 10, \ell = 1$

(e) $i = 10, \ell = 25$

(f) $i = 10, \ell = 50$

(g) $i = 50, \ell = 1$

(h) $i = 50, \ell = 25$

(i) $i = 50, \ell = 50$

(j) $i = 90, \ell = 1$

(k) $i = 90, v = 25$

(l) $i = 90, \ell = 50$

Figure 5.15: Log plots showing convergence of the inner sum over n for the case of an adS black hole with flat horizon, $M = 4$, $\Lambda = -3$. The blue line represents (5.122), the orange line represents (5.123) and the green line represents (5.124). The value of n runs along the x-axis. The calculation was performed at each integer value of n for $n \in [0, 70]$. Each individual point in the plot represents a different value of n. The radius is given by $r = r_h + 10^{-2+3i/100}$, where i is given below each plot. The value of ℓ is also given. Each line approaches a constant as n increases, indicating good convergence for all values of ℓ and r. Qualitatively similar behaviour is obtained for other values of ℓ and r.

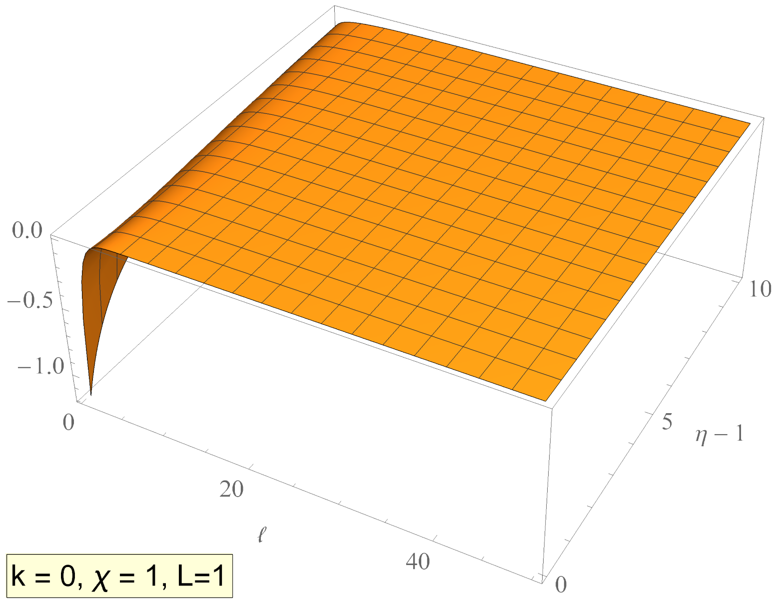

Figure 5.16: The ℓ-integrand (5.125) in the case of an adS black hole with flat horizon, $M = 4$, $\Lambda = -3$. This converges quickly to zero as ℓ increases, but this convergence is not uniform. The convergence is more rapid as η increases.

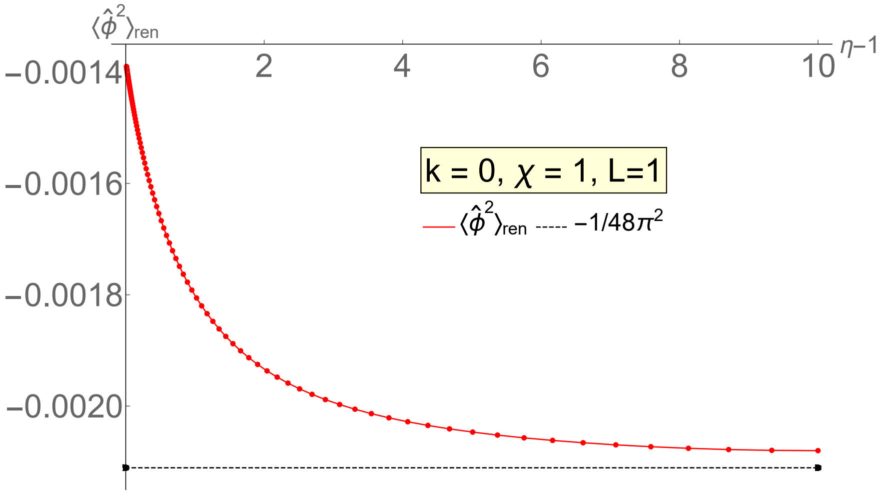

Figure 5.17: The behaviour of $\langle\hat{\phi}^2\rangle_{ren}$ with Dirichlet boundary conditions imposed in the case of an adS black hole with flat horizon, $M = 4$, $\Lambda = -3$. The VP is calculated by integrating over a grid of ℓ-modes up to $\ell_1 = 50$ and then summing over 70 n-modes. The resulting function is negative throughout the spacetime, and monotonically decreasing, approaching the CadS limit $-1/48\pi^2$ at the boundary. This limit is shown by the dashed black line.

this does not affect our accuracy as much, we can approximate the tail of the integrand by assuming it takes the form $a \times \ell^{-(1+\epsilon)}$, for some constants a, ϵ. We can find these values by using the Mathematica function `FindFit`. The constant a will depend on the value of r (or, equivalently, η). The values of ϵ are all found to be close to 4 (we lose some accuracy far from the horizon), and so the integrand is $\sim \mathcal{O}(\ell^{-5})$, which matches the order of the ℓ-summand in the $k = 1$ case. The tail of the integrand can then be approximated as

$$\int_{\ell_1}^{\infty} a\ell^{-(1+\epsilon)} d\ell = \frac{a}{\epsilon}\ell_1^{-\epsilon}. \tag{5.129}$$

The various values of the tail of the integral are given in Table 5.20.

The largest error comes from the density of the grid over the ℓ-integral. Comparing numerical results far from the horizon with the CadS limit, we find that our result is correct to 5 significant figures.

Varying Λ

In section 5.2, we saw that there were two scaling symmetries associated with the $k = 0$ metric. This means that varying both M and χ simply results in a rescaling of the VP according to (5.118), where $M \to \tilde{\rho}_1 M$ and $\chi \to \tilde{\rho}_2 \chi$.

In the $k = 1$ case, we fixed $M = 0.5$ and varied χ in order to see how the cosmological constant affects the VP. We do the same in the $k = 0$ case, keeping $M = 0.5$ fixed and varying χ. We first look at $\chi = 0.5$, which corresponds to $\Lambda = -3$. To apply this rescaling, we set $\tilde{\rho}_1 = 1/8$ and $\tilde{\rho}_2 = 1/2$ in (5.118). We find that there is, in fact, no change in the VP in this case, and we obtain exactly the same plot as given in Figure 5.17. Note that η is a dimensionless quantity and does not get scaled as we alter χ. Instead of plotting in terms of χ, it is more beneficial to plot in terms of r, as this allows us to see the difference between the cases more clearly. The plot of the VP when $\chi = 0.5$ is given as a function of η in Figure 5.21a and as a function of r in Figure 5.22a.

Next we look at $\chi = 0.05$, which corresponds to $\Lambda = -3 \times 10^{-6}$. We apply the scaling (5.118) by setting $\tilde{\rho}_1 = 1/8$ and $\tilde{\rho}_2 = 1/20$. We find the VP in this case by multiplying our original results in Figure 5.17 by a factor 10^{-6} (see Figure 5.21b for the plot as a function of η, and Figure 5.22b for the plot as a function of r).

Finally we look at $\chi = 5$, which corresponds to $\Lambda = -3 \times 10^{6}$. We apply the scaling (5.118) by setting $\tilde{\rho}_1 = 1/8$ and $\tilde{\rho}_2 = 5$. We find the VP in this case by multiplying our original results in Figure 5.17 by a factor of 10^{6} (see Figure 5.21c for the plot as a function of η, and Figure 5.22c for the plot as a function of r).

When we plot as a function of η (Figure 5.21), it is much harder to compare the rate of convergence, since the coordinate η is invariant under the rescaling, and so all cases seem to converge to the CadS limit at the same rate as we move away from the horizon. The only difference appears to be in the value of the VP on the horizon - for smaller

i	Relative error
10	-2.0206×10^{-12}
20	-1.3913×10^{-11}
30	-8.3753×10^{-11}
40	-3.9353×10^{-10}
50	-1.2049×10^{-9}
60	-1.8857×10^{-9}
70	-1.1476×10^{-9}
80	-1.3174×10^{-10}
90	1.0697×10^{-10}
100	6.1048×10^{-11}

Table 5.18

i	Relative error
10	-0.005981
20	-0.005806
30	-0.005489
40	-0.004959
50	-0.004168
60	-0.003139
70	-0.002011
80	-0.001043
90	-0.0004368
100	-0.0001541

Table 5.19

Relative errors in the case $M = 4,\ \Lambda = -3$. The radial coordinate is given by $r = r_h + 10^{-2+3i/100}$, where the value of i is given in the left-hand column.

Table 5.18: The relative error $\frac{\langle\hat{\phi}^2\rangle_{70} - \langle\hat{\phi}^2\rangle_{60}}{\langle\hat{\phi}^2\rangle_{60}}$, where $\langle\hat{\phi}^2\rangle_y$ is the VP calculated with the n-sum truncated at $\pm y$.

Table 5.19: The relative error $\frac{\langle\hat{\phi}^2\rangle_{1/20} - \langle\hat{\phi}^2\rangle_{1/10}}{\langle\hat{\phi}^2\rangle_{1/10}}$, where $\langle\hat{\phi}^2\rangle_y$ is the VP calculated with y steps between ℓ-modes when $\ell < 4$, and half-integer steps for $\ell > 4$.

i	Approximate value of integral tail
10	-2.2717×10^{-8}
20	-2.1166×10^{-8}
30	-1.8351×10^{-8}
40	-1.3689×10^{-8}
50	-7.2016×10^{-9}
60	-6.9139×10^{-10}
70	2.7660×10^{-9}
80	-6.4986×10^{-10}
90	-2.2453×10^{-6}
100	-0.0004390

Table 5.20: The approximate value of the tail of the ℓ-integral in the case of a black hole with flat event horizon, $M = 4,\ \Lambda = -3$. The radial coordinate is given by $r = r_h + 10^{-2+3i/100}$, where the value of i is given in the left-hand column.

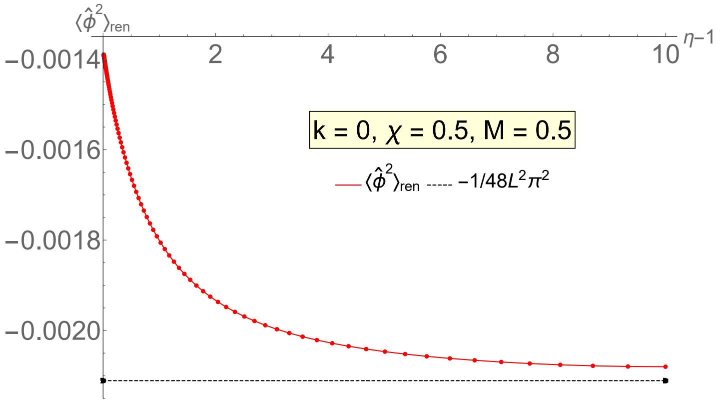

(a) $\chi = 0.5$

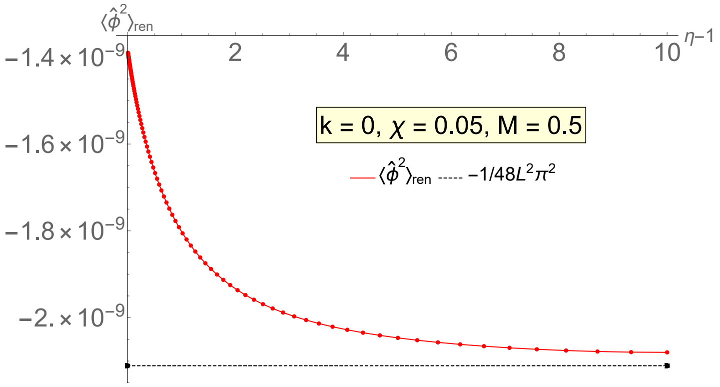

(b) $\chi = 0.05$

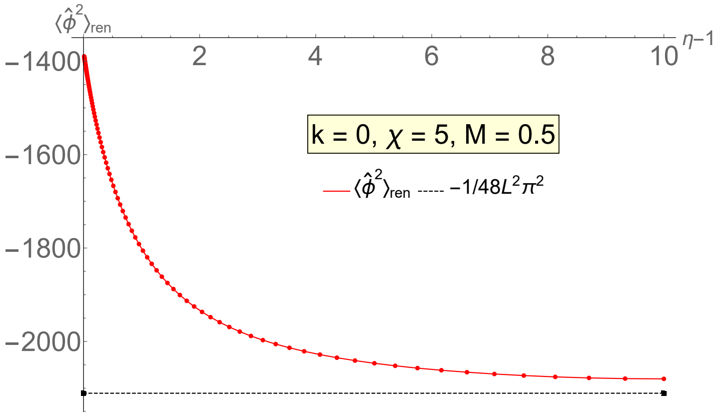

(c) $\chi = 5$

Figure 5.21: The behaviour of $\langle\hat{\phi}^2\rangle_{ren}$ with Dirichlet boundary conditions imposed on an adS black hole with flat horizon, where we fix $M = 0.5$ and vary the value of χ. All plots are as functions of η. The VP was calculated with 70 terms in the n-sum and a grid of terms over ℓ up to $\ell_1 = 50$. All plots are formed by rescaling the original data used in Figure 5.17. The resulting functions all approach the CadS limit $-1/48\pi^2 L^2$, shown as a dashed black line in each plot.

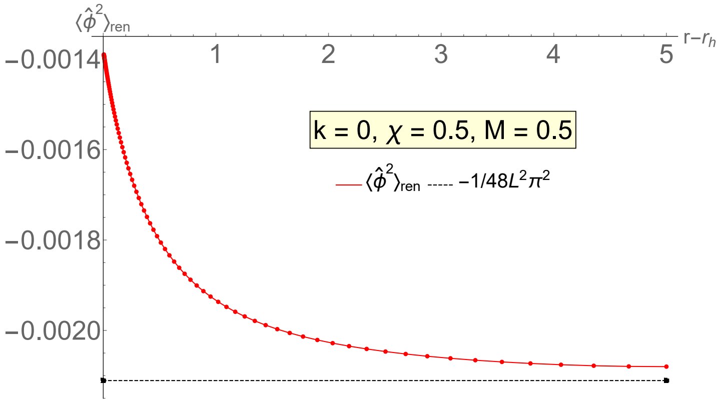

(a) $\chi = 0.5$

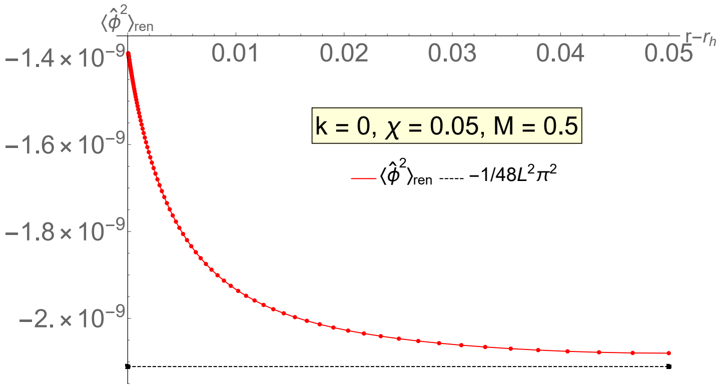

(b) $\chi = 0.05$

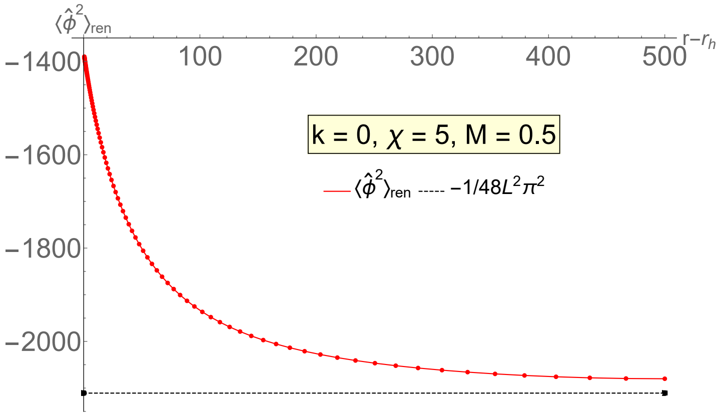

(c) $\chi = 5$

Figure 5.22: The behaviour of $\langle\hat{\phi}^2\rangle_{ren}$ with Dirichlet boundary conditions imposed on an adS black hole with flat horizon, this time plotted as functions of r. The difference in behaviour as we vary χ is now more noticeable, with the convergence to the CadS limit (the black dashed line) slower for larger χ.

χ, there is only a very small difference between the horizon value and the CadS limit (around 10^{-9} when $\chi = 0.05$), whilst for large values of χ, the difference is much greater (around 600 for $\chi = 5$).

Varying χ does of course alter the rate of convergence to the CadS limit, which can be clearly seen when we look at the plots as functions of r in Figure 5.22. Now we can see that convergence is much slower for large values of χ, with convergence to the CadS limit not occurring until $r \sim 500$ for $\chi = 5$. The convergence is much quicker for smaller values of χ (we can see convergence to the CadS limit occurring for $r \sim 5$ when $\chi = 0.5$). It is important to remember that all of these results are calculated simply by rescaling the original calculation, so there is no change in the number of terms in the n-sum or the density of the grid in the ℓ-integral required to obtain accurate results.

5.6.3 Numerical results for hyperbolic horizons

The VP is calculated in the case of black hole with hyperbolic horizon for mass $M = 3$, cosmological constant $\Lambda = -3$ and horizon radius $r_h = 2$. These values are chosen to allow us to compare with the cases in the $k = 1, 0$ cases with $r_h = 2, \Lambda = -3$, where, since $L = 1$, all results are expected to converge to the CadS limit $-1/48\pi^2$ (3.2).

We test convergence for the n-sum by constructing the log plots (5.122-5.124). These plots are shown in Figure 5.23. We truncate the n-sum at $n = 70$, and calculate each term with 100 digits of precision. As we saw previously in the $k = 1, 0$ cases, the log plots approach a constant value for large n, suggesting good convergence in the n-sum. This convergence is not as rapid for large ℓ and r. This is not necessarily a problem for large ℓ since the individual terms in the sum become incredibly small as ℓ increases and so should not affect the accuracy of our final result. For large r, we would need to use more terms in the n-sum to accurately capture results this far from the horizon.

The convergence of the ℓ-integrand is shown in Figure 5.24. Again, this converges quickly to zero, with quicker convergence occurring close to the horizon. It is possible that an increase in the number of terms in the n-sum would allow for faster convergence far from the horizon. We integrate over a grid in ℓ, by calculating a discrete number of terms in the integral, and then creating an interpolation function over these terms. As in the $k = 0$ case, we are forced to use a denser grid in ℓ close to $\ell = 0$ in order to properly capture the behaviour of the integrand in our interpolation function. We calculate every half-integer ℓ for $\ell \in [4, 50]$ and every 1/20-integer ℓ for $\ell \in (0, 4]$. We cut off the integral at $\ell_1 = 50$.

The integral is performed as in the $k = 0$ case, by calculating the n-sum and then interpolating over ℓ to get a smooth function in ℓ across a grid in η. The integral is performed numerically. The resulting plot is shown in Figure 5.25 in terms of coordinate η, where the horizon is located at $\eta = 1$. As in all previous cases, the VP approaches the value $-1/48\pi^2$. In fact, this approach occurs at a much quicker rate than in the $k = 1, 0$ cases, with convergence occurring at $\eta - 1 \sim 7$ (see Figure 5.30 for a direct comparison between all three event horizon topologies). In fact, our results were found to quickly lose accuracy after this point, due to the truncation of the n-sum and ℓ-integral. In the next subsection, we shall look at various accuracy tests, and see how we can improve these results close to the boundary.

Accuracy tests for $k = -1$

Errors arise in the calculation of the VP in the hyperbolic horizon case in a similar way to the flat horizon case. We introduce errors by truncating the n-sum at $n = 50$, by cutting off the ℓ-integral at $\ell_1 = 50$ and by using a discrete grid of ℓ values for the integrand.

Thus, accuracy tests are very similar to the previous $k = 0$ case. To test for errors arising from the truncation of the n-sum, we calculate the relative error between the case where we truncate the sum at $n = 60$ and the case where we truncate the sum at $n = 70$. These values can be seen in Table 5.26. This introduces the smallest error in the calculation, which matches results found in previous cases (see Tables 5.4, 5.7, 5.10, 5.13, 5.18).

Errors also arise from the grid we use in the ℓ-integrand. In our calculation, we evaluate the integrand at every half-integer ℓ for $\ell > 4$, and at every 1/20-integer for $\ell < 2$. We can compare this with the same calculation performed with the ℓ-integrand evaluated at every 1/10-integrand for $\ell < 4$. Relative errors are given in Table 5.27. We find that these errors are larger close to the horizon, and smaller further away.

We approximate the tail of the integral as in the $k = 0$ case, by assuming it has the form $a \times \ell^{-(1+\epsilon)}$ for some values of a and ϵ, where a will depend on the value of r. Using `FindFit` in `Mathematica`, we find that the value of ϵ is close to 4 near the horizon (as we would expect) but far from the horizon, this value begins to increase. This is because we lose accuracy far from the horizon. As mentioned in the previous subsection, convergence to the CadS limit is lost above $\eta - 1 \sim 8$. This means that the error from the cut-off of the integral gets bigger the further we get from the horizon (see Table 5.28). Therefore, to increase accuracy further from the horizon, and allow us to accurately plot results for larger values of η we must shift the value of ℓ_1 and not cut off the integral so soon. However, when $\Lambda = -3$ and $r_h = 2$, we see convergence to the CadS limit (3.2) for the values of η that we have considered, so there is no need, in this case, to increase ℓ_1.

For small values of η, we conclude, as in the $k = 0$ case, that the largest errors are introduced via the density of the grid in ℓ that is used.

Varying Λ

We look at different values of Λ by fixing $M = 0.5$ and then varying the value of χ (5.4). We choose to look at three different values of χ, which each give us different

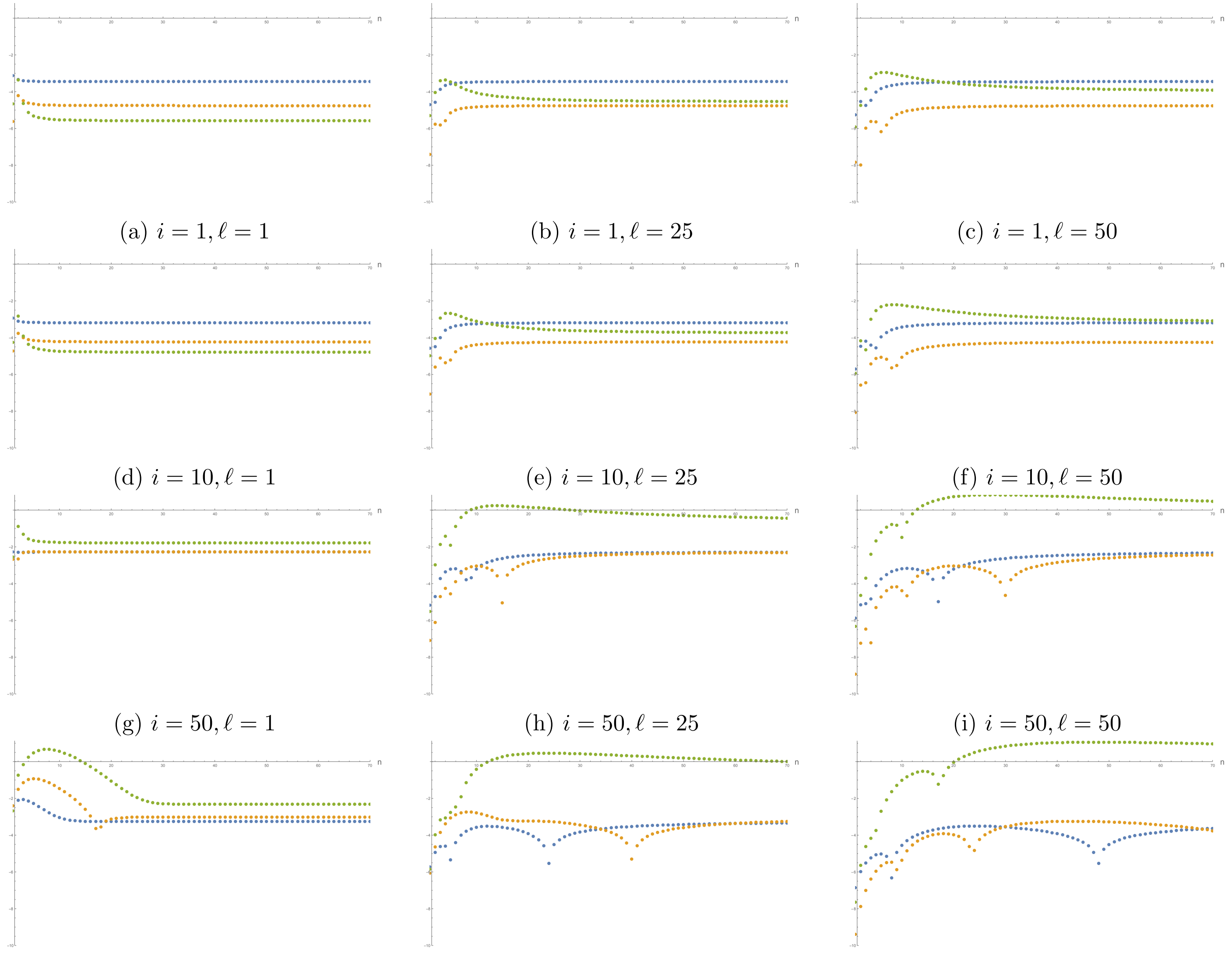

(a) $i = 1, \ell = 1$ (b) $i = 1, \ell = 25$ (c) $i = 1, \ell = 50$

(d) $i = 10, \ell = 1$ (e) $i = 10, \ell = 25$ (f) $i = 10, \ell = 50$

(g) $i = 50, \ell = 1$ (h) $i = 50, \ell = 25$ (i) $i = 50, \ell = 50$

(j) $i = 90, \ell = 1$ (k) $i = 90, \ell = 25$ (l) $i = 90, \ell = 50$

Figure 5.23: Log plots showing convergence of the inner sum over n for the case of an adS black hole with hyperbolic horizon, $M = 3$, $\Lambda = -3$. The blue line represents (5.122), the orange line represents (5.123) and the green line represents (5.124). The value of n runs along the x-axis. The calculation was performed at each integer value of $n \in [0, 70]$. Each individual point in the plot represents a different value of n. The radius is given by $r = r_h + 10^{-2+3i/100}$, where i is given below each plot. The value of ℓ is also given. Each line approaches a constant as n increases, indicating good convergence in the n-sum for all values of ℓ and r. Qualitatively similar behaviour is obtained for other values of ℓ and r.

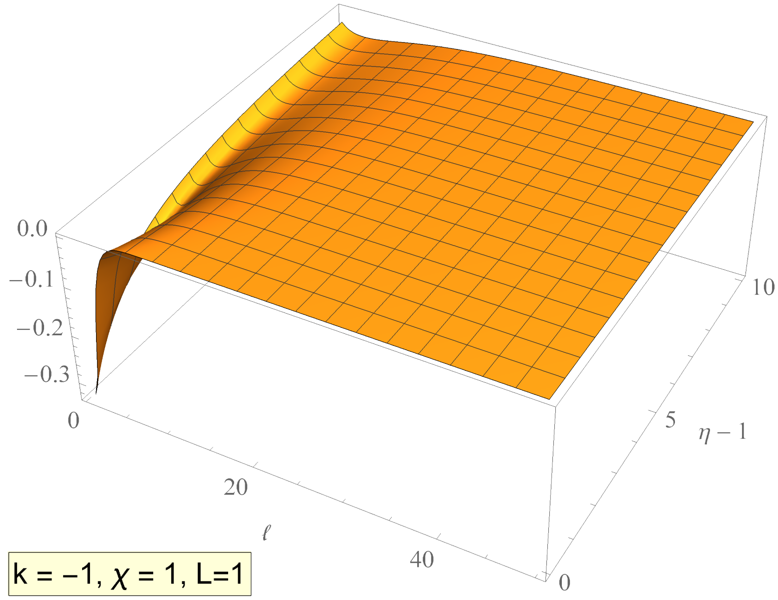

Figure 5.24: The ℓ-integrand (5.125) on an adS black hole with hyperbolic horizon, $M=3,\ \Lambda=-3$. This converges quickly to zero as ℓ increases, but this convergence is not uniform. The convergence is more rapid for small values of η.

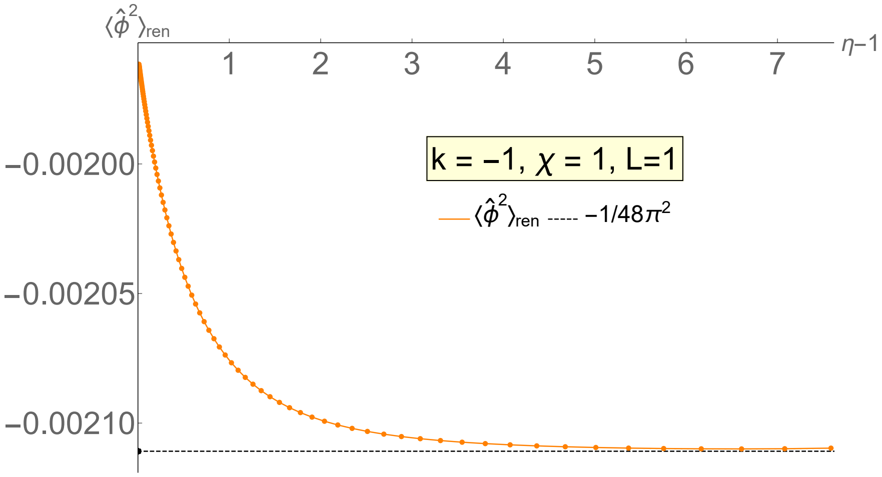

Figure 5.25: The behaviour of $\langle\hat{\phi}^2\rangle_{ren}$ with Dirichlet boundary conditions imposed on an adS black hole with hyperbolic horizon, $M=5,\ \Lambda=-3$. The VP is calculated by truncating the n-sum at $n=70$, and then integrating over a grid of ℓ up to $\ell_1=50$. The resulting function is negative throughout the spacetime, and monotonically decreasing as η increases, approaching the CadS limit $-1/48\pi^2$ (3.2) at the boundary. This limit is shown by the dashed black line.

i	Relative error
10	-3.7973×10^{-14}
20	-2.7260×10^{-13}
30	-1.7764×10^{-12}
40	-9.6470×10^{-12}
50	-3.7827×10^{-11}
60	-8.7374×10^{-11}
70	-9.6884×10^{-11}
80	-4.8292×10^{-11}
90	-1.2847×10^{-11}
100	-2.5689×10^{-12}

Table 5.26

i	Relative error
10	0.0002767
20	0.0002709
30	0.0002600
40	0.0002403
50	0.0002076
60	0.0001607
70	0.0001060
80	0.00005724
90	0.00002511
100	9.2392×10^{-6}

Table 5.27

Relative errors in the case $M = 3, \Lambda = -3$. The radial coordinate is given by $r = r_h + 10^{-2+3i/100}$, where the value of i is given in the left-hand column.

Table 5.26: The relative error $\frac{\langle\hat{\phi}^2\rangle_{70}-\langle\hat{\phi}^2\rangle_{60}}{\langle\hat{\phi}^2\rangle_{60}}$, where $\langle\hat{\phi}^2\rangle_y$ is the VP calculated with the n-sum truncated at $\pm y$.

Table 5.27: The relative error $\frac{\langle\hat{\phi}^2\rangle_{1/20}-\langle\hat{\phi}^2\rangle_{1/10}}{\langle\hat{\phi}^2\rangle_{1/10}}$, where $\langle\hat{\phi}^2\rangle_y$ is the VP calculated with y steps between ℓ-modes when $\ell < 4$, and half-integer steps for $\ell > 4$.

i	Approximate value of integral tail
10	-1.2831×10^{-8}
20	-1.1985×10^{-8}
30	-1.0302×10^{-8}
40	-6.5160×10^{-9}
50	-8.1413×10^{-10}
60	3.9646×10^{-8}
70	8.6364×10^{-8}
80	9.2432×10^{-8}
90	-2.1769×10^{-6}
100	-0.0004357

Table 5.28: The approximate value of the tail of the ℓ-integral in the case of a black hole with hyperbolic event horizon, $M = 3,\ \Lambda = -3$. The radial coordinate is given by $r = r_h + 10^{-2+3i/100}$, where the value of i is given in the left-hand column.

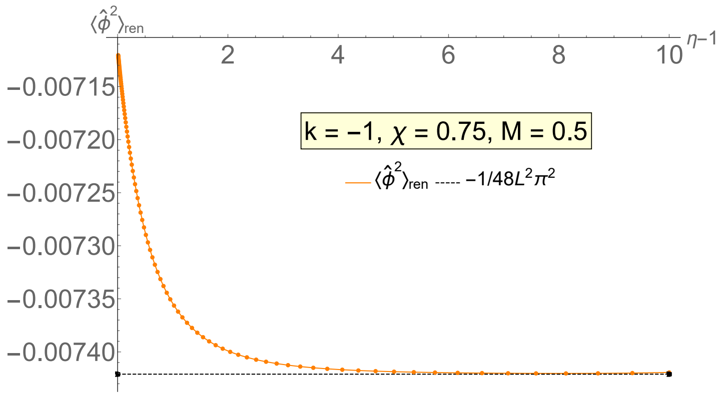

(a) $\chi = 0.75$

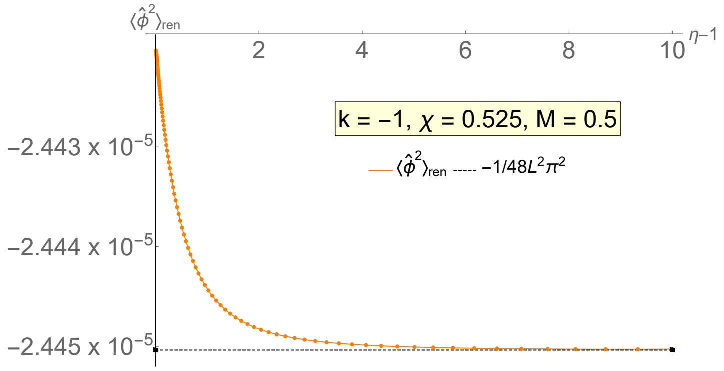

(b) $\chi = 0.525$

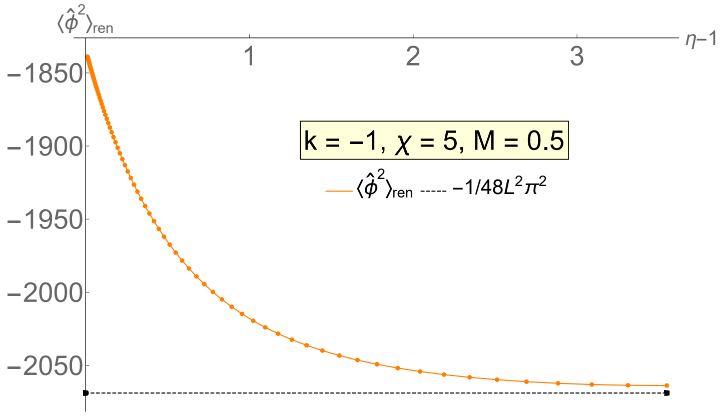

(c) $\chi = 5$

Figure 5.29: The behaviour of $\langle\hat{\phi}^2\rangle_{ren}$ with Dirichlet boundary conditions imposed on an adS black hole with hyperbolic horizon, where we fix $M = 0.5$ and vary the value of χ. All plots are as functions of η. The VP was calculated by truncating the n-sum at $n = 70$ and truncating the ℓ-integral at $\ell = \ell_1$, where $\ell_1 = 50$ when $\chi = 0.75,\ 0.525$ and $\ell_1 = 130$ when $\alpha = 10$. A denser grid in ℓ is required close to $\ell = 0$ when $\chi = 0.75$. All cases approach the CadS limit (3.2), shown by the dotted black line.

magnitudes of Λ. It should be noted that we must have $\chi > 0.5$ for the black hole to exist.

The first case we look at is $\chi = 0.75$ (see Figure 5.29a for results of renormalised VP) which corresponds to $\Lambda = -\frac{675}{64} \sim -10$. This case is similar to the initial $k = -1$ case considered, as Λ is similar in size. We truncate the n-sum at $n = 70$, and truncate the ℓ-integral at $\ell_1 = 50$, using a half-integer grid in ℓ for $\ell \in [2, 50]$ and a 1/10-integral grid in ℓ for $\ell < 2$. As before, the results approach the CadS value $-1/48\pi^2 L^2$ (3.2). In this case, the convergence to the CadS limit occurs at $\eta - 1 \sim 7$, similar to the initial case, although here the accuracy far from the horizon is better, meaning that we do not lose convergence until $\eta - 1 > 10$. This can be seen by performing similar accuracy tests to the previous case. The difference between the expected asymptotic value (3.2) and the results at $\eta = 11$ differ by $\sim 10^{-6}$.

The second case we consider is $\chi = 0.525$ (see Figure 5.29b for the results of renormalised VP), which corresponds to $\Lambda \sim -3.4749 \times 10^{-2}$. Due to the nature of the integrand, we need to calculate a denser grid of ℓ-modes closer to 0 in order to properly capture its behaviour. We use a half-integer grid in ℓ for $\ell \in [4, 50]$ and a 1/20-integer grid in ℓ for $\ell < 4$. This denser grid means that we obtain good convergence far from the horizon. The results for the VP again converge to the expected CadS limit as η increases, and the VP remains negative throughout the spacetime.

The final case involves a large cosmological constant, where we choose $\chi = 5$ (see Figure 5.29c for results of renormalised VP), which corresponds to $\Lambda \sim -2.94 \times 10^6$. The convergence of the VP to the CadS value (3.2) now occurs much closer to the event horizon. Due to the nature of the integrand, we cut-off the ℓ-integral at $\ell_1 = 130$, but find that we do not require such a fine grid close to $\ell = 0$. We use a 1/2-integer grid for all values of ℓ. We can see that convergence to the CadS limit occurs at $\eta - 1 \sim 3$. To obtain accurate results for larger values of η, we would need to cut-off the integral at a much larger value of ℓ_1.

To summarise, for small Λ, we can afford to cut off the integral at a smaller value of ℓ_1, but we must use a denser grid over ℓ. For a larger value of Λ, we must use a larger ℓ_1, but the grid does not have to be as dense.

A comparison of VP results for all three types of event horizon topology is given in Figure 5.30, for $L = 1, \chi = 1$. This allows us to directly compare the speed of convergence across all three cases, as well as the value of VP on the event horizon $\eta = 1$.

5.7 Extension to general coupling

In this section, we discuss the extension of the theory presented in sections 5.3-5.6 to include scalar fields of nonzero mass or general coupling.

When $m = 0$ and $\xi = 1/6$, the tail of the Hadamard parametrix (1.187), $V(x, x')$, vanishes at leading order and so we do not need to calculate it in order to renormalise

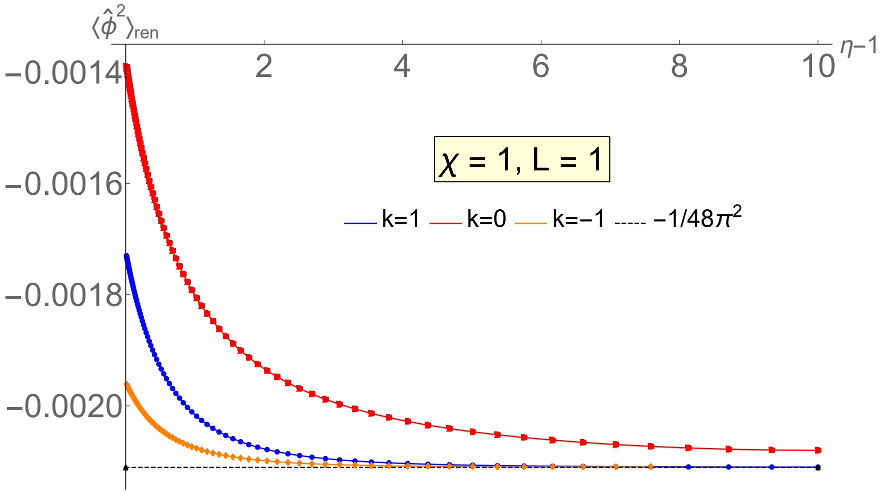

Figure 5.30: The behaviour of $\langle\hat{\phi}^2\rangle_{ren}$ with Dirichlet boundary conditions imposed on an adS black hole with varying black hole topology. In each case, $L = 1, \chi = 1$, which means that the event horizon radius is the same in each case, as is the CadS limit approached at the boundary. This case allows us to directly compare speed of convergence across all three cases considered.

the VP.

For general coupling, the tail does not vanish at leading order, and in particular, we have to write it in the form (1.229) in order to use the extended coordinates method. The tail coefficients $\mathcal{T}_{ij}$ can be found by substituting (1.220, 1.223) into (1.189, 1.190) and comparing coefficients at each order of ϵ, where the extended coordinates (s, w) are treated as $\mathcal{O}(\epsilon)$. This procedure can be carried out in `Mathematica`, and the results are given in Table 5.31.

The terms in the tail, that is, terms of the form $\log(\ell_0^2 s^2)s^{2i-2j}w^{2j}$ (1.230), are then written in the same mode-sum representation as the Euclidean Green's function (5.20-5.23) and the direct part of the Hadamard parametrix (5.42, 5.61, 5.75).

This is done in the $k = 1$ case in [13]. This work is presented in section 5.7.1. We seek to extend this work to the $k = 0$ and $k = -1$ cases in sections 5.7.2, 5.7.3 respectively.

5.7.1 Spherical horizons

In the $k = 1$ case, we write the tail terms (1.230) in the same form as the Euclidean Green's function (5.20, 5.21), that is,

$$s^{2i-2j}w^{2j}\log(\ell_0^2 s^2) = \sum_{\ell=0}^{\infty}(2\ell+1)P_\ell(\cos\gamma_S)\sum_{n=-\infty}^{\infty}e^{in\kappa\Delta\tau}\chi_{n\ell}(i,j|r) \tag{5.130}$$

$\mathcal{T}_{00}^{(l)}$	$-\frac{1}{2}\xi f''(r)+\frac{f''(r)}{12}-\frac{2\xi f'(r)}{r}+\frac{f'(r)}{3r}-\frac{\xi f(r)}{r^2}+\frac{f(r)}{6r^2}+\frac{k\xi}{r^2}-\frac{k}{6r^2}+\frac{m^2}{2}$
$\mathcal{T}_{10}^{(l)}$	$\frac{1}{48}\xi f(r)f^{(4)}(r)-\frac{1}{240}f(r)f^{(4)}(r)+\frac{\xi f(r)f^{(3)}(r)}{6r}-\frac{7f(r)f^{(3)}(r)}{240r}-\frac{k\xi^2 f''(r)}{4r^2}+\frac{k\xi f''(r)}{24r^2}-\frac{1}{8}m^2\xi f''(r)+\frac{1}{48}m^2 f''(r)$ $+\frac{\xi^2 f(r)f''(r)}{4r^2}+\frac{\xi f(r)f''(r)}{6r^2}-\frac{f(r)f''(r)}{30r^2}+\frac{1}{16}\xi^2 f''(r)^2-\frac{1}{48}\xi f''(r)^2+\frac{1}{480}f''(r)^2-\frac{k\xi^2 f'(r)}{r^3}+\frac{k\xi f'(r)}{6r^3}-\frac{m^2\xi f'(r)}{2r}$ $+\frac{m^2 f'(r)}{24r}+\frac{\xi^2 f(r)f'(r)}{r^3}-\frac{\xi f(r)f'(r)}{3r^3}+\frac{f(r)f'(r)}{40r^3}+\frac{\xi^2 f'(r)^2}{r^2}-\frac{5\xi f'(r)^2}{24r^2}+\frac{f'(r)^2}{120r^2}+\frac{1}{48}\xi f^{(3)}(r)f'(r)-\frac{1}{240}f^{(3)}(r)f'(r)$ $+\frac{\xi^2 f'(r)f''(r)}{2r}-\frac{\xi f'(r)f''(r)}{24r}-\frac{f'(r)f''(r)}{120r}-\frac{k\xi^2 f(r)}{2r^4}+\frac{k\xi f(r)}{12r^4}-\frac{m^2\xi f(r)}{4r^2}+\frac{\xi^2 f(r)^2}{4r^4}$ $-\frac{\xi f(r)^2}{12r^4}+\frac{f(r)^2}{120r^4}+\frac{k^2\xi^2}{4r^4}-\frac{k^2}{120r^4}+\frac{km^2\xi}{4r^2}+\frac{m^4}{16}$
$\mathcal{T}_{11}^{(l)}$	$\frac{1}{480}f^{(4)}(r)f(r)^2-\frac{\xi f^{(3)}(r)f(r)^2}{24r}+\frac{f^{(3)}(r)f(r)^2}{80r}-\frac{1}{48}m^2 f(r)f''(r)-\frac{\xi f(r)^2 f''(r)}{6r^2}+\frac{f(r)^2 f''(r)}{40r^2}+\frac{1}{48}\xi f(r)f''(r)^2-\frac{1}{240}f(r)f''(r)^2$ $+\frac{k\xi f(r)f'(r)}{4r^3}-\frac{kf(r)f'(r)}{24r^3}-\frac{\xi f(r)^2 f'(r)}{6r^3}+\frac{f(r)^2 f'(r)}{30r^3}-\frac{\xi f(r)f'(r)^2}{24r^2}+\frac{f(r)f'(r)^2}{240r^2}+\frac{1}{48}\xi f^{(3)}(r)f(r)f'(r)$ $-\frac{1}{480}f^{(3)}(r)f(r)f'(r)+\frac{\xi f(r)f'(r)f''(r)}{6r}-\frac{f(r)f'(r)f''(r)}{40r}-\frac{k^2\xi f(r)}{12r^4}+\frac{k^2 f(r)}{60r^4}-\frac{km^2 f(r)}{24r^2}+\frac{m^2 f(r)^2}{24r^2}+\frac{\xi f(r)^3}{12r^4}-\frac{f(r)^3}{60r^4}$
$\mathcal{T}_{10}^{(p)}$	$-\frac{k\xi f''(r)}{24r^2}+\frac{kf''(r)}{144r^2}+\frac{\xi f(r)f''(r)}{24r^2}-\frac{f(r)f''(r)}{144r^2}-\frac{k\xi f'(r)}{6r^3}+\frac{kf'(r)}{36r^3}+\frac{\xi f(r)f'(r)}{6r^3}-\frac{f(r)f'(r)}{36r^3}-\frac{k\xi f(r)}{6r^4}$ $+\frac{kf(r)}{36r^4}-\frac{m^2 f(r)}{24r^2}+\frac{\xi f(r)^2}{12r^4}-\frac{f(r)^2}{72r^4}+\frac{k^2\xi}{12r^4}-\frac{k^2}{72r^4}+\frac{km^2}{24r^2}$
$\mathcal{T}_{11}^{(p)}$	$\frac{k\xi f(r)f''(r)}{12r^2}-\frac{kf(r)f''(r)}{72r^2}-\frac{\xi f(r)^2 f''(r)}{12r^2}+\frac{f(r)^2 f''(r)}{72r^2}+\frac{k\xi f(r)f'(r)}{4r^3}-\frac{kf(r)f'(r)}{24r^3}-\frac{m^2 f(r)f'(r)}{24r}-\frac{\xi f(r)^2 f'(r)}{4r^3}+\frac{f(r)^2 f'(r)}{24r^3}+\frac{\xi f(r)f'(r)^2}{6r^2}$ $-\frac{f(r)f'(r)^2}{36r^2}+\frac{\xi f(r)f'(r)f''(r)}{24r}-\frac{f(r)f'(r)f''(r)}{144r}-\frac{k^2\xi f(r)}{6r^4}+\frac{k^2 f(r)}{36r^4}-\frac{km^2 f(r)}{12r^2}+\frac{k\xi f(r)^2}{3r^4}-\frac{kf(r)^2}{18r^4}+\frac{m^2 f(r)^2}{12r^2}-\frac{\xi f(r)^3}{6r^4}+\frac{f(r)^3}{36r^4}$
$\mathcal{T}_{10}^{(r)}$	$-\frac{k\xi f(r)^2 f''(r)}{24r^2}+\frac{kf(r)^2 f''(r)}{144r^2}+\frac{\xi f(r)^3 f''(r)}{24r^2}-\frac{f(r)^3 f''(r)}{144r^2}-\frac{1}{24}\kappa^2\xi f(r)f''(r)+\frac{1}{144}\kappa^2 f(r)f''(r)-\frac{k\xi f(r)^2 f'(r)}{12r^3}$ $+\frac{kf(r)^2 f'(r)}{72r^3}-\frac{k\xi f(r)f'(r)^2}{48r^2}+\frac{kf(r)f'(r)^2}{288r^2}+\frac{m^2 f(r)^2 f'(r)}{24r}-\frac{1}{96}m^2 f(r)f'(r)^2+\frac{\xi f(r)^3 f'(r)}{12r^3}-\frac{f(r)^3 f'(r)}{72r^3}$ $-\frac{7\xi f(r)^2 f'(r)^2}{48r^2}+\frac{7f(r)^2 f'(r)^2}{288r^2}-\frac{\kappa^2\xi f(r)f'(r)}{6r}+\frac{\kappa^2 f(r)f'(r)}{36r}+\frac{\xi f(r)f'(r)^3}{24r}-\frac{f(r)f'(r)^3}{144r}-\frac{\xi f(r)^2 f'(r)f''(r)}{24r}$ $+\frac{1}{96}\xi f(r)f'(r)^2 f''(r)+\frac{f(r)^2 f'(r)f''(r)}{144r}-\frac{1}{576}f(r)f'(r)^2 f''(r)+\frac{k^2\xi f(r)^2}{12r^4}-\frac{k^2 f(r)^2}{72r^4}+\frac{km^2 f(r)^2}{24r^2}$ $-\frac{k\xi f(r)^3}{6r^4}+\frac{kf(r)^3}{36r^4}+\frac{\kappa^2 k\xi f(r)}{12r^2}-\frac{\kappa^2 kf(r)}{72r^2}-\frac{m^2 f(r)^3}{24r^2}+\frac{1}{24}\kappa^2 m^2 f(r)+\frac{\xi f(r)^4}{12r^4}-\frac{f(r)^4}{72r^4}-\frac{\kappa^2\xi f(r)^2}{12r^2}+\frac{\kappa^2 f(r)^2}{72r^2}$

Table 5.31: Tail coefficients $\mathcal{T}_{ij}$. The index l, p and r denotes logarithm, polynomial and rational respectively.

for some regularisation parameters $\chi_{n\ell}$. These can be determined by inverting (5.130). This is done by multiplying both sides by $e_{\ell'}^{-in'\kappa\Delta\tau}(\cos\gamma_S)$ and integrating over $\cos\gamma_S$ and $\Delta\tau$ using [120, eq. 14.17.6]. This inversion procedure is that same as that used in section 5.4.1 (in fact, much of the calculation here mirrors that in section 5.4.1). We obtain

$$\chi_{n\ell}(i,j|r) = \frac{\kappa}{4\pi}\int_{\Delta\tau=0}^{2\pi/\kappa}\int_{\cos\gamma_S=-1}^{1} e^{-in\kappa\Delta\tau}P_\ell(\cos\gamma_S)s^{2i-2j}w^{2j}\log(\ell_0^2 s^2)\; d(\cos\gamma_S)\; d\Delta\tau. \tag{5.131}$$

We use expressions for s and z in (5.44) to write

$$\begin{aligned}\chi_{n\ell}(i,j|r) = \frac{\kappa}{4\pi}(2r^2)^{i-j}\int_{\Delta\tau=0}^{2\pi/\kappa} e^{-in\kappa\Delta\tau}w^{2j}\int_{\cos\gamma_S=-1}^{1} P_\ell(\cos\gamma_S)(z-\cos\gamma_S)^{i-j}\\ \times\left[\log(2\ell_0^2 r^2)+\log(z-\cos\gamma_S)\right]\; d(\cos\gamma_S)\; d\Delta\tau.\end{aligned} \tag{5.132}$$

The integral over $\cos\gamma_S$ can be performed by using the identity [120, eq. 14.7.10]

$$P_\ell(x) = \frac{(-1)^\ell}{2^\ell \ell!}\left(\frac{d}{dx}\right)^\ell (1-x^2)^\ell \tag{5.133}$$

so that the first integral that we want to evaluate is given by

$$I_1 = \int_{\cos\gamma_S=-1}^{1}(z-\cos\gamma_S)^{i-j}\left(\frac{d}{d\cos\gamma_S}\right)^\ell(1-\cos^2\gamma_S)^\ell\; d(\cos\gamma_S). \tag{5.134}$$

Integrating by parts, we obtain

$$\begin{aligned}I_1 = &\left[(z-\cos\gamma_S)^{i-j}\left(\frac{d}{d\cos\gamma_S}\right)^{\ell-1}(1-\cos^2\gamma_S)^\ell\right]_{\cos\gamma_S=-1}^{1}\\ &-(-1)^{i-j}(i-j)\int_{\cos\gamma_S=-1}^{1}\left(\frac{d}{d\cos\gamma_S}\right)^{\ell-1}(1-\cos^2\gamma_S)^\ell(z-\cos\gamma_S)^{i-j-1}\; d(\cos\gamma_S).\end{aligned} \tag{5.135}$$

The first term in (5.135) vanishes, and we integrate the second term by parts again. In total, we integrate (5.134) by parts ℓ times to obtain

$$I_1 = (i-j-\ell+1)_\ell\int_{\cos\gamma_S=-1}^{1}(1-\cos^2\gamma_S)^\ell(z-\cos\gamma_S)^{i-j-\ell}\; d(\cos\gamma_S) \tag{5.136}$$

where $(a)_\ell$ is the Pochhammer symbol defined by [120, eq. 5.2.4]

$$(a)_0 = 1, \quad (a)_\ell = a(a+1)(a+2)...(a+\ell-1). \tag{5.137}$$

If $\ell > i-j$, then (5.136) is zero.

The integral over the logarithm is also calculated using (5.133) and then integrating ℓ times by parts. We find

$$\begin{aligned} I_2 &= \int_{\cos\gamma_S=-1}^{1} \log(z-\cos\gamma_S)(z-\cos\gamma_S)^{i-j}\left(\frac{d}{d\cos\gamma_S}\right)^{\ell}(1-\cos^2\gamma_S)^{\ell}\; d(\cos\gamma_S) \\ &= \int_{\cos\gamma_S=-1}^{1} B_{\ell ij}(z,\cos\gamma_S)(1-\cos^2\gamma_S)^{\ell}\; d(\cos\gamma_S) \end{aligned} \tag{5.138}$$

where

$$B_{\ell ij}(z,\cos\gamma_S) = \begin{cases} (-1)^{i-j-\ell+1}(i-j)!(\ell-i+j-1)!(z-\cos\gamma_S)^{i-j-\ell}, & \text{for } \ell > i-j, \\ (z-\cos\gamma_S)^{i-j-\ell}(i-j-\ell+1)_{\ell}\left[\log(z-\cos\gamma_S)\right. & \\ \qquad\qquad \left.+\psi(i-j+1)-\psi(i-j+1-\ell)\right], & \text{for } \ell \le i-j. \end{cases} \tag{5.139}$$

We consider the case where $\ell > i-j$ first. Substituting (5.136, 5.138) into (5.132), we obtain

$$\begin{aligned} \chi_{n\ell}(i,j|r) = \frac{\kappa(-1)^{i-j+1}(i-j)!(\ell-i+j-1)!(2r^2)^{i-j}}{2^{\ell+2}\pi\;\ell!} \int_{\Delta\tau=-1}^{1} e^{-in\kappa\Delta\tau} w^{2j} \\ \times \int_{\cos\gamma_S=-1}^{1} (z-\cos\gamma_S)^{i-j-\ell}(1-\cos^2\gamma_S)^{\ell}\; d(\cos\gamma_S). \end{aligned} \tag{5.140}$$

The integral over $\cos\gamma_S$ can now be performed using [120, eq. 14.12.11], and so we find

$$\chi_{n\ell}(i,j|r) = \frac{\kappa(i-j)!(2r^2)^{i-j}}{2\pi} \int_{\Delta\tau=0}^{2\pi/\kappa} e^{-in\kappa\Delta\tau} w^{2j}(z^2-1)^{\frac{i-j+1}{2}} Q_{\ell}^{-i+j-1}(z)d\Delta\tau. \tag{5.141}$$

Using the relation [12, eq. 36],

$$(z^2-1)^{j/2}Q_{\nu}^{-j}(z) = \sum_{k=0}^{j} \frac{(-1)^k}{2^{j+1}}\binom{j}{k}\frac{(2\nu+2j-4k+1)}{(\nu-k+\frac{1}{2})_{j+1}} Q_{\nu+j-2k}(z), \tag{5.142}$$

the regularisation parameters for the tail can be written

$$\begin{aligned} \chi_{n\ell}(i,j|r) = \frac{\kappa(i-j)!r^{2i-2j}}{4\pi} \sum_{k=0}^{i-j+1}(-1)^k\binom{i-j+1}{k}\frac{(\ell+i-j-2k+\frac{3}{2})}{(\ell-k+\frac{1}{2})_{i-j+2}} \\ \times \int_{0}^{2\pi/\kappa} e^{-in\kappa\Delta\tau} w^{2j} Q_{\ell+i-j+1-2k}(z)d\Delta\tau. \end{aligned} \tag{5.143}$$

The parameter z depends on $\Delta\tau$. We factor out this time dependence in the same way as in section 5.4.1, by defining μ_1 via (5.49) and using the addition theorem (5.53).

The regularisation parameters are therefore given by

$$\begin{aligned}\chi_{n\ell}(i,j|r) =&\frac{\kappa(i-j)!r^{2i-2j}}{4\pi}\sum_{k=0}^{i-j+1}(-1)^k\binom{i-j+1}{k}\frac{(\ell+i-j-2k+\frac{3}{2})}{(\ell-k+\frac{1}{2})_{i-j+2}}\\ &\times\int_0^{2\pi/\kappa}e^{-in\kappa\Delta\tau}w^{2j}\Big[P_{\ell+i-j+1-2k}(\mu_1)Q_{\ell+i-j-1-2k}(\mu_1)\\ &+2\sum_{m=1}^{\infty}(-1)^m P^{-m}_{\ell+i-j+1-2k}(\mu_1)Q^{m}_{\ell+i-j+1-2k}(\mu_1)\cos(m\kappa\Delta\tau)\Big]\,d\Delta\tau.\end{aligned} \tag{5.144}$$

The integral over $\Delta\tau$, after substituting w with our definition in (5.37), is then equivalent to that evaluated in (5.55). Evaluating this integral gives

$$\begin{aligned}\chi_{n\ell}(i,j|r) =&\frac{(-1)^n}{2\kappa^{2j}}(i-j)!(2j)!r^{2i-2j}\sum_{k=0}^{i-j+1}(-1)^k\binom{i-j+1}{k}\frac{(\ell+i-j-2k+\frac{3}{2})}{(\ell-k+\frac{1}{2})_{i-j+2}}\\ &\times\Bigg[\frac{P_{\ell+i-j+1-2k}(\mu_1)Q_{\ell+i-j+1-2k}(\mu_1)}{(j+n)!(j-n)!}\\ &+\sum_{m=\max\{1,n-j\}}^{n+j}\frac{P^{-m}_{\ell+i-j+1-2k}(\mu_1)Q^{m}_{\ell+i-j+1-2k}(\mu_1)}{(j+n-m)!(j-n+m)!}\\ &+\sum_{m=\max\{1,-n-j\}}^{j-n}\frac{P^{-m}_{\ell+i-j+1-2k}(\mu_1)Q^{m}_{\ell+i-j+1-2k}(\mu_1)}{(j+n+m)!(j-n-m)!}\Bigg]\end{aligned} \tag{5.145}$$

for $\ell > i-j$.

We now look at the case where $\ell \leq i-j$. We begin by naïvely substituting (5.136, 5.138) into (5.132) to obtain

$$\begin{aligned}\chi_{n\ell}(i,j|r) =&\frac{(-1)^l\kappa(2r^2)^{i-j}(i-j-\ell+1)_l}{2^{\ell+2}\pi\ l!}\int_{\Delta\tau=0}^{2\pi/\kappa}e^{-in\kappa\Delta\tau}w^{2j}\\ &\times\int_{\cos\gamma_S=-1}^{1}(z-\cos\gamma_S)^{i-j-\ell}(1-\cos^2\gamma_S)^{\ell}\left[\log(z-\cos\gamma_S)\right.\\ &\left.+\psi(i-j+1)-\psi(i-j+1-\ell)+\log\left(2\ell_0^2r^2\right)\right]\,d(\cos\gamma_S)\,d\Delta\tau.\end{aligned} \tag{5.146}$$

The integral over $\cos\gamma_S$ in (5.146) is not easily performed in terms of known functions. It is easier to return to (5.132) and look at the integral over $\cos\gamma_S$, which is

$$I_3 = \int_{\cos\gamma_S=-1}^{1}\log\left(2\ell_0^2r^2(z-\cos\gamma_S)\right)(z-\cos\gamma_S)^{i-j}P_\ell(\cos\gamma_S)\,d(\cos\gamma_S). \tag{5.147}$$

We can write

$$(z-\cos\gamma_S)^{\lambda} = \frac{d}{d\lambda}\left(\frac{(z-\cos\gamma_S)^{\lambda}}{\log(z-\cos\gamma_S)}\right) \tag{5.148}$$

and so

$$(z-\cos\gamma_S)^{i-j} = \left(2\ell_0^2 r^2\right)^{-i+j}\left[\frac{d}{d\lambda}\left(\frac{\left[2\ell_0^2 r^2(z-\cos\gamma_S)\right]^\lambda}{\log\left(2\ell_0^2 r^2(z-\cos\gamma_S)\right)}\right)\right]_{\lambda=i-j}. \tag{5.149}$$

The integral (5.147) can then be written

$$I_3 = \left[\frac{d}{d\lambda}\int_{\cos\gamma_S=-1}^{1}\left(2\ell_0^2 r^2\right)^{\lambda-i+j}(z-\cos\gamma_S)^\lambda P_\ell(|cos\gamma_S)\ d(\cos\gamma_S)\right]_{\lambda=i-j}. \tag{5.150}$$

The integral in (5.150) is the same as (5.136), and so the regularisation parameters (5.132) can be written

$$\begin{aligned}\chi_{n\ell}(i,j|r) &= \frac{\kappa}{4\pi}\left(\frac{2}{\kappa^2}\right)^j \frac{(-1)^\ell}{2^\ell \ell!}(2r^2)^{i-j}\int_{\Delta\tau=0}^{2\pi/\kappa} e^{-in\kappa\Delta\tau}(1-\cos\kappa\Delta\tau)^j \\ &\times\left[\frac{d}{d\lambda}\int_{-1}^{1}\left(2\ell_0^2 r^2\right)^{\lambda-i+j}(\lambda-\ell+1)_\ell(z-\cos\gamma_S)^{\lambda-\ell}(1-\cos^2\gamma_S)^\ell\ d(\cos\gamma_S)\right]_{\lambda=i-j} d\Delta\tau\end{aligned} \tag{5.151}$$

where we have now used the definition of w from (5.37). The integral over $\cos\gamma_S$ can be evaluated using [120, eq. 14.12.11],

$$\int_{\cos\gamma_S=-1}^{1}(z-\cos\gamma_S)^{\lambda-l}(1-\cos^2\gamma_S)^l\ d(\cos\gamma_S) = 2^{\ell+1}\ell!(z^2-1)^{(\lambda+1)/2}\mathbf{Q}_\ell^{-\lambda-1}(z) \tag{5.152}$$

where the functions $\mathbf{Q}_\nu^\mu$ are Olver's definition of Legendre functions [120] (see equation B.17). Note that (5.152) only holds in the case $\ell \neq 0$. The regularisation parameters for $\ell \leq i-j,\ \ell \neq 0$ are therefore given by

$$\begin{aligned}\chi_{n\ell}(i,j|r) =& \frac{\kappa}{2\pi}\left(\frac{2}{\kappa^2}\right)^j (2r^2)^{i-j}(-1)^\ell\int_{\Delta\tau=0}^{2\pi/\kappa} e^{-in\kappa\Delta\tau}(1-\cos\kappa\Delta\tau)^j \\ &\times\left[\frac{d}{d\lambda}\left(2\ell_0^2 r^2\right)^{\lambda-i+j}(\lambda-\ell+1)_\ell(z^2-1)^{(\lambda+1)/2}\mathbf{Q}_\ell^{-\lambda-1}(z)\right]_{\lambda=i-j} d\Delta\tau.\end{aligned} \tag{5.153}$$

When $\ell = 0$, the integral over $\cos\gamma_S$ is much more straightforward:

$$\int_{\cos\gamma_S=-1}^{1}(z-\cos\gamma_S)^\lambda\ d(\cos\gamma_S) = \frac{(z+1)^{1+\lambda}-(z-1)^{1+\lambda}}{1+\lambda}. \tag{5.154}$$

The regularisation parameters for $\ell = 0$ are therefore given by

$$\begin{aligned}\chi_{n0}(i,j|r) =& \frac{\kappa}{4\pi}\left(\frac{2}{\kappa^2}\right)^j (2r^2)^{i-j}\int_0^{2\pi/\kappa} e^{-in\kappa\Delta\tau}(1-\cos\kappa\Delta\tau)^j \\ &\times\left[\frac{d}{d\lambda}\left(2\ell_0^2 r^2\right)^{\lambda-i+j}\frac{(z+1)^{1+\lambda}-(z-1)^{1+\lambda}}{1+\lambda}\right]_{\lambda=i-j} d\Delta\tau.\end{aligned} \tag{5.155}$$

The regularisation parameters for the tail on an adS black hole with spherical event horizon are therefore given by (5.145, 5.153, 5.155). The integrals over $\Delta\tau$ in the latter two cases must be computed numerically. This numerical calculation is out of the scope of this thesis, which primarily focuses on massless, conformally coupled scalar fields. The numerical calculation of the renormalised VP on an adS black hole with spherical horizon was carried out by Breen and Taylor in [13] for a variety of scalar field mass, with both minimal ($\xi = 0$) and conformal ($\xi = 1/6$) coupling. They extend the work presented in this section to arbitrary dimensions, with numerical results for $d = 4, 5, 6, 7, 8, 9$.

5.7.2 Flat horizons

In the $k = 0$ case, we assume that the tail terms (1.230) can be written in the same form as the Euclidean Green's function (5.20,5.22), that is,

$$s^{2i-2j} w^{2j} \log(\ell_0^2 s^2) = \sum_{n=-\infty}^{\infty} e^{in\kappa\Delta\tau} \int_{\ell=0}^{\infty} \ell J_0(\ell\gamma_R) \chi_{n\ell}(i,j|r)\, d\ell. \tag{5.156}$$

We invert (5.156) as in section 5.4.2, that is by multiplying both sides by $e^{-in'\kappa\Delta\tau}\gamma_R J_0(\ell'\gamma_R)$, integrating over γ_R and $\Delta\tau$, and employing the completeness relation [120, eq. 1.17.13]. We find

$$\chi_{n\ell}(i,j|r) = \frac{\kappa}{2\pi} \int_{\Delta\tau=0}^{2\pi/\kappa} e^{-in\kappa\Delta\tau} w^{2j} \int_{\gamma_R=0}^{\infty} \gamma_R J_0(\ell\gamma_R) s^{2i-2j} \log(\ell_0^2 s^2)\, d\gamma_R\, d\Delta\tau. \tag{5.157}$$

We can write

$$s^{2i-2j} \log(\ell_0^2 s^2) = \lim_{\mu \to i-j} \ell_0^{-2\mu} \frac{\partial}{\partial\mu} \left[(\ell_0^2 s^2)^{\mu} \right], \tag{5.158}$$

where μ is an arbitrary complex parameter and the limit is understood in the sense of analytic continuation. The integral over γ_R then looks like

$$\begin{aligned} &\int_{\gamma_R=0}^{\infty} \gamma_R J_0(\ell\gamma_R) s^{2i-2j} \log(\ell_0^2 s^2)\, d\gamma_R \\ &\qquad = \lim_{\mu\to i-j} \ell_0^{-2\mu} \frac{\partial}{\partial\mu} \left[(2\ell_0^2 r^2)^{\mu} \int_{\gamma_R=0}^{\infty} \gamma_R J_0(\ell\gamma_R) (z^2+\gamma_R^2)^{\mu}\, d\gamma_R \right], \end{aligned} \tag{5.159}$$

where we have written s and z as in (5.63). The integral over γ_R can be performed using [141, eq. 6.565.4], which assumes $\mathrm{Re}(\mu) < -1$. We obtain

$$\begin{aligned} &\int_{\gamma_R=0}^{\infty} \gamma_R J_0(\ell\gamma_R) s^{2i-2j} \log(\ell_0^2 s^2)\, d\gamma_R \\ &\qquad = \lim_{\mu\to i-j} \ell_0^{-2\mu} \frac{\partial}{\partial\mu} \left[\frac{(2\ell_0^2 r^2)^{\mu} 2^{\mu+1} z^{\mu+1}}{\ell^{\mu+1}\Gamma(-\mu)} K_{\mu+1}(\ell z) \right]. \end{aligned} \tag{5.160}$$

This step is a little questionable, since in the limit $\mu \to i-j$ we have $\mathrm{Re}(\mu) > -1$, which seems to invalidate the use of [141, eq. 6.565.4]. One can see that, should one take the limit $\mu \to i-j$ prior to taking the derivative with respect to μ, the right-hand-side of (5.160) would be zero due to the $1/\Gamma(-\mu)$ term. After taking the derivative, we are, in fact, left with a convergent, non-zero quantity. All terms in (5.160) vanish in the limit $\mu \to i-j$ except when the derivative acts on $\Gamma(-\mu)$. We note that

$$\lim_{\mu \to i-j} \frac{\partial}{\partial \mu} \frac{1}{\Gamma(-\mu)} = \lim_{\mu \to i-j} \frac{-\psi(-\mu)}{\Gamma(-\mu)} = (i-j)!. \tag{5.161}$$

Assuming that the above steps are valid, the regularisation parameters can then be written

$$\chi_{n\ell}(i,j|r) = \frac{\kappa(2r)^{2(i-j)} z^{i-j+1} (i-j)!}{\pi \ell^{i-j+1}} \int_{\Delta\tau=0}^{2\pi/\kappa} e^{-in\kappa\Delta\tau} w^{2j} K_{i-j+1}(\ell z) \, d\Delta\tau. \tag{5.162}$$

The parameter z depends on both r and $\Delta\tau$. We factor out the $\Delta\tau$ dependence by using [142, eq. 11.3.8] to write

$$K_{i-j+1}(\ell z) = \sum_{m=-\infty}^{\infty} K_{i-j+1+m}(\ell\mu_0) I_m(\ell\mu_0) \cos(m\kappa\Delta\tau) \sec\left((i-j+1)\left(\frac{\pi-\kappa\Delta\tau}{2}\right)\right) \tag{5.163}$$

with μ_0 defined in (5.66). Substituting (5.163) into (5.162), we obtain

$$\begin{aligned}\chi_{n\ell}(i,j|r) = {} & \frac{\kappa(2r)^{2(i-j)} z^{i-j+1} (i-j)!}{\pi \ell^{i-j+1}} \left(\frac{2}{\kappa^2}\right)^j \sum_{m=-\infty}^{\infty} K_{i-j+1+m}(\ell\mu_0) I_m(\ell\mu_0) \\ & \times \int_{\Delta\tau=0}^{2\pi/\kappa} e^{-in\kappa\Delta\tau} (1-\cos\kappa\Delta\tau)^j \cos(m\kappa\Delta\tau) \sec\left((i-j+1)\left(\frac{\pi-\kappa\Delta\tau}{2}\right)\right) \, d\Delta\tau\end{aligned} \tag{5.164}$$

using the definition of w from (5.37). To evaluate the integral over $\Delta\tau$, we split the calculation into two cases. When $i-j+1$ is even, that is, if $i-j+1 = 2a$ for $a \in \mathbb{N}$, then

$$\sec\left((i-j+1)\left(\frac{\pi-\kappa\Delta\tau}{2}\right)\right) = (-1)^a \sec\left(\frac{\kappa\Delta\tau}{2}\right). \tag{5.165}$$

The integral over $\Delta\tau$ is then, after some rearranging using the binomial theorem,

$$\frac{1}{2^j\kappa} \sum_{p=0}^{2j} (-1)^{a+3j-p} \begin{pmatrix} 2j \\ p \end{pmatrix} \int_0^{2\pi} \frac{e^{i(-n+p-j+m)x} + e^{i(-n+p+j-m)x}}{e^{ix/2} + e^{-ix/2}} dx \tag{5.166}$$

where we have performed the substitution $x = \kappa\Delta\tau$.

When $i = j+1$ is odd, that is, if $i = j+1 = 2a+1$ for $a \in \mathbb{N}$, then

$$\sec\left((i-j+1)\left(\frac{\pi-\kappa\Delta\tau}{2}\right)\right) = (-1)^{a+1} \csc\left(\frac{\kappa\Delta\tau}{2}\right) \tag{5.167}$$

and the integral over $\Delta\tau$ is

$$\frac{1}{2^j\kappa}\sum_{p=0}^{2j}(-1)^{a+1+3j-p}\left(\begin{array}{c}2j\\p\end{array}\right)\int_0^{2\pi}\frac{e^{i(-n+p-j+m)x}+e^{i(-n+p+j-m)x}}{e^{ix/2}-e^{-ix/2}}dx. \tag{5.168}$$

This integral can then be performed numerically to allow us to determine regularisation parameters for the tail in the case of a planar horizon. This calculation depends on the fact that the integration performed in (5.160) is valid. This step is yet to be verified. Should the integration not be valid, the best course of action would be to return to (5.159) and perform the integration over γ_R numerically. This would be computationally expensive, as one would then have to numerically integrate over $\Delta\tau$ as well.

5.7.3 Hyperbolic horizons

Finally, we consider the hyperbolic $k=-1$ case, where we assume the tail terms (1.230) can be written in the same form as the Euclidean Green's function (5.20,5.23), that is,

$$s^{2i-2j}w^{2j}\log(\ell_0^2s^2)=\sum_{n=-\infty}^{\infty}e^{in\kappa\Delta\tau}\int_{\ell=0}^{\infty}\ell\tanh(\ell\pi)P_{-\frac{1}{2}+i\ell}(\cosh\gamma_H)\chi_{n\ell}(i,j|r)\;d\ell. \tag{5.169}$$

We invert this as we did in section 5.4.3, that is, by multiplying both sides by $e^{-in'\kappa\Delta\tau}P_{-\frac{1}{2}+i\ell'}(\cosh\gamma_H)$, and integrating over $\cosh\gamma_H$ and $\Delta\tau$ via the completeness relation derived in (G.41). We obtain

$$\chi_{n\ell}(i,j|r)=\frac{\kappa}{2\pi}\int_{\Delta\tau=0}^{2\pi/\kappa}e^{-in\kappa\Delta\tau}w^{2j}\int_{\cosh\gamma_H=1}^{\infty}P_{-\frac{1}{2}+i\ell}(\cosh\gamma_H)s^{2i-2j}\times\log(\ell_0^2s^2)\;d(\cosh\gamma_H)\;d\Delta\tau. \tag{5.170}$$

If we write $s^{2i-2j}\log(\ell_0^2s^2)$ using (5.158), then the integral over $\cosh\gamma_H$ becomes

$$\int_{\cosh\gamma_H=1}^{\infty}P_{-\frac{1}{2}-i\ell}(\cosh\gamma_H s^{2i-2j}\log(\ell_0^2s^2)\;d(\cosh\gamma_H)=\lim_{\mu\to i-j}\ell_0^{-2\mu}\frac{\partial}{\partial\mu}\left[(2\ell_0^2r^2)^{\mu}\int_{\cosh\gamma_H=0}^{\infty}P_{-\frac{1}{2}+i\ell}(\cosh\gamma_H)(z+\cosh\gamma_H)^{\mu}\;d(\cosh\gamma_H)\right] \tag{5.171}$$

where z is defined in (5.77). The integral over $\cosh\gamma_H$ cannot be performed in terms of known functions. The best course of action would be to calculate this numerically, but this would be computationally intensive, as one would then need to calculate the integral over $\Delta\tau$ numerically as well. This is left as an open problem.

5.8 Summary

In this chapter, we have calculated the VP in SadS using the extended coordinates method. This calculation was performed for three distinct topological black holes - spherical, flat and hyperbolic. The extended coordinates method can only be applied in the Euclidean background, forcing our calculation to be performed with respect to the Hartle-Hawking vacuum state.

We began our calculation in section 5.3 by finding a mode-sum representation for the Euclidean Green's function. This mode-sum representation has a different form depending on the event horizon topology. The radial equation cannot be solved analytically, so we use a numerical method implemented in `Mathematica`.

In section 5.4, we renormalise the vacuum expectation values by writing the Hadamard parametrix in terms of extended coordinates (s, w). This allows us to subtract the Hadamard parametrix from the Euclidean Green's function mode-by-mode, giving us a much quicker convergence compared to previous renormalisation methods.

From studying our numerical results in section 5.6, we find that the qualitative behaviour of the VP is similar across all cases of event horizon topology. In all situations considered, the VP was found to be a monotonically decreasing function, approaching the CadS limit $-1/48\pi^2L^2$ at the boundary. This mirrors the results in CadS for thermal states, which approach the same limit when Dirichlet conditions are imposed.

The rate of convergence differs across the different topological cases. The size of the VP on the event horizon is also different in each case, with the majority of cases considered always being negative on the horizon, except the case corresponding to $k = 1, \chi = 0.05, M = 0.5$. We noted that in this case, the black hole is thermodynamically unstable (unlike in all the other cases considered), and conjectured that the sign of the VP on the event horizon with Dirichlet conditions imposed may depend on the thermodynamic stability.

In the case of a black hole with flat horizon topology, we could rescale the solution to alter the value of Λ, whereas in the other cases, we have to repeat the calculation from scratch. Through analysis of accuracy of solutions, we noted how the number of modes used (or the grid of modes over the integral in the $k = -1$ case) must change as we alter the value of Λ.

Chapter 6

Quantum field theory on topological black holes with Robin boundary conditions

In this chapter, we extend the calculation of VP in chapter 5 to include scalar fields that satisfy Robin boundary conditions in SadS. The results in this chapter can be compared with the results given in chapter 3, where the VP was calculated in CadS with Robin conditions imposed. In section 6.1, we find the values of the Robin parameter α that allow for stable mode solutions. In section 6.2, we give details of the numerical calculations performed. The results are then given in section 6.3.

6.1 Stability of classical scalar fields

In section 4.2, we solved the homogeneous Klein-Gordon equation (1.56) on SadS for a massless, conformally coupled classical scalar field mode $\phi_{\omega\ell m}$. The mode solution $\phi_{\omega\ell m}$ takes the form (4.15), where the radial function $X_{\omega\ell}(r)$ satisfies the radial equation (4.17) together with boundary conditions imposed at $r \to \infty$. In this chapter, we impose Robin conditions, that is

$$[\Omega\ X_{\omega\ell}(r)]\cos\alpha + \frac{d}{d\rho}[\Omega\ X_{\omega\ell}(r)]\sin\alpha = 0 \tag{6.1}$$

where Ω is the conformal factor relating ESU to SadS - this is not the same as the conformal factor (2.10) relating ESU to CadS. The coordinate ρ is the dimensionless radial coordinate defined on ESU (2.9). There is no simple relationship between the ESU radial coordinate ρ and the SadS radial coordinate r, but near to the boundary $r \to \infty$, we can write

$$\Omega \sim \frac{r}{L}, \quad \frac{d\rho}{dr} \sim \frac{1}{L}\frac{dr^*}{dr} \tag{6.2}$$

where r^* is the tortoise coordinate defined by

$$\frac{dr^*}{dr} = \frac{1}{f(r)}. \tag{6.3}$$

The approximation (6.2) can be found by comparing the ESU metric (2.9) and the SadS metric (5.1) as $r \to \infty$ ($\rho \to \pi/2$). The Robin parameter α is analogous to the Robin parameter introduced in chapter 3, and defined such that $\alpha \in [0, \pi)$. Dirichlet boundary conditions are recovered when $\alpha = 0$ and Neumann boundary conditions are recovered when $\alpha = \pi/2$.

It is useful to rewrite the boundary condition (6.1) in terms of the tortoise coordinate r^*, defined by (6.3). The tortoise coordinate r^* takes values in $(-\infty, 0)$, where $r^* \to -\infty$ as we approach the event horizon $r \to r_h$ and $r^* \to 0$ as we approach the boundary $r \to \infty$.

Using (6.2) and applying the chain rule, we obtain, as $r^* \to 0$,

$$\frac{d}{d\rho} = \frac{dr}{d\rho}\frac{dr^*}{dr}\frac{d}{dr^*} \sim L\frac{d}{dr^*}. \tag{6.4}$$

Therefore, the boundary conditions (6.1) as $r^* \to 0$ can be written

$$\tilde{X}_{\omega\ell} \cos\alpha + L\frac{d\tilde{X}_{\omega\ell}}{dr^*}\sin\alpha = 0 \tag{6.5}$$

where

$$\tilde{X}_{\omega\ell}(r) = rX_{\omega\ell}(r). \tag{6.6}$$

When we imposed Robin boundary conditions in CadS, we found that there existed a critical value $\alpha = \alpha_{crit}$. For $\alpha > \alpha_{crit}$, there exist unstable modes; that is, modes which grow exponentially in time (see section 3.2.4).

In SadS, we see a similar picture. If we impose Dirichlet or Neumann boundary conditions, a massless, conformally coupled scalar field ϕ does not have any unstable modes. For Robin conditions, the situation is not as straightforward. In SadS with a spherical horizon, it is shown in [143, 144] that unstable dynamics exist for $\alpha \in (\alpha_{crit}, \pi)$, despite the initial value problem being well-defined for all values of α [118, 145]. The value of α_{crit} is not the same as in chapter 3; indeed, the value of α_{crit} in SadS depends on the event horizon radius r_h.

We begin in section 6.1.1 by proving the existence of α_{crit} in SadS using a variational method [146]. This follows the method of [144], which we extend to cover the $k = 0, -1$ cases of topological black holes. In section 6.1.2, we determine the value of α_{crit} numerically, using the methods of [143].

6.1.1 Existence of α_{crit}

We prove the existence of α_{crit} by using a variational method [146]. We consider the Hamiltonian $\mathcal{H}$ with a discrete spectrum of eigenvalues E, that is

$$\mathcal{H}|\Psi\rangle = E|\Psi\rangle \tag{6.7}$$

for some eigenvector $|\Psi\rangle$. Then we have

$$\langle\Psi|\mathcal{H}|\Psi\rangle = E\langle\Psi|\Psi\rangle. \tag{6.8}$$

Rearranging, we can write the eigenvalues E as

$$E = \frac{\langle\Psi|\mathcal{H}|\Psi\rangle}{\langle\Psi|\Psi\rangle}. \tag{6.9}$$

Equation (6.9) holds for any eigenvector $|\Psi\rangle$. We now extend this for any test function $|\Psi\rangle$, and the right-hand-side of (6.9) becomes a functional. The variational principle [146] states that the minimum of the right-hand-side of (6.9) is equal to the minimum eigenvalue, that is

$$\min\{E\} = \min\left\{\frac{\langle\Psi|\mathcal{H}|\Psi\rangle}{\langle\Psi|\Psi\rangle}\right\}. \tag{6.10}$$

This means that, if the right-hand-side of (6.10) is negative, for any test function $|\Psi\rangle$, then there exists a negative eigenvalue.

We apply this method to the radial equation (4.17). In terms of the tortoise coordinate r^* (6.3), the radial equation (4.17) is written

$$-\frac{d^2\tilde{X}_{\omega\ell}}{dr^{*2}} + V_\ell(r)\tilde{X}_{\omega\ell} = \omega^2\tilde{X}_{\omega\ell} \tag{6.11}$$

where $\tilde{X}_{\omega\ell}$ is given by (6.6), the potential $V_\ell(r)$ is given by

$$V_\ell(r) = f(r)\left(\frac{\nu_\ell^{(k)}}{r^2} + \frac{2M}{r^3}\right) \tag{6.12}$$

and $\nu_\ell^{(k)}$ is defined by (4.18). We note that $V_\ell(r) \geq 0$ for all $r \in [r_h, \infty)$. Unstable modes occur when $\omega^2 < 0$.

One may ask whether complex values of ω need to be considered to obtain all regions of instability, rather than just purely imaginary ω. Holzegel and Warnick [143] show that we require $\omega^2 < 0$ to allow us to obtain positive self-adjoint expectations of the operator $\hat{A}$, where $\hat{A}$ is given by

$$\hat{A}\phi = \tilde{\nabla}_i^\dagger(a^{ij}\tilde{\nabla}_j\phi) + V\phi \tag{6.13}$$

for $\tilde{\nabla}$ "twisted" derivatives and V the potential. These "twisted" derivatives are defined by differentiating in ESU and then performing a conformal transform to SadS [143].

This is only proven for spherical asymptotically-adS black holes. We assume here that this holds for topological black holes ($k = 0, -1$) but this remains unproven.

We use the variational principle (6.10) with E replaced by ω^2 and the Hamiltonian $\mathcal{H}$ replaced by the radial operator $-\frac{d^2}{dr^{*2}} + V_\ell(r)$ to show that there exist certain cases where $\omega^2 < 0$.

We multiply both sides of (6.11) by $\tilde{X}^*_{\omega\ell}$ and then integrate over r^* to give

$$\int_{-\infty}^{0} \left[-\frac{d^2\tilde{X}_{\omega\ell}}{dr^{*2}} \tilde{X}^*_{\omega\ell} + V_\ell(r)|\tilde{X}_{\omega\ell}|^2 \right] dr^* = \omega^2 \int_{-\infty}^{0} |\tilde{X}_{\omega\ell}|^2 dr^*. \tag{6.14}$$

The integration on the left-hand-side can be performed using integration by parts,

$$\left[-\tilde{X}^*_{\omega\ell} \frac{d\tilde{X}_{\omega\ell}}{dr^*} \right]_{-\infty}^{0} + \int_{-\infty}^{0} \left[\left| \frac{d\tilde{X}_{\omega\ell}}{dr^*} \right|^2 + V_\ell(r)|\tilde{X}_{\omega\ell}|^2 \right] dr^* = \omega^2 \int_{-\infty}^{0} |\tilde{X}_{\omega\ell}|^2 dr^*. \tag{6.15}$$

The first term on the left-hand-side disappears when Neumann and Dirichlet boundary conditions are imposed on the radial function. The remaining integrals must both be positive, so in this case, we must have $\omega^2 > 0$ and therefore all classical scalar field modes must be stable. This is just as we expected.

When Robin boundary conditions are imposed on $\tilde{X}_{\omega\ell}(r)$, the first term on the left-hand-side of (6.15) is not zero. We assume that $\cos\alpha \neq 0$ and, using (6.5), we write,

$$L \tan\alpha \left(\lim_{r^* \to 0} \left| \frac{d\tilde{X}_{\omega\ell}}{dr^*} \right|^2 \right) + \mathcal{J} = \omega^2 \int_{-\infty}^{0} |\tilde{X}_{\omega\ell}|^2 dr^* \tag{6.16}$$

where

$$\mathcal{J} = \int_{-\infty}^{0} \left[V_\ell(r)|\tilde{X}_{\omega\ell}|^2 + \left| \frac{d\tilde{X}_{\omega\ell}}{dr^*} \right|^2 \right] dr^* > 0. \tag{6.17}$$

The derivative in the first term on the left-hand-side of (6.16) is evaluated at the boundary, that is $r^* \to 0$. The first thing we notice is that, when $\alpha \in [0, \pi/2]$, then $\tan\alpha \geq 0$ and, from (6.16), we must have $\omega^2 > 0$. In these cases, all modes are stable.

However, when $\alpha \in (\pi/2, \pi)$, the left-hand-side of (6.16) is not necessarily positive. We use Proposition 1 from [144] to show that this results in the existence of unstable modes. We evaluate the left-hand-side of (6.16) for a test function $\tilde{X}_{\omega\ell}(r^*) = \exp\left(-\frac{r^*}{L}\tan\alpha\right)$. The left-hand-side of (6.16) becomes

$$\frac{1}{L}\tan^3\alpha + \int_{-\infty}^{0} V_\ell(r) e^{-\frac{2r^*}{L}\tan\alpha} dr^* + \left[-\frac{1}{2L}\tan\alpha \; e^{-\frac{2r^*}{L}\tan\alpha} \right]_{-\infty}^{0}. \tag{6.18}$$

If this is negative, then the right-hand-side of (6.16) must also be negative. Since the integral on the right-hand-side of (6.16) must be positive, this means that there must exist a spectrum of negative eigenvalues $\omega^2 < 0$. These negative eigenvalues will correspond to unstable scalar field modes.

Equation (6.18) can be negative when $\tan\alpha < 0$. In this case, (6.18) becomes

$$\frac{1}{L}\left(\tan^2\alpha - \frac{1}{2}\right)\tan\alpha + \int_{-\infty}^{0} V_\ell(r) e^{-\frac{2r^*}{L}\tan\alpha} dr^*. \tag{6.19}$$

The potential $V_\ell(r)$ is continuous for $r \in [r_h, \infty)$ and is therefore bounded on any closed interval. We can also note that $V_\ell(r) \to 0$ as $r \to r_h$ and that the potential approaches a finite limit as $r \to \infty$. Then there must exist a maximum for $V_\ell(r)$, that is

$$V_\ell(r) \leq V_{max}. \tag{6.20}$$

Then we must have

$$\begin{aligned}
&\frac{1}{L}\left(\tan^2\alpha - \frac{1}{2}\right)\tan\alpha + \int_{-\infty}^{0} V_\ell(r) e^{-\frac{2r^*}{L}\tan\alpha} dr^* \\
&\leq \frac{1}{L}\left(\tan^2\alpha - \frac{1}{2}\right)\tan\alpha + \int_{-\infty}^{0} V_{max} e^{-\frac{2r^*}{L}\tan\alpha} dr^* \\
&= \frac{1}{L}\left(\tan^2\alpha - \frac{1}{2}\right)\tan\alpha - \frac{L\, V_{max}}{2\tan\alpha}
\end{aligned} \tag{6.21}$$

which is negative provided

$$V_{max} < \frac{1}{L^2}(2\tan^2\alpha - 1)\tan^2\alpha. \tag{6.22}$$

This holds for a range of $\tan\alpha$ regardless of the value of V_{max}. This can be seen from the fact that the right-hand-side of (6.22) is quadratic in $\tan^2\alpha$ and is unbounded as $\alpha \to \pi/2$, implying that there exists some values of α close to $\alpha = \pi/2$ for which (6.22) holds.

Hence the Schrödinger operator on the left-hand-side of (6.11) has a spectrum containing negative eigenvalues ω^2. These negative values correspond to unstable scalar field modes, thus proving that for some values of $\alpha \in (\pi/2, \pi)$, there exist unstable modes.

6.1.2 Numerical evaluation of α_{crit}

We now want to determine the critical value $\pi/2 < \alpha_{crit} < \pi$ for which unstable field modes exist when $\alpha \in (\alpha_{crit}, \pi)$. We can determine this critical value using the method of [143]. In [143], this calculation is performed only for black holes of spherical event horizon topology. Here, we extend this calculation to black holes of flat and hyperbolic event horizon topology.

To determine α_{crit}, we seek solutions of (6.11) when ω^2 crosses zero. For each event horizon topology, the potential $V_\ell(r)$ satisfies $V_\ell(r) > V_0(r)$ for $r \in [r_h, \infty)$. It is therefore sufficient to consider modes for which $\ell = 0$.

Setting $\ell = 0 = \omega^2$, the radial equation (4.17) has the form

$$\frac{d}{dr}\left\{\left[r^2k - \left(kr_h + \frac{r_h^3}{L^2}\right)r + \frac{r^4}{L^2}\right]\frac{dX_{00}}{dr}\right\} + \left[-\nu_0^{(k)} + \frac{2r^2}{L^2}\right]X_{00} = 0, \tag{6.23}$$

where we have written the black hole mass M in terms of the horizon radius r_h. When $k = 1, 0$, we have $\nu_0^{(k)} = 0$ and when $k = -1$, we have $\nu_0^{(-1)} = \frac{1}{2}$. Using dimensionless variables $R = r/L, R_h = r_h/L$, the radial equation becomes

$$\frac{d}{dR}\left\{[R^2k - (kR_h + R_h^3)R + R^4]\frac{dX_{00}}{dR}\right\} + [-\nu_0^{(k)} + 2R^2]X_{00} = 0. \tag{6.24}$$

This is greatly simplified in the $k = 0$ case, leaving us with

$$\frac{d}{dR}\left\{[-R_h^3R + R^4]\frac{dX_{00}}{dR}\right\} + 2R^2X_{00} = 0. \tag{6.25}$$

We can reduce this to a single perturbation equation by defining $\bar{R} = R/R_h$, and obtaining

$$\frac{d}{d\bar{R}}\left\{\left[\bar{R}^4 - \bar{R}\right]\frac{dX_{00}}{d\bar{R}}\right\} + 2\bar{R}^2X_{00} = 0. \tag{6.26}$$

The fact that the perturbation equation now appears to be independent of horizon radius is due to the scaling symmetries of the $k = 0$ metric (see section 5.2). In section 5.2, we discussed the two different scaling symmetries, the $\tilde{\rho}_1$-scaling (5.9) and the $\tilde{\rho}_2$-scaling (5.13). The $\tilde{\rho}_1$-scaling leaves both R and R_h invariant, and therefore $\bar{R}$ is also unchanged. Under the $\tilde{\rho}_2$-scaling, we have $R \to \tilde{\rho}_2R$ and $R_h \to \tilde{\rho}_2R_h$, and so $\bar{R}$ is again unchanged. This means that in the $k = 0$ case, the value of α_{crit} will not change under these scalings. Note that this is not reflected in Figure 6.1 since varying r_h/L does affect the value of α_{crit}.

To find α_{crit}, we first solve (6.24) by numerically integrating outwards from the horizon towards the boundary. Appropriate initial conditions for the numerical integration can be derived by defining a new independent variable $x = R - R_h$ and writing (6.24) in the approximate form

$$\left\{\frac{d^2}{dx^2} + \frac{1}{x}\frac{d}{dx} + \frac{2R_h^2 - \nu_0^{(k)}}{(R_hk + 3R_h^3)x}\right\}X_{00}^{init.} = 0 \tag{6.27}$$

where higher order terms in x can be ignored close to the horizon. Solutions of (6.27) are Bessel functions,

$$X_{00}^{init.} = \mathcal{C}_1J_0(2\sqrt{Ax}) + \mathcal{C}_2Y_0(2\sqrt{Ax}) \tag{6.28}$$

where $\mathcal{C}_1, \mathcal{C}_2$ are constants of integration and

$$A = \frac{2R_h^2 - \nu_0^{(k)}}{kR_h + 3R_h^3}. \tag{6.29}$$

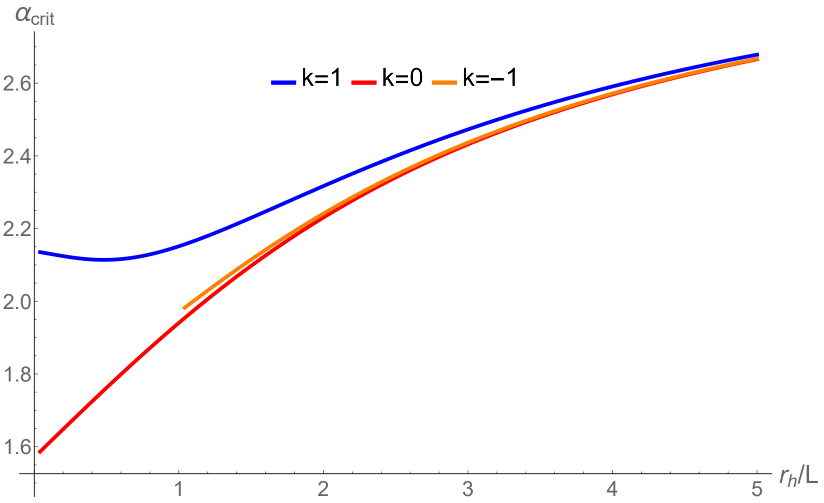

Figure 6.1: Plot of α_{crit} as a function of r_h/L for black holes with spherical ($k=1$, blue curve), flat ($k=0$, red curve) and hyperbolic ($k=-1$, orange curve) event horizon. When $\alpha > \alpha_{crit}$, unstable classical scalar field modes exist.

Since $Y_0(2\sqrt{Ax})$ is divergent at the horizon as $x \to 0$, we set $\mathcal{C}_2 = 0$ and, without loss of generality, $\mathcal{C}_1 = 1$. We then use (6.28) as the initial condition in the numerical integration of (6.24), integrating from $R = R_h + \epsilon$, where $\epsilon = 10^{-5}$, to $R = 1000$.

We then use the boundary conditions (6.5) to determine α_{crit}. In terms of R and X_{00}, these boundary conditions are written

$$X_{00}(R) \cos\alpha_{crit} + R\frac{d}{dR}[RX_{00}(R)] \sin\alpha_{crit} = 0 \tag{6.30}$$

as $R \to \infty$. We substitute in our numerical solution X_{00} and rearrange to find $\cot\alpha_{crit}$, evaluating the numerical solution at $R = 1000$.

This procedure is performed over a grid in R_h, for $R_h = \frac{1}{25}, \frac{2}{25}, ..., 5$. We can then interpolate over this grid in R_h. Our results are plotted in Figure 6.1. The blue curve for black holes with event horizon of positive curvature ($k = 1$) agrees with the results given in [143, Fig. 2]. As $r_h \to 0$, the value of α_{crit} in the $k = 1$ case approaches the value in CadS (3.33).

In the $k = 0$ case, the graph of $\cot\alpha_{crit}$ as a function of R_h is a straight line. This is to be expected since the scaling symmetries (5.9, 5.13) means that $\cot\alpha_{crit}$ scales linearly with R_h.

The orange curve for hyperbolic black holes in Figure 6.1 begins at the minimum event horizon radius (4.11). Above this value, the line lies very close to the curve for planar black holes (the red curve).

The curves for $k = 0, -1$ are monotonically increasing as we increase R_h, whilst the $k =$

1 curve decreases for small R_h, reaches a minimum, and then monotonically increases as $R_h \to \infty$. As R_h grows, the three curves merge, suggesting that α_{crit} is approximately the same for all black hole solutions with large event horizon radius.

In the next section, we use the interpolation functions plotted in Figure 6.1 to determine the values of α_{crit} for the various values of black hole mass M, surface gravity κ and event horizon radius r_h for which we calculate the renormalised VP.

6.2 Numerical calculation of renormalised vacuum polarisation with Robin boundary conditions

The renormalised VP is calculated in the Euclidean background using the extended coordinates method. This calculation is an extension of the calculation performed in section 5.5. The main difference is that we impose Robin boundary conditions (rather than Dirichlet boundary conditions) on the radial Green's function $X_{n\ell}^{(k),\alpha}(r,r')$, which satisfies the radial equation (5.24). The superscript α is now used to remind us that Robin conditions have been imposed.

We write $X_{n\ell}^{(k),\alpha}(r,r')$ in the same form as in (5.28), that is

$$X_{n\ell}^{(k),\alpha}(r,r') = \mathcal{N}_{n\ell}^{\alpha} p_{n\ell}(r_<) q_{n\ell}(r_>) \tag{6.31}$$

for $r_< = \min\{r, r'\}$, $r_> = \max\{r, r'\}$. The functions $p_{n\ell}$ and $q_{n\ell}$ are both solutions of the homogeneous version of (5.24). The function $p_{n\ell}$ has regularity conditions imposed on the horizon, and $q_{n\ell}^{\alpha}$ has Robin conditions imposed on the boundary. The normalisation constant $\mathcal{N}_{n\ell}^{\alpha}$, which is given by the Wronskian relation (5.30), must then also depend on the Robin parameter α.

Since the radial functions satisfying Dirichlet and Neumann boundary conditions, that is $q_{n\ell}^{0}(r), q_{n\ell}^{\frac{\pi}{2}}(r)$ respectively, are linearly independent, we may write, for any $\alpha \in [0, \alpha_{crit})$,

$$q_{n\ell}^{\alpha}(r) = \mathcal{A}_{n\ell}^{\alpha} q_{n\ell}^{0}(r) + \mathcal{B}_{n\ell}^{\alpha} q_{n\ell}^{\frac{\pi}{2}}(r) \tag{6.32}$$

where $\mathcal{A}_{n\ell}^{\alpha}, \mathcal{B}_{n\ell}^{\alpha}$ are constants defined such that $\mathcal{A}_{n\ell}^{0} = 1, \mathcal{B}_{n\ell}^{0} = 0$ when $\alpha = 0$ and $\mathcal{A}_{n\ell}^{\pi/2} = 0, \mathcal{B}_{n\ell}^{\pi/2} = 1$ when $\alpha = \pi/2$.

To leading order, we can write

$$q_{n\ell}^{0}(r) = \frac{1}{r^2} + \mathcal{O}(r^{-3}), \quad q_{n\ell}^{\frac{\pi}{2}}(r) = \frac{1}{r} + \mathcal{O}(r^{-3}). \tag{6.33}$$

This can be seen from the Frobenius approximation (5.98) used in chapter 5. Substituting (6.32-6.33) into (6.5), we obtain

$$r\left(\mathcal{A}_{n\ell}^{\alpha} q_{n\ell}^{0}(r) + \mathcal{B}_{n\ell}^{\alpha} q_{n\ell}^{\frac{\pi}{2}}(r)\right)\cos\alpha + Lf(r)\frac{d}{dr}\left[r\left(\mathcal{A}_{n\ell}^{\alpha} q_{n\ell}^{0}(r) + \mathcal{B}_{n\ell}^{\alpha} q_{n\ell}^{\frac{\pi}{2}}(r)\right)\right]\sin\alpha \tag{6.34}$$

$$= \mathcal{B}_{n\ell}^{\alpha}\cos\alpha - \frac{\mathcal{A}_{n\ell}^{\alpha}}{L}\sin\alpha + \mathcal{O}(r^{-1}) = 0 \quad \text{as } r \to \infty. \tag{6.35}$$

This implies

$$\frac{\mathcal{A}^{\alpha}_{n\ell}}{\mathcal{B}^{\alpha}_{n\ell}} = L\cot\alpha. \tag{6.36}$$

Without loss of generality, we can set $\mathcal{A}^{\alpha}_{n\ell} = L\cos\alpha, \mathcal{B}^{\alpha}_{n\ell} = \sin\alpha$ and then

$$q^{\alpha}_{n\ell}(r) = q^{0}_{n\ell}(r)L\cos\alpha + q^{\frac{\pi}{2}}_{n\ell}(r)\sin\alpha. \tag{6.37}$$

The Wronskian relation (5.30) then fixes the normalisation constant as

$$\mathcal{N}^{\alpha}_{n\ell} = \frac{\mathcal{N}^{0}_{n\ell}\mathcal{N}^{\frac{\pi}{2}}_{n\ell}}{\mathcal{N}^{\frac{\pi}{2}}_{n\ell}L\cos\alpha + \mathcal{N}^{0}_{n\ell}\sin\alpha} \tag{6.38}$$

where $\mathcal{N}^{0}_{n\ell}$ are the normalisation constants determined when Dirichlet conditions are applied to the radial function, and $\mathcal{N}^{\frac{\pi}{2}}_{n\ell}$ are the normalisation constants determined when Neumann conditions are applied to the radial function.

The VP is renormalised using the extended coordinates method, which involves writing the Hadamard parametrix in a mode-sum representation matching that of the Euclidean Green's function. The Hadamard parametrix is unaffected by boundary conditions imposed on the Euclidean Green's function, and so we can use the results from the previous chapter. The renormalised VP is then written as

$$\langle\hat{\phi}^2\rangle^{\alpha}_{ren} = \frac{1}{4\pi^2}\int_{\ell=0}^{\infty} d\ell \sum_{n=-\infty}^{\infty} \mathcal{P}_{\ell}(0)\left[\kappa X^{(k),\alpha}_{n\ell}(\eta) - \frac{1}{2}\sum_{i=0}^{2}\sum_{j=0}^{i}\mathcal{D}_{ij}(r)\Psi_{n\ell}(i,j|r)\right] - \frac{f'(r)}{48\pi^2 r} \tag{6.39}$$

where $\mathcal{P}_{\ell}(\gamma)$ is given by (5.87), the regularisation parameters $\Psi_{n\ell}(i,j|r)$ are given by (5.88) and the regularisation coefficients $\mathcal{D}_{ij}(r)$ are given in Table 5.1. The integral over ℓ is understood to be a sum when $k=1$. The equation (6.39) can be compared with the renormalised VP when Dirichlet conditions are imposed (5.115).

As in section 5.5, we calculate each term in the ℓ and n sum in (6.39) individually. In the $k=0,-1$ cases, we have an integral over ℓ and must compute the terms over a grid of values of ℓ. This grid is usually chosen to be denser close to $\ell=0$ to properly capture the behaviour of the integrand. The $p_{n\ell}$ terms are not affected by Robin boundary conditions, so we can use results from the previous chapter. For the $q^{\alpha}_{n\ell}$ terms, we only need to calculate $q^{0}_{n\ell}$ and $q^{\frac{\pi}{2}}_{n\ell}$. All other $q^{\alpha}_{n\ell}$ can be determined by taking a linear combination of $q^{0}_{n\ell}$ and $q^{\frac{\pi}{2}}_{n\ell}$ using (6.37). This greatly simplifies our numerical calculations and reduces computation time. We calculate $q^{\frac{\pi}{2}}_{n\ell}$ using `NDSolve` in `Mathematica` to numerically solve the radial equation (5.96), using the Frobenius series (5.98) as initial condition, this time with $\alpha_2 = 1$ to give us the radial function satisfying Neumann boundary conditions.

The radial function is calculated over a grid in dimensionless coordinate η, given in

(5.3), where

$$X_{n\ell}^{(k),\alpha}(\eta) = \lim_{r'\to r} X_{n\ell}^{(k),\alpha}(r,r') = \frac{p_{n\ell}(r)\mathcal{N}_{n\ell}^{0}\mathcal{N}_{n\ell}^{\frac{\pi}{2}}}{\mathcal{N}_{n\ell}^{\frac{\pi}{2}}L\cos\alpha + \mathcal{N}_{n\ell}^{0}\sin\alpha}\left[q_{n\ell}^{0}(r)\cos\alpha + q_{n\ell}^{\frac{\pi}{2}}(r)L\sin\alpha\right]. \tag{6.40}$$

We calculate over a grid of every $\pi/10$-integer α for $\alpha \in [0, \alpha_{crit})$.

6.3 Numerical results

In section 5.6, we fixed χ and L and varied the value of k, where the parameter χ is given by (5.4). This allowed us to easily compare between different cases, since the event horizon radius and the asymptotic CadS value (3.2) at the boundary were the same for all k. In this section, we find it more useful to fix the surface gravity κ and L as this allows us to compare with our thermal results from CadS given in section 3.5.

Since the $k = -1$ case is the most expensive in terms of computation time, we choose values of κ and L that match those used in section 5.6.3. We must extend these results to include Neumann conditions, which requires us to calculate another set of radial modes $q_{n\ell}^{\frac{\pi}{2}}$. The grid over ℓ is kept the same as in the Dirichlet case, as is the truncation of the ℓ-integrand and the n-sum. Both the n-sum and the ℓ-integral converge rapidly, with convergence tests giving qualitatively similar results to those found in section 5.6. The Hadamard parametrix is unaffected by boundary conditions, so we can use the results calculated previously. The major source of error in our final results with Neumann conditions imposed is the grid over ℓ used to evaluate the integrand. This is the same as the error obtained in section 5.6.3 with Dirichlet conditions imposed.

In the $k = 0$ case, scaling symmetries (section 5.2) mean that we only need to calculate for one value of κ and L, and then rescale to give results for values of κ and L that match the $k = -1$ case. We still need to calculate an extra set of radial modes $q_{n\ell}^{\frac{\pi}{2}}$. This is done to match the original set of radial modes $q_{n\ell}^{0}$ that were calculated in section 5.6.2, where $\kappa = 3$ and $L = 1$. The grid over ℓ is the same as the grid used for the Dirichlet calculation, and the ℓ-integral and n-sum are truncated at the same values. The convergence in the n-sum and ℓ-integral in the Neumann case are qualitatively the same as in the Dirichlet case.

A linear combination of $q_{n\ell}^{0}$ and $q_{n\ell}^{\frac{\pi}{2}}$ is then taken to allow us to calculate results on the planar background for a range of Robin boundary conditions. Again, we calculate for every 1/10-integer α for $\alpha \in [0, \alpha_{crit})$. Once we have calculated all results for the $\kappa = 3, L = 1$ case, we can then use our scaling symmetries to give results for values of κ, L that allow for comparison with the $k = -1$ case.

In the $k = 1$ case, we must begin our calculation from scratch to allow us to match values of κ and L to those considered in the $k = -1, 0$ cases. This includes a complete calculation of radial modes $p_{n\ell}, q_{n\ell}^{0}$ and $q_{n\ell}^{\frac{\pi}{2}}$ as well as the regularisation parameters

$\Psi_{n\ell}(i,j|r)$ in each of the cases that we consider. This is not as computationally expensive as it would be to calculate a completely new set of results in the $k=-1$ case, since we have a sum over ℓ in the $k=1$ case rather than an integral, meaning that we have significantly fewer values of ℓ to consider.

The values of κ (to four decimal places) and L that we consider are given in Table 6.1. We split these into three cases, that is $(L=8000/861, \kappa=0.1183), (L=8/15, \kappa=3.5938)$ and $(L=1/990, \kappa=14800.5)$. There is a fourth case that we consider where we fix L and r_h across all topological black holes, that is $(L=1, r_h=2)$. This matches the results given in Figure 5.30. We also find it convenient to define a parameter β, related to the Robin parameter α by

$$\cot\beta = L\cot\alpha. \tag{6.41}$$

Dirichlet and Neumann conditions are still recovered for $\beta=0$ and $\beta=\frac{\pi}{2}$ respectively. The value of β_{crit} in each case is also given to four decimal places in Table 6.1.

When $(L=8000/861, \kappa=0.1183)$, there do not exist any black holes with spherical horizon, whereas when $(L=8/15, \kappa=3.5938)$, there exist two possible black hole solutions with spherical event horizon. We label these two solutions $k=1(+)$ and $k=1(-)$, with $k=1(+)$ being the black hole with the larger event horizon radius r_h. When $L=1, r_h=2$, there exists only one solution with spherical horizon topology. The existence of these solutions can be seen by plotting the black hole temperature against horizon radius, where

$$T = \frac{\kappa}{2\pi} = \frac{kL^2+3r_h^2}{4\pi r_h L^2}. \tag{6.42}$$

The plot of the temperature can be seen in Figure 6.2.

For $k=0,-1$ the temperature is a monotonically increasing function of horizon radius. Planar black holes exist for all temperatures due to the scaling symmetries (section 5.2). Under $\tilde{\rho}_1$-scaling (5.9), $T\to\tilde{\rho}_1^{-1}T$, whilst under $\tilde{\rho}_2$-scaling (5.13), $T\to\tilde{\rho}_2 T$. Hyperbolic black holes have a minimum event horizon radius (4.11) which corresponds to $T=0$.

When $k=1$, there exists a minimum temperature. This minimum temperature occurs at $r_h = r_{h\ min}$ (4.11), and is given by

$$T_{min} = \frac{\sqrt{3}}{2\pi L}. \tag{6.43}$$

When $r_h > r_{h\ min}$, the black holes are thermodynamically stable, whereas when $r_h < r_{h\ min}$, the black holes are thermodynamically unstable [137]. Thus, when $T > T_{min}$, we obtain two black holes with spherical horizon radius, whereas when $T < T_{min}$, there are no black hole solutions with spherical horizon radius.

The results for the renormalised VP are given in Figures 6.3 – 6.8. We first consider topological black holes with $L=1$ and $r_h=2$. This corresponds to the case where

	M	r_h	κ	β_{crit}
$\mathbf{L=1}$				
$k=1$	5	2	3.25	2.3166
$k=0$	4	2	3	2.2301
$k=-1$	3	2	2.75	2.2412
$\mathbf{L=\frac{8000}{861}}$				
$k=0$	1.8262	6.8064	0.1183	2.2300
$k=-1$	0.5	9.7561	0.1183	2.9018
$\mathbf{L=\frac{8}{15}}$				
$k=1(-)$	0.1104	0.1948	3.5938	1.8833
$k=1(+)$	0.1104	0.4866	3.5938	1.8998
$k=0$	0.5563	0.6815	3.5938	2.2301
$k=-1$	0.5	0.8	3.5938	1.8829
$\mathbf{L=\frac{1}{990}}$				
$k=1(-)$	0.00002	0.00003	14800.5	1.5714
$k=1(+)$	0.00002	0.0101	14800.5	1.5747
$k=0$	0.5000	0.0101	14800.5	2.2302
$k=-1$	0.5	0.0101	14800.5	1.5747

Table 6.1: The values of L, κ, M and r_h for which we present numerical results for the renormalised VP. We also give the critical value of the parameter β, related to α_{crit} by (6.41). For values of β greater than the critical value, there exist unstable classical scalar field modes.

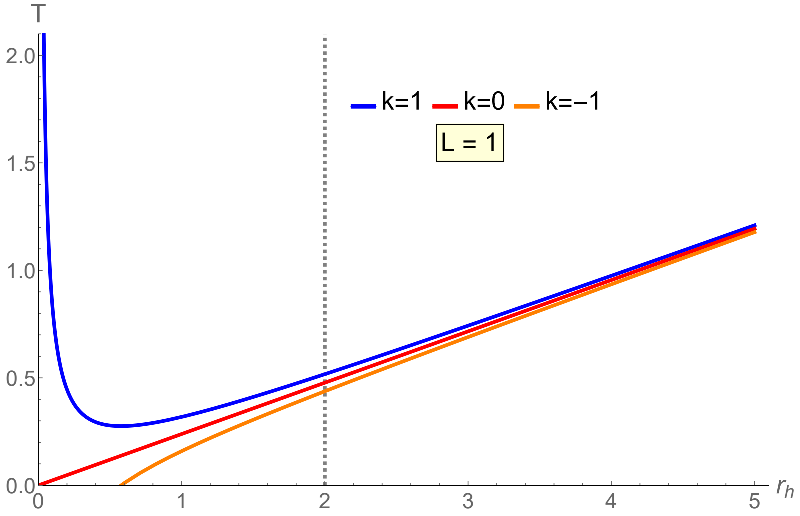

(a) Temperature T as a function of horizon radius r_h when $L = 1$. The dotted line represents $r_h = 2$. The intersection of the dotted line with the three curves corresponds to the three black holes considered in Figure 6.4.

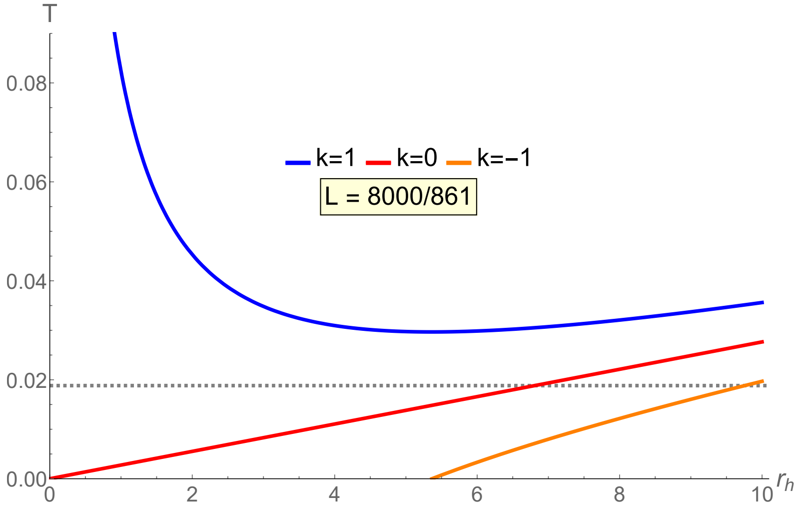

(b) Temperature T as a function of horizon radius r_h when $L = 8000/861$. The dotted line represents $T = 37843/640000\pi$, that is $\kappa = 0.1183$ (four decimal places). The intersection of the dotted line with the $k = 0, -1$ curves corresponds to the two black holes considered in Figure 6.5. This line does not intersect with the curve corresponding to $k = 1$, meaning there are no black holes with spherical event horizon in this case.

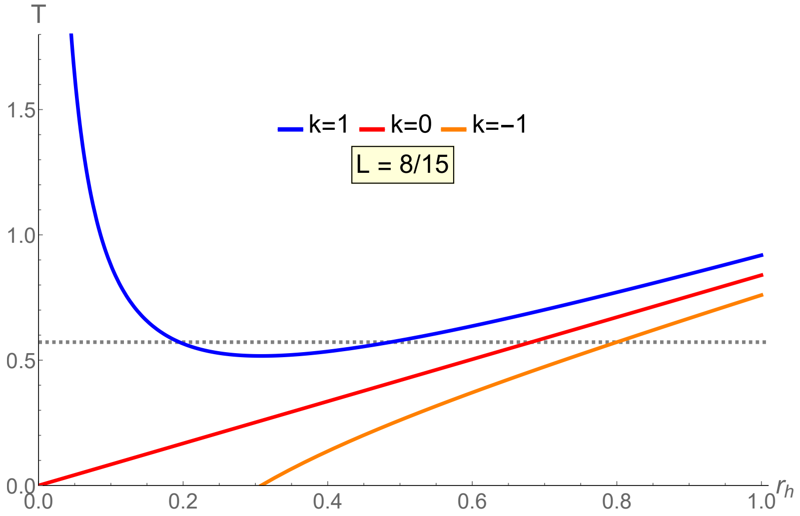

(c) Temperature T as a function of horizon radius r_h when $L = 8/15$. The dotted line represents $T = 115/64\pi$, that is $\kappa = 3.5938$ (four decimal places). The intersection of the dotted line with the three curves corresponds to the black holes considered in Figure 6.7. This line intersects with the curve corresponding to $k = 1$ twice, meaning there are two black holes with spherical event horizon in this case.

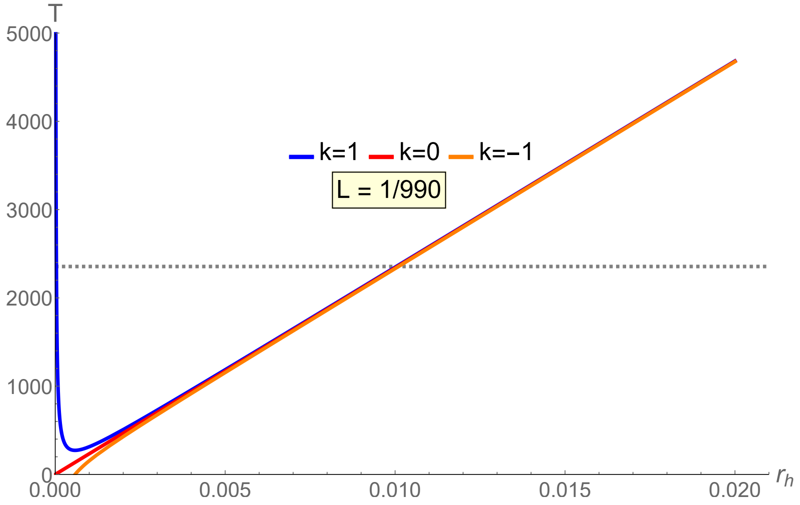

(d) Temperature T as a function of horizon radius r_h when $L = 1/990$. The dotted line represents $T = 29601/2\pi$, that is $\kappa = 14800.5$. The intersection of the dotted line with the three curves corresponds to the black holes considered in Figure 6.8. This line intersects with the curve corresponding to $k = 1$ twice, meaning there are two black holes with spherical event horizon in this case.

Figure 6.2: Black hole temperature T (6.42) as a function of event horizon radius r_h for varying values of adS radius of curvature L. In each plot, blue lines represent black holes with spherical horizon ($k = 1$), red lines represent black holes with planar horizon ($k = 0$) and orange lines represent black holes with hyperbolic horizon ($k = -1$). The dotted lines in each plot correspond to the value of r_h or T considered in this section (see Table 6.1). In all four plots, the curves are qualitatively the same.

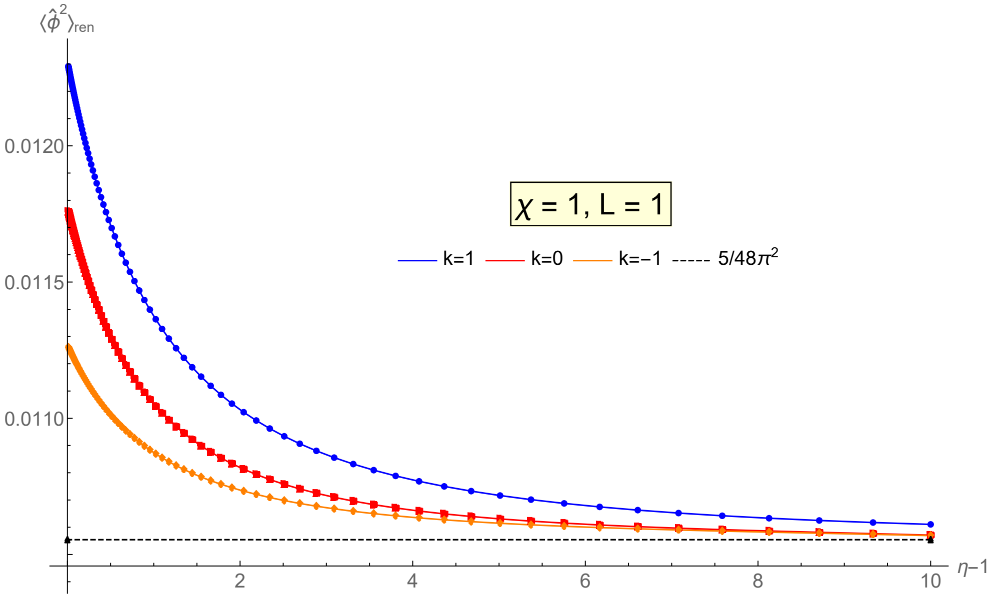

Figure 6.3: The behaviour of $\langle\hat{\phi}^2\rangle_{ren}$ with Neumann boundary conditions imposed on an adS black hole with varying black hole topology. We fix $L = 1, \chi = 1$, which means that the event horizon radius is the same in each case, as is the CadS limit approached at the boundary. This case allows us to directly compare rate of convergence across all three cases considered. This can also be compared with results with Dirichlet boundary conditions imposed, given in Figure 5.30.

$\chi = 1$ (5.4). In Figure 6.3, we present results for the VP when Neumann conditions are imposed. These results can be directly compared with the results when Dirichlet conditions are imposed (Figure 5.30). In both Dirichlet and Neumann cases, and for all values of k, the VP is a monotonically decreasing function of radius η. At the boundary, the VP approaches the Neumann CadS limit $5/48\pi^2L^2$ (3.3) when Neumann conditions are imposed on the scalar field. This is similar to the Dirichlet case, where the VP approached the Dirichlet limit $-1/48\pi^2L^2$ (3.2). The order of the lines changes depending on whether Dirichlet or Neumann conditions are imposed. For Dirichlet boundary conditions (Figure 5.30), the VP for $k = -1$ black holes is smaller than the VP for $k = 1$ black holes, which is smaller than the VP for $k = 0$ black holes. For Neumann conditions (Figure 6.3), the VP for $k = 0$ black holes is again the smallest of the three, but the result for $k = 1$ is now the largest. This suggests that for some intermediate value of β, the ordering of the $k = 0$, $k = 1$ results swaps positions.

In Figure 6.4, we impose general Robin boundary conditions on scalar field modes with $L = 1$, $\chi = 1$. In Figures 6.4(a), (c), (e), we present surface plots of the VP as a function of radial coordinate η (5.3) and Robin parameter β (6.41). In Figures 6.4(b), (d), (f), we give plots of the VP as a function of η for a variety of values of β. Figures 6.4(a), (b), give results for black holes with spherical event horizon ($k = 1$), Figures 6.4(c), (d), give results for black holes with planar event horizon ($k = 0$) and Figures 6.4(e), (f), give results for black holes with hyperbolic event horizon ($k = -1$).

In all cases in Figure 6.4, the value of the VP on the event horizon ($\eta = 1$) increases as β increases, and diverges as $\beta \to \beta_{crit}$. Note that β_{crit} changes as we vary the value of k; the value of β_{crit} in each case is given below each figure. Similar behaviour was observed in CadS (see section 3.5), where the value of the VP at the origin increased as we increased Robin parameter α, and diverged as $\alpha \to \alpha_{crit}$. This divergence as $\beta \to \beta_{crit}$ is to be expected, since the black hole becomes classically unstable for $\beta > \beta_{crit}$.

The line plots in Figures 6.4(b), (d), (f), clearly demonstrate that for all $\beta \neq 0$, the VP approaches the Neumann CadS limit $5/48\pi^2L^2$ (3.3) at the boundary $\eta \to \infty$. When $\beta = 0$, the VP approaches the Dirichlet CadS limit $-1/48\pi^2L^2$ (3.2). This is similar to the behaviour observed for both vacuum and thermal states in section 3.5, and discussed in detail in section 3.6. We therefore deduce that the VP on a topological SadS black hole approaches its vacuum value on CadS spacetime as the adS boundary is approached.

We can see from Figure 6.4 that, although the VP is always a monotonically decreasing function of η when Dirichlet and Neumann boundary conditions are imposed (although these appear constant in Figure 6.4, this is simply due to the scale used - see Figures 5.30, 6.3), there is a range of values of $\beta \in (0, \pi/2)$ for which the VP is monotonically increasing in η and has a maximum on the boundary. This is again similar to behaviour observed in CadS in section 3.5.

In Figure 6.5, we look at the VP for temperature below T_{min} (6.43), for which there exist no spherical black holes. In this case, we fix the adS radius of curvature $L =$

$8000/861 \approx 9.29$ and the surface gravity $\kappa \approx 0.12$. The VP takes very small values since the temperature is very small, however the qualitative behaviour is very similar to that in Figure 6.4. On the event horizon, the value of the VP increases with β, and on the boundary, all results approach the Neumann CadS limit (3.3) except when $\beta = 0$. The VP is a monotonically decreasing function of η for all β, except for those values of β within an interval contained in $(0, \pi/2)$.

In the final two cases that we consider, we increase the temperature so that we obtain two black holes with spherical horizons, one which we denote $k = 1(+)$, with the larger event horizon radius, and one which we denote $k = 1(-)$, with the smaller event horizon radius. In Figures 6.6, 6.7 the temperature is still fairly close to T_{min}, and the difference between event horizon radius for $k = 1(+)$ and $k = 1(-)$ is not that great. Here we consider black holes with adS radius of curvature $L \approx 0.53$ and surface gravity $\kappa \approx 3.59$. Figure 6.6 shows the results for the VP for Dirichlet (Figure 6.6(a)) and Neumann (Figure 6.6(b)) boundary conditions. In both cases, the VP is a monotonically decreasing function of η, approaching the CadS value (3.2, 3.3) at the boundary. The VP for the thermodynamically unstable $k = 1(-)$ black hole (the light blue curve in Figure 6.6) is significantly larger than the results for the other three black holes. The order of the curves does not change as we vary between Dirichlet and Neumann boundary conditions, unlike in Figures 5.30, 6.4. This shows that the relative order of the results for the VP must depend on the temperature of the black holes as well as the Robin parameter β.

Figure 6.7 shows the VP for general Robin boundary conditions for the same black holes as in Figure 6.6. The VP again converges to the CadS value of the spacetime boundary (3.2, 3.3), but this convergence appears to be slower than for the black holes in Figure 6.4.

Finally, in Figure 6.8, we give results for the renormalised VP for black holes with high temperature, where the adS radius of curvature $L \approx 0.001$ is relatively small, and the surface gravity $\kappa \approx 14801$ is very large. In this case, the VP for thermodynamically unstable black holes with $k = 1(-)$ is many times larger than the VP for the other black holes ($k = 1(+), 0, -1$). It is also much more difficult to calculate numerically, as convergence to the CadS limit as η increases is a lot slower than in other cases, requiring a grid in η to extend to much higher values. We would also need to truncate the ℓ- and n-sums at much higher values than in the $k = 1(+)$ case. For these reasons, we do not show the results for $k = 1(-)$, and instead focus on the other three cases. The behaviour is qualitatively the same as in all the other cases. The VP approaches the Neumann CadS limit (3.3) for all $\beta \neq 0$, and the Dirichlet CadS limit (3.2) for $\beta = 0$. The value of the VP on the event horizon increases as we increase β, diverging as $\beta \to \beta_{crit}$.

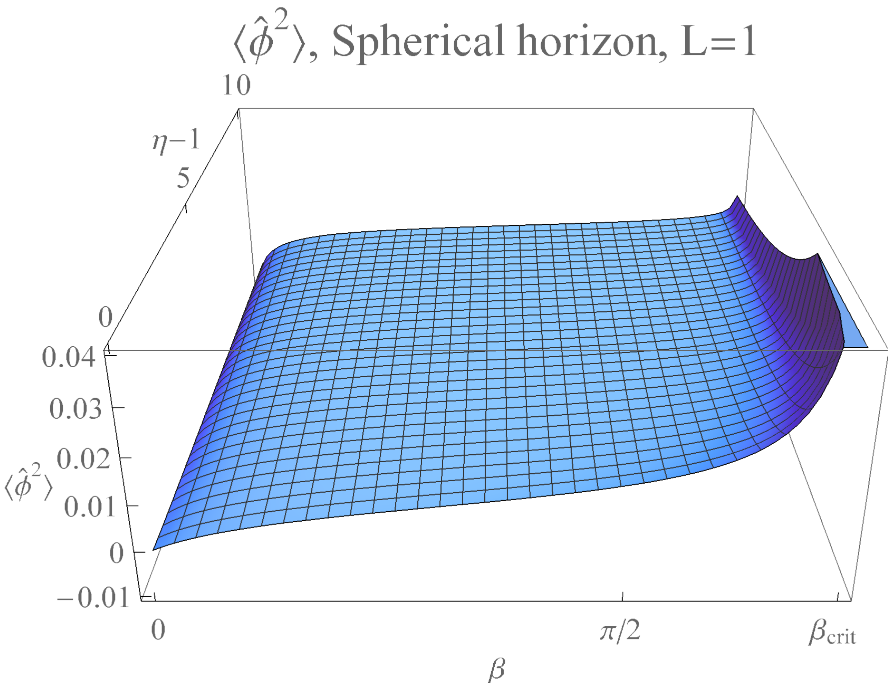

(a) $k = 1, M = 5, \beta_{crit} = 2.3166$

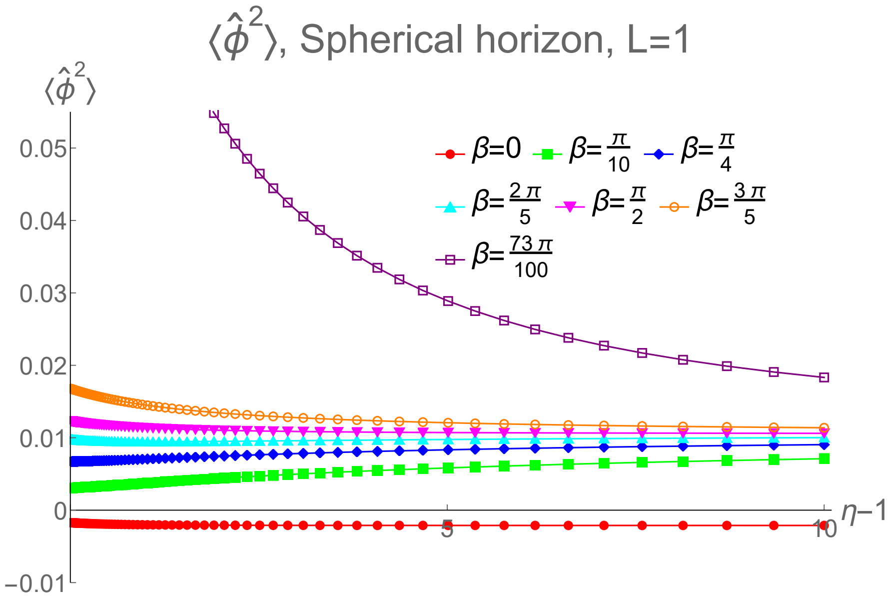

(b) $k = 1, M = 5, \beta_{crit} \simeq \frac{74\pi}{100}$

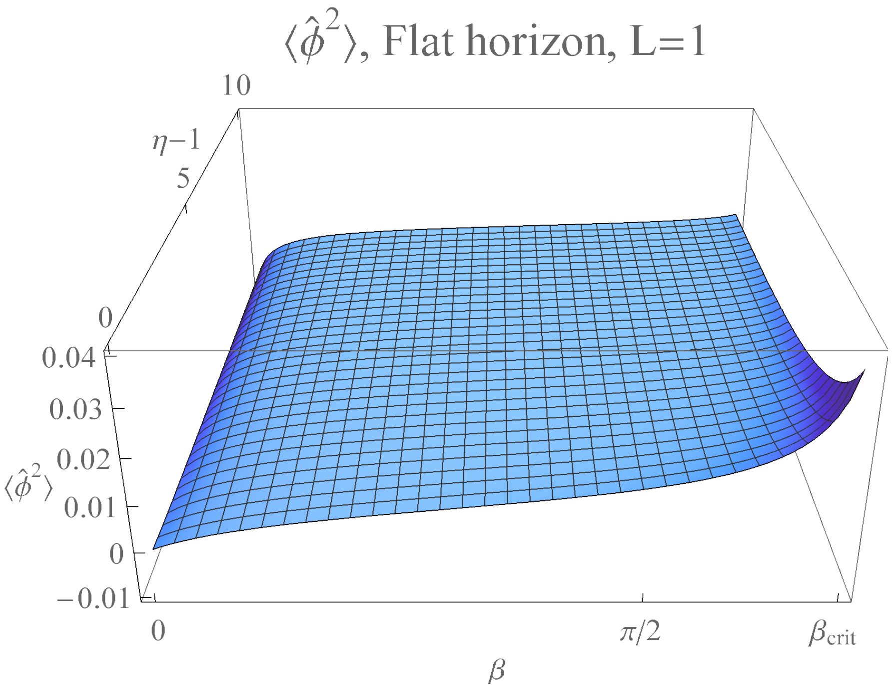

(c) $k = 0, M = 4, \beta_{crit} = 2.2301$

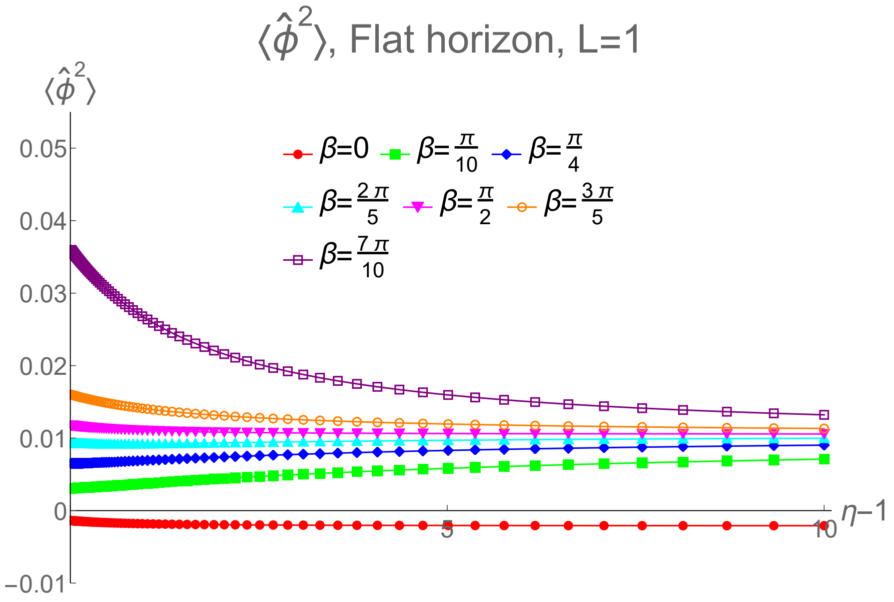

(d) $k = 0, M = 4, \beta_{crit} \simeq \frac{71\pi}{100}$

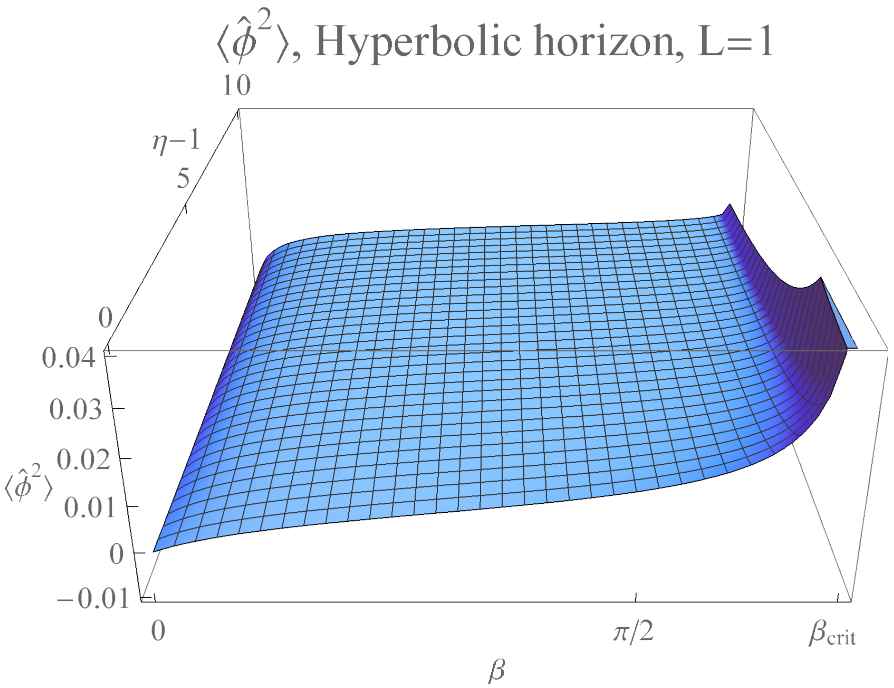

(e) $k = -1, M = 3, \beta_{crit} = 2.2411$

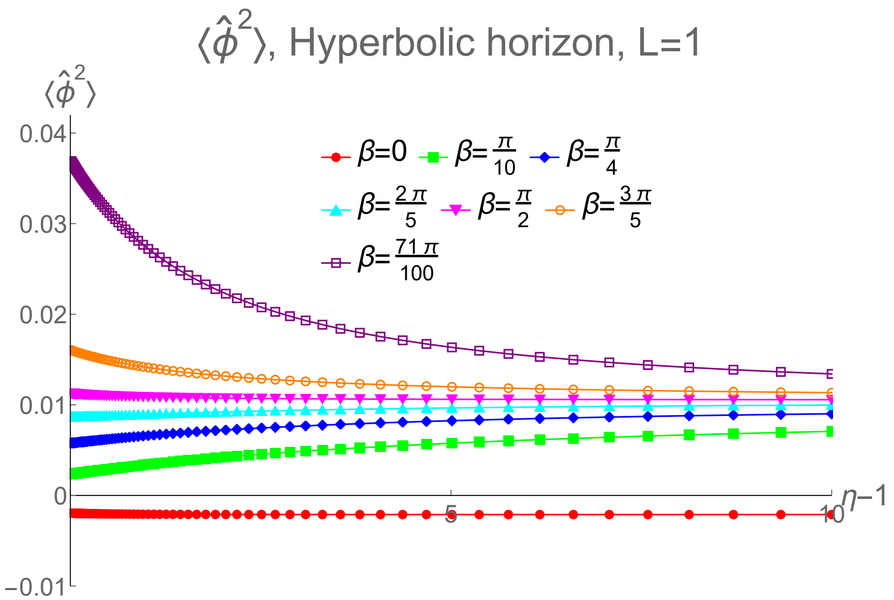

(f) $k = -1, M = 3, \beta_{crit} \simeq \frac{71\pi}{100}$

Figure 6.4: Renormalised VP for topological black holes with adS radius of curvature $L = 1$ and event horizon radius $r_h = 2$. In figures (a), (c), (e), the results are given as a function of the radial coordinate η and the Robin parameter β for $\beta \in [0, \beta_{crit})$. Figures (b), (d), (f), show line plots of the renormalised VP for a selection of values of β.

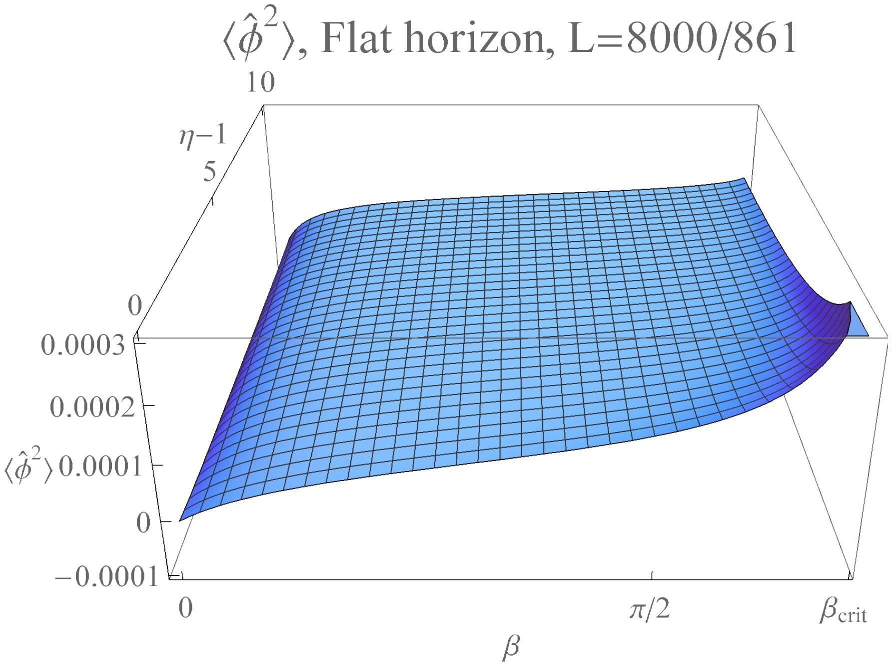

(a) $k = 0, r_h = 6.8064, \beta_{crit} = 2.2300$

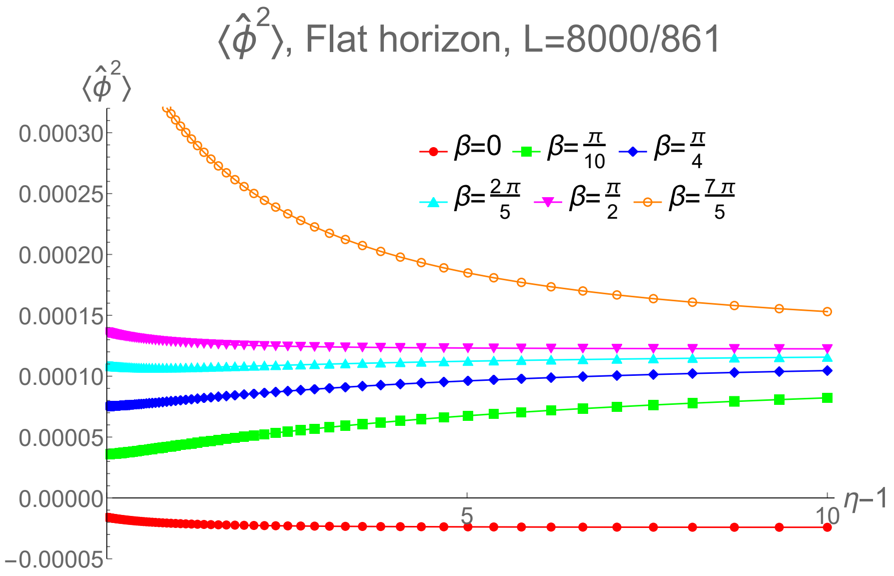

(b) $k = 0, r_h = 6.8064, \beta_{crit} \simeq \frac{71\pi}{100}$

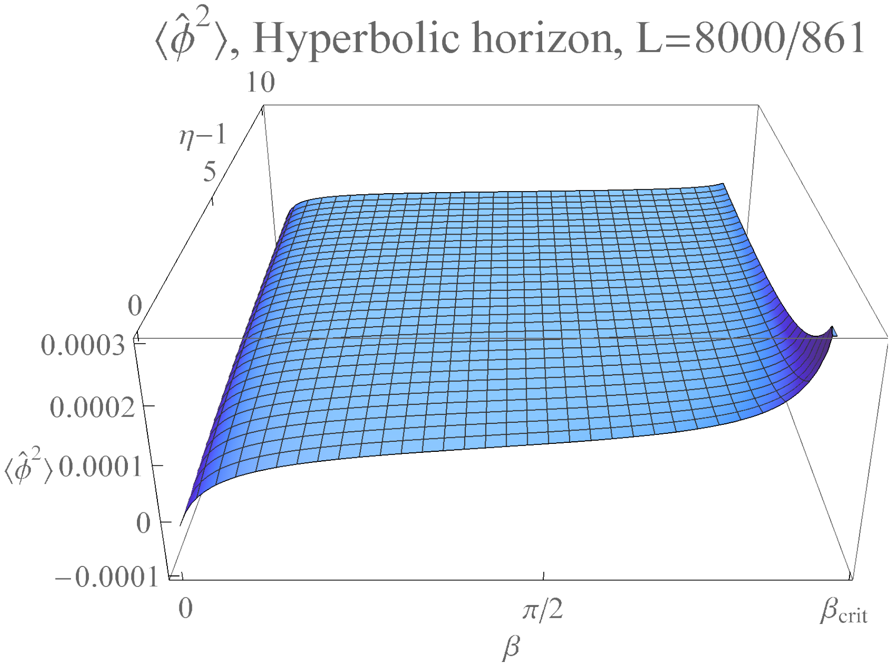

(c) $k = -1, r_h = 9.7561, \beta_{crit} = 2.9018$

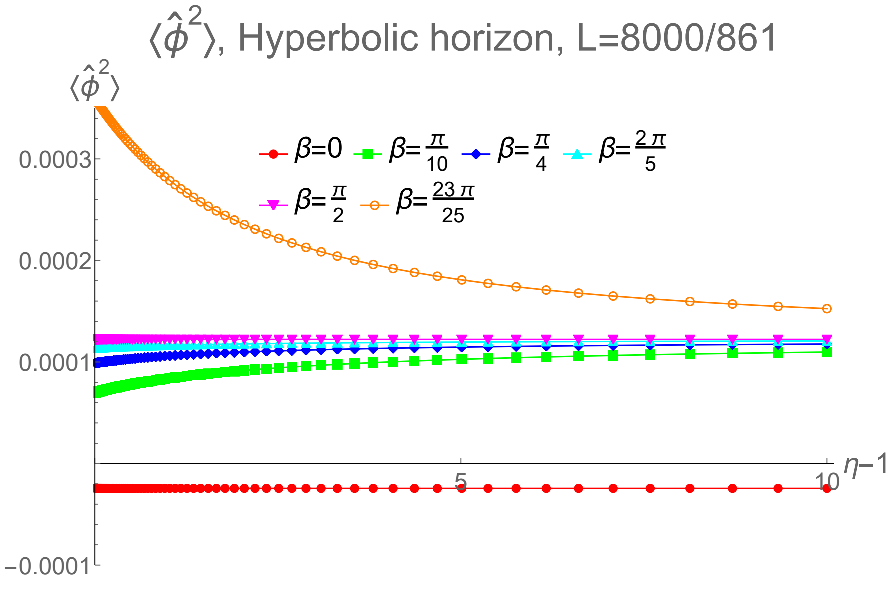

(d) $k = -1, r_h = 9.7561, \beta_{crit} \simeq \frac{92\pi}{100}$

Figure 6.5: Renormalised VP for topological black holes with adS radius of curvature $L = 8000/861 \approx 9.29$ and surface gravity $\kappa = 37843/320000 \approx 0.12$. In figures (a), (c), the results are given as a function of the radial coordinate η and the Robin parameter β for $\beta \in [0, \beta_{crit})$. Figures (b), (d), show line plots of the renormalised VP for a selection of values of β.

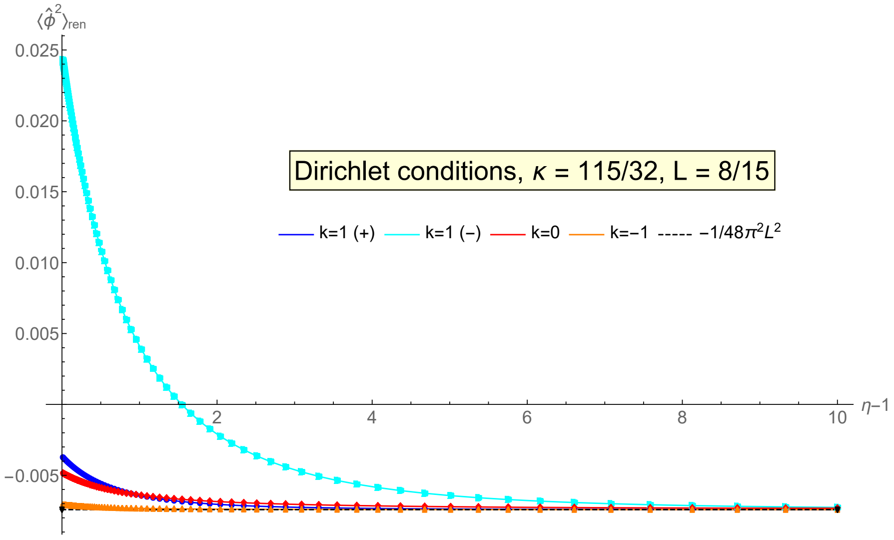

(a) Renormalised VP with Dirichlet boundary conditions imposed.

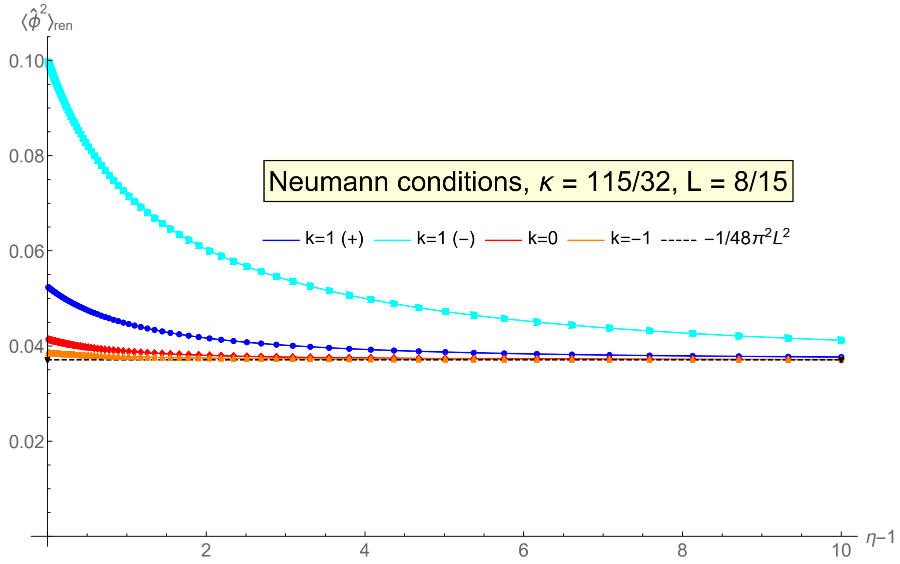

(b) Renormalised VP with Neumann boundary conditions imposed.

Figure 6.6: Renormalised VP for topological black holes with adS radius of curvature $L = 8/15 \approx 0.53$ and surface gravity $\kappa = 115/32 \approx 3.59$. In Figure (a), Dirichlet conditions are applied to the scalar field, whilst in Figure (b), Neumann conditions are applied to the scalar field.

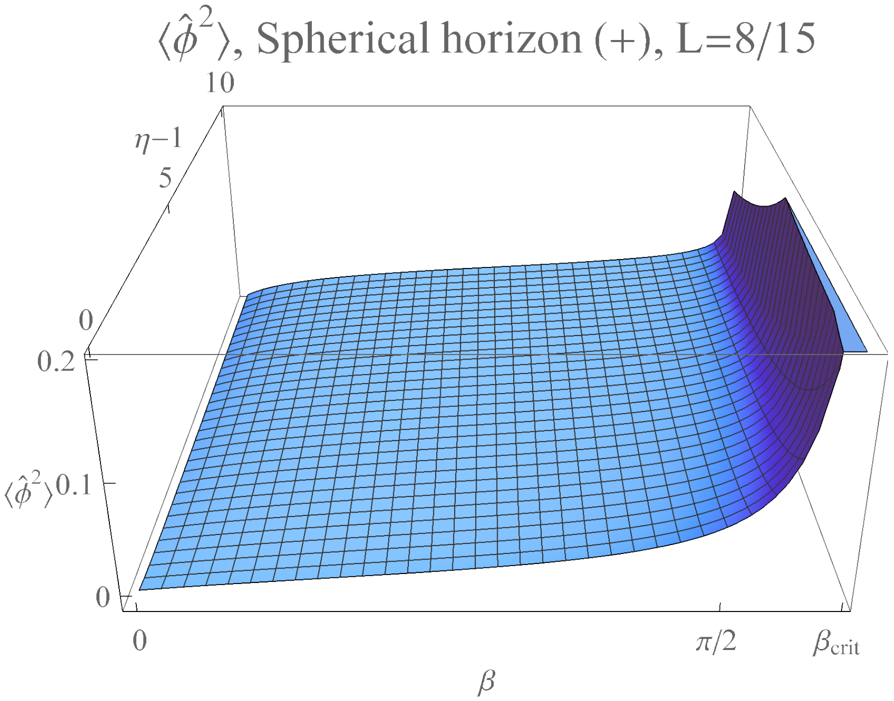

(a) $k = 1(+), r_h = 0.1948, \beta_{crit} = 1.8833$

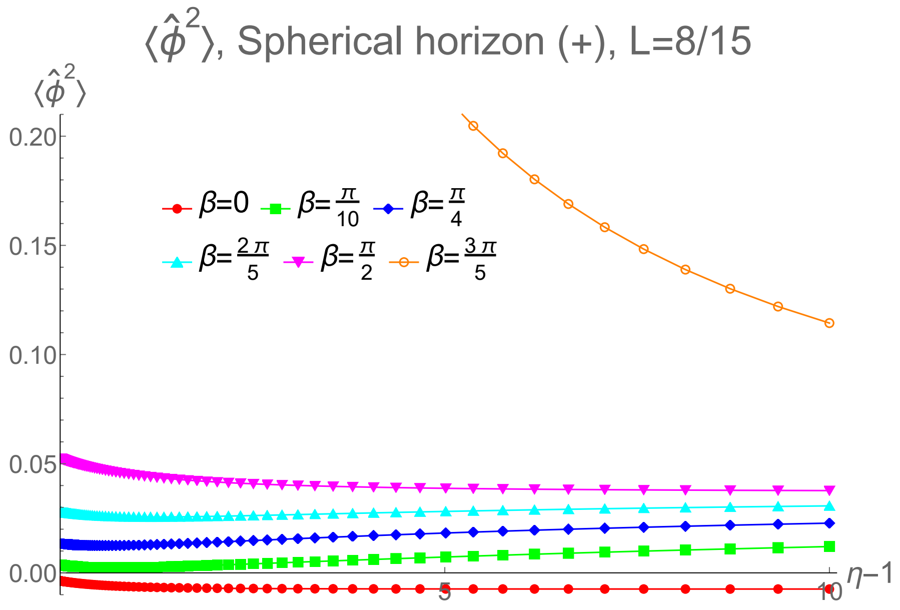

(b) $k = 1(+), r_h = 0.1948, \beta_{crit} \simeq \frac{60\pi}{100}$

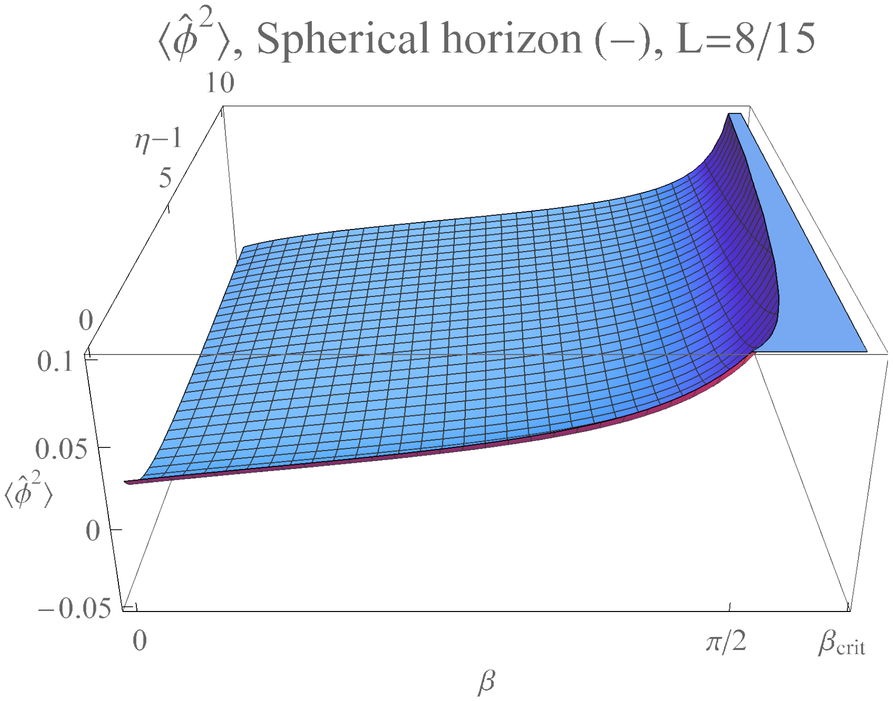

(c) $k = 1(-), r_h = 0.4866, \beta_{crit} = 1.8998$

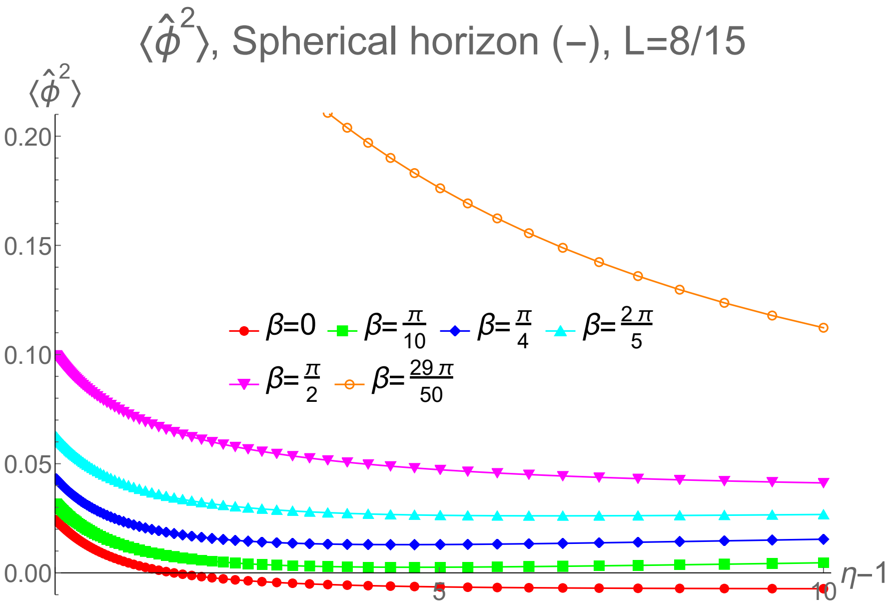

(d) $k = 1(-), r_h = 0.4866, \beta_{crit} \simeq \frac{60\pi}{100}$

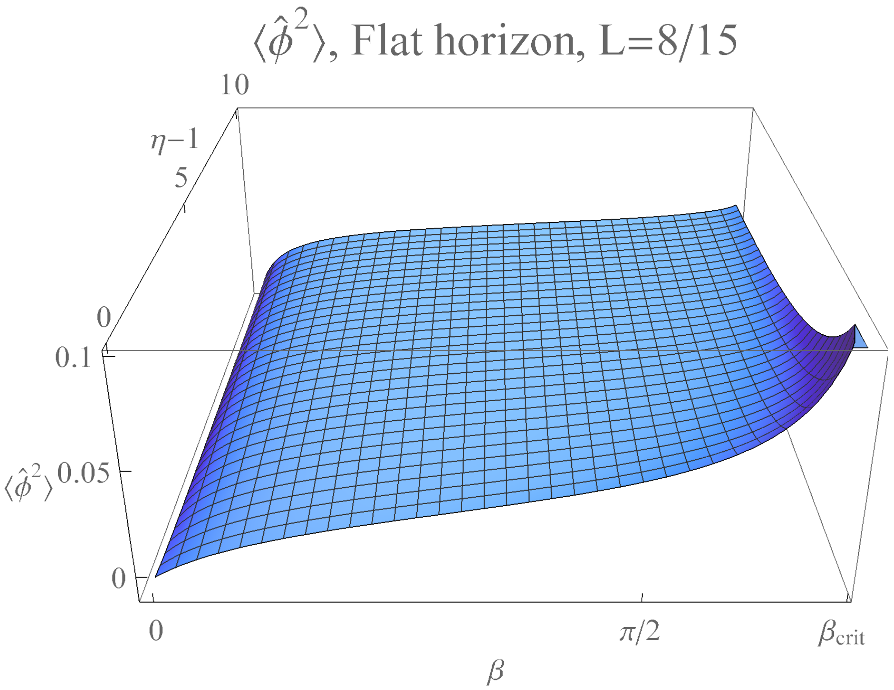

(e) $k = 0, r_h = 0.6815, \beta_{crit} = 2.2301$

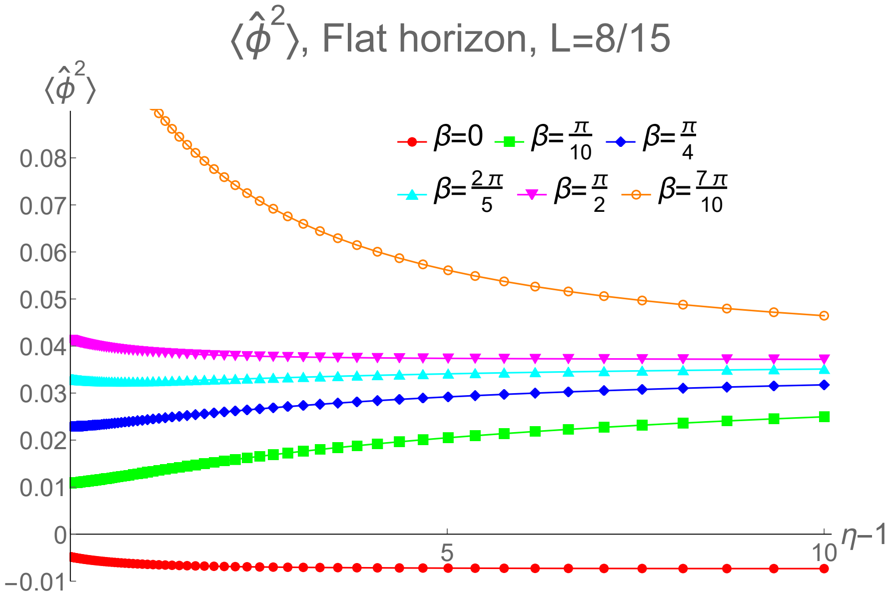

(f) $k = 0, r_h = 0.6815, \beta_{crit} \simeq \frac{71\pi}{100}$

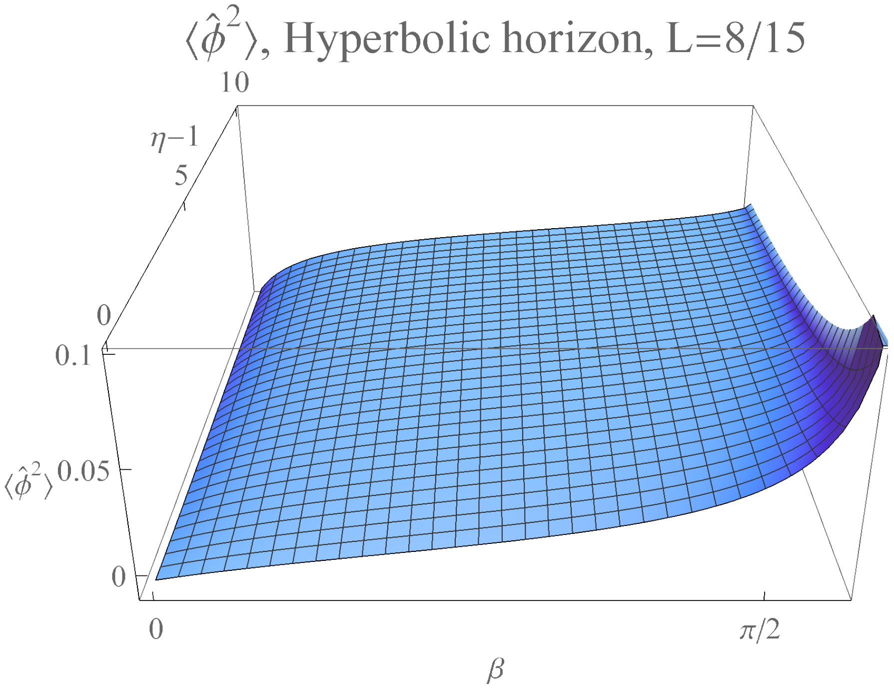

(g) $k = -1, r_h = 0.8, \beta_{crit} = 1.8829$

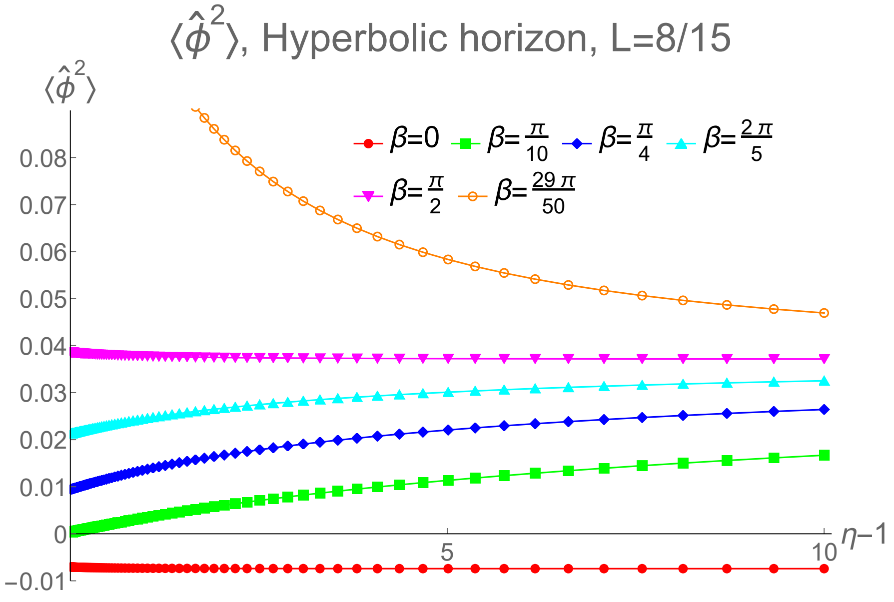

(h) $k = -1, r_h = 0.8, \beta_{crit} \simeq \frac{60\pi}{100}$

Figure 6.7: Renormalised VP for topological black holes with adS radius of curvature $L = 8/15 \approx 0.53$ and surface gravity $\kappa = 115/32 \approx 3.59$. In figures (a), (c), (e), (g), the results are given as a function of the radial coordinate η and the Robin parameter β for $\beta \in [0, \beta_{crit})$. Figures (b), (d), (f), (h), show line plots of the renormalised VP for a selection of values of β.

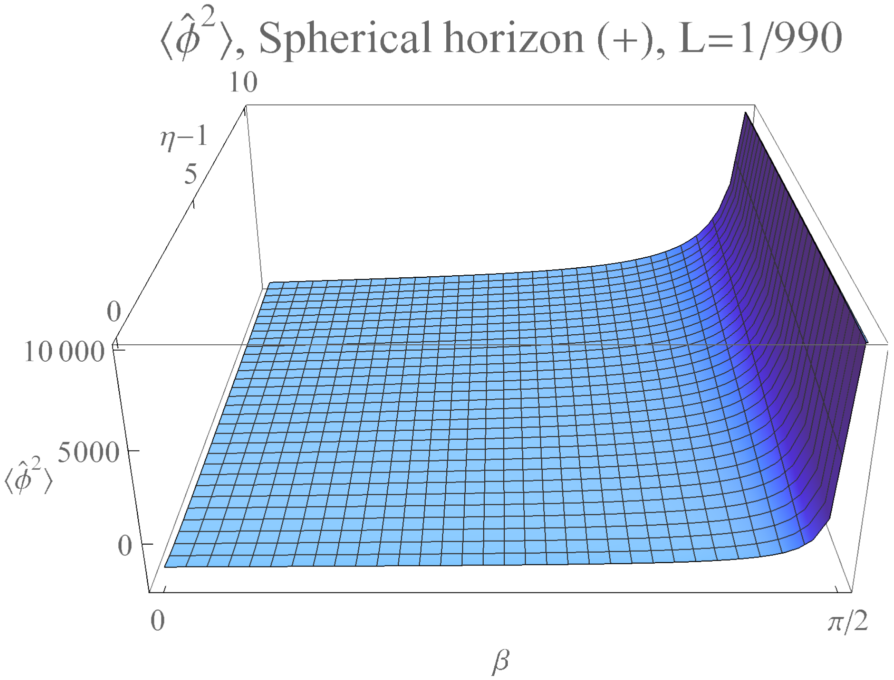

(a) $k = 1(+), r_h = 0.0101, \beta_{crit} = 1.5747$

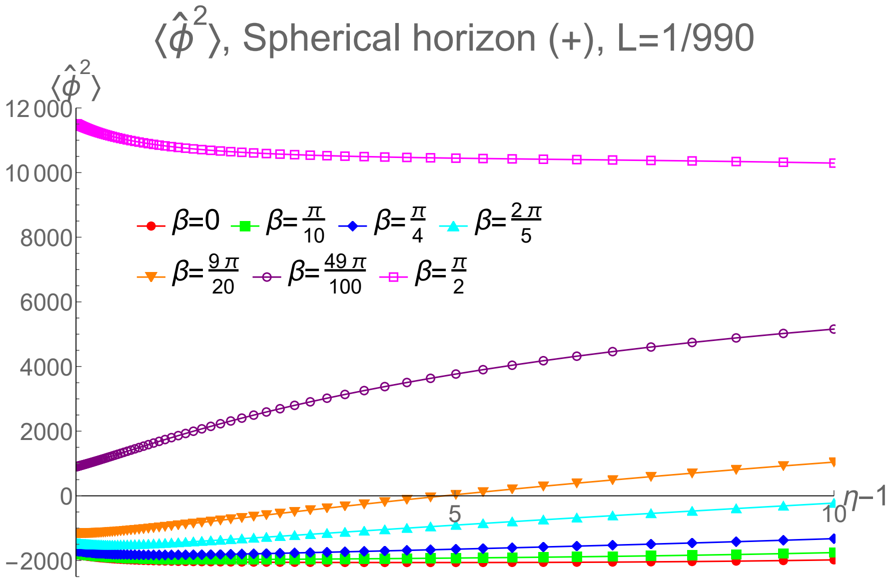

(b) $k = 1(+), r_h = 0.0101, \beta_{crit} \simeq \frac{50\pi}{100}$

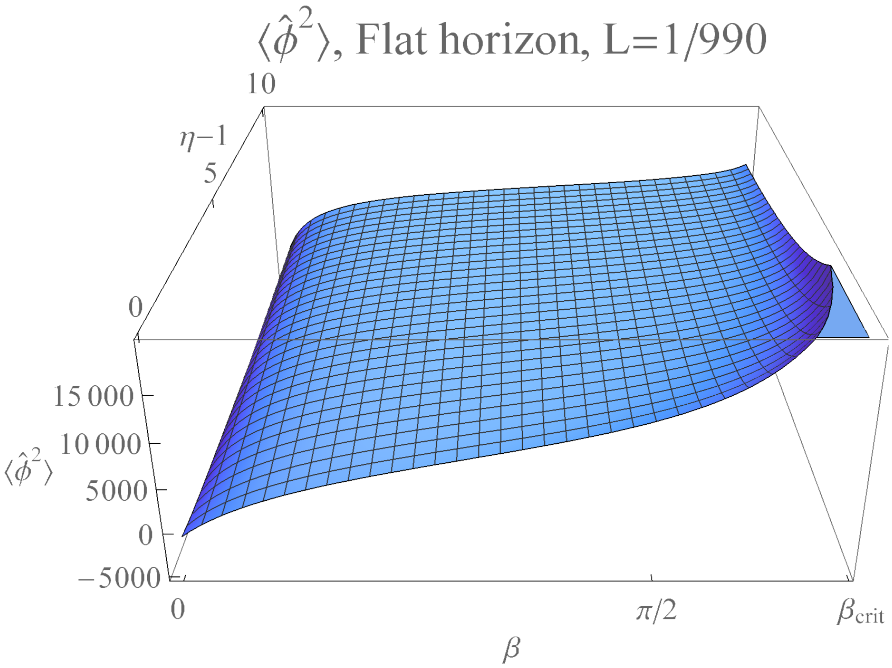

(c) $k = 0, r_h = 0.0101, \beta_{crit} = 2.2302$

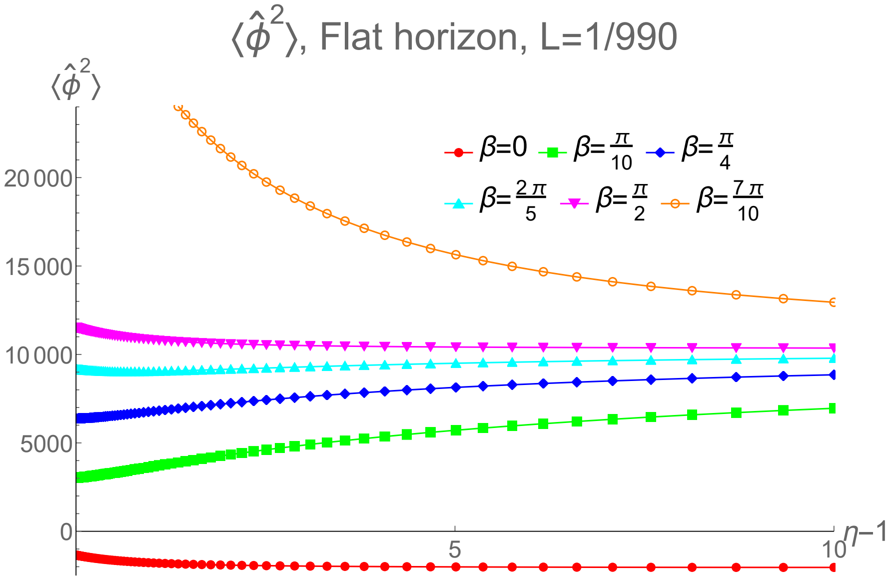

(d) $k = 0, r_h = 0.0101, \beta_{crit} \simeq \frac{71\pi}{100}$

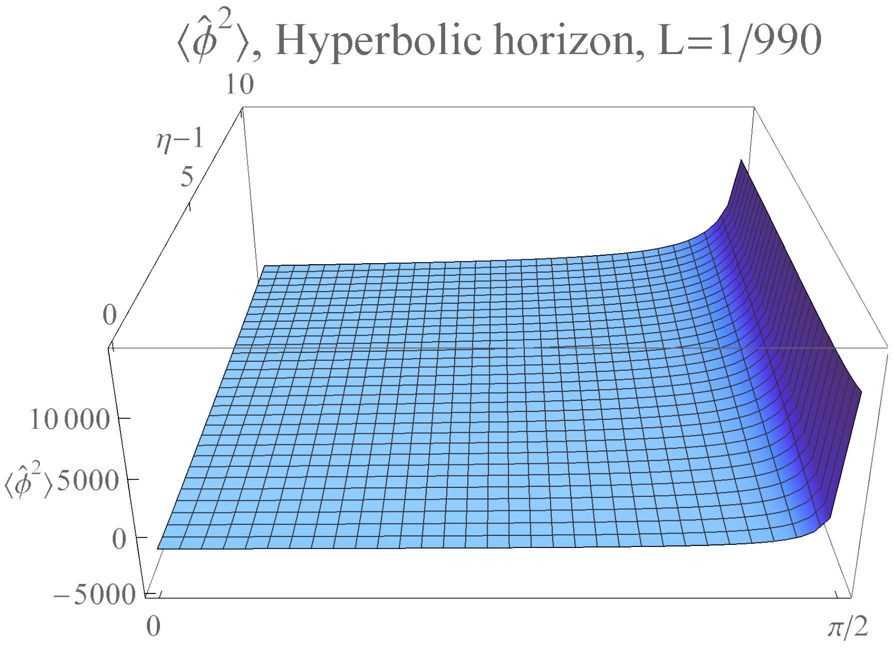

(e) $k = -1, r_h = 0.0101, \beta_{crit} = 1.5747$

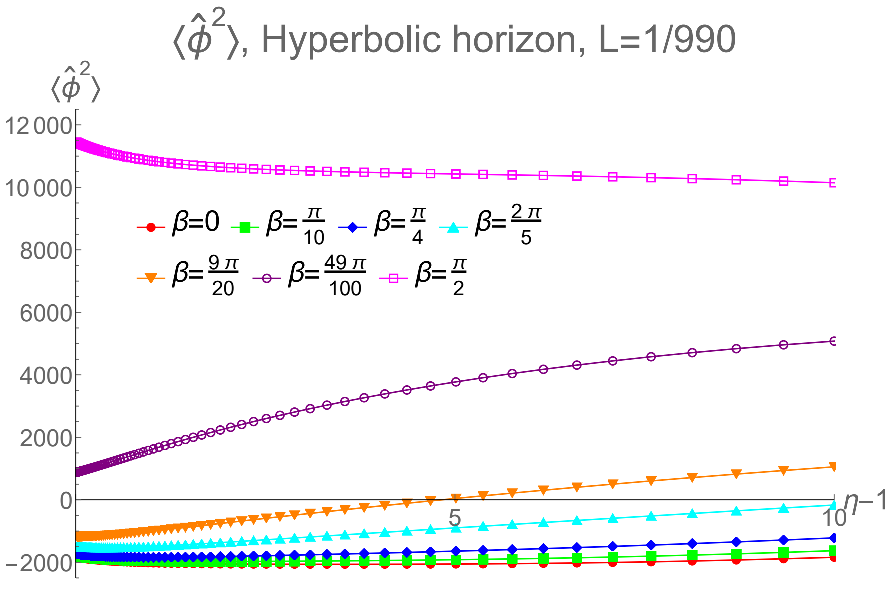

(f) $k = -1, r_h = 0.0101, \beta_{crit} \simeq \frac{50\pi}{100}$

Figure 6.8: Renormalised VP for topological black holes with adS radius of curvature $L = 1/990 \approx 0.001$ and surface gravity $\kappa = 29601/2 \approx 14801$. In figures (a), (c), (e), the results are given as a function of the radial coordinate η and the Robin parameter β for $\beta \in [0, \beta_{crit})$. Figures (b), (d), (f), show line plots of the renormalised VP for a selection of values of β.

6.4 Summary

In this chapter, we have explored the effects of imposing Robin boundary conditions on scalar fields in topological black hole spacetimes.

In section 6.1, we showed that there exists a critical value of Robin parameter α such that $\pi/2 < \alpha_{crit} < \pi$. For $\alpha > \alpha_{crit}$ there exist unstable modes and the scalar fields are classically unstable. This is similar to the behaviour in CadS. However, in SadS, the value of α_{crit} depends on the adS radius of curvature L and the event horizon radius r_h, whilst in CadS, the value of α_{crit} is the same for all values of L.

We calculate the renormalised VP using the extended coordinates method, first discussed in section 1.3.4. The details of the numerical calculation are discussed in section 6.2. The numerical calculation builds on the calculation performed in chapter 5 rather straightforwardly, as we find that all Robin conditions can be applied simply via a linear combination of radial modes with Neumann and Dirichlet conditions imposed (6.37). The Hadamard parametrix is not affected by boundary conditions, and results from chapter 5 are used again.

The results for the renormalised VP, given in section 6.3, demonstrates similar behaviour to the results found in CadS in chapter 3. The value of the VP on the event horizon $r = r_h$ increases as we increase the value of the Robin parameter β (6.41). The VP approaches the CadS Dirichlet limit (3.2) when $\beta = 0$ and the CadS Neumann limit (3.3) for $\beta \neq 0$. The VP is a monotonically decreasing function of radius η for all Robin parameter β except for when β lies in an interval contained in $(0, \pi/2)$, where the VP is a monotonically increasing function in η.

Part IV

Conclusions

Chapter 7

Conclusions and outlook

This thesis covers recent research into scalar field theory on anti-de Sitter spacetime, with a focus on the calculation of the renormalised vacuum polarisation on both the covering space (CadS) and topological black hole spacetimes (SadS). The main goals of this thesis were to

- Calculate the renormalised vacuum polarisation $\langle\hat{\phi}^2\rangle_{ren}$ on CadS for a range of Robin boundary conditions imposed on scalar fields,
- Calculate the renormalised vacuum polarisation on SadS for black holes with positive, negative and zero horizon curvature,
- Calculate the renormalised vacuum polarisation on SadS for a range of Robin boundary conditions imposed on scalar fields.

Numerical results for all of these calculations have been obtained via computation in `Mathematica`. See Figures 3.7 - 3.9 for results in CadS, Figures 5.3 - 5.30 for results in SadS with Dirichlet boundary conditions imposed on scalar fields, and Figures 6.4 - 6.8 for results in SadS with Robin conditions imposed on scalar fields.

The quantum state is global, and so the boundary conditions and the topology of the event horizon affect the global properties of expectation values. The effects of Robin conditions on the vacuum polarisation are qualitatively similar in both CadS and SadS. For Robin parameter $\alpha \in [0, \pi)$, there exists a critcal value $\alpha_{crit} \in (\pi/2, \pi)$ such that mode solutions are found to be unstable for $\alpha \in [\alpha_{crit}, \pi)$. For $\alpha \in (0, \alpha_{crit})$, the vacuum polarisation approaches the CadS Neumann limit $\langle\hat{\phi}_N^2\rangle_{ren} = \frac{5}{48\pi^2 L^2}$ as $r \to \infty$, and only approaches the CadS Dirichlet limit $\langle\hat{\phi}_D^2\rangle_{ren} = -\frac{1}{48\pi^2 L^2}$ when $\alpha = 0$.

In CadS, we derived $\alpha_{crit} = -\tan^{-1}(\pi/2)$. In SadS, the value of α_{crit} depends on the event horizon radius r_h and the curvature of the event horizon. The values of α_{crit} in SadS are given in Figure 6.1 as a function of r_h/L, where L is the adS lengthscale.

We first considered CadS in the Lorentzian background, attempting to calculate differences between vacuum and thermal states, which would give rise to regularised results. When Robin conditions were imposed, these results suffered from errors (see Figure 3.6) due to the representation of the Green's function and the '$i\epsilon$' prescription employed in section 3.3.2.

We then looked at CadS in the Euclidean background, where an '$i\epsilon$' prescription is not required due to the uniqueness of the Euclidean Green's function G_E. Here, we calculated results with Robin conditions by taking a linear combination of Neumann and Dirichlet results along with a regular contribution G_R^E (see equations (3.124) - (3.127).

In SadS, we considered three different topological black hole solutions, namely the $k = 1$ case, where the event horizon has positive curvature, the $k = 0$ case, where the event horizon has zero curvature, and the $k = -1$ case, where the event horizon has negative curvature. In all cases, the vacuum polarisation was seen to be qualitatively the same. The magnitude of the vacuum polarisation on the event horizon was different in each case, but converges to the relevant limit as we approach the boundary. With Dirichlet and Neumann conditions imposed, the vacuum polarisation was always found to be a monotonically decreasing function, but this was not always the case when more general Robin conditions are imposed.

We implemented Hadamard renormalisation in SadS by using the extended coordinates method, which involves writing the Hadamard parametrix as a mode sum and performing the subtraction mode-by-mode. This method was found to converge very quickly. For more analysis on rates of convergence and accuracy of results, see sections 5.6.1, 5.6.2 and 5.6.3. This calculation was performed separately for Neumann and Dirichlet conditions. To consider Robin conditions, we were able to take a linear combination of radial modes, using equation (6.37) to save on computation time.

There are several ways to extend this work. The first is to employ results derived here in the calculation of the stress-energy tensor (SET) in both CadS and SadS spacetimes. This is more straightforward in CadS, where results already exist for the SET with Neumann and Dirichlet boundary conditions imposed [110]. To calculate the SET, one would simply need to apply the SET operator (1.177) to G_α^E, using a linear combination of G_N^E, G_D^E (3.124). This amounts to a linear combination of $\langle \hat{T}_{\mu\nu} \rangle_N, \langle \hat{T}_{\mu\nu} \rangle_D$, given in [110], together with an additional regular part, which would need to be calculated.

The extension of the VP to the SET in SadS is more complicated since there do not exist any known closed-form results for the SET with Dirichlet or Neumann results imposed. In order to calculate the SET in SadS, we would require results for the VP to be calculated to a high enough order in r that would allow us to take derivatives. We would also need to calculate derivatives of the tail of the Hadamard parametrix, which cannot be found in suitable mode-sum form in the $k = 0, -1$ cases (see section 5.7).

Results for the VP are yet to be found for topological black holes with compact event horizons in the $k = 0, -1$ cases. These black holes were discussed briefly in section

4.1. The mode-sums in these cases are expected to be summations over ℓ rather than the integrals found in (5.115), so numerical computation of these results should be less intensive since a dense grid of modes is not required. The difficulty with this extension is finding a useful coordinate system that allows for the compactification of the event horizon.

All work presented in this thesis has been for a massless, conformally coupled scalar field. This could be extended for general mass and coupling, a subject which was gently touched on in section 5.7. The work could also be extended to Reissner-Nordström-adS (RNadS), where $Q \neq 0$ in (4.2). The extension from SadS to RNadS is thought to be fairly straightforward as many of the calculations are performed analytically without specifying $f(r)$.

Part V

Appendices

Appendix A

Hadamard form of Green's function

In this appendix, we determine the form of biscalars $U(x,x'), V(x,x'), W(x,x')$ in the Hadamard form of the Green's function (1.185), keeping points separated. These results are rederived from [4]. We substitute (1.185) in the Klein-Gordon equation (1.58). This gives us

$$(\Box - m^2 - \xi R)\left(\frac{U}{\sigma} + V\ln\sigma + W\right) = -\frac{\delta^4(x-x')}{\sqrt{-g(x)}} \tag{A.1}$$

where we have suppressed the $i\epsilon$ terms for convenience. We can calculate

$$\begin{aligned}
\Box\frac{U}{\sigma} = \nabla^\mu\nabla_\mu\frac{U}{\sigma} &= (\nabla^\mu\nabla_\mu U)\frac{1}{\sigma} + 2(\nabla_\mu U)\left(\nabla^\mu\frac{1}{\sigma}\right) + U\left(\nabla^\mu\nabla_\mu\frac{1}{\sigma}\right)\\
&= (\Box U)\frac{1}{\sigma} + 2U_{;\mu}(-\sigma^{-2})\sigma^{;\mu} + U\nabla^\mu(-\sigma^{-2}\nabla_\mu\sigma)\\
&= \frac{1}{\sigma}\Box U - \frac{2}{\sigma^2}U_{;\mu}\sigma^{;\mu} + U\left(\frac{2}{\sigma^3}\nabla^\mu\sigma\nabla_\mu\sigma - \frac{1}{\sigma^2}\Box\sigma\right)\\
&= \frac{1}{\sigma}\Box U - \frac{2}{\sigma^2}U_{;\mu}\sigma^{;\mu} + \frac{2U}{\sigma^2}\Delta^{-1/2}(\Delta^{1/2})_{;\mu}\sigma^{;\mu}
\end{aligned} \tag{A.2}$$

where we have used (1.180, 1.184) between the third and final lines to allow us to rearrange, and we use the shorthand $U_{;\mu} = \nabla_\mu U$. We also have

$$\begin{aligned}
\Box[V\ln\sigma] = \nabla^\mu\nabla_\mu[V\ln\sigma] &= (\nabla^\mu\nabla_\mu V)\ln\sigma + 2(\nabla_\mu V)(\nabla^\mu\ln\sigma) + V(\nabla^\mu\nabla_\mu\ln\sigma)\\
&= (\Box V)\ln\sigma + 2V_{;\mu}\frac{1}{\sigma}\sigma^{;\mu} + V\nabla^\mu\left(\frac{1}{\sigma}\nabla_\mu\sigma\right)\\
&= (\Box V)\ln\sigma + \frac{2}{\sigma}V_{;\mu}\sigma^{;\mu} + V\left(-\frac{1}{\sigma^2}\right)\nabla^\mu\sigma\nabla_\mu\sigma + \frac{V}{\sigma}\Box\sigma\\
&= (\Box V)\ln\sigma + \frac{2}{\sigma}V_{;\mu}\sigma^{;\mu} + \frac{2V}{\sigma} - \frac{2V}{\sigma}\Delta^{-1/2}(\Delta^{1/2})_{;\mu}\sigma^{;\mu}
\end{aligned} \tag{A.3}$$

using the same identities as before. Substituting into (A.1) and rearranging, we find, when $x' \neq x$,

$$\begin{aligned}(\Box - m^2 - \xi R)W = &-\frac{1}{\sigma}(\Box - m^2 - \xi R)U + \frac{2}{\sigma^2}U_{;\mu}\sigma^{;\mu} - \frac{2U}{\sigma^2}\Delta^{-1/2}(\Delta^{1/2})_{;\mu}\sigma^{;\mu} \\ &- (\Box - m^2 - \xi R)V\ln\sigma - \frac{2}{\sigma}V_{;\mu}\sigma^{;\mu} - \frac{2V}{\sigma} \\ &+ \frac{2V}{\sigma}\Delta^{-1/2}(\Delta^{1/2})_{;\mu}\sigma^{;\mu}.\end{aligned} \tag{A.4}$$

Since logarithmic terms must vanish independently of other terms, we must have

$$(\Box - m^2 - \xi R)V = 0. \tag{A.5}$$

Using the series expansion (1.187) for $V(x,x')$, (A.5) gives us

$$\begin{aligned}(\Box - m^2 - \xi R)\sum_{n=0}^{\infty}V_n\sigma^n = &\sum_{n=0}^{\infty}\Big[(\Box V_n)\sigma^n + 2V_{n;\mu}n\sigma^{n-1}\sigma^{;\mu} \\ &+n(n-1)\sigma^{n-2}V_n\sigma^{;\mu}\sigma_{;\mu} + nV_n\sigma^{n-1}\Box\sigma - (m^2+\xi R)V_n\sigma^n\Big] \\ = &\sum_{n=0}^{\infty}\Big[2V_{n;\mu}n\sigma^{n-1}\sigma^{;\mu} + 2n(n+1)\sigma^{n-1}V_n \\ &-2nV_n\sigma^{n-1}\Delta^{-1/2}(\Delta^{1/2})_{;\mu} + (\Box - m^2 - \xi R)V_n\sigma^n\Big] = 0\end{aligned} \tag{A.6}$$

from which we can derive the recurrence relation (1.189).

Equation (A.4) now takes the form

$$\begin{aligned}\sigma^2(\Box - m^2 - \xi R)W = &-\sigma(\Box - m^2 - \xi R)U + 2U_{;\mu}\sigma^{;\mu} - 2U\Delta^{-1/2}(\Delta^{1/2})_{;\mu}\sigma^{;\mu} \\ &- 2\sigma V_{;\mu}\sigma^{;\mu} - 2\sigma V + 2\sigma V\Delta^{-1/2}(\Delta^{1/2})_{;\mu}\sigma^{;\mu}.\end{aligned} \tag{A.7}$$

Comparing coefficients of σ^0, we must have

$$2U_{;\mu}\sigma^{;\mu} - 2U\Delta^{-1/2}(\Delta^{1/2})_{;\mu}\sigma^{;\mu} = 0. \tag{A.8}$$

Solving this allows us to obtain (1.186). Substituting the series solution (1.187) for V and (1.188) for W into (A.7), we have

$$\begin{aligned}\sigma(\Box - m^2 - \xi R)\sum_{n=0}^{\infty}W_n\sigma^n + (\Box - m^2 - \xi R)\Delta^{1/2} + 2\left(\sum_{n=0}^{\infty}V_n\sigma^n\right)_{;\mu}\sigma^{;\mu} \\ +2\sum_{n=0}^{\infty}V_n\sigma^n - 2\sum_{n=0}^{\infty}V_n\sigma^n\Delta^{-1/2}(\Delta^{1/2})_{;\mu}\sigma^{;\mu} = 0.\end{aligned} \tag{A.9}$$

We can note

$$(V_n\sigma^n)_{;\mu}\sigma^{;\mu} = \sigma^n V_{n;\mu}\sigma^{;\mu} + nV_n\sigma^{n-1}\sigma_{;\mu}\sigma^{;\mu} = \sigma^n V_{n;\mu}\sigma^{;\mu} + 2n\sigma^n V_n \tag{A.10}$$

using (1.180), and

$$\begin{aligned}\sigma(\Box - m^2 - \xi R)(W_n \sigma^n) =& \sigma^{n+1}(\Box - m^2 - \xi R)W_n + 2n\sigma^n W_{n;\mu}\sigma^{;\mu} \\ & + 2n(n+1)\sigma^n W_n - 2n\sigma^n W_n \Delta^{-1/2}(\Delta^{1/2})_{;\mu}\sigma^{;\mu} \qquad \text{(A.11)}\end{aligned}$$

using (1.184). Substitution of (A.10, A.11) into (A.9) and comparing coefficients of σ^0, we obtain (1.190) as our defining equation for V_0. Comparing coefficients of σ^{n+1} we obtain the recurrence relation (1.191) for the W_n.

Appendix B

Solving the wave equation in ESU

In this appendix, we solve the wave equation (3.8) using separation of variables. We begin by writing

$$\phi^{ESU}(t,\rho,\theta,\varphi) = \mathcal{A}(t)\mathcal{B}(\rho,\theta,\varphi). \tag{B.1}$$

The equation can then be rearranged as follows:

$$\frac{1}{\mathcal{A}}\frac{d^2\mathcal{A}}{dt^2} = \frac{1}{\mathcal{B}}\left\{\frac{1}{\sin^2\rho}\left[\frac{\partial}{\partial\rho}\left(\sin^2\rho\frac{\partial\mathcal{B}}{\partial\rho}\right) + \frac{1}{\sin\theta}\frac{\partial}{\partial\theta}\left(\sin\theta\frac{\partial\mathcal{B}}{\partial\theta}\right) + \frac{1}{\sin^2\theta}\frac{\partial^2\mathcal{B}}{\partial\varphi^2}\right] - \mathcal{B}\right\} \tag{B.2}$$

where the left-hand side now depends solely on t, and the right-hand side depends on ρ, θ, φ. This means we can set both sides equal to a constant. We have

$$\mathcal{A}''(t) = -\omega^2\mathcal{A} \tag{B.3}$$

for $\omega \in \mathbb{R}$, where we note that the separation constant must be negative in order to give us time-periodic solutions. We find our solutions to be

$$\mathcal{A}(t) = C_1 e^{-i\omega t} + C_2 e^{i\omega t} \tag{B.4}$$

where for positive frequency modes we simply set $C_2 = 0$ and $\omega > 0$. Looking at $\mathcal{B}(\rho,\theta,\varphi)$, we have

$$(1-\omega^2)\mathcal{B} = \frac{1}{\sin^2\rho}\left[\frac{\partial}{\partial\rho}\left(\sin^2\rho\frac{\partial\mathcal{B}}{\partial\rho}\right) + \frac{1}{\sin\theta}\frac{\partial}{\partial\theta}\left(\sin\theta\frac{\partial\mathcal{B}}{\partial\theta}\right) + \frac{1}{\sin^2\theta}\frac{\partial^2\mathcal{B}}{\partial\varphi^2}\right]. \tag{B.5}$$

We write

$$\mathcal{B}(\rho,\theta,\varphi) = X(\rho)Y(\theta,\varphi) \tag{B.6}$$

and hence find

$$\frac{1}{Y}\left[\frac{1}{\sin\theta}\frac{\partial}{\partial\theta}\left(\sin\theta\frac{\partial Y}{\partial\theta}\right) + \frac{1}{\sin^2\theta}\frac{\partial^2 Y}{\partial\varphi^2}\right] = (1-\omega^2)\sin^2\rho - \frac{1}{X}\frac{d}{d\rho}\left(\sin^2\rho\frac{dX}{d\rho}\right). \tag{B.7}$$

The left-hand side of this PDE depends on θ, φ whilst the right-hand side depends only on ρ, so we can set both sides equal to a constant. The left-hand side evaluated gives

$$Y(\theta, \varphi) = Y_{\ell m}(\theta, \varphi), \tag{B.8}$$

the spherical harmonics, provided the separation constant has the form $-\ell(\ell+1)$ [120, eq. 14.30.11]. Then the radial equation has the form

$$\left[\frac{d}{d\rho}\left(\sin^2\rho\frac{d}{d\rho}\right) - (1-\omega^2)\sin^2\rho - \ell(\ell+1)\right] X = 0. \tag{B.9}$$

We write

$$X(\rho) = (\sin\rho)^A H(\rho) \tag{B.10}$$

for some constant A that we will determine. Substituting in the radial equation (B.9), we find

$$\begin{aligned}\sin^2\rho\,\frac{d^2H}{d\rho^2} &+ (2A+2)\sin\rho\cos\rho\,\frac{dH}{d\rho}\\ &+ \left[A(A+1)\cos^2\rho - (A+1-\omega^2)\sin^2\rho - \ell(\ell+1)\right] H(\rho) = 0.\end{aligned} \tag{B.11}$$

Making the substitution $x = \cos\rho$, we now find

$$(1-x^2)\frac{d^2H}{dx^2} - (2A+3)x\frac{dH}{dx} + \left[\omega^2 - (A+1)^2 + \frac{A(A+1) - \ell(\ell+1)}{1-x^2}\right] H(x) = 0. \tag{B.12}$$

To make this look like the Legendre differential equation [120, eq. 14.2.2], we want $2A+3 = 2$, and so we set $A = -\frac{1}{2}$. The ODE (B.12) now takes the form

$$(1-x^2)H''(x) - 2xH'(x) + \left[\nu(\nu+1) - \frac{\mu^2}{1-x^2}\right] H(x) = 0 \tag{B.13}$$

where $\nu = \omega - \frac{1}{2}$ and $\mu^2 = (\ell + \frac{1}{2})^2$. The solutions can therefore be written

$$H(x) = B_1 P^{\ell+\frac{1}{2}}_{\omega-\frac{1}{2}}(x) + B_2 Q^{\ell+\frac{1}{2}}_{\omega-\frac{1}{2}}(x) \tag{B.14}$$

for constants B_1, B_2, where $P^\nu_\mu(x)$ and $Q^\nu_\mu(x)$ are the Legendre functions of the first and second kind respectively. Then the full radial function $X(\rho)$ is

$$X(\rho) = (\sin\rho)^{-1/2}\left(B_1 P^{\ell+\frac{1}{2}}_{\omega-\frac{1}{2}}(\cos\rho) + B_2 Q^{\ell+\frac{1}{2}}_{\omega-\frac{1}{2}}(\cos\rho)\right). \tag{B.15}$$

We need the solution to be regular at the origin $\rho = 0$. Using [120, eq. 14.8.1], we find

$$P^{\ell+\frac{1}{2}}_{\omega-\frac{1}{2}}(\cos\rho) \sim (1-\cos\rho)^{-\frac{(2\ell+1)}{4}} \quad \text{as } \rho \to 0. \tag{B.16}$$

The $P^{\ell+\frac{1}{2}}_{\omega-\frac{1}{2}}$ terms in the radial function (B.15) are therefore not regular at the origin, so we must set $B_1 = 0$. The $Q^{\ell+\frac{1}{2}}_{\omega-\frac{1}{2}}$ terms are in general ill-defined whenever $\ell+\omega$ is a negative integer (this can be seen by substituting $\mu \to \ell + \frac{1}{2}$ and $\nu \to \omega - \frac{1}{2}$ in [120, eq. 14.3.2] and looking at where the arguments of the Gamma functions are negative integers and hence undefined). We introduce Olver's definition of the Legendre function of the second kind [120, eq. 14.3.10],

$$\mathbf{Q}^{\ell+\frac{1}{2}}_{\omega-\frac{1}{2}}(\cos\rho) = \frac{Q^{\ell+\frac{1}{2}}_{\omega-\frac{1}{2}}(\cos\rho)}{\Gamma(\omega+\ell+1)} \tag{B.17}$$

which is valid for all ℓ and ω. In fact, for $\omega < \ell$ we find $\mathbf{Q}^{\ell+\frac{1}{2}}_{\omega-\frac{1}{2}}(\cos\rho) = 0$ (this can be seen from the expansion [120, eq. 14.3.2], which has a factor $\cos((\ell+\frac{1}{2})\pi)$ in the first term, which is zero for all integer ℓ, and a factor $\frac{1}{\Gamma(\omega-\ell)}$ in the second term, which is zero for $\omega < \ell$ and $\omega \in \mathbb{Z}$). To check that (B.15) is regular near the origin, we can note that [120, eq. 14.8.5]

$$\mathbf{Q}^{\ell+\frac{1}{2}}_{\omega-\frac{1}{2}}(\cos\rho) \sim (1-\cos\rho)^{\frac{2\ell+1}{4}} \quad \text{as } \rho \to 0. \tag{B.18}$$

Then, expanding using Taylor series, we find that

$$\frac{(1-\cos\rho)^{\frac{2\ell+1}{4}}}{(\sin\rho)^{1/2}} \sim \frac{\rho^{\ell}}{2^{\frac{2\ell+1}{4}}} + \mathcal{O}(\rho^{2\ell+\frac{1}{2}}), \tag{B.19}$$

implying, for $\ell \neq 0$

$$\lim_{\rho\to 0} \frac{(1-\cos\rho)^{\frac{2\ell+1}{4}}}{(\sin\rho)^{1/2}} = 0 \tag{B.20}$$

and for $\ell = 0$

$$\lim_{\rho\to 0} \frac{(1-\cos\rho)^{\frac{1}{4}}}{(\sin\rho)^{1/2}} = 2^{-1/4}. \tag{B.21}$$

The important thing here is that the solution (B.15) is always regular as $\rho \to 0$.

Absorbing other constants into the normalisation constant $\mathcal{C}_{\omega\ell}$, our positive frequency modes are given by

$$\phi^{ESU}_{\omega\ell m} = \mathcal{C}_{\omega\ell} e^{-i\omega t} (\sin\rho)^{-1/2} \mathbf{Q}^{\ell+\frac{1}{2}}_{\omega-\frac{1}{2}}(\cos\rho) Y_{\ell m}(\theta,\varphi). \tag{B.22}$$

Appendix C

Evaluation of (3.41)

In this appendix we give details of the evaluation of the integral in (3.41):

$$\begin{aligned}\mathfrak{I} &= \int_0^{\pi/2} \tan^2\rho\, X_{n\ell}(\rho) X_{n'\ell}(\rho)\ d\rho \\ &= \int_0^{\pi/2} \sin\rho\, \mathbf{Q}^{\ell+1/2}_{\omega-1/2}(\cos\rho)\mathbf{Q}^{\ell+1/2}_{\omega'-1/2}(\cos\rho)\ d\rho \\ &= \frac{1}{\Gamma(\ell+\omega+1)\Gamma(\ell+\omega'+1)} \int_0^1 Q^{\ell+1/2}_{\omega-1/2}(x) Q^{\ell+1/2}_{\omega'-1/2}(x)\ dx. \qquad \text{(C.1)}\end{aligned}$$

From the ODE satisfied by the Legendre functions, we have

$$\begin{aligned}&\frac{d}{dx}\left[(1-x^2)\left(Q^{\ell+1/2}_{\omega'-1/2}(x)\frac{dQ^{\ell+1/2}_{\omega-1/2}}{dx} - Q^{\ell+1/2}_{\omega-1/2}(x)\frac{dQ^{\ell+1/2}_{\omega'-1/2}}{dx}\right)\right] \\ &\qquad = ({\omega'}^2-\omega^2) Q^{\ell+1/2}_{\omega-1/2}(x) Q^{\ell+1/2}_{\omega'-1/2}(x). \qquad \text{(C.2)}\end{aligned}$$

Integrating both sides from A to B, for $B > A$, gives

$$\begin{aligned}&({\omega'}^2-\omega^2)\int_A^B Q^{\ell+1/2}_{\omega-1/2}(x) Q^{\ell+1/2}_{\omega'-1/2}(x)\ dx \\ &\quad = (1-B^2)\left[Q^{\ell+1/2}_{\omega'-1/2}(B)\frac{dQ^{\ell+1/2}_{\omega-1/2}}{dx}(B) - Q^{\ell+1/2}_{\omega-1/2}(B)\frac{dQ^{\ell+1/2}_{\omega'-1/2}}{dx}(B)\right] \\ &\quad\quad - (1-A^2)\left[Q^{\ell+1/2}_{\omega'-1/2}(A)\frac{dQ^{\ell+1/2}_{\omega-1/2}}{dx}(A) - Q^{\ell+1/2}_{\omega-1/2}(A)\frac{dQ^{\ell+1/2}_{\omega'-1/2}}{dx}(A)\right]. \qquad \text{(C.3)}\end{aligned}$$

From standard properties of Legendre functions [120], we find that, in the limit $B \to 1$,

$$(1-B^2) Q^{\ell+1/2}_{\omega-1/2}(B)\frac{dQ^{\ell+1/2}_{\omega'-1/2}}{dx}(B) \propto (1-B^2)^{\ell+1/2} \to 0 \qquad \text{(C.4)}$$

and so

$$(\omega'^2-\omega^2)\int_A^1 Q^{\ell+1/2}_{\omega-1/2}(x)Q^{\ell+1/2}_{\omega'-1/2}(x)\ dx$$
$$=(1-A^2)\left[Q^{\ell+1/2}_{\omega-1/2}(A)\frac{dQ^{\ell+1/2}_{\omega'-1/2}}{dx}(A)-Q^{\ell+1/2}_{\omega'-1/2}(A)\frac{dQ^{\ell+1/2}_{\omega-1/2}}{dx}(A)\right]. \quad \text{(C.5)}$$

Considering the case $\omega\neq\omega'$, on taking the limit $A\to 0$ the right-hand-side of (C.5) is zero due to the boundary conditions (3.21). When $\omega'\to\omega$, we use properties of Legendre functions close to the origin [120, eq. 14.5.3, 14.5.4] to give

$$(\omega'^2-\omega^2)\int_0^1 Q^{\ell+1/2}_{\omega-1/2}(x)Q^{\ell+1/2}_{\omega'-1/2}(x)\ dx$$
$$=2^{2\ell-1}\pi\sin\left(\frac{1}{2}(\omega+\omega'+2\ell)\pi\right)$$
$$\times\left[\frac{\Gamma(\frac{1}{2}(\omega+\ell+2))\Gamma(\frac{1}{2}(\omega'+\ell+1))}{\Gamma(\frac{1}{2}(\omega-\ell))\Gamma(\frac{1}{2}(\omega'-\ell+1))}-\frac{\Gamma(\frac{1}{2}(\omega+\ell+1))\Gamma(\frac{1}{2}(\omega'+\ell+2))}{\Gamma(\frac{1}{2}(\omega-\ell+1))\Gamma(\frac{1}{2}(\omega'-\ell))}\right]$$
$$+\,2^{2\ell-1}\pi\sin\left(\frac{1}{2}(\omega-\omega')\pi\right)$$
$$\times\left[\frac{\Gamma(\frac{1}{2}(\omega+\ell+2))\Gamma(\frac{1}{2}(\omega'+\ell+1))}{\Gamma(\frac{1}{2}(\omega-\ell))\Gamma(\frac{1}{2}(\omega'-\ell+1))}+\frac{\Gamma(\frac{1}{2}(\omega+\ell+1))\Gamma(\frac{1}{2}(\omega'+\ell+2))}{\Gamma(\frac{1}{2}(\omega-\ell+1))\Gamma(\frac{1}{2}(\omega'-\ell))}\right]. \quad \text{(C.6)}$$

We now divide both sides by $(\omega'^2-\omega^2)$ and evaluate the limit $\omega'\to\omega$ using L'Hopital's rule to obtain

$$\int_0^1 Q^{\ell+1/2}_{\omega-1/2}(x)Q^{\ell+1/2}_{\omega'-1/2}(x)\ dx=\frac{2^{2\ell-2}\pi\Gamma(\frac{1}{2}(\ell+\omega+1))\Gamma(\frac{1}{2}(\ell+\omega+2))}{\omega\Gamma(\frac{1}{2}(\omega-\ell+1))\Gamma(\frac{1}{2}(\omega-\ell))}$$
$$\times\left[\sin((\omega+\ell)\pi)(-\zeta(\omega-\ell+1)-\zeta(\omega-\ell))+\pi\right]\delta_{\omega\omega'}, \quad \text{(C.7)}$$

where $\zeta(z)$ is defined in (3.42). Noting the dependence of ω on n by writing $\omega=\omega_{n\ell}$, then, using relations for Gamma functions [120, eq. 5.5.5], we recover the result (3.41) for the integral $\mathfrak{I}$:

$$\mathfrak{I}=\delta_{nn'}\frac{\pi\left[\pi-\sin(\pi(\omega_{n\ell}+\ell))\left(\zeta(\ell+\omega_{n\ell}+1)+\zeta(\omega_{n\ell}-\ell)\,\right)\right]}{8\,\omega_{n\ell}\,\Gamma(\ell+\omega_{n\ell}+1)\Gamma(\omega_{n\ell}-\ell)}. \quad \text{(C.8)}$$

Appendix D

The Hadamard parametrix in CadS

The singular part of the Green's function $G_S(x, x')$, referred to as the Hadamard parametrix, is formed from Synge's world function $\sigma(x, x')$ and the van Vleck-Morette determinant $\Delta(x, x')$ (see Section 1.3.2). The Hadamard parametrix is then given by (1.192). In four-dimensions, for massless, conformally coupled scalar fields, the lowest order term in $V(x, x')$ vanishes [4], and so we can just consider the direct part of the Hadamard parametrix for the purposes of our calculation. In adS, Kent and Winstanley [111] found that the tail of the Hadamard parametrix vanishes identically in four-dimensions for massless, conformally coupled scalar fields.

In this appendix, we calculate the world function and the van Vleck-Morette determinant in CadS to allow us to find the Hadamard parametrix. The world function $\sigma(x, x')$ is given by

$$2\sigma(x, x') = s(x, x')^2 \tag{D.1}$$

where $s(x, x')$ is the geodesic distance between two points x, x'. Following work done in [5,123,126] we consider two points ξ, ξ' on $\mathbb{E}^{(2,3)}$ and parametrise the geodesic between these two points by a parameter p, such that $\xi(0) = \xi,\ \xi(1) = \xi'$. We will calculate the world function on $\mathbb{E}^{(2,3)}$ and then perform a transformation to find the world function in the embedded space (which is adS space - see Section 2.1). The world function in $\mathbb{E}^{(2,3)}$ is

$$\sigma_{\mathbb{E}}(\xi, \xi') = \frac{1}{2}\eta_{\mu\nu}(\xi^\mu - \xi'^\mu)(\xi^\nu - \xi'^\nu) \tag{D.2}$$

where $\eta_{\mu\nu}$ is the metric over $\mathbb{E}^{(2,3)}$ given in (2.1). Restricting to the hyperboloid with radius L and using the coordinate parametrisation given in (2.3) we can write

$$\begin{aligned}\eta_{\mu\nu}\xi^\mu\xi^\nu = L^2 \left[\eta_{00}\cos^2 t\ \sec^2\rho + \eta_{11}\tan^2\rho\ \cos^2\theta + \eta_{22}\tan^2\rho\ \sin^2\theta\ \cos^2\varphi\right.\\ \left.+\eta_{33}\tan^2\rho\ \sin^2\theta\ \sin^2\varphi + \eta_{44}\sin^2 t\ \sec^2\rho\right]\end{aligned} \tag{D.3}$$

and hence

$$\eta_{\mu\nu}\xi^{\mu}\xi^{\nu} = \eta_{\mu\nu}\xi'^{\mu}\xi'^{\nu} = -L^2. \tag{D.4}$$

We also find

$$\begin{aligned}
\eta_{\mu\nu}\xi^{\mu}\xi'^{\nu} &= L^2 \left[\eta_{00}\cos t\ \cos t'\ \sec\rho\ \sec\rho' + \eta_{11}\tan\rho\ \tan\rho'\ \cos\theta\ \cos\theta'\right.\\
&\quad +\eta_{22}\tan\rho\ \tan\rho'\ \sin\theta\ \sin\theta'\ \cos\varphi\ \cos\varphi'\\
&\quad \left.+\eta_{33}\tan\rho\ \tan\rho'\ \sin\theta\ \sin\theta'\ \sin\varphi\ \sin\varphi' + \eta_{44}\sin t\sin t'\ \sec\rho\ \sec\rho'\right]\\
&= L^2\left[-(\cos t\ \cos t' + \sin t\ \sin t')\sec\rho\ \sec\rho' + \tan\rho\ \tan\rho'\ \cos\theta\ \cos\theta'\right.\\
&\quad \left.+\tan\rho\ \tan\rho'\ \sin\theta\ \sin\theta'(\sin\varphi\ \sin\varphi' + \cos\varphi\ \cos\varphi')\right]\\
&= L^2\left[-\cos\Delta t\ \sec\rho\ \sec\rho' + \tan\rho\ \tan\rho'(\cos\theta\ \cos\theta' + \sin\theta\ \sin\theta'\ \cos\Delta\varphi)\right]
\end{aligned} \tag{D.5}$$

and so we conclude

$$\eta_{\mu\nu}\xi'^{\mu}\xi^{\nu} = \eta_{\mu\nu}\xi^{\mu}\xi'^{\nu} = \frac{L^2[-\cos\Delta t + \sin\rho\sin\rho'\cos\gamma]}{\cos\rho\cos\rho'} \tag{D.6}$$

where γ is the geodesic distance on the sphere given in (1.222). Then the world function on $\mathbb{E}^{(2,3)}$ restricted to the hyperboloid of radius L is given by

$$\sigma_{\mathbb{E},L}(\xi,\xi') = L^2\left[-1 + \frac{\cos\Delta t - \sin\rho\sin\rho'\cos\gamma}{\cos\rho\cos\rho'}\right]. \tag{D.7}$$

Now, $\sigma_{\mathbb{E},L}$ is related to the world function σ on adS via [126, eq. 2.73]

$$\cos\left(\frac{\sqrt{2\sigma}}{L}\right) = 1 + \frac{\sigma_{\mathbb{E},L}}{L^2} \tag{D.8}$$

which, when rearranged, leaves us with

$$\sigma(x,x') = 2L^2\left[\cos^{-1}\left(\frac{\cos\Delta t - \sin\rho\sin\rho'\cos\gamma}{\cos\rho\cos\rho'}\right)\right]^2. \tag{D.9}$$

We now turn our attention to the van Vleck-Morette determinant, which can be calculated from the world function via (1.184). We shall begin by considering $\Box s$. To calculate this, we fix ξ' such that the geodesic distance is only measured in the direction of the polar coordinate, i.e $s = \theta$. Then we obtain [111, 147]

$$\Box s = \frac{3}{L}\cot\left(\frac{s}{L}\right). \tag{D.10}$$

We can also write

$$\Box s = g_{\mu\nu}s^{;\mu\nu} = \sqrt{2}g_{\mu\nu}(\sqrt{\sigma})^{;\mu\nu} \tag{D.11}$$

using (D.1). Performing the derivatives,

$$\Box s = \sqrt{2}\left(\frac{1}{2}\sigma^{-1/2}\sigma_{;\mu}\right)^{;\mu} = \sqrt{2}\left(-\frac{1}{4}\sigma^{-3/2}\sigma^{;\mu}\sigma_{;\mu} + \frac{1}{2}\sigma^{-1/2}\sigma_{;\mu}^{;\mu}\right). \tag{D.12}$$

Using (1.180), we can write

$$\Box s = \frac{1}{\sqrt{2\sigma}}(\Box\sigma - 1). \tag{D.13}$$

Substituting into (1.184), and using (D.11) on the left-hand-side, we find

$$\frac{3\sqrt{2\sigma}}{L}\cot\left(\frac{\sqrt{2\sigma}}{L}\right) = 3 - 2\Delta^{-1/2}\Delta^{1/2}_{;\mu}\sigma^{;\mu}. \tag{D.14}$$

Since adS is maximally symmetric, we can note the following:

$$\begin{aligned}\Delta^{-1/2}(\Delta^{1/2})_{;\mu}\sigma^{;\mu} &= \Delta^{-1/2}\frac{d\Delta^{1/2}}{d\sigma}\sigma_{;\mu}\sigma^{;\mu} \\ &= \frac{\sigma}{\Delta}\frac{d\Delta}{d\sigma} = \sigma\frac{d\ln\Delta}{d\sigma}\end{aligned} \tag{D.15}$$

where we have used (1.180) between the first and second lines. Substituting into (D.14) and rearranging, we obtain the straightforward ODE

$$\frac{d\ln\Delta}{d\sigma} = 3\left(\frac{1}{2\sigma} - \frac{1}{L\sqrt{2\sigma}}\cot\left(\frac{\sqrt{2\sigma}}{L}\right)\right). \tag{D.16}$$

Integrating both sides with respect to σ, we have

$$\begin{aligned}\ln\Delta &= \frac{3}{2}\ln\sigma - 3\ln\left(\sin\left(\frac{\sqrt{2\sigma}}{L}\right)\right) + c \\ &= \ln\left[\sigma^{3/2}\csc^3\left(\frac{\sqrt{2\sigma}}{L}\right)\right] + c\end{aligned} \tag{D.17}$$

where c is an integration constant. We can determine the integration constant using the boundary condition (1.182) and thus find

$$\Delta(x,x') = \left[\frac{\sqrt{2\sigma}}{L}\csc\left(\frac{\sqrt{2\sigma}}{L}\right)\right]^3. \tag{D.18}$$

Appendix E

Evaluating the sums in (3.121, 3.123)

In this appendix, we focus on the evaluation of the sums in (3.121, 3.123), the Euclidean thermal Green's functions with Dirichlet and Neumann conditions imposed. We shall begin by writing (3.121, 3.123) in the form

$$G^E_{\beta,D}(\mathbf{x},\mathbf{x}') = \frac{\kappa}{16\pi^2 L^2}\cos\rho\cos\rho'\sum_{n=-\infty}^{\infty} e^{in\kappa\Delta\tau}\{S - S'\} \tag{E.1}$$

$$G^E_{\beta,N}(\mathbf{x},\mathbf{x}') = \frac{\kappa}{16\pi^2 L^2}\cos\rho\cos\rho'\sum_{n=-\infty}^{\infty} e^{in\kappa\Delta\tau}\{S + S'\} \tag{E.2}$$

where

$$S = \frac{1}{\sqrt{\sin\rho\sin\rho'}}\sum_{\ell=0}^{\infty}(2\ell+1)P_\ell(\cos\gamma)|\Gamma(in\kappa+\ell+1)|^2 P^{-\ell-\frac{1}{2}}_{in\kappa-\frac{1}{2}}(\cos\rho_<)P^{-\ell-\frac{1}{2}}_{in\kappa-\frac{1}{2}}(-\cos\rho_>), \tag{E.3}$$

$$S' = \frac{1}{\sqrt{\sin\rho\sin\rho'}}\sum_{\ell=0}^{\infty}(2\ell+1)P_\ell(\cos\gamma)|\Gamma(in\kappa+\ell+1)|^2 P^{-\ell-\frac{1}{2}}_{in\kappa-\frac{1}{2}}(\cos\rho)P^{-\ell-\frac{1}{2}}_{in\kappa-\frac{1}{2}}(\cos\rho'). \tag{E.4}$$

It is important to note that the order of ρ, ρ' is not important when used in S', but is important in S. To evaluate these sums, we use the generalised addition theorem for Gegenbauer functions [148],

$$C^{\alpha}_{\lambda}(xx' - z(1-x^2)^{1/2}(1-x'^2)^{1/2}) = \frac{\Gamma(2\alpha-1)}{[\Gamma(\alpha)]^2}\sum_{\ell=0}^{\infty}\frac{(-1)^\ell 4^\ell\Gamma(\lambda-\ell+1)\Gamma(\ell+\alpha)^2}{\Gamma(\lambda+2\alpha+\ell)}$$
$$\times\,(2\ell+2\alpha-1)(1-x^2)^{\ell/2}(1-x'^2)^{\ell/2}C^{\alpha+\ell}_{\lambda-\ell}(x)C^{\alpha+\ell}_{\lambda-\ell}(x')C^{\alpha-1/2}_{\ell}(z), \tag{E.5}$$

which is valid for all complex λ, α provided

$$\left| z + (z^2+1)^{1/2} \right| < \left| (x+1)(x'+1)/(x-1)(x'-1) \right|. \tag{E.6}$$

Replacing $\alpha \to 1, \lambda \to in\kappa - 1, z \to \cos\gamma$ and $\{x, x'\} \to \{\cos\rho, -\cos\rho'\}$ if $\rho' < \rho$ or $\{x, x'\} \to \{-\cos\rho, \cos\rho'\}$ if $\rho > \rho'$, we obtain

$$\begin{aligned} C^1_{in\kappa-1}(\cos\psi) = \sum_{\ell=0}^{\infty} & \frac{(-1)^\ell 4^\ell \Gamma(in\kappa-\ell)\Gamma(\ell+1)^2}{\Gamma(in\kappa+\ell+1)}(2\ell+1)(\sin\rho)^\ell(\sin\rho')^\ell \\ & \times C^{\ell+1}_{in\kappa-\ell-1}(\cos\rho_<)C^{\ell+1}_{in\kappa-\ell-1}(-\cos\rho_>)C^{1/2}_\ell(\cos\gamma) \end{aligned} \tag{E.7}$$

where ψ is defined by (3.130). Using the relationship between Gegenbauer and Legendre functions [120, 14.3.21], we can write

$$P^{-\frac{1}{2}-\ell}_{in\kappa-\frac{1}{2}}(\cos\rho) = \frac{2^{-\frac{1}{2}-\ell}\Gamma(2+2\ell)\Gamma(in\kappa-\ell)}{\Gamma(in\kappa+\ell+1)\Gamma(\ell+\frac{3}{2})(\sin\rho)^{-\frac{1}{2}-\ell}}C^{\ell+1}_{in\kappa-\ell-1}(\cos\rho) \tag{E.8}$$

$$P_\ell(\cos\gamma) = C^{\frac{1}{2}}_\ell(\cos\gamma) \tag{E.9}$$

and so (E.7) becomes

$$\begin{aligned} C^1_{in\kappa-1}(\cos\psi) = \sum_{\ell=0}^{\infty} & \frac{(2\ell+1)}{\sqrt{\sin\rho\sin\rho'}} \frac{2^{4\ell+1}[\Gamma(\ell+1)]^2[\Gamma(\ell+\frac{3}{2})]^2\Gamma(in\kappa+\ell+1)}{[\Gamma(2\ell+2)]^2\Gamma(in\kappa-\ell)} \\ & \times P^{-\frac{1}{2}-\ell}_{in\kappa-\frac{1}{2}}(\cos\rho_<)P^{-\frac{1}{2}-\ell}_{in\kappa-\frac{1}{2}}(-\cos\rho_>)P_\ell(\cos\gamma). \end{aligned} \tag{E.10}$$

Using standard results for the Gamma function [120, eq. 5.5.3, 5.5.5], we obtain

$$\frac{2^{4\ell-1}[\Gamma(\ell+1)]^2[\Gamma(\ell+\frac{3}{2})]^2\Gamma(in\kappa+\ell+1)}{[\Gamma(2\ell+2)]^2\Gamma(in\kappa-\ell)} = \frac{i\sinh(n\pi\kappa)}{2}|\Gamma(in\kappa+\ell+1)|^2. \tag{E.11}$$

Then we can say

$$C^1_{in\kappa-1}(\cos\psi) = \frac{i\sinh(n\pi\kappa)}{2}S. \tag{E.12}$$

Converting to Legendre functions on the left-hand-side of (E.12), we find

$$S = \frac{\sqrt{2\pi}n\kappa}{\sinh(n\pi\kappa)\sqrt{\sin\psi}}P^{-\frac{1}{2}}_{in\kappa-\frac{1}{2}}(\cos\psi). \tag{E.13}$$

Using [120, 14.5.12] allows us to write

$$\frac{P^{-\frac{1}{2}}_{in\kappa-\frac{1}{2}}(\cos\psi)}{\sqrt{\sin\psi}} = \sqrt{\frac{2}{\pi}}\frac{\sinh(n\kappa\psi)}{n\kappa\sin\psi}, \tag{E.14}$$

and so

$$S = \frac{2\sinh(n\kappa\psi)}{\sinh(n\kappa\pi)\sin\psi}. \tag{E.15}$$

To evaluate S', we use the addition theorem for Gegenbauer functions (E.5) again, but this time with $\{x, x'\} = \{\cos\rho, \cos\rho'\}$, and α, λ, z unchanged, so that

$$\begin{aligned} C^1_{in\kappa-1}(\cos\psi^*) = \sum_{\ell=0}^{\infty} &\frac{(-1)^\ell 4^\ell \Gamma(in\kappa-\ell)[\Gamma(\ell+1)]^2}{\Gamma(in\kappa+\ell+1)}(2\ell+1)(\sin\rho)^\ell(\sin\rho')^\ell \\ &\times C^{\ell+1}_{in\kappa-\ell-1}(\cos\rho)C^{\ell+1}_{in\kappa-\ell-1}(\cos\rho')C^{1/2}_\ell(\cos\gamma), \end{aligned} \tag{E.16}$$

with ψ^* defined by (3.131). We restrict the inverse cosine function to $[0, \pi]$ so that $\psi^* \in [\pi, 2\pi]$. Rearranging as before, we find

$$S' = \frac{2\sinh(n\kappa\psi^*)}{\sinh(n\kappa\pi)\sin\psi^*}. \tag{E.17}$$

Substituting (E.15, E.17) into (E.1, E.2), we arrive at

$$G^E_{D,T} = \frac{\kappa}{16\pi^2 L^2}\cos\rho\cos\rho'\,\{X - Y\} \tag{E.18}$$

$$G^E_{N,T} = \frac{\kappa}{16\pi^2 L^2}\cos\rho\cos\rho'\,\{X + Y\} \tag{E.19}$$

where

$$X = \frac{2}{\sin\psi}\sum_{n=-\infty}^{\infty} e^{in\kappa\Delta\tau}\frac{\sinh(n\kappa\psi)}{\sinh(n\kappa\pi)} \tag{E.20}$$

$$Y = \frac{2}{\sin\psi^*}\sum_{n=-\infty}^{\infty} e^{in\kappa\Delta\tau}\frac{\sinh(n\kappa\psi^*)}{\sinh(n\kappa\pi)}. \tag{E.21}$$

Using [141, 1.445.4], we can write

$$X = \frac{4}{\pi\sin\psi}\sum_{k=1}^{\infty}(-1)^{k-1}k\sin(k\psi)\sum_{n=-\infty}^{\infty}\frac{e^{in\kappa\Delta\tau}}{k^2+n^2\kappa^2} \tag{E.22}$$

where we have swapped the order of summation since we have a uniformly convergent double sum. Now, the sum over n can be rearranged as follows:

$$\sum_{n=-\infty}^{\infty}\frac{e^{in\kappa\Delta\tau}}{k^2+n^2\kappa^2} = \frac{1}{k^2} + 2\sum_{n=1}^{\infty}\frac{\cos(n\kappa\Delta\tau)}{k^2+n^2\kappa^2}. \tag{E.23}$$

Substituting in (E.22), we have

$$X = \frac{4}{\pi\sin\psi}\sum_{k=1}^{\infty}\frac{(-1)^{k-1}}{k}\sin(k\psi) + \frac{8}{\pi\sin\psi}\sum_{k=1}^{\infty}(-1)^{k-1}k\sin(k\psi)\sum_{n=1}^{\infty}\frac{\cos(n\kappa\Delta\tau)}{k^2+n^2\kappa^2}. \tag{E.24}$$

In the second sum, we use [141, 1.445.2] to evaluate the sum over n, which leaves us with

$$\begin{aligned} X = &\frac{4}{\pi \sin\psi}\sum_{k=1}^{\infty}\frac{(-1)^{k-1}}{k}\sin(k\psi) \\ &+\frac{8}{\pi\sin\psi}\sum_{k=1}^{\infty}(-1)^{k-1}k\sin(k\psi)\left(\frac{\pi\cosh k(\frac{\pi}{\kappa}-\Delta\tau)}{2\kappa k\sinh(\frac{k\pi}{\kappa})}-\frac{1}{2k^2}\right). \end{aligned} \tag{E.25}$$

Rearranging, we see that the final term in the sum cancels with the term at the front, leaving us with

$$X = \frac{4}{\kappa\sin\psi}\sum_{k=1}^{\infty}(-1)^{k-1}\sin(k\psi)\frac{\cosh k(\frac{\pi}{\kappa}-\Delta\tau)}{\sinh(\frac{k\pi}{\kappa})}. \tag{E.26}$$

The hyperbolic functions can be rearranged to give

$$X = -\frac{4}{k\sin\psi}\sum_{k=1}^{\infty}\sin k(\psi-\pi)e^{-k\Delta\tau}+\frac{8}{\kappa\sin\psi}\sum_{k=1}^{\infty}(-1)^{k-1}\sin(k\psi)\frac{\cosh(k\Delta\tau)}{e^{2k\pi/\kappa}-1}. \tag{E.27}$$

Using [141, 1.461.1], we can evaluate the first sum to arrive at

$$\begin{aligned} X =&-\frac{4\sin(\psi-\pi)}{\kappa\sin\psi(\cosh\Delta\tau-\cos(\psi-\pi))}+\frac{8}{\kappa\sin\psi}\sum_{k=1}^{\infty}(-1)^{k-1}\sin(k\psi)\frac{\cosh k\Delta\tau}{e^{2k\pi/\kappa}-1} \\ =&\frac{2}{\kappa(\cosh\Delta\tau+\cos\psi)}-\frac{8}{\kappa\sin\psi}\sum_{k=1}^{\infty}(-1)^{k}\sin(k\psi)\frac{\cosh k\Delta\tau}{e^{2k\pi/\kappa}-1}. \end{aligned} \tag{E.28}$$

Similarly for Y, we find

$$Y = \frac{2}{\kappa(\cosh\Delta\tau+\cos\psi^*)}-\frac{8}{\kappa\sin\psi^*}\sum_{k=1}^{\infty}(-1)^{k}\sin(k\psi^*)\frac{\cosh k\Delta\tau}{e^{2k\pi/\kappa}-1}. \tag{E.29}$$

Substituting (E.28, E.29) into (E.18, E.19), we arrive at our desired results (3.128, 3.129).

Appendix F

The Hadamard parametrix in ESU

In this appendix, we calculate the Hadamard parametrix in the Euclidean background of ESU, following a very similar method to Appendix D. Using the Euclidean ESU metric (2.7) and coordinates (2.8), we obtain

$$\begin{aligned}\eta_{\mu\nu}\xi^\mu\xi^\nu &= (\xi^0)^2 + (\xi^1)^2 + (\xi^2)^2 + (\xi^3)^2 + (\xi^4)^2 \\ &= L^2\left[\tau^2 + \sin^2\rho\ \cos^2\theta + \sin^2\rho\ \sin^2\theta\ \cos^2\varphi + \sin^2\rho\ \sin^2\theta\ \sin^2\varphi + \cos^2\rho\right] \\ &= L^2\left[\tau^2+1\right], \end{aligned} \tag{F.1}$$

and similarly

$$\eta_{\mu\nu}\xi'^\mu\xi'^\nu = L^2\left[\tau'^2+1\right]. \tag{F.2}$$

We also find

$$\begin{aligned}\eta_{\mu\nu}\xi^\mu\xi'^\nu = L^2\big[&\tau\tau' + \sin\rho\ \sin\rho'\ \cos\theta\ \cos\theta' \\ &+ \sin\rho\ \sin\rho'\ \sin\theta\ \sin\theta'\ \cos\varphi\ \cos\varphi' \\ &+ \sin\rho\ \sin\rho'\ \sin\theta\ \sin\theta'\ \sin\varphi\ \sin\varphi' + \cos\rho\ \cos\rho'\big], \end{aligned} \tag{F.3}$$

and, after rearranging,

$$\eta_{\mu\nu}\xi^\mu\xi'^\nu = \eta_{\mu\nu}\xi'^\mu\xi^\nu = L^2\left[\tau\tau' + \sin\rho\ \sin\rho'\ \cos\gamma + \cos\rho\ \cos\rho'\right] \tag{F.4}$$

where γ is the geodesic distance on the sphere given in (1.222).

The world function in ESU is then given by

$$\sigma_{ESU}(\xi,\xi') = L^2\left[\frac{1}{2}\tau^2 + \frac{1}{2}\tau'^2 - \tau\tau' + 1 - \sin\rho\ \sin\rho'\ \cos\gamma - \cos\rho\ \cos\rho'\right]. \tag{F.5}$$

In section 3.6, we require the ESU world function in the partial limit $\rho' \to \rho$, $\theta' \to \theta$, $\varphi' \to \varphi$. In this case the world function (F.5) becomes

$$\lim_{\mathbf{x}'\to\mathbf{x}} \sigma_{ESU} = \frac{1}{2}L^2\Delta\tau^2 \tag{F.6}$$

where $\Delta\tau = \tau - \tau'$.

The van Vleck-Morette determinant $\Delta(x, x')$ is given in [4, eq. 53] as a series in σ by

$$\Delta^{1/2}(x, x') = 1 + \frac{1}{12} R_{\mu\nu} \sigma^{;\mu} \sigma^{;\nu} + \mathcal{O}(\sigma^{3/2}). \tag{F.7}$$

In ESU, the Ricci tensor is

$$R_{\mu\nu} = \begin{pmatrix} 0 & 0 & 0 & 0 \\ 0 & 2 & 0 & 0 \\ 0 & 0 & 2\sin^2\rho & 0 \\ 0 & 0 & 0 & 2\sin^2\rho\sin^2\theta \end{pmatrix}, \tag{F.8}$$

and so we find

$$\begin{aligned} \frac{1}{12} R_{\mu\nu} \sigma^{;\mu} \sigma^{;\nu} = \frac{L^2}{6} \big[&\sin\rho\cos\rho' - \cos\rho\sin\rho'\cos\gamma \\ &+ \sin^3\rho\sin\rho'(\sin\theta\cos\theta' - \cos\theta\sin\theta'\cos\Delta\varphi + \sin^3\theta\sin\theta'\sin\Delta\varphi) \big] . \end{aligned} \tag{F.9}$$

Therefore, in the partial limit $\rho' \to \rho,\ \theta' \to \theta,\ \varphi' \to \varphi$, the term $\frac{1}{12} R_{\mu\nu} \sigma^{;\mu} \sigma^{;\nu}$ vanishes and (F.7) becomes

$$\lim_{\mathbf{x}' \to \mathbf{x}} \Delta^{1/2} = 1 + \mathcal{O}(\Delta\tau^3). \tag{F.10}$$

Appendix G

The Euclidean Green's function in SadS

In this appendix, we solve the Euclidean Klein-Gordon equation on SadS (5.17) by writing the Green's function G^E in the form (5.20). The D'Alembertian of the Euclidean Green's function on SadS can be written

$$
\begin{aligned}
\Box G^E =& \frac{1}{\sqrt{g}}\partial_\mu(\sqrt{g}g^{\mu\nu}\partial_\nu G^E) \\
=& \frac{\kappa}{2\pi r^2\mathcal{F}_k(\theta)}\partial_\mu\left(r^2\mathcal{F}_k(\theta)g^{\mu\nu}\partial_\nu\sum_{n=-\infty}^{\infty}e^{in\kappa\Delta\tau}\mathcal{G}_n^{(k)}\right) \\
=& \frac{\kappa}{2\pi r^2\mathcal{F}_k(\theta)}\left[\partial_\tau\left(r^2\mathcal{F}_k(\theta)g^{\tau\tau}\partial_\tau\sum_{n=-\infty}^{\infty}e^{in\kappa\Delta\tau}\mathcal{G}_n^{(k)}\right)+\partial_i\left(r^2\mathcal{F}_k(\theta)g^{ij}\partial_j\sum_{n=-\infty}^{\infty}e^{in\kappa\Delta\tau}\mathcal{G}_n^{(k)}\right)\right] \\
=& \frac{\kappa}{2\pi r^2\mathcal{F}_k(\theta)}\left[\sum_{n=-\infty}^{\infty}\partial_i\left(r^2\mathcal{F}_k(\theta)g^{ij}\partial_j e^{in\kappa\Delta\tau}\mathcal{G}_n^{(k)}\right)-n^2\kappa^2r^2\mathcal{F}_k(\theta)f(r)^{-1}e^{in\kappa\Delta\tau}\mathcal{G}_n^{(k)}\right]
\end{aligned}
\tag{G.1}
$$

where Greek indices run over all four coordinates, whilst Roman indices run over the spatial coordinates (r, θ, φ). The wave equation (5.17) becomes

$$
\begin{aligned}
\sum_{n=-\infty}^{\infty}\frac{\kappa e^{in\kappa\Delta\tau}}{2\pi r^2\mathcal{F}_k(\theta)}\left(-n^2\kappa^2r^2\frac{\mathcal{F}_k(\theta)}{f(r)}\mathcal{G}_n^{(k)}+\partial_i(r^2\mathcal{F}_k(\theta)g^{ij}\partial_j\mathcal{G}_n^{(k)})-\frac{1}{6}Rr^2\mathcal{F}_k(\theta)\mathcal{G}_n^{(k)}\right)& \\
=-\sum_{n=-\infty}^{\infty}\frac{\kappa e^{in\kappa\Delta\tau}}{2\pi r^2}\delta(r-r')\delta(\Omega_k,\Omega'_k).&
\end{aligned}
\tag{G.2}
$$

Taking everything over to the left-hand side, we obtain

$$
\sum_{n=-\infty}^{\infty}e^{in\kappa\Delta\tau}\mathcal{M}_n^{(k)}=0 \tag{G.3}
$$

where

$$\mathcal{M}_n^{(k)} = \frac{\kappa}{2\pi r^2 \mathcal{F}_k(\theta)} \left(-n^2\kappa^2 r^2 \frac{\mathcal{F}_k(\theta)}{f(r)} \mathcal{G}_n^{(k)} + \partial_i (r^2 \mathcal{F}_k(\theta) g^{ij} \partial_j \mathcal{G}_n^{(k)}) \right. \\ \left. -\frac{1}{6} R r^2 \mathcal{F}_k(\theta) \mathcal{G}_n^{(k)} + \mathcal{F}_k(\theta) \delta(r-r') \delta(\Omega_k, \Omega_k') \right). \tag{G.4}$$

We multiply (G.3) by $e^{-im\kappa\Delta\tau}$ and then integrate over $\Delta\tau$, i.e.

$$\int_{\Delta\tau=0}^{2\pi/\kappa} e^{-in\kappa\Delta\tau} \sum_{n=-\infty}^{\infty} e^{in\kappa\Delta\tau} \mathcal{M}_n^{(k)} d\Delta\tau = 0. \tag{G.5}$$

Swapping the sum and integral, and then performing the integral, we can see

$$\sum_{n=-\infty}^{\infty} \frac{2\pi}{\kappa} \delta_{mn} \mathcal{M}_n^{(k)} = 0 \quad \Rightarrow \quad \mathcal{M}_m^{(k)} = 0. \tag{G.6}$$

In other words,

$$\begin{aligned} -\frac{1}{r^2}\delta(r-r')\delta(\Omega_k, \Omega_k') =& \frac{1}{r^2\mathcal{F}_k(\theta)} \partial_i (r^2 \mathcal{F}_k(\theta) g^{ij} \partial_j \mathcal{G}_n^{(k)}) - \left(\frac{1}{6} R + \frac{n^2\kappa^2}{f(r)} \right) \mathcal{G}_n^{(k)} \\ =& \frac{1}{r^2\mathcal{F}_k(\theta)} [\partial_r (r^2 \mathcal{F}_k(\theta) f(r) \partial_r \mathcal{G}_n^{(k)}) + \partial_a (\mathcal{F}_k(\theta) h^{ab} \partial_b \mathcal{G}_n^{(k)})] \\ & - \left(\frac{1}{6} R + \frac{n^2\kappa^2}{f(r)} \right) \mathcal{G}_n^{(k)} \end{aligned} \tag{G.7}$$

where h_{ab} is the two-metric over the topological horizon, that is

$$h_{ab} = \begin{pmatrix} 1 & 0 \\ 0 & \mathcal{F}_k^2(\theta) \end{pmatrix}. \tag{G.8}$$

We must now consider each topological event horizon separately.

G.1 Spherical horizon

First, we look at the spherical case, where $k = 1$ and $\mathcal{F}_1(\theta) = \sin\theta$. The eigenfunctions of the Laplacian on the 2-sphere are Legendre polynomials [147],

$$\frac{1}{\sin\theta} \partial_a (\sin\theta \; h^{ab} \partial_b P_\ell(\cos\gamma_S)) = -\ell(\ell+1) P_\ell(\cos\gamma_S) \tag{G.9}$$

for integer ℓ, where γ_S is the geodesic distance on the sphere defined in (5.25). We can write $\delta(\Omega_1, \Omega_1')$ as a sum over Legendre polynomials via [1, eq. 10]

$$\delta(\Omega_1, \Omega_1') = \sum_{\ell=0}^{\infty} \frac{2\ell+1}{4\pi} P_\ell(\cos\gamma_S). \tag{G.10}$$

We can then write $\mathcal{G}_n$ as

$$\mathcal{G}_n^{(1)}(r,\theta,\varphi;r',\theta',\varphi') = \sum_{\ell=0}^{\infty} \frac{(2\ell+1)}{4\pi} P_\ell(\cos\gamma_S) X_{n\ell}^{(1)}(r,r') \tag{G.11}$$

for some radial Green's function $X_{n\ell}^{(1)}(r,r')$. Substituting this into (G.7), we find

$$\begin{aligned} &-\sum_{\ell=0}^{\infty} \frac{1}{r^2}\delta(r-r')\frac{2\ell+1}{4\pi}P_\ell(\cos\gamma_S) \\ &\quad = \sum_{\ell=0}^{\infty} \frac{2\ell+1}{4\pi} P_\ell(\cos\gamma_S)\left[\frac{1}{r^2}\partial_r(r^2 f(r)\partial_r X_{n\ell}^{(1)}) - \left(\frac{\ell(\ell+1)}{r^2} + \frac{1}{6}R + \frac{n^2\kappa^2}{f(r)}\right) X_{n\ell}^{(1)}\right]. \end{aligned} \tag{G.12}$$

Taking everything over to one side, we can write

$$\sum_{\ell=0}^{\infty} \frac{(2\ell+1)}{2} P_\ell(\cos\gamma_S) \mathscr{P}_{n\ell}^{(1)} = 0 \tag{G.13}$$

where

$$\mathscr{P}_{n\ell}^{(1)} = \frac{1}{2\pi}\left[\frac{1}{r^2}\partial_r(r^2 f(r)\partial_r X_{n\ell}^{(1)}) - \left(\frac{\ell(\ell+1)}{r^2} + \frac{1}{6}R + \frac{n^2\kappa^2}{f(r)}\right) X_{n\ell}^{(1)} + \frac{1}{r^2}\delta(r-r')\right]. \tag{G.14}$$

We multiply (G.13) by $P_m(\cos\gamma_S)$ and integrate over $\cos\gamma_S$, i.e.

$$\int_{\cos\gamma_S=-1}^{1} P_m(\cos\gamma_S) \sum_{\ell=0}^{\infty} \frac{(2\ell+1)}{2} P_\ell(\cos\gamma_S) \mathscr{P}_{n\ell}^{(1)} \; d(\cos\gamma_S) = 0. \tag{G.15}$$

Swapping the summation and integral, and performing the integral using the orthogonality relation for Legendre polynomials [120, eq. 14.17.6], we can see that

$$\sum_{\ell=0}^{\infty} \delta_{m\ell} \mathscr{P}_{n\ell}^{(1)} = 0 \quad \Rightarrow \quad \mathscr{P}_{nm}^{(1)} = 0. \tag{G.16}$$

This relation gives us the radial equation (5.24) for $k=1$.

G.2 Flat horizon

The eigenfunctions of the Laplacian on $\mathbb{R}^2$ are Bessel functions [147],

$$\frac{1}{\theta}\partial_a(\theta h^{ab}\partial_b J_0(\ell\gamma_R)) = -\ell^2 J_0(\ell\gamma_R) \tag{G.17}$$

for all real, non-negative ℓ, where γ_R is the geodesic distance in the Euclidean plane (5.26). In this case, the spectrum of eigenvalues is continuous. From [120, eq. 1.17.13, 1.17.21], we can write

$$\begin{aligned}\delta(\Omega_0,\Omega_0') =&\frac{1}{2\pi}\int_{\ell=0}^{\infty}\ell\sum_{m=-\infty}^{\infty}J_m(\ell\theta)J_m(\ell\theta')\exp(im\Delta\varphi)\,d\ell\\ =&\frac{1}{2\pi}\int_{\ell=0}^{\infty}\ell J_0(\ell\gamma_R)\,d\ell\end{aligned}\tag{G.18}$$

where we have used [120, eq. 10.23.7]. We can then write $\mathcal{G}_n^{(0)}$ in the form

$$\mathcal{G}_n^{(0)}(r,\theta,\varphi;r',\theta',\varphi')=\frac{1}{2\pi}\int_{\ell=0}^{\infty}\ell J_0(\ell\gamma_R)X_{n\ell}^{(0)}(r,r')\,d\ell.\tag{G.19}$$

Substituting into (G.7), we obtain

$$\begin{aligned}&-\frac{1}{2r^2\pi}\delta(r-r')\int_{\ell=0}^{\infty}\ell J_0(\ell\gamma_R)\,d\ell\\ &\quad=\frac{1}{2\pi}\int_{\ell=0}^{\infty}\ell J_0(\ell\gamma_R)\left[\frac{1}{r^2}\partial_r(r^2f(r)\partial_rX_{n\ell})-\left(\frac{\ell^2}{r^2}+\frac{1}{6}R+\frac{n^2\kappa^2}{f(r)}\right)X_{n\ell}^{(0)}\right]d\ell.\end{aligned}\tag{G.20}$$

We bring everything over to one side to write

$$\int_{\ell=0}^{\infty}\ell J_0(\ell\gamma_R)\mathscr{P}_{n\ell}^{(0)}\,d\ell=0\tag{G.21}$$

where

$$\mathscr{P}_{n\ell}^{(0)}=\frac{1}{2\pi}\left[\frac{1}{r^2}\partial_r(r^2f(r)\partial_rX_{n\ell}^{(0)})-\left(\frac{\ell^2}{r^2}+\frac{1}{6}R+\frac{n^2\kappa^2}{f(r)}\right)X_{n\ell}^{(0)}+\frac{1}{r^2}\delta(r-r')\right].\tag{G.22}$$

We multiply (G.21) by $\gamma_R J_0(m\gamma_R)$ and integrate over γ_R, i.e.

$$\int_{\gamma_R=0}^{\infty}\gamma_R J_0(m\gamma_R)\int_{\ell=0}^{\infty}\ell J_0(\ell\gamma_R)\mathscr{P}_{n\ell}^{(0)}d\ell\,d\gamma_R=0.\tag{G.23}$$

Interchanging the order of integration,

$$\int_{\ell=0}^{\infty}\ell\left(\int_{\gamma_R=0}^{\infty}\gamma_R J_0(m\gamma_R)J_0(\ell\gamma_R)d\gamma_R\right)\mathscr{P}_{n\ell}^{(0)}\,d\ell=0\tag{G.24}$$

where the integral over γ_R can now be performed using [120, eq. 1.17.13], and hence

$$\int_{\ell=0}^{\infty}\delta(\ell-m)\mathscr{P}_{n\ell}^{(0)}d\ell=0\quad\Rightarrow\quad\mathscr{P}_{nm}^{(0)}=0.\tag{G.25}$$

The relation gives us the radial equation (5.24) for $k=0$.

G.3 Hyperbolic horizon

From [147], the eigenfunctions of the Laplacian on the hyperbolic background are conical (Mehler) functions,

$$\frac{1}{\sinh\theta}\partial_a\left(\sinh\theta\ h^{ab}\partial_b P_{-\frac{1}{2}+i\ell}(\cosh\gamma_H)\right) = -\left(\frac{1}{4}+\ell^2\right)P_{-\frac{1}{2}+i\ell}(\cosh\gamma_H) \tag{G.26}$$

where $\ell \in \mathbb{R}_{>0}$ and γ_H is the geodesic distance on the hyperbolic background (5.27). As in the previous case, the spectrum of eigenvalues is again continuous. We therefore require a representation of the delta function involving an integral over conical functions. One of the main results for the conical functions is the generalised Mehler-Fock transform [120, sec. 14.20(vi)] , which says that for some function $\mathscr{F}(\ell)$, we can write

$$\mathscr{F}(\ell) = \frac{\ell}{\pi}\sinh(\ell\pi)\left|\Gamma\left(\frac{1}{2}-\mu+i\ell\right)\right|^2\int_{x=1}^{\infty}P^{\mu}_{-\frac{1}{2}+i\ell}(x)\mathscr{G}(x)\ dx \tag{G.27}$$

where

$$\mathscr{G}(x) = \int_0^{\infty}P^{\mu}_{-\frac{1}{2}+i\ell}(x)\mathscr{F}(\ell)d\ell \tag{G.28}$$

for $\mu \geq 0$. Rearranging (G.27), we can say

$$\begin{aligned}\mathscr{G}(x) = \int_{\ell=0}^{\infty}P^{\mu}_{-\frac{1}{2}+i\ell}(x)\frac{\ell}{\pi}\sinh(\ell\pi)&\left|\Gamma\left(\frac{1}{2}-\mu+i\ell\right)\right|^2\\ &\times\int_{x'=1}^{\infty}P^{\mu}_{-\frac{1}{2}+i\ell}(x)P^{\mu}_{-\frac{1}{2}+i\ell}(x')\mathscr{G}(x')\ dx'\ d\ell\end{aligned} \tag{G.29}$$

which, after interchanging the order of integration, implies that we can write the delta function

$$\delta(x-x') = \int_{\ell=0}^{\infty}\frac{\ell}{\pi}\sinh(\ell\pi)\left|\Gamma\left(\frac{1}{2}-\mu+i\ell\right)\right|^2P^{\mu}_{-\frac{1}{2}+i\ell}(x)P^{\mu}_{-\frac{1}{2}+i\ell}(x')\ d\ell. \tag{G.30}$$

Substituting $x = \cosh\theta$ and using the exponential representation of the delta function [120, eq. 1.17.21], we find

$$\begin{aligned}&\delta(\Omega_{-1},\Omega'_{-1}) = \delta(\cosh\theta-\cosh\theta')\delta(\varphi-\varphi')\\ &= \frac{1}{2\pi^2}\int_{\ell=0}^{\infty}\ell\sinh(\ell\pi)\left[\sum_{\mu=-\infty}^{\infty}\left|\Gamma\left(\frac{1}{2}-\mu+i\ell\right)\right|^2P^{\mu}_{-\frac{1}{2}+i\ell}(\cosh\theta)P^{\mu}_{-\frac{1}{2}+i\ell}(\cosh\theta')e^{i\mu\Delta\varphi}\right]d\ell.\end{aligned} \tag{G.31}$$

From [120, eq. 14.18.4], we can write

$$\begin{aligned}P_{-\frac{1}{2}+i\ell}(\cosh\gamma_H) &= \sum_{\mu=-\infty}^{\infty}(-1)^{\mu}P^{-\mu}_{-\frac{1}{2}+i\ell}(\cosh\theta)P^{\mu}_{-\frac{1}{2}+i\ell}(\cosh\theta')e^{i\mu\Delta\varphi}\\ &= \sum_{\mu=-\infty}^{\infty}(-1)^{\mu}\frac{\Gamma(\frac{1}{2}-\mu+i\ell)}{\Gamma(\frac{1}{2}+\mu+i\ell)}P^{\mu}_{-\frac{1}{2}+i\ell}(\cosh\theta)P^{\mu}_{-\frac{1}{2}+i\ell}(\cosh\theta')e^{i\mu\Delta\varphi}\end{aligned} \tag{G.32}$$

where we have used [120, eq. 14.9.13] between the first and second lines. Now, using standard relations for Gamma functions [120, eq. 5.5.3], we can write

$$\frac{\Gamma(\frac{1}{2}-\mu+i\ell)}{\Gamma(\frac{1}{2}+\mu+i\ell)} = \frac{(-1)^\mu}{\pi}\cosh(\ell\pi)\left|\Gamma\left(\frac{1}{2}-\mu+i\ell\right)\right|^2 \tag{G.33}$$

and therefore

$$\begin{aligned} P_{-\frac{1}{2}+i\ell}(\cosh\gamma_H) = \frac{\cosh(\ell\pi)}{\pi}\sum_{\mu=-\infty}^{\infty}\left|\Gamma\left(\frac{1}{2}-\mu+i\ell\right)\right|^2 \\ \times P^{\mu}_{-\frac{1}{2}+i\ell}(\cosh\theta)P^{\mu}_{-\frac{1}{2}+i\ell}(\cosh\theta')e^{i\mu\Delta\varphi}. \end{aligned} \tag{G.34}$$

Substituting into (G.31), our delta function can be written

$$\delta(\Omega_{-1},\Omega'_{-1}) = \frac{1}{2\pi}\int_{\ell=0}^{\infty}\ell\tanh(\ell\pi)P_{-\frac{1}{2}+i\ell}(\cosh\gamma_H)\,d\ell. \tag{G.35}$$

We therefore let our Green's function take the form

$$\mathcal{G}_n^{(-1)}(r,\theta,\varphi;r',\theta',\varphi') = \frac{1}{2\pi}\int_{\ell=0}^{\infty}\ell\tanh(\ell\pi)P_{-\frac{1}{2}+i\ell}(\cosh\gamma_H)X_{n\ell}^{(-1)}(r,r')\,d\ell. \tag{G.36}$$

Substituting into (G.7), we obtain

$$\begin{aligned} -\frac{1}{2r^2\pi}\delta(r-r')\int_{\ell=0}^{\infty}\ell\tanh(\ell\pi)P_{-\frac{1}{2}+i\ell}(\cosh\gamma_H)d\ell \\ = \frac{1}{2\pi}\int_{\ell=0}^{\infty}\ell\tanh(\ell\pi)P_{-\frac{1}{2}+i\ell}(\cosh\gamma_H)\left[\frac{1}{r^2}\partial_r(r^2f(r)\partial_r X_{n\ell}^{(-1)})\right. \\ \left.-\left(\frac{1}{4r^2}+\frac{\ell^2}{r^2}+\frac{1}{6}R+\frac{n^2\kappa^2}{f(r)}\right)X_{n\ell}^{(-1)}\right]\,d\ell. \end{aligned} \tag{G.37}$$

Bringing everything over to one side, we find

$$\int_{\ell=0}^{\infty}\ell\tanh(\ell\pi)P_{-\frac{1}{2}+i\ell}(\cosh\gamma_H)\mathscr{P}_{n\ell}^{(-1)}\,d\ell = 0 \tag{G.38}$$

where

$$\mathscr{P}_{n\ell}^{(-1)} = \frac{1}{2\pi}\left[\frac{1}{r^2}\partial_r(r^2f(r)\partial_r X_{n\ell}^{(-1)}) - \left(\frac{1}{4r^2}+\frac{\ell^2}{r^2}+\frac{1}{6}R+\frac{n^2\kappa^2}{f(r)}\right)X_{n\ell}^{(-1)}+\frac{1}{r^2}\delta(r-r')\right]. \tag{G.39}$$

Returning to (G.27-G.28), we can rearrange in a different way to obtain

$$\mathscr{F}(\ell) = \int_{m=0}^{\infty}\frac{\ell}{\pi}\sinh(\ell\pi)\left|\Gamma\left(\frac{1}{2}-\mu+i\ell\right)\right|^2\int_{x=1}^{\infty}P^{\mu}_{-\frac{1}{2}+i\ell}(x)P^{\mu}_{-\frac{1}{2}+im}(x)dx\;\mathscr{F}(m)\,dm \tag{G.40}$$

and so derive

$$\delta(\ell - m) = \frac{\ell}{\pi}\sinh(\ell\pi)\left|\Gamma\left(\frac{1}{2} - \mu + i\ell\right)\right|^2 \int_{x=1}^{\infty} P^{\mu}_{-\frac{1}{2}+i\ell}(x) P^{\mu}_{-\frac{1}{2}+im}(x)\ dx. \tag{G.41}$$

Substituting (G.34) into (G.38), we find

$$\int_{\ell=0}^{\infty} \frac{\ell}{\pi}\sinh(\ell\pi) \sum_{\mu=-\infty}^{\infty} \left|\Gamma\left(\frac{1}{2} - \mu + i\ell\right)\right|^2 P^{\mu}_{-\frac{1}{2}+i\ell}(\cosh\theta) P^{\mu}_{-\frac{1}{2}+i\ell}(\cosh\theta') e^{i\mu\Delta\varphi} \mathscr{P}^{(-1)}_{n\ell}\ d\ell = 0. \tag{G.42}$$

We multiply both sides by $P^{\mu}_{-\frac{1}{2}+im}(\cosh\theta)P^{\mu}_{-\frac{1}{2}+im}(\cosh\theta')$ and integrate over $\cosh\theta$ and $\cosh\theta'$ from 1 to ∞. Interchanging the order of the integral and the sum, and using (G.41), we find

$$\int_{\ell=0}^{\infty} \frac{\pi}{\ell}\,\mathrm{cosech}(\ell\pi) \sum_{\mu=-\infty}^{\infty} \frac{1}{|\Gamma(\frac{1}{2} - \mu + i\ell)|^2} \delta(\ell - m) e^{i\mu\Delta\varphi} \mathscr{P}^{(-1)}_{n\ell} d\ell = 0. \tag{G.43}$$

We can now multiply by $e^{-i\nu\Delta\varphi}$ and then integrate over $\Delta\varphi$,

$$\int_{\ell=0}^{\infty} \frac{\pi}{\ell}\,\mathrm{cosech}(\ell\pi) \sum_{\mu=-\infty}^{\infty} \frac{1}{|\Gamma(\frac{1}{2} - \mu + i\ell)|^2} \delta(\mu - \nu)\delta(\ell - m)\ \mathscr{P}^{(-1)}_{n\ell} d\ell = 0. \tag{G.44}$$

Finally, performing the integral over ℓ and the sum over μ, we find

$$\frac{\pi}{m}\frac{\mathrm{cosech}(m\pi)}{|\Gamma(\frac{1}{2} - \nu + im)|^2} \mathscr{P}^{(-1)}_{nm} = 0 \quad \Rightarrow \quad \mathscr{P}^{(-1)}_{nm} = 0. \tag{G.45}$$

This final relation gives the relevant radial ODE (5.24) for $k = -1$.

Appendix H

Calculating $\Box\sigma$

In this appendix, we calculate $\Box\sigma$ in SadS spacetime, given by the metric (5.1). This is required for the calculation of the van Vleck-Morette determinant from (1.184). By definition, we have

$$\Box\sigma = g^{\mu\nu}(\partial_\mu\partial_\nu\sigma - \Gamma^\lambda_{\mu\nu}\sigma_{,\lambda}). \tag{H.1}$$

For the remainder of this appendix, we shall use the indices (i, j) to refer to coordinates (τ, r), whilst indices (a, b) will refer to angular coordinates. By writing $\sigma = \sigma(t, r, \gamma)$ where $\gamma = \gamma(\theta, \varphi)$ is the geodesic distance, this means

$$\sigma_{,a} = \sigma_{,\gamma}\gamma_{,a} \tag{H.2}$$

via the chain rule, and so the second derivatives of σ are

$$\sigma_{,ab} = [\sigma_{,\gamma}\gamma_{,a}]_{,b} = \sigma_{,\gamma\gamma}\gamma_{,a}\gamma_{,b} + \sigma_{,\gamma}\gamma_{,ab}. \tag{H.3}$$

We have the following results for the Christoffel symbols:

$$\Gamma^a_{ij} = \frac{1}{2}g^{ab}[\partial_i g_{bj} + \partial_j g_{ib} - \partial_b g_{ij}] = 0 \tag{H.4}$$

$$\Gamma^i_{ab} = -\frac{1}{2}g^{ir}\partial_r g_{ab} = -rg^{ir}h_{ab} \tag{H.5}$$

$$\Gamma^c_{ab} = \frac{1}{2}r^{-2}h^{cd}[r^2\partial_a h_{db} + r^2\partial_b h_{da} - \partial_d h_{ab}r^2] \equiv \tilde{\Gamma}^k_{ij} \tag{H.6}$$

where h_{ab} is the 2-metric that determines the geometry of the black hole event horizon (G.8). Using (H.2-H.6) we find

$$\begin{aligned}\Box\sigma &= g^{ij}\sigma_{,ij} - g^{ij}\Gamma^k_{ij}\sigma_{,k} + r^{-2}h^{ab}\gamma_{,a}\gamma_{,b}\sigma_{,\gamma\gamma} + r^{-2}h^{ab}\gamma_{,ab}\sigma_{,\gamma} \\ &\quad + r^{-2}h^{ab}rg^{ir}\sigma_{,i}h_{ab} - r^{-2}h^{ab}\tilde{\Gamma}^c_{ab}\gamma_{,c}\sigma_{,\gamma} \\ &= g^{ij}\sigma_{,ij} - g^{ij}\Gamma^k_{ij}\sigma_{,k} + r^{-2}h^{ab}\gamma_{,a}\gamma_{,b}\sigma_{,\gamma\gamma} + \frac{2}{r}g^{rr}\sigma_{,r} + \frac{1}{r^2}\sigma_\gamma\hat{\Box}\gamma\end{aligned} \tag{H.7}$$

where

$$\hat{\Box}\gamma = h^{ab}[\gamma_{,ab} - \tilde{\Gamma}^{c}_{ab}\gamma_{,c}]. \tag{H.8}$$

Our method for calculating $\hat{\Box}\gamma$ follows that in [147]. In S^2, the D'Alembertian is given by

$$\Box = (\sin\theta)^{-1}\frac{d}{d\theta}\left(\sin\theta\frac{d}{d\theta}\right) + (\sin\theta)^{-2}\frac{d^2}{d\varphi^2}. \tag{H.9}$$

If we fix the point x' at the North pole (i.e. $\theta' = 0$), then the geodesic distance between the points $x = (\theta, \varphi)$ and x' is given by $\gamma_S = \theta$ and so

$$\hat{\Box}\gamma_S = (\sin\gamma_S)^{-1}\frac{d}{d\gamma_S}(\sin\gamma_S) = (\sin\gamma_S)^{-1}\cos\gamma_S = \cot\gamma_S. \tag{H.10}$$

In $\mathbb{R}^2$, the D'Alembertian is given by

$$\Box = \frac{1}{\theta}\frac{d}{d\theta}\left(\theta\frac{d}{d\theta}\right) + \frac{1}{\theta^2}\frac{d^2}{d\varphi^2}. \tag{H.11}$$

When we have coordinates centred about x', the geodesic distance between $x = (\theta, \varphi)$ and x' is $\gamma_R = \theta$ and so

$$\hat{\Box}\gamma_R = \frac{1}{\gamma_R}\frac{d}{d\gamma_R}\gamma_R = \gamma_R^{-1}. \tag{H.12}$$

Finally, in the hyperbolic plane, the D'Alembertian is

$$\Box = (\sinh\theta)^{-1}\frac{d}{d\theta}\left(\sinh\theta\frac{d}{d\theta}\right) + (\sinh\theta)^{-2}\frac{d^2}{d\varphi^2}. \tag{H.13}$$

The geodesic distance between x and x' is $\gamma_H = \theta$ for coordinates centred about x', and hence

$$\hat{\Box}\gamma_H = (\sinh\gamma_H)^{-1}\frac{d}{d\gamma_H}(\sinh\gamma_H) = (\sinh\gamma_H)^{-1}\cosh\gamma_H = \coth\gamma_H. \tag{H.14}$$

Appendix I

Frobenius series approximation to radial function

In this appendix, we find the indices α_1, α_2 in the Frobenius series approximations (5.93, 5.98) of solutions of the homogeneous version of (5.24). We shall begin near the horizon. Substituting (5.93) into (5.91) gives

$$\sum_{j=0}^{\infty} a_j \left[(\alpha_1 + j)(\alpha_1 + j - 1) + (\alpha_1 + j) - \frac{n^2\kappa^2}{f_1(r)^2} \right] (r - r_h)^{\alpha_1 + j - 2} + \sum_{j=0}^{\infty} a_j \left[\left(\frac{2}{r} + \frac{f_1'(r)}{f_1(r)} \right) (\alpha_1 + j) - \frac{1}{6 f_1(r)} R + \frac{\nu_\ell}{r^2 f_1(r)} \right] (r - r_h)^{\alpha_1 + j - 1} = 0 \quad \text{(I.1)}$$

where we have now defined $f(r) = (r - r_h) f_1(r)$ for some function $f_1(r)$ that is finite and non-zero at $r = r_h$. At leading order, we find

$$a_0 \left[\alpha_1(\alpha_1 - 1) + \alpha_1 - \frac{n^2\kappa^2}{f_1(r_h)^2} \right] = 0 \quad \text{(I.2)}$$

where $f_1(r_h) = 2\kappa$. Since a_0 must be non-zero for non-trivial solutions, we find

$$\alpha_1 = \pm \frac{n}{2}. \quad \text{(I.3)}$$

The coefficients a_j for $j \geq 0$ are found via a recurrence relation that can easily be computed in Mathematica.

We now turn our attention to the radial function $q_{n\ell}$, which satisfies boundary conditions at infinity. We search for a Frobenius series of the form (5.98). Substituting this into (5.96), we obtain

$$\sum_{j=0}^{\infty} b_j \left[(\alpha_2 + j)(\alpha_2 + j - 1) - 2(\alpha_2 + j) - \frac{6}{6 f_2(s)} \right] s^{\alpha_2 + j - 2} + \sum_{j=0}^{\infty} b_j \frac{f_2'(s)}{f_2(s)} (\alpha_2 + j) s^{\alpha_2 + j - 1} + \sum_{j=0}^{\infty} b_j \left[\frac{\nu_\ell}{f_2(s)} - \frac{n^2 \kappa^2}{f_2(s)} \right] s^{\alpha_2 + j} = 0 \quad \text{(I.4)}$$

where we have written $f(s) = f_2(s)/s^2$. At leading order, noting that $f_2(0) = L^{-2}$, we find

$$\alpha_2(\alpha_2 - 1) - 2\alpha_2 - \frac{L^2 R}{6} = 0. \quad \text{(I.5)}$$

Solving this quadratic, we find

$$\alpha_2 = \frac{3}{2} \pm \frac{1}{2} \sqrt{9 + \frac{2L^2}{3} R}. \quad \text{(I.6)}$$

As before, the coefficients b_j can be found by using Mathematica to evaluate the recurrence relation.

References

[1] P. Candelas, "Vacuum polarization in Schwarzschild spacetime," *Physical Review D*, vol. 21, no. 8, p. 2185, 1980.

[2] P. Candelas and K. Howard, "Vacuum $\langle \varphi^2 \rangle$ in Schwarzschild spacetime," *Physical Review D*, vol. 29, no. 8, p. 1618, 1984.

[3] S. Christensen and S. Fulling, "Trace anomalies and the Hawking effect," *Physical Review D*, vol. 15, no. 8, p. 2088, 1977.

[4] Y. Décanini and A. Folacci, "Hadamard renormalization of the stress-energy tensor for a quantized scalar field in a general spacetime of arbitrary dimension," *Physical Review D*, vol. 78, no. 4, p. 044025, 2008.

[5] S. J. Avis, C. J. Isham, and D. Storey, "Quantum field theory in anti-de Sitter space-time," *Physical Review D*, vol. 18, no. 10, p. 3565, 1978.

[6] C. Dappiaggi and H. R. Ferreira, "Hadamard states for a scalar field in anti–de sitter spacetime with arbitrary boundary conditions," *Physical Review D*, vol. 94, no. 12, p. 125016, 2016.

[7] T. Morley, P. Taylor, and E. Winstanley, "Quantum field theory on global anti-de Sitter space-time with Robin boundary conditions," *arXiv preprint arXiv:2004.02704*, 2020.

[8] T. Morley, P. Taylor, and E. Winstanley, "Vacuum polarization on topological black holes," *Classical and Quantum Gravity*, vol. 35, no. 23, p. 235010, 2018.

[9] T. Morley, P. Taylor, and E. Winstanley, "Vacuum polarization on topological black holes with Robin boundary conditions," *arXiv preprint arXiv:2010.01562*, 2020.

[10] A. Flachi and T. Tanaka, "Vacuum polarization in asymptotically anti-de Sitter black hole geometries," *Physical Review D*, vol. 78, no. 6, p. 064011, 2008.

[11] P. Taylor and C. Breen, "Mode-sum prescription for the vacuum polarization in odd dimensions," *Physical Review D*, vol. 94, no. 12, p. 125024, 2016.

[12] P. Taylor and C. Breen, "Mode-sum prescription for vacuum polarization in black hole spacetimes in even dimensions," *Physical Review D*, vol. 96, no. 10, p. 105020, 2017.

[13] C. Breen and P. Taylor, "Vacuum polarization for varying quantum scalar field parameters in Schwarzschild–anti–de Sitter spacetime," *Physical Review D*, vol. 98, no. 10, p. 105006, 2018.

[14] N. D. Birrell and P. C. W. Davies, *Quantum fields in curved space.* Cambridge University Press, 1984.

[15] C. J. Fewster, "Lectures on quantum field theory in curved spacetime," 2008, https://www.mis.mpg.de/publications/other-series/ln/lecturenote-3908.html.

[16] V. Mukhanov and S. Winitzki, *Introduction to quantum effects in gravity.* Cambridge University Press, 2007.

[17] D. Tong, "Lectures on quantum field theory," *Part III Cambridge University Mathematics Tripos, Michaelmas*, 2006, http://www.damtp.cam.ac.uk/user/tong/qft.html.

[18] A. Zee, *Quantum field theory in a nutshell.* Princeton University Press, 2010.

[19] V. E. Ambrus, *Dirac fermions on rotating space-times.* PhD thesis, University of Sheffield, 2014.

[20] C. W. Misner, K. S. Thorne, and J. A. Wheeler, *Gravitation.* Macmillan, 1973.

[21] R. M. Wald, *General relativity.* University of Chicago Press, 2010.

[22] S. M. Carroll, "The cosmological constant," *Living Reviews in Relativity*, vol. 4, no. 1, p. 1, 2001.

[23] S. E. Rugh and H. Zinkernagel, "The quantum vacuum and the cosmological constant problem," *Studies in History and Philosophy of Science Part B: Studies in History and Philosophy of Modern Physics*, vol. 33, no. 4, p. 663, 2002.

[24] S. Perlmutter, G. Aldering, G. Goldhaber, R. Knop, P. Nugent, P. Castro, S. Deustua, S. Fabbro, A. Goobar, D. Groom, *et al.*, "Measurements of Ω and Λ from 42 high-redshift supernovae," *The Astrophysical Journal*, vol. 517, no. 2, p. 565, 1999.

[25] A. G. Riess, A. V. Filippenko, P. Challis, A. Clocchiatti, A. Diercks, P. M. Garnavich, R. L. Gilliland, C. J. Hogan, S. Jha, R. P. Kirshner, *et al.*, "Observational evidence from supernovae for an accelerating universe and a cosmological constant," *The Astronomical Journal*, vol. 116, no. 3, p. 1009, 1998.

[26] C. M. Will, "The confrontation between general relativity and experiment," *Astrophysics and Space Science*, vol. 283, no. 4, p. 543, 2003.

[27] B. P. Abbott, R. Abbott, T. Abbott, M. Abernathy, F. Acernese, K. Ackley, C. Adams, T. Adams, P. Addesso, R. Adhikari, *et al.*, "Observation of gravitational waves from a binary black hole merger," *Physical Review Letters*, vol. 116, no. 6, p. 061102, 2016.

[28] B. P. Abbott, R. Abbott, T. Abbott, F. Acernese, K. Ackley, C. Adams, T. Adams, P. Addesso, R. Adhikari, V. Adya, *et al.*, "GW170817: observation of gravitational waves from a binary neutron star inspiral," *Physical Review Letters*, vol. 119, no. 16, p. 161101, 2017.

[29] K. Akiyama, A. Alberdi, W. Alef, K. Asada, R. Azulay, A.-K. Baczko, D. Ball, M. Baloković, J. Barrett, D. Bintley, *et al.*, "First M87 event horizon telescope results. IV. Imaging the central supermassive black hole," *The Astrophysical Journal Letters*, vol. 875, no. 1, p. L4, 2019.

[30] S. W. Hawking, "Particle creation by black holes," *Communications in mathematical physics*, vol. 43, no. 3, p. 199, 1975.

[31] R. M. Wald, "The back reaction effect in particle creation in curved spacetime," *Communications in Mathematical Physics*, vol. 54, no. 1, p. 1, 1977.

[32] S. M. Carroll, *Spacetime and geometry. An introduction to general relativity.* Cambridge University Press, 2004.

[33] P.-H. Lambert, "Introduction to black hole evaporation," *PoS*, vol. Modave2013, p. 001, 2013.

[34] S. A. Fulling, *Aspects of quantum field theory in curved spacetime*, vol. 17. Cambridge University Press, 1989.

[35] W. G. Unruh, "Notes on black-hole evaporation," *Physical Review D*, vol. 14, no. 4, p. 870, 1976.

[36] L. C. Crispino, A. Higuchi, and G. E. Matsas, "The Unruh effect and its applications," *Reviews of Modern Physics*, vol. 80, no. 3, p. 787, 2008.

[37] D. G. Boulware, "Quantum field theory in Schwarzschild and Rindler spaces," *Physical Review D*, vol. 11, no. 6, p. 1404, 1975.

[38] J. B. Hartle and S. W. Hawking, "Path-integral derivation of black-hole radiance," *Physical Review D*, vol. 13, no. 8, p. 2188, 1976.

[39] M. Casals, S. R. Dolan, B. C. Nolan, A. C. Ottewill, and E. Winstanley, "Quantization of fermions on Kerr space-time," *Phys. Rev. D*, vol. 87, p. 064027, Mar 2013.

[40] E. Poisson, *A relativist's toolkit: the mathematics of black-hole mechanics.* Cambridge University Press, 2004.

[41] S. Christensen, "Vacuum expectation value of the stress tensor in an arbitrary curved background: The covariant point-separation method," *Physical Review D*, vol. 14, no. 10, p. 2490, 1976.

[42] R. Balbinot, A. Fabbri, and I. Shapiro, "Vacuum polarization in Schwarzschild space-time by anomaly induced effective actions," *Nuclear Physics B*, vol. 559, no. 1-2, p. 301, 1999.

[43] V. Frolov and I. Novikov, *Black hole physics: basic concepts and new developments*, vol. 96. Springer Science & Business Media, 2012.

[44] T. Jacobson, "Note on Hartle-Hawking vacua," *Physical Review D*, vol. 50, no. 10, p. R6031, 1994.

[45] S. Deser, M. J. Duff, and C. Isham, "Non-local conformal anomalies," *Nuclear Physics B*, vol. 111, no. 1, p. 45, 1976.

[46] R. M. Wald, "Trace anomaly of a conformally invariant quantum field in curved spacetime," *Physical Review D*, vol. 17, no. 6, p. 1477, 1978.

[47] R. M. Wald, *Quantum field theory in curved spacetime and black hole thermodynamics*. University of Chicago Press, 1994.

[48] V. Moretti, "Local ζ-function techniques vs. point-splitting procedure: a few rigorous results," *Communications in Mathematical Physics*, vol. 201, no. 2, p. 327, 1999.

[49] V. Moretti, "Proof of the symmetry of the off-diagonal heat-kernel and Hadamard's expansion coefficients in general C^∞ Riemannian manifolds," *Communications in Mathematical Physics*, vol. 208, no. 2, p. 283, 1999.

[50] V. Moretti, "One-loop stress-tensor renormalization in curved background: the relation between ζ-function and point-splitting approaches, and an improved point-splitting procedure," *Journal of Mathematical Physics*, vol. 40, no. 8, p. 3843, 1999.

[51] V. Moretti, "Proof of the symmetry of the off-diagonal Hadamard/Seeley–deWitt's coefficients in C^∞ Lorentzian manifolds by a local Wick rotation," *Communications in Mathematical Physics*, vol. 212, no. 1, p. 165, 2000.

[52] S. Hollands and R. M. Wald, "Local Wick polynomials and time ordered products of quantum fields in curved spacetime," *Communications in Mathematical Physics*, vol. 223, no. 2, p. 289, 2001.

[53] S. Hollands and R. M. Wald, "Existence of local covariant time ordered products of quantum fields in curved spacetime," *Communications in Mathematical Physics*, vol. 231, no. 2, p. 309, 2002.

[54] V. Moretti, “Comments on the stress-energy tensor operator in curved spacetime,” *Communications in Mathematical Physics*, vol. 232, no. 2, p. 189, 2003.

[55] S. Hollands and R. M. Wald, “On the renormalization group in curved spacetime,” *Communications in Mathematical Physics*, vol. 237, no. 1-2, p. 123, 2003.

[56] S. Hollands and R. M. Wald, “Conservation of the stress tensor in perturbative interacting quantum field theory in curved spacetimes,” *Reviews in Mathematical Physics*, vol. 17, no. 3, p. 227, 2005.

[57] E. Poisson, A. Pound, and I. Vega, “The motion of point particles in curved spacetime,” *Living Reviews in Relativity*, vol. 14, no. 1, pp. 1–190, 2011.

[58] J. H. Van Vleck, “The correspondence principle in the statistical interpretation of quantum mechanics,” *Proceedings of the National Academy of Sciences of the United States of America*, vol. 14, no. 2, p. 178, 1928.

[59] C. Morette, “On the definition and approximation of Feynman’s path integrals,” *Physical Review*, vol. 81, no. 5, p. 848, 1951.

[60] M. Visser, “Van Vleck determinants: Geodesic focusing in Lorentzian spacetimes,” *Physical Review D*, vol. 47, no. 6, p. 2395, 1993.

[61] M. Brown and A. Ottewill, “Photon propagators and the definition and approximation of renormalized stress tensors in curved space-time,” *Physical Review D*, vol. 34, no. 6, p. 1776, 1986.

[62] V. E. Ambruş, C. Kent, and E. Winstanley, “Analysis of scalar and fermion quantum field theory on anti-de sitter spacetime,” *International Journal of Modern Physics D*, vol. 27, no. 11, p. 1843014, 2018.

[63] K. Howard, “Vacuum $\langle T_{\mu\nu} \rangle$ in Schwarzschild spacetime,” *Physical Review D*, vol. 30, no. 12, p. 2532, 1984.

[64] K. W. Howard and P. Candelas, “Quantum stress tensor in Schwarzschild spacetime,” *Physical Review Letters*, vol. 53, no. 5, p. 403, 1984.

[65] J. Schwinger, “The theory of quantized fields. i,” *Physical Review*, vol. 82, no. 6, p. 914, 1951.

[66] B. S. DeWitt, “Quantum field theory in curved spacetime,” *Physics Reports*, vol. 19, no. 6, pp. 295–357, 1975.

[67] Y. Decanini and A. Folacci, “Off-diagonal coefficients of the Dewitt-Schwinger and Hadamard representations of the Feynman propagator,” *Physical Review D*, vol. 73, no. 4, p. 044027, 2006.

[68] P. R. Anderson, W. A. Hiscock, and D. A. Samuel, “Stress-energy tensor of quantized scalar fields in static spherically symmetric spacetimes,” *Physical Review D*, vol. 51, no. 8, p. 4337, 1995.

[69] P. R. Anderson, “A method to compute $\langle \varphi^2 \rangle$ in asymptotically flat, static, spherically symmetric spacetimes,” *Physical Review D*, vol. 41, no. 4, p. 1152, 1990.

[70] E. Winstanley and P. M. Young, “Vacuum polarization for lukewarm black holes,” *Physical Review D*, vol. 77, no. 2, p. 024008, 2008.

[71] C. Breen and A. C. Ottewill, “Extended Green-Liouville asymptotics and vacuum polarization for lukewarm black holes,” *Physical Review D*, vol. 82, no. 8, p. 084019, 2010.

[72] C. Breen and A. C. Ottewill, “Hadamard renormalisation of the stress energy tensor on the horizons of a spherically symmetric black hole space-time,” *Physical Review D*, vol. 85, no. 6, p. 064026, 2012.

[73] C. Breen and A. C. Ottewill, “Hadamard renormalization of the stress energy tensor in a spherically symmetric black hole space-time with an application to lukewarm black holes,” *Physical Review D*, vol. 85, no. 8, p. 084029, 2012.

[74] M. Fawcett, “The energy-momentum tensor near a black hole,” *Communications in Mathematical Physics*, vol. 89, no. 1, pp. 103–115, 1983.

[75] B. P. Jensen, J. G. Mc Laughlin, and A. C. Ottewill, “Anisotropy of the quantum thermal state in Schwarzschild space-time,” *Physical Review D*, vol. 45, no. 8, p. 3002, 1992.

[76] A. C. Ottewill and P. Taylor, “Renormalized vacuum polarization and stress tensor on the horizon of a Schwarzschild black hole threaded by a cosmic string,” *Classical and Quantum Gravity*, vol. 28, no. 1, p. 015007, 2010.

[77] V. Frolov, “Vacuum polarization near the event horizon of a charged rotating black hole,” *Physical Review D*, vol. 26, no. 4, p. 954, 1982.

[78] A. DeBenedictis, “$\langle \varphi^2 \rangle$ in the spacetime of a cylindrical black hole,” *General Relativity and Gravitation*, vol. 31, no. 10, p. 1549, 1999.

[79] G. Freitas and M. Casals, “A novel method for renormalization in quantum-field theory in curved spacetime,” *International Journal of Modern Physics D*, vol. 27, no. 11, p. 1843001, 2018.

[80] A. Levi and A. Ori, “Pragmatic mode-sum regularization method for semiclassical black-hole spacetimes,” *Physical Review D*, vol. 91, no. 10, p. 104028, 2015.

[81] A. Levi and A. Ori, “Mode-sum regularization of $\left\langle \phi^2 \right\rangle$ in the angular-splitting method,” *Physical Review D*, vol. 94, no. 4, p. 044054, 2016.

[82] A. Levi and A. Ori, “Versatile method for renormalized stress-energy computation in black-hole spacetimes,” *Physical Review Letters*, vol. 117, no. 23, p. 231101, 2016.

[83] A. Levi, E. Eilon, A. Ori, and M. van de Meent, "Renormalized stress-energy tensor of an evaporating spinning black hole," *Physical Review Letters*, vol. 118, no. 14, p. 141102, 2017.

[84] A. Lanir, A. Levi, A. Ori, and O. Sela, "Two-point function of a quantum scalar field in the interior region of a Reissner-Nordstrom black hole," *Physical Review D*, vol. 97, no. 2, p. 024033, 2018.

[85] A. Lanir, A. Levi, and A. Ori, "Mode-sum renormalization of $\langle\Phi^2\rangle$ for a quantum scalar field inside a Schwarzschild black hole," *Physical Review D*, vol. 98, no. 8, p. 84017, 2018.

[86] S. W. Hawking and G. F. R. Ellis, *The large scale structure of space-time.* Cambridge University Press, 1973.

[87] I. Bengtsson, "Anti-de sitter space," *Lecture notes*, 1998, http://3dhouse.se/ingemar/relteori/Kurs.pdf.

[88] U. Moschella, "The de Sitter and anti-de Sitter sightseeing tour," in *Einstein, 1905–2005*, p. 120, Springer, 2006.

[89] L. M. Sokołowski, "The bizarre anti-de Sitter spacetime," *International Journal of Geometric Methods in Modern Physics*, vol. 13, no. 9, p. 1630016, 2016.

[90] M. Socolovsky, "Schwarzschild black hole in anti-de Sitter space," *Advances in Applied Clifford Algebras*, vol. 28, no. 1, p. 18, 2018.

[91] C. B. Bayona and N. R. Braga, "Anti-de Sitter boundary in Poincare coordinates," *General Relativity and Gravitation*, vol. 39, no. 9, p. 1367, 2007.

[92] J. Maldacena, "The large-N limit of superconformal field theories and supergravity," *International Journal of Theoretical Physics*, vol. 38, no. 4, p. 1113, 1999.

[93] S. S. Gubser, I. R. Klebanov, and A. M. Polyakov, "Gauge theory correlators from non-critical string theory," *Physics Letters B*, vol. 428, no. 1-2, p. 105, 1998.

[94] E. Witten, "Anti de Sitter space and holography," *Advances in Theoretical and Mathematical Physics*, vol. 2, no. 2, p. 253, 1998.

[95] A. Zaffaroni, "Introduction to the AdS-CFT correspondence," *Classical and Quantum Gravity*, vol. 17, no. 17, p. 3571, 2000.

[96] A. V. Ramallo, "Introduction to the AdS/CFT correspondence," in *Lectures on Particle Physics, Astrophysics and Cosmology*, p. 411, Springer, 2015.

[97] V. E. Hubeny, "The AdS/CFT correspondence," *Classical and Quantum Gravity*, vol. 32, no. 12, p. 124010, 2015.

[98] M. Natsuume, *AdS/CFT duality user guide.* Springer, 2015.

[99] S. Kovacs, "N= 4 supersymmetric Yang-Mills theory and the AdS/SCFT correspondence," *PhD thesis hep-th/9908171*, 1999.

[100] S. Weinberg, "Implications of dynamical symmetry breaking," *Physical Review D*, vol. 13, no. 4, p. 974, 1976.

[101] T. Mohaupt, "Introduction to string theory," in *Quantum gravity*, p. 173, Springer, 2003.

[102] B. Zwiebach, *A first course in string theory.* Cambridge University Press, 2004.

[103] D. McMahon, *String theory demystified.* McGraw-Hill, 2009.

[104] J. Louis, T. Mohaupt, and S. Theisen, "String theory: An overview," in *Approaches to Fundamental Physics*, p. 289, Springer, 2007.

[105] L. Susskind, "The world as a hologram," *Journal of Mathematical Physics*, vol. 36, no. 11, p. 6377, 1995.

[106] G. t'Hooft, "Dimensional reduction in quantum gravity," *Salamfestschrift: a collection of talks*, vol. 4, p. 1, 1993.

[107] D. Birmingham, "Topological black holes in anti-de Sitter space," *Classical and Quantum Gravity*, vol. 16, no. 4, p. 1197, 1999.

[108] P. Breitenlohner and D. Z. Freedman, "Positive energy in anti-de Sitter backgrounds and gauged extended supergravity," *Physics Letters B*, vol. 115, no. 3, p. 197, 1982.

[109] P. Breitenlohner and D. Z. Freedman, "Stability in gauged extended supergravity," *Annals of Physics*, vol. 144, no. 2, p. 249, 1982.

[110] B. Allen, A. Folacci, and G. Gibbons, "Anti-de Sitter space at finite temperature," *Physics Letters B*, vol. 189, no. 3, p. 304, 1987.

[111] C. Kent and E. Winstanley, "Hadamard renormalized scalar field theory on anti-de Sitter spacetime," *Physical Review D*, vol. 91, no. 4, p. 044044, 2015.

[112] J. P. M. Pitelli, V. S. Barroso, and R. A. Mosna, "Boundary conditions and renormalized stress-energy tensor on a Poincaré patch of AdS_2," *Physical Review D*, vol. 99, no. 12, p. 125008, 2019.

[113] J. Pitelli, "Comment on Hadamard states for a scalar field in anti–de Sitter spacetime with arbitrary boundary conditions," *Physical Review D*, vol. 99, no. 10, p. 108701, 2019.

[114] D. Deutsch and P. Candelas, "Boundary effects in quantum field theory," *Physical Review D*, vol. 20, no. 12, p. 3063, 1979.

[115] A. Romeo and A. A. Saharian, “Casimir effect for scalar fields under Robin boundary conditions on plates,” *Journal of Physics A: Mathematical and General*, vol. 35, no. 5, p. 1297, 2002.

[116] C. Dappiaggi, H. R. Ferreira, and A. Marta, “Ground states of a Klein-Gordon field with Robin boundary conditions in global anti–de Sitter spacetime,” *Physical Review D*, vol. 98, no. 2, p. 025005, 2018.

[117] V. S. Barroso and J. Pitelli, “Boundary conditions and vacuum fluctuations in AdS_4,” *General Relativity and Gravitation*, vol. 52, no. 3, p. 1, 2020.

[118] A. Ishibashi and R. M. Wald, “Dynamics in non-globally-hyperbolic static spacetimes: III. Anti-de Sitter spacetime,” *Classical and Quantum Gravity*, vol. 21, no. 12, p. 2981, 2004.

[119] J. Bros, H. Epstein, and U. Moschella, “Towards a general theory of quantized fields on the anti-de Sitter space-time,” *Communications in Mathematical Physics*, vol. 231, no. 3, p. 481, 2002.

[120] F. W. Olver, D. W. Lozier, R. F. Boisvert, and C. W. Clark, *NIST handbook of mathematical functions hardback and CD-ROM.* Cambridge University Press, 2010.

[121] C. Murdia, Y. Nomura, and P. Rath, “Coarse-graining holographic states: A semiclassical flow in general spacetimes,” *Physical Review D*, vol. 102, no. 8, p. 086001, 2020.

[122] J. Spanier and K. B. Oldham, *An atlas of functions.* Hemisphere Publishing Corporation, New York, 1987.

[123] C. Burgess and C. Lutken, “Propagators and effective potentials in anti-de Sitter space,” *Physical Letters B*, vol. 153, no. 153, p. 137, 1985.

[124] B. S. Kay, M. J. Radzikowski, and R. M. Wald, “Quantum field theory on spacetimes with a compactly generated Cauchy horizon,” *Communications in Mathematical Physics*, vol. 183, no. 3, p. 533, 1997.

[125] O. Gannot and M. Wrochna, “Propagation of singularities on AdS spacetimes for general boundary conditions and the holographic Hadamard condition,” *Journal of the Institute of Mathematics of Jussieu*, p. 1, 2018.

[126] C. Kent, *Quantum scalar field theory on anti-de Sitter space.* PhD thesis, University of Sheffield, 2013.

[127] D. R. Brill, J. Louko, and P. Peldan, “Thermodynamics of (3+1)-dimensional black holes with toroidal or higher genus horizons,” *Physical Review D*, vol. 56, no. 6, p. 3600, 1997.

[128] J. P. Lemos, “Two-dimensional black holes and planar general relativity,” *Classical and Quantum Gravity*, vol. 12, no. 4, p. 1081, 1995.

[129] J. S. Lemos, “Three dimensional black holes and cylindrical general relativity,” *Physics Letters B*, vol. 353, no. 1, p. 46, 1995.

[130] J. P. Lemos and V. T. Zanchin, “Rotating charged black strings and three-dimensional black holes,” *Physical Review D*, vol. 54, no. 6, p. 3840, 1996.

[131] L. Vanzo, “Black holes with unusual topology,” *Physical Review D*, vol. 56, no. 10, p. 6475, 1997.

[132] R.-G. Cai and Y.-Z. Zhang, “Black plane solutions in four-dimensional spacetimes,” *Physical Review D*, vol. 54, no. 8, p. 4891, 1996.

[133] R. B. Mann, “Pair production of topological anti-de sitter black holes,” *Classical and Quantum Gravity*, vol. 14, no. 5, p. L109, 1997.

[134] W. Smith and R. Mann, “Formation of topological black holes from gravitational collapse,” *Physical Review D*, vol. 56, no. 8, p. 4942, 1997.

[135] R. Mann, “Black holes of negative mass,” *Classical and Quantum Gravity*, vol. 14, no. 10, p. 2927, 1997.

[136] R. B. Mann, “Topological black holes - outside looking in,” *AnIPS*, vol. 13, p. 311, 1997.

[137] S. W. Hawking and D. N. Page, “Thermodynamics of black holes in anti-de Sitter space,” *Communications in Mathematical Physics*, vol. 87, no. 4, p. 577, 1983.

[138] S. Åminneborg, I. Bengtsson, S. Holst, and P. Peldan, “Making anti-de Sitter black holes,” *Classical and Quantum Gravity*, vol. 13, no. 10, p. 2707, 1996.

[139] R. Emparan and H. S. Reall, “Black holes in higher dimensions,” *Living Reviews in Relativity*, vol. 11, no. 1, p. 6, 2008.

[140] Y. Chen and E. Teo, “Black holes with bottle-shaped horizons,” *Physical Review D*, vol. 93, no. 12, p. 124028, 2016.

[141] I. S. Gradshteyn and I. M. Ryzhik, *Table of integrals, series, and products.* Academic Press, 2014.

[142] G. N. Watson, *A treatise on the theory of Bessel functions.* Cambridge University Press, 1995.

[143] G. H. Holzegel and C. M. Warnick, “Boundedness and growth for the massive wave equation on asymptotically anti-de Sitter black holes,” *Journal of Functional Analysis*, vol. 266, no. 4, p. 2436, 2014.

[144] B. Araneda and G. Dotti, “Instability of asymptotically anti-de Sitter black holes under Robin conditions at the timelike boundary,” *Physical Review D*, vol. 96, no. 10, p. 104020, 2017.

[145] C. M. Warnick, “The massive wave equation in asymptotically AdS spacetimes,” *Communications in Mathematical Physics*, vol. 321, no. 1, p. 85, 2013.

[146] D. J. Griffiths and D. F. Schroeter, *Introduction to quantum mechanics.* Cambridge University Press, 2018.

[147] B. Allen and T. Jacobson, “Vector two-point functions in maximally symmetric spaces,” *Communications in Mathematical Physics*, vol. 103, no. 4, p. 669, 1986.

[148] L. Durand, P. M. Fishbane, and L. Simmons Jr, “Expansion formulas and addition theorems for Gegenbauer functions,” *Journal of Mathematical Physics*, vol. 17, no. 11, p. 1933, 1976.